Emergent Phenomena in Quantum Dynamics of Non-Thermal Systems

Yiqiu Han

A dissertation

submitted to the Faculty of

the Department of Physics

in partial fulfillment

of the requirements for the degree of

Doctor of Philosophy

Boston College

Morrissey College of Arts and Sciences

Graduate School

June 2024

Emergent Phenomena in Quantum Dynamics of Non-Thermal Systems

Yiqiu Han

Advisor: Xiao Chen, Ph.D.

The development of highly controllable quantum coherent simulators such as superconducting qubits and Rydberg atom arrays has stimulated the study of non-equilibrium quantum dynamics, opening the door to exciting topics including dynamical phase transitions, thermalization, transport, and quantum error correction. This thesis addresses various questions from non-equilbrium quantum dynamics, with a concentration on measurement-induced phase transitions (MIPT), adaptive dynamics with feedback mechanism, and Hilbert space fragmentation. In the first part, we study the hybrid quantum automaton (QA) circuits with different symmetries subject to local composite measurements. For $\mathbb{Z}_2$-symmetric hybrid QA circuits, there exists an entanglement phase transition from a volume-law phase to a critical phase by varying the measurement rate. The special feature of QA circuits enables us to interpret the entanglement dynamics in terms of a stochastic particle model. With the help of this stochastic model, we further investigate the entanglement fluctuations and quantum error correcting property of the volume-law phase in QA circuits with no symmetry, and study the entanglement dynamics in QA circuits with U(1) symmetry. Despite being a hallmark of non-unitary quantum dynamics, MIPT is absent in the density matrix averaged over measurement outcomes. In the second part, we introduce an adaptive quantum circuit subject to measurements with feedback. The feedback is applied according to the measurement outcome and steers the system towards a unique state above certain measurement threshold. We show that there exists an absorbing phase transition in both quantum trajectories and quantum channels. In the end, we turn to the phenomenon of Hilbert space fragmentation (HSF), whereby dynamical constraints fragment Hilbert space into many disconnected sectors, providing a simple mechanism by which thermalization can be arrested. However, little is known about how thermalization occurs in situations where the constraints are not exact. To study this, we consider a situation in which a fragmented 1d chain with pair-flip constraints is coupled to a thermal bath at its boundary. For product states quenched under Hamiltonian dynamics, we numerically observe an exponentially long thermalization time, manifested in both entanglement dynamics and the relaxation of local observables. To understand this, we study an analogous model of random unitary circuit dynamics, where we rigorously prove that the thermalization time scales exponentially with system size. Slow thermalization in this model is shown to be a consequence of strong bottlenecks in configuration space, demonstrating a new way of producing anomalously slow thermalization dynamics.

Contents

List of Figures

List of Tables

Publication/Preprint List

- **Yiqiu Han**, Xiao Chen, Ethan Lake, *Exponentially slow thermalization and the robustness of Hilbert space fragmentation*, arXiv:2401.11294.
- **Yiqiu Han**, Xiao Chen, *Entanglement dynamics in U(1) symmetric hybrid quantum automaton circuits*, Quantum **7**, 1200 (2023).
- Vikram Ravindranath, **Yiqiu Han**, Zhicheng Yang, Xiao Chen, *Entanglement steering in adaptive circuits with feedback*, Phys. Rev. B **108**, L041103.
- **Yiqiu Han**, Xiao Chen, *Entanglement structure in the volume-law phase of hybrid quantum automaton circuits*, Phys. Rev. B **107**, 014306.
- **Yiqiu Han**, Xiao Chen, *Measurement-induced criticality in $\mathbb{Z}_2$-symmetric quantum automaton circuits*, Phys. Rev. B **105**, 064306.

Acknowledgements

Many years later, as she faced the committee squad, Yiqiu Han was to remember that distant afternoon when her relativity professor took her to discover the beauty of physics.

One hundred years of PhD

As someone with mathematical background when I began my PhD program six years ago, being able to learn and think about physics has felt like a dream come true. As this journey comes to an end, I would like to express my gratitude to everyone who has supported me along the way.

First and foremost, I would like to extend my greatest gratitude to my advisor, Prof. Xiao Chen, for introducing me to the exciting field of non-equilibrium quantum dynamics and teaching me how to think as a physicist. During our first project, I struggled to explain the physics of a random quantum circuit with minimal structure. He taught me a physicist's insight of discerning what is important and what to neglect, and introduced me to the art of approximation, which was new to me as someone from a mathematical background. He also made me realize that the physical idea behind seemingly intricate mathematical structures is often simple. Together, we developed a way to interpret the entanglement dynamics of this quantum system through a classical stochastic model, which has become a central theme of my future research. Beyond physics, he serves as an inspiring role model in running, and I fondly recall the moment he passed me like a lightning bolt during the Boston Marathon. Over these years, I've observed that good physicists are typically tough to themselves, both physically and mentally. This relentless pursuit of excellence, not for surpassing others but for expanding one's potential in life, has profoundly influenced me.

I would like to thank Ethan Lake, my partner in crime. He always has an endless stream of ideas, quirky yet profound. I enjoyed and learned a lot from our countless conversations about physics, and his unique way of explaining concepts by interrogating and forcing one to think with him together, making the ideas crystal clear. Beyond physics, I am grateful to him for introducing me to rock climbing, a sport that emphasizes problem-solving and mental training. I also appreciate his love and support, and I cherish every moment we spent together.

I want to thank Prof. Zhicheng Yang for the inspiring discussions on our collaboration on two projects, also for his and Prof. Yohei Fuji's help on my postdoc application. I also thank the rest of my committee: Prof. Ying Ran, Prof. Brian Zhou and Prof. Benedetta Flebus. Although we do not have much overlap in our research, I appreciate their thought-provoking questions from outside of the quantum dynamics community, from which I have learned a lot. Additionally, I would like to thank Prof. Ziqiang Wang and Kun Jiang for their guidance during my early exploration

of superconductivity at BC. I would like to extend my gratitude to the other faculty members and staff of the physics department, who have made my six-year journey at BC a pleasure.

I am thankful to my academic brother and close friend Vikram Ravindranath for teaching me tensor networks and Julia, as well as for discussions ranging from physics to cultural differences, sharing a similar taste in jokes and sometimes frustrations in academia. I really appreciate the weekly physics reading club with him and other group members Hanchen Liu, Eliot Heinrich, Qucheng Gao and Taichi Murakami. I would like to thank my academic friends I met at conferences and summer schools (and climbing gyms): Alexey Khudorozhkov, Ege Eren, Hisanori Oshima, Xiaozhou Feng, Zhuxi Luo and so on. In addition, I want to thank my classmates at BC for surviving the PhD program together: Xinyue Zhang, Hong Li and Xiaodong Hu, and many more friends that are still in the process. Specifically, I want to thank Xiaodong for letting me use his LaTex template for this dissertation.

I thank the seats by the windows in O'Neil Library for supporting me physically over these years.

Beyond physics, I am fortunate to have made a lot of friends. I would like to thank Xindi Wang for sharing our love of arts and our countless trips to concerts, museums, and bookstores. I am grateful to my climbing partners, Siqi Lin, Wenyue Shi, Tianli Wang and Ziyi Cao, for their belays and the routes we've worked on together. I also appreciate Siqi, Ethan, and Punky for accompanying me to numerous jazz and rock concerts; the Boston music scene will always be remembered. Additionally, I would like to thank friends from the Chinese diaspora community in Boston, especially Fen, Punky, Lao Ji, Lao Xi, and Fiona, for standing up for justice together, even though many of us still don't know each other's real names or professions. Outside of Boston, I want to thank my friends Tingting Jia, Dan Xie, Yuan Zhou, Yihan Lin, Yuyan Wang, Han Sun, Ruyi Yu, Yujuan Ding, Yao Huang, Qiuyang Li, Jingyuan Chen, Fang Lin, Chuang Du and Hungyu Yang — you guys are amazing. Furthermore, I am thankful to my high school teacher Shengguo Cai for sparking my passion for physics.

Finally, I am deeply grateful to my parents and my grandma for their unwavering love and care.

Chapter 1

Introduction

One of the most important topics in condensed matter physics is quantum phases of matter. Much of our understanding of quantum phases is based upon systems in equilibrium, where there is no net flow of matter or energy. Typically, a d-dimensional isolated quantum system satisfying the *Eigenstate Thermalization Hypothesis* (ETH) will eventually evolve into a state described locally by statistical mechanics [1, 2, 3]. One can think of a small subset of the degrees of freedom as a subsystem A, then the rest of the system A^c will act as a heat bath which leads to thermal descriptions of A when probed with local observables. The reduced density matrix ρ_A obtained by tracing out the degrees of freedom in A^c of the state ρ will approach the Gibbs state. Meanwhile, as an important measure of entanglement and correlation between degrees of freedom, the von Neumann bipartite entanglement entropy defined as

$$S_A \equiv -\ln \mathrm{Tr} \rho_A \ln \rho_A \tag{1.1}$$

exhibits a volume-law scaling under the infinite time limit, i.e.,

$$\lim_{t\to\infty} S_A(t) \sim L_A^d, \tag{1.2}$$

which means that every degree of freedom within A is entangled with those in A^c in equilibrium.

A natural question arises: Is thermalization an inevitable fate for all quantum systems? Indeed, there exist mechanisms that impede thermalization [1, 2, 4, 5, 6]. One example is many-body localization [7, 8], which evades thermalization through strong quenched disorder. Another mechanism that does not rely on spatial disorder is through imposing dynamical constraints, thereby rendering the dynamics non-ergodic. This results in the Hilbert space being split into exponentially many dynamically disconnected fragments, a phenomenon known as *Hilbert space fragmentation* [9, 10, 11, 12, 13, 14, 15, 16, 17, 18, 19, 20, 21, 22, 23].

An alternative way of approaching this question is investigating the dynamics of monitored random quantum circuits. Quantum circuit models are the minimal models to study entanglement dynamics in quantum systems, since any unitary operation acting on a d-dimensional Hilbert space can be decomposed into a sequence of local unitary gates. A

generic system with only local unitary evolution exhibits a ballistic growth of S_A until saturating to a state with volume-law entanglement [24]. When measurements are also involved, the non-unitary dynamics can exhibit many emergent phenomena which are inaccessible in pure unitary dynamics or in systems in equilibrium. If post-selection is prohibited, the state is averaged over measurement outcomes, resulting in a decohered maximally-mixed state. However, if measurement outcomes are recorded and one can keep track of the quantum trajectory, a dynamical entanglement phase transition from a volume-law phase where $S_A \sim L_A^d$ to an area-law phase where $S_A \sim L_A^{d-1}$ emerges as one increases the measurement rate p [25, 26, 27].

The measurement-induced phase transition (MIPT) was first observed in Haar random and Clifford random circuits composed of local two-qubit unitary gates and single qubit projective measurement gates[28, 25, 26, 27, 29, 30, 31]. In particular, at the phase transition point p_c, aspects of critical phenomena come into play, with, e.g., emergent two-dimensional conformal symmetry emerging in certain (1+1)-dimensional [(1+1)D] circuits[28, 32]. At first, this finding is rather surprising, since every measurement can reduce the entanglement, while only local unitary operators near the bipartition boundary can increase the entanglement. This apparent contradiction can be understood via quantum error correction [29, 30, 33]: When p is small, the hybrid quantum circuit is dynamically generating a robust quantum error correcting code, where the quantum information is protected by unitary evolution against projective measurements acting as errors; For $p > p_c$, the unitary evolution fails to protect the quantum information, and the system undergoes a phase transition to a disentangled area-law state.

Since its discovery, MIPTs have been generalized to other monitored open quantum dynamics[34, 35]. Aside from the interpretation in terms of quantum error correction, it can also be understood as a symmetry-breaking phase transition in the enlarged replica space[36, 37, 38, 39], where the entanglement entropy corresponds to the domain wall free energy. Recently, it was shown in Ref.[40] that the quantum automaton (QA) circuit subject to composite measurement can also exhibit an entanglement phase transition. This model provides a new physical picture for interpreting the phase transition in terms of bit-string dynamics and the entanglement transition within this model belongs to the directed percolation (DP) universality class[41]. Monitoring quantum systems can also stabilize interesting phases which cannot exist in equilibrium. One example is non-unitary free-fermion dynamics. In this system, there is an emergent critical phase protected by continuous weak measurement [42, 43]. Another class of examples are given by monitored quantum systems with additional discrete symmetries, which can possess highly entangled volume-law phases with conventional or topological order[44, 45, 39]. In addition, the area-law phase can also have a richer phase diagram characterized by different orders[44, 45, 46].

Motivated by the questions addressed above, this thesis will focus on various aspects in non-equilibrium quantum dynamics. In the first three chapters, we will explore the measurement-induced criticality as well as entanglement and transport properties in the volume-law phase of the aforementioned hybrid QA circuits under different symmetries. Hybrid QA circuits consist of QA unitaries that map one basis state to another up to a phase in the computational basis, interspersed with composite measurements that impose a rotation after projective measurements, so that the wave function is always an equal-weight superposition of all the allowed basis states with the phases carrying the quantum information. Due to this basis-preserving feature, we are able to perform large-scale numerical simulations, and interpret

the entanglement dynamics in terms of a stochastic two-species particle model.

In Chapter.2, we study the entanglement dynamics of hybrid QA circuits with $\mathbb{Z}_2$ symmetry, with a focus on the second Rényi entropy $S_A^{(n=2)}$, where

$$S_A^{(n)} = \frac{1}{1-n} \ln [\mathrm{Tr}(\rho_A^n)]. \tag{1.3}$$

We find that there is a transition from a volume-law phase to a critical phase with logarithmic entanglement scaling as one increases the measurement rate p. We further show that the critical point p_c belongs to the parity-conserving universality class [41, 47, 48], and the critical phase $p > p_c$ exhibits diffusive dynamical exponent, which can be explained using the stochastic model where the particles perform branching-annihiltaing random walks.

In Chapter.3, we focus on the weakly-monitored volume-law phase of the QA circuit with no symmetry. In particular, we will study the fluctuation of the entanglement in this random dynamics and the quantum error correction property of the volume-law phase. Previous studies for 1d random Haar circuits suggested that the entanglement entropy can be mapped to the free energy of the directed polymer in a random environment (DPRE) which has fluctuation belonging to the Kardar-Parisi-Zhang (KPZ) universality class [28, 25, 49, 50]. Such fluctuations lead to a subleading correction term scaling as $L^{1/3}$ in the entanglement entropy in the volume-law phase, which has also been numerically verified for random Clifford circuits [51, 52]. We numerically show that the entanglement entropy of a subsystem in both the early-time dynamics and the steady state in the hybrid QA circuit also exhibit sample-to-sample fluctuations with the same scaling behavior. Again, this KPZ scaling can be understood through random walks in a fixed random environment from the stochastic particle model. Furthermore, we investigate the quantum error correcting property of the hybrid QA circuit in terms, and find that there are two different kinds of code distance corresponding to different errors that both scale polynomially in L.

In Chapter.4, we turn to the entanglement dynamics of hybrid QA circuits with U(1) symmetry with a focus on the second Rényi entropy $S^{(n=2)}$. For a generic *unitary* quantum circuit under U(1) symmetry, it has been demonstrated that although the von-Neumann entanglement entropy continues to grow linearly, the growth of higher Rényi entropies is limited by the diffusive transport and therefore exhibits sub-ballistic growth [53, 54, 55, 56]. Mathematically it is rigorously proven that the growth of $S^{(n>1)}$ is at most diffusive, with a logarithmic correction [53], i.e.,

$$S^{(n>1)} \leq \frac{n}{n-1} \mathcal{O}(\sqrt{t \ln t}). \tag{1.4}$$

We show that for QA circuits, the entanglement growth saturates this upper bound. This saturation is caused by the "slow modes" that contain extensively long domains of spin 0s or 1s whose boundary expands diffusively (up to a logarithmic correction) under time evolution. We further numerically investigate the monitored dynamics and find that contrary to non-automaton random circuits where any non-zero rate of measurements leads to linear growth of the second Rényi entropy, the diffusive entanglement growth still persists in the volume-law phase of U(1)-symmetric hybrid QA circuits. As the measurement rate increases, there is a phase transition from a volume-law phase to a critical phase where S_A increases logarithmically in time, which is similar to the critical phase observed in $\mathbb{Z}_2$-symmetric QA circuits.

While the MIPT is an intriguing phenomenon in out-of-equilibrium quantum dynamics, it remains invisible in quan-

tum channels where postselection is impossible, posing great challenges to experimental observations. Recently, a new class of non-equilibrium dynamics called adaptive dynamics appears, which uses feedback mechanism to influence the system's evolution by measurement outcomes, enabling the realization of non-trivial density matrices and a variety of quantum ordered phases [57, 58, 59, 60, 61, 62]. In Chapter. 5, we introduce a class of adaptive random circuits with feeback that exhibits a phase transition that is observable in both quantum trajectories and quantum channels. Aside from the measurement rate p, we add another parameter which is the feedback rate r. The feedback is designed to "steer" the system towards particular final states. When $p \times r$ is large enough, the steady state is a mixture of two ferromagnetically ordered states instead of a maximally mixed state involving exponentially many configurations. Thus, there is an order-disorder phase transition in the quantum dynamics, which can be observed at the level of both quantum trajectory and quantum channel [59, 60]. By explicitly mapping the motion of domain walls to a classical branching-annihilating random walk (BAW) process, we show that the order-disorder phase transition in our adaptive circuit model belongs to the parity-conserving (PC) universality class. Furthermore, the familiar MIPT is observed at the level of the quantum trajectory. Interestingly, we find that these two transitions typically occur at *different* critical measurement rates.

In Chapter.6, we go back to the question addressed at the beginning of this introduction and concentrate on systems with Hilbert space fragmentation. Since the ergodicity-breaking mechanism of HSF relies on fine-tuned dynamical constraints in stead of disorder, the ergodicty is expected to be restored once the constraints are broken. We are interested in how the thermalization dynamics is affected by the structure of HSF in the presence of constraint-breaking perturbations. We will focus on a one-dimensional spin chain called "pair-flip" model that exhibits HSF [63], and couple one end to a heat bath. We will show that the thermalization dynamics is anomalously slow. This slowness is due to the strong bottlenecks the system encounters as one tries to explore the Hilbert space under the contraint-breaking bath, a phenomenon which arises from the type of constraints and the local nature of the coupling to the bath. We rigorously prove an exponentially large lower bound on t_{th} in the setting where the system undergoes a constrained form of random unitary (RU) dynamics, and provide numerical evidence that t_{th} for Hamiltonian dynamics is similarly long. In an upcoming work, we show that this anomalously slow thermalization can be generalized to other HSF systems, and they can be classified into three categories according to different mechanisms of forming HSF.

Chapter 2

Measurement-induced criticality in $\mathbb{Z}_2$-symmetric quantum automaton circuits

2.1 Introduction

In this chapter, we construct a hybrid QA circuit with $\mathbb{Z}_2$ symmetry and study its entanglement dynamics. We show that if we impose this $\mathbb{Z}_2$ symmetry, there exists an entanglement phase transition from a highly entangled volume-law phase to a critical phase with logarithmic entanglement scaling, with the transition occurring by varying the measurement rate p (See Fig. 2.1). We generalize the classical bit-string picture developed in Ref.[40] and demonstrate that the entanglement phase transition belongs to the parity-conserving (PC) universality class with dynamical exponent $z = 1.744$[47, 48, 41]. Due to the $\mathbb{Z}_2$ symmetry, this universality class is distinct from the aforementioned DP universality class. We further derive a two-species particle model based on the bit-string picture to calculate the entanglement dynamics from a short-range entangled state. The particles in this model can diffuse, branch, and annihilate in pairs, and the purity for a subsystem is equivalent to the fraction of configurations where particles of different species never encounter one another. In particular, the prefactor of the logarithmic scaling of the second Rényi entropy at the transition point p_c is related to the local persistence coefficient of the two-species particle model and is a universal constant for PC universality class.

Unlike the conventional measurement-induced phase transition in which there is an area-law entangled phase when the measurement rate p is larger than some critical threshold p_c, here we observe a critical *phase*, characterized by logarithmic entanglement scaling when $p > p_c$. Specifically, this phase has dynamical exponent $z = 2$ and is protected by the combination of the $\mathbb{Z}_2$ symmetry and the special features of the QA circuit. We show that the underlying bit-strings have diffusive dynamics, and provide an interpretation of the critical entanglement scaling in terms of the two-species particle model. We further analyze the purification dynamics starting from a mixed density matrix with extensive entropy[30]. We find that when $p > p_c$, the entropy decays diffusively in time which is consistent with the entanglement dynamics results.

The rest of the chapter is organized as follows. In Sec. 2.2, we construct a hybrid QA circuit with $\mathbb{Z}_2$ symmetry. We

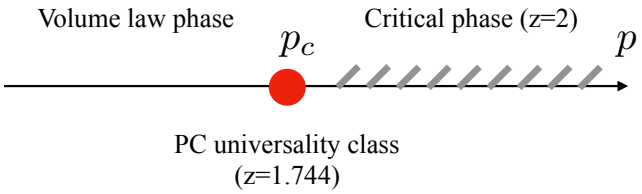

Figure 2.1: A cartoon picture for the phase diagram of the hybrid QA circuit in the presence of $\mathbb{Z}_2$ symmetry. The dynamical exponents of the quantum phase transition at $p = p_c$ and the quantum critical phase $p > p_c$ are inherited from the associated classical bit-string dynamics, respectively.

numerically compute the entanglement entropy for this circuit in Sec. 2.3 in terms of a Clifford stabilizer representation. In addition, we provide an interpretation of second Rényi entropy in terms of classical particle model. In Sec. 2.4, we analyze the purification dynamics and find that the results for critical point and critical phase are consistent with that in Sec. 2.3. We summarize our results in Sec. 2.5.

2.2 QA model with $\mathbb{Z}_2$ symmetry

In this section, we construct a hybrid QA circuit with $\mathbb{Z}_2$ symmetry. We aim to study how the information encoded in the quantum state evolves under the competition between quantum automaton unitary operators and non-unitary measurements, which will be specified later in this section. Given a subregion A, a particularly useful quantity to measure this is the n^{th} Rényi entropy:

$$\begin{aligned} S_A^{(n)} &= \frac{1}{1-n} \ln \left[\mathrm{Tr}(\rho_A^n) \right] \\ \rho_A &= \mathrm{Tr}_B |\psi\rangle\langle\psi|. \end{aligned} \tag{2.1}$$

where B is the complement of A. In this chapter, we will focus on the second Rényi entropy with $n = 2$ and take the base to be the natural logarithm base.

The QA circuit is built up of unitary operators that permute a set of vectors in a specific orthonormal basis (namely, the computational basis) up to some random phase, i.e.,

$$U|n\rangle = e^{i\theta_n}|\pi(n)\rangle, \tag{2.2}$$

where $\pi \in S_N$ is an element of the permutation group on the product states $|n\rangle$ in the computational basis with cardinality N. Through out this chapter, we build the computational basis from the Pauli Z basis. The $\mathbb{Z}_2$ symmetry is imposed by requiring that the parity of the computational basis remains fixed under the unitary evolution. From the previous definition it is clear that the automaton unitary evolution does not create entanglement when acting on product states in the computational basis. However, it can generate entanglement in a wavefunction which involves a superposition of the basis states—for example, we can apply the measurement $(1 + Z_1 Z_2 \cdots Z_L)/\sqrt{2}$ to a product state polarized in $+x$ direction with an even number of qubits L to make it $\mathbb{Z}_2$ even. When the automaton unitary operator acts on such an

initial state,

$$|\psi_I\rangle = U|\psi_0\rangle = U \circ \frac{1+Z_1Z_2\cdots Z_L}{\sqrt{2}} \bigotimes_i \frac{1}{\sqrt{2}}(|0\rangle + |1\rangle)$$
$$= \frac{1}{\sqrt{2^{L-1}}} \sum_n e^{i\theta_n}|\pi(n)\rangle, \tag{2.3}$$

we can obtain a highly entangled state for sufficiently generic θ_n. In the above equation, each $|n\rangle$ contains an even number of 1's and 0's, and together they form a $\mathbb{Z}_2$-symmetric computational basis $\{|n\rangle\}$ with cardinality $N = 2^{L-1}$. In this chapter, we consider unitaries U composed of local unitary QA gates. With this construction, the entanglement can grow linearly in time, and saturates to volume-law scaling at late times.

Aside from the QA unitary operators, non-unitary local measurements are also introduced into the QA circuit. Since the QA unitary evolution does not enlarge the number of basis states involved in the wave function, repeated local projective measurements in the Z direction will continually reduce the number of available basis states, and will ultimately lead to a product state with no entanglement. Therefore, there is no entanglement phase transition when the measurement rate is finite.

To resolve this issue, Ref.[40] introduced a composite measurement which applies a rotation to the spin into $|\pm x\rangle$ following the projection in the Z direction so as to preserve the basis states. In such a hybrid QA circuit model, the wave function at any time is an equal weight superposition of all the basis states, and there exists an entanglement phase transition belonging to DP universality class at finite measurement rate. In our system, we need to modify this composite measurement slightly to preserve the $\mathbb{Z}_2$ symmetry. We therefore define the composite measurement as

$$M^\sigma_{L/R} = R \circ P^\sigma_{L/R}, \tag{2.4}$$

which acts on two qubits. This measurement is a combination of the projection operator $P^\sigma_{L/R}$ on the left/right qubit into the spin $\sigma = \{0, 1\}$, together with a two-site rotation operation

$$R = \frac{1}{\sqrt{2}} \begin{pmatrix} 1 & 0 & 0 & 1 \\ 0 & 1 & 1 & 0 \\ 0 & 1 & -1 & 0 \\ 1 & 0 & 0 & -1 \end{pmatrix} \tag{2.5}$$

that maps $|00\rangle$ to $(|00\rangle + |11\rangle)/\sqrt{2}$, $|11\rangle$ to $(|00\rangle - |11\rangle)/\sqrt{2}$ and $|01\rangle$ to $(|01\rangle + |10\rangle)/\sqrt{2}$, $|10\rangle$ to $(|01\rangle - |10\rangle)/\sqrt{2}$. For instance, when M^0_L is applied to a two-site wave function with even parity defined as follows,

$$M^0_L|\psi\rangle = R \circ P^0_L[\frac{1}{\sqrt{2}}(e^{i\theta_0}|00\rangle + e^{i\theta_1}|11\rangle)]$$
$$= e^{i\theta_0}R|00\rangle \tag{2.6}$$
$$= \frac{1}{\sqrt{2}}e^{i\theta_0}(|00\rangle + |11\rangle).$$

After imposing the composite measurement, the wave function is still an equal weight superposition of all the basis

states with the same parity: the only thing that changes is the information stored in $|\psi\rangle$, among which only half of the phases are preserved after each application of $M^{\sigma}_{L/R}$. Therefore, we anticipate that measurements will act to disentangle the many-qubit system, while still preserving the $\mathbb{Z}_2$ symmetry.

2.3 Entanglement Transition

2.3.1 Clifford QA circuit and entanglement dynamics

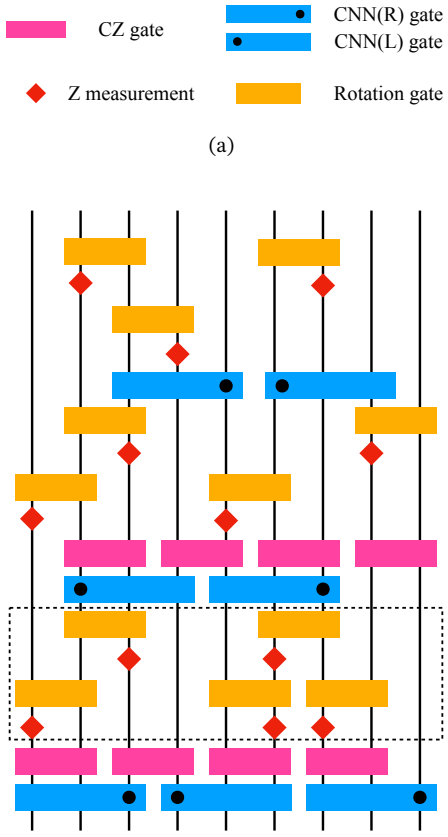

Figure 2.2: (a) A schematic for the gates appearing in our circuit. (b) The arrangement of gates in a single time step of our $\mathbb{Z}_2$-symmetric hybrid QA circuit. Each time step involves three layers of CNN gates and two layers of CZ gates, interspersed with three measured layers. The dashed box represents a measured layer enclosing two rows of composite measurements, with the first/second row containing randomly distributed $M^{\sigma}_{L/R}$ applied on sites $(2i-1, 2i)[(2i, 2i+1)]$ for $i \in [1, L/2]$. As with the CNN gates, the projection of $M^{\sigma}_{L/R}$ is chosen to be applied on the left/right qubit with equal probability. In general, the composite measurement appears in a measured layer with probability p.

We choose a subset of Clifford gates to construct a QA circuit with $\mathbb{Z}_2$ symmetry (an example is illustrated in Fig. 2.2), and explore the entanglement dynamics by varying the composite measurement rate p. First we prepare a product state with L qubits polarized in the $+x$ direction and measure the Pauli string $Z_1 Z_2 \cdots Z_L$ to implement $\mathbb{Z}_2$ symmetry. We take this as the initial state $|\psi_I\rangle$, and then apply the hybrid circuit, consisting of $\mathbb{Z}_2$-symmetric QA unitaries and

composite measurements, to $|\psi_I\rangle$. We then compute the entanglement entropy of a consecutive subsystem A.

Notably, the entanglement dynamics of a Clifford circuit can be efficiently simulated by applying the stabilizer formalism from the Gottesman-Knill theorem [64]. A stabilizer of a pure state $|\psi\rangle$ is a Pauli string operator g that acts trivially on $|\psi\rangle$, i.e., $g|\psi\rangle = |\psi\rangle$. Such state with L qubits can be uniquely specified by a stabilizer group G generated by L independent and mutually commuting stabilizers,

$$\begin{aligned} G &= \langle \mathcal{G} \rangle = \langle g_1, \ldots, g_L \rangle \\ &= \Big\{ \prod_{i=1}^{L} g_i^{p_i} | p_i \in \{0,1\}, g_i|\psi\rangle = |\psi\rangle, [g_i, g_j] = 0 \Big\}, \end{aligned} \tag{2.7}$$

where $\mathcal{G} = \{g_1, \ldots, g_L\}$ is the generating set of G. By definition, a Clifford unitary gate maps a Pauli string operator to another one, i.e., $UgU^\dagger = g', \forall g \in G$. On the other hand, any Pauli measurement O_i acting on the ith site becomes a generator of the stabilizer group, with the rest of the generators rearranged so that O_i commutes with all elements in G. Consequently, instead of tracing the trajectory of $|\psi\rangle$ with 2^L degrees of freedom, we can keep track of the generating set of its stabilizer group whose information can be conveniently stored in a $L \times 2L$ binary matrix. Hence, we are able to perform the simulation on a large system with hundreds of qubits.

The unitary evolution is composed of two types of gates, both of which preserve the $\mathbb{Z}_2$ symmetry. The first type are CNOTNOT(CNN) gates, which are three-qubit gates that flip two qubits according to the value of the third (control) qubit. If the control qubit is on the left we denote the corresponding gate as CNN_L; it acts as

$$\begin{aligned} \text{CNN}_L|1\sigma_1\sigma_2\rangle &= |1(1-\sigma_1)(1-\sigma_2)\rangle \\ \text{CNN}_L|0\sigma_1\sigma_2\rangle &= |0\sigma_1\sigma_2\rangle., \end{aligned} \tag{2.8}$$

with the leftmost qubit acting as the control. The case when the rightmost qubit acts as the control analogously defines a right CNN gate CNN_R. In the circuit under consideration, we choose CNN_L and CNN_R gates randomly, with equal probability. Notice that in each time step, we apply three layers of random CNN gates as shown in Fig. 3.2(b).

The second type of gate that appears in the unitary evolution part of the circuit is the CZ gate. This gate is diagonal in the computational basis, and assigns a π phase to $|11\rangle$. Explicitly,

$$\text{CZ} = \begin{pmatrix} 1 & 0 & 0 & 0 \\ 0 & 1 & 0 & 0 \\ 0 & 0 & 1 & 0 \\ 0 & 0 & 0 & -1 \end{pmatrix}. \tag{2.9}$$

In the circuit, we apply two layers of CZ gate in each time step.

The randomly-applied composite measurements can be constructed by Clifford gates defined as $M^{\sigma}_{L/R}$ in Sec. 2.2. We introduce the composite measurements into the circuit and define the measurement rate p as the density of $M^{\sigma}_{L/R}$ in each measured layer. As we increase p from 0, the entanglement entropy decreases. Numerically, we observe an

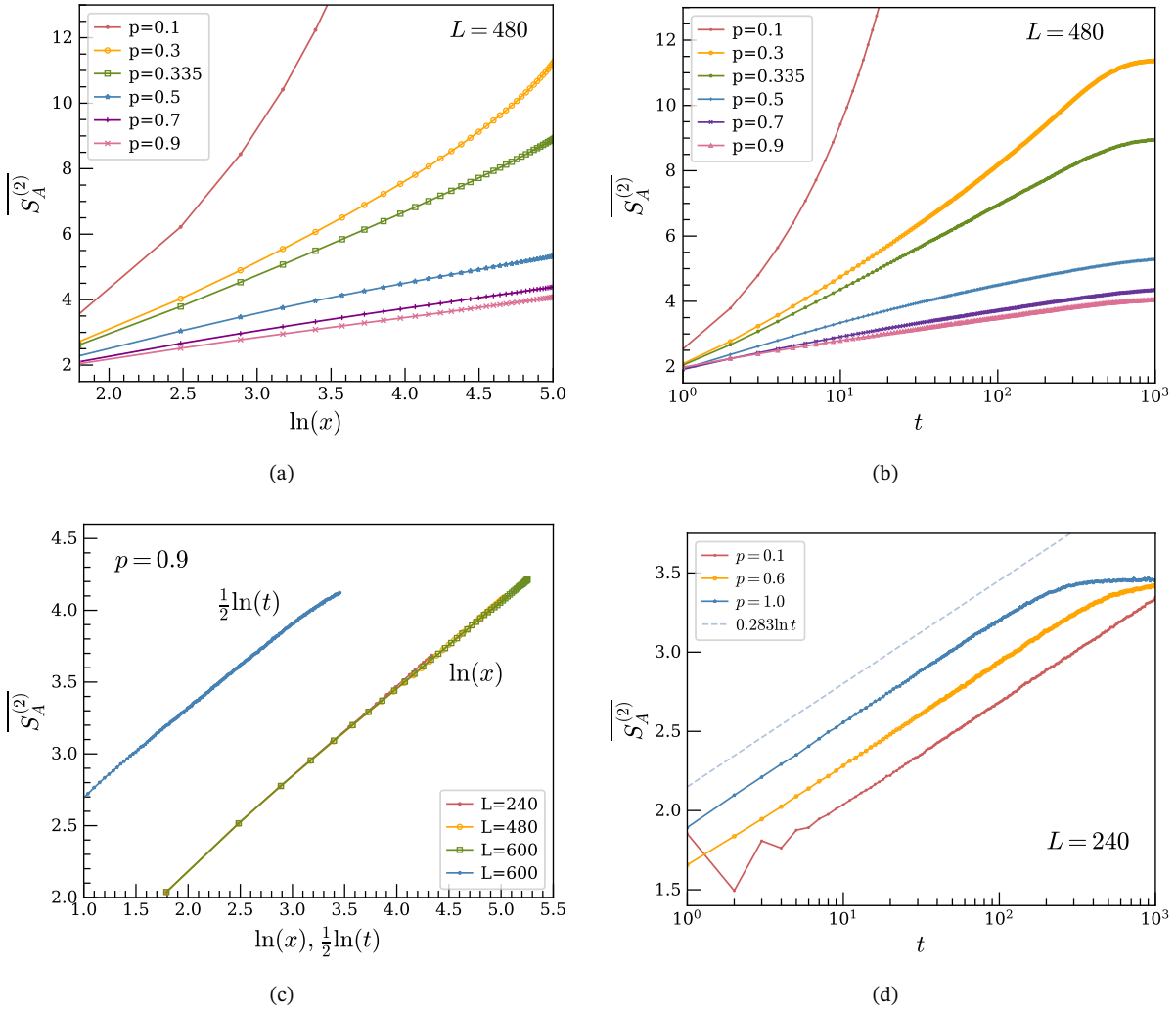

Figure 2.3: (a) The steady state $\overline{S_A^{(2)}}$ vs $\ln(x)$ for $L = 480$, where $x \equiv \sin(\pi L_A/L)L/\pi$. (b) The entanglement dynamics for half of the system $\overline{S_A^{(2)}}$ vs t on the semi-logarithm scale for $L = 480$. (c) An example of the data collapse of the steady state $\overline{S_A^{(2)}}$ vs $\ln x$ for different system sizes at $p = 0.9$. The slope for $L = 600$ is $\lambda_2(0.9) = 0.605$. We also plot $\overline{S_A^{(2)}}$ vs $\frac{1}{2}\ln(t)$ for comparison and we can see that it is roughly parallel to the steady state curves. Numerically, $\lambda_1(0.9) = 0.291$. The ratio between these two slopes is 2.079. On average, $\lambda_2/\lambda_1 = 2.009$ for $p > p_c$. Similarly, for $p = p_c$, $\lambda_2 = 1.947$ and $\lambda_1 = 1.12$, leading to a ratio $\lambda_2/\lambda_1 = 1.738$. (d) The entanglement dynamics of the QA circuit with no CNN gates for $L = 240$ plotted on the semi-log scale. We find that $\overline{S_A^{(2)}(t)} = 0.283\ln(t)$ for all p. All of the numerical data for entanglement entropy are calculated with periodic boundary conditions, and in the natural logarithm base.

entanglement transition at $p_c \approx 0.335$. The value of the critical point is consistent with that observed in the purification dynamics in Sec. 2.4 and the classical bit-string dynamics in Appendix 2.A. As shown in Fig. 2.3(a), when $p < p_c$, the entanglement entropy has volume-law scaling. The volume-law coefficient decreases as we increase p. When $p \geq p_c$, Fig. 2.3(a) indicates that the steady state entanglement scales logarithmically in the subsystem size. In our numerical simulations, we impose periodic boundary conditions and observe that

$$\overline{S_A^{(2)}(L_A, p)} = \lambda_2(p) \ln \Big[\frac{L}{\pi} \sin \big(\frac{\pi L_A}{L} \big) \Big], \tag{2.10}$$

where the overbar represents an ensemble average. This is interesting and is distinct from conventional measurement-induced phase transitions in interacting systems, where an area-law entangled phase appears for $p > p_c$. In our model, the area-law phase is replaced by a critical phase with $\lambda_2(p)$ changing continuously with p. This critical phase is a special feature of the QA circuit with $\mathbb{Z}_2$ symmetry. As we will explain later, this is related to the underlying classical bit-string dynamics with $\mathbb{Z}_2$ symmetry.

Aside from the steady state, we also study the entanglement dynamics starting from an initial state $|\psi_0\rangle$. When $p < p_c$, $S_A(t)$ grows linearly at early times and saturates to a volume-law entangled steady state, while for $p \geq p_c$ we observe a logarithmic entanglement growth before saturation,

$$\overline{S_A^{(2)}(t, p)} = \lambda_1(p) \ln(t), \tag{2.11}$$

as shown in Fig. 2.3(b). Similar to $\lambda_2(p)$, $\lambda_1(p)$ also depends on p. We find that when $p = p_c$, $\lambda_2/\lambda_1 = 1.738$, while when $p > p_c$ and the circuit is measurement-dominated, the ratio is independent of p, with $\lambda_2/\lambda_1 = 2.009$.

We also simulate the entanglement dynamics for the QA circuit in the absence of CNN gates. The numerics in Fig. 2.3(d) shows that in such a circuit, the system is critical and has logarithmic entanglement scaling. In particular, $\overline{S_A^{(2)}(t)} = \lambda_1 \ln(t)$ where $\lambda_1 = 0.283$ for all p. On the other hand, the steady state entanglement entropy $\overline{S_A^{(2)}} = \lambda_2 \ln(x)$ with $\lambda_2 = 0.591$ for all p. Hence the ratio is $\lambda_2/\lambda_1 = 2.088$ which is close to that in the critical phase of the circuit with CNN gates. In the following sections, we will give an interpretation for λ_1 and λ_2 and show that the ratios between them are related to the dynamical exponents of the underlying classical bit-string model.

2.3.2 bit-string dynamics with $\mathbb{Z}_2$ symmetry

For the second Rényi entropy, the purity $\mathrm{Tr}(\rho_A^2)$ is equivalent to the expectation value of the SWAP_A operator which acts on the tensor product of two identical copies of the state [65, 66],

$$\mathrm{Tr}(\rho_A^2) = \langle\psi|_2 \otimes \langle\psi|_1 \mathsf{SWAP}_A |\psi\rangle_1 \otimes |\psi\rangle_2. \tag{2.12}$$

For the wave function $|\psi\rangle$ expanded in the basis in subregion A and B,

$$|\psi\rangle = \frac{1}{\sqrt{N}} \sum_{i,j} e^{i\theta_{ij}} |\alpha_i\rangle_A |\beta_j\rangle_B, \tag{2.13}$$

the SWAP_A operator then exchanges the spin configurations $|\alpha\rangle$ within the A region of the copies of the system (here $N = 2^{L-1}$ is the total number of basis states).

To understand the entanglement dynamics in the non-unitary evolution described by $\tilde{U}_t$, we insert two complete sets of basis states in Eq. (2.14) and find [40],

$$\begin{aligned}
\mathrm{Tr}(\rho_A^2) &= \sum_{n_1,n_2} \langle\psi|_2\langle\psi|_1 \mathsf{SWAP}_A |n_1\rangle|n_2\rangle\langle n_2|\langle n_1|\psi\rangle_1|\psi\rangle_2 \\
&= \sum_{n_1,n_2} \langle\psi_0|_2\langle\psi_0|_1 \tilde{U}_t^\dagger \otimes \tilde{U}_t^\dagger |n_1'\rangle|n_2'\rangle\langle n_2|\langle n_1|\tilde{U}_t \otimes \tilde{U}_t|\psi_0\rangle_1|\psi_0\rangle_2 \\
&= \frac{1}{N^2} \sum_{n_1,n_2} e^{-i\Theta_{n_1'}} e^{-i\Theta_{n_2'}} e^{i\Theta_{n_1}} e^{i\Theta_{n_2}},
\end{aligned} \tag{2.14}$$

where

$$\begin{aligned}
|n_1'\rangle|n_2'\rangle &= \mathsf{SWAP}_A |n_1\rangle|n_2\rangle \\
&= \mathsf{SWAP}_A |\alpha_1\beta_1\rangle|\alpha_2\beta_2\rangle \\
&= |\alpha_2\beta_1\rangle|\alpha_1\beta_2\rangle.
\end{aligned} \tag{2.15}$$

and

$$e^{i\Theta_n} = \sqrt{N}\langle n|\tilde{U}_t|\psi_0\rangle,\ e^{-i\Theta_n} = \sqrt{N}\langle\psi_0|\tilde{U}_t^\dagger|n\rangle. \tag{2.16}$$

The problem of computing $\mathrm{Tr}(\rho_A^2)$ can therefore be converted into evaluating the phases in (2.16).

When estimating the overlap of $\tilde{U}_t|\psi_0\rangle$ with any basis state $\langle n|$, we can deduce the effective action of $\tilde{U}_t$ on $\langle n|$ and compute its overlap with $|\psi_0\rangle$ even though the composite measurement is non-unitary. Consider applying a composite measurement $M_{L/R}^\sigma$ on $|\psi\rangle$ which is the equal weight superposition of all the allowed states,

$$\begin{aligned}
\langle n|M_{L/R}^\sigma|\psi\rangle &= \langle n|R \circ P_{L/R}^\sigma|\psi\rangle \\
&= \langle T_{L/R}^\sigma(n)|\psi\rangle = \frac{1}{\sqrt{N}} e^{i\theta_{T_{L/R}^\sigma(n)}}.
\end{aligned} \tag{2.17}$$

Here $|T_{L/R}^\sigma(n)\rangle$ refers to the state $|n\rangle$ with the spin at site L/R forced to be in the σ state, while its neighboring spin at site R/L is chosen to preserve the parity. Suppose the hybrid QA circuit has the non-unitary dynamics of the form $\tilde{U}_t = M_t U_t M_{t-1} U_{t-1} \cdots$, the overlap can be evaluated by applying $\tilde{U}$ from left to right on $\langle n|$,

$$\begin{aligned}
\langle n|\tilde{U}_t|\psi_0\rangle &= \langle n(t'=0)|M_t U_t M_{t-1} U_{t-1} \cdots |\psi_0\rangle \\
&= \langle n(t'=1)|U_t M_{t-1} U_{t-1} \cdots |\psi_0\rangle \\
&= e^{i\theta_{n(t'=1)}} \langle n(t'=1)|M_{t-1} U_{t-1} \cdots |\psi_0\rangle \\
&= \cdots = \frac{1}{\sqrt{N}} e^{i\Theta_n},
\end{aligned} \tag{2.18}$$

where Θ_n is the accumulated phase under time evolution,

$$e^{i\Theta_n} = e^{i\theta_{n(t=1)}} e^{i\theta_{n(t=2)}} \ldots e^{i\theta_{n(t=T)}}. \tag{2.19}$$

To compute the dynamics of the purity, we investigate the evolution of bit-strings and the associated phases. We define the difference between bit-string pairs as

$$h(x,t) = |n_1(x,t) - n_1'(x,t)|. \tag{2.20}$$

At each site, $h(x)$ can only be either 0 or 1, and can be conveniently described in terms of the particle representation illustrated in Fig. 2.4(b) where $\circ$ denotes empty site and $\bullet$ denotes occupied site. For instance, under the CNN_L gate, we have $\bullet\circ\circ \leftrightarrow \bullet\bullet\bullet$ and $\bullet\circ\bullet \leftrightarrow \bullet\bullet\circ$. Under time evolution governed by $\text{CNN}_{L/R}$ gates, the particles can diffuse, branch and annihilate on the lattice. Even if the initial configuration only has one particle, the particle number grows linearly in time and the steady state has roughly $L/2$ particles. On the other hand, under the composite measurement,

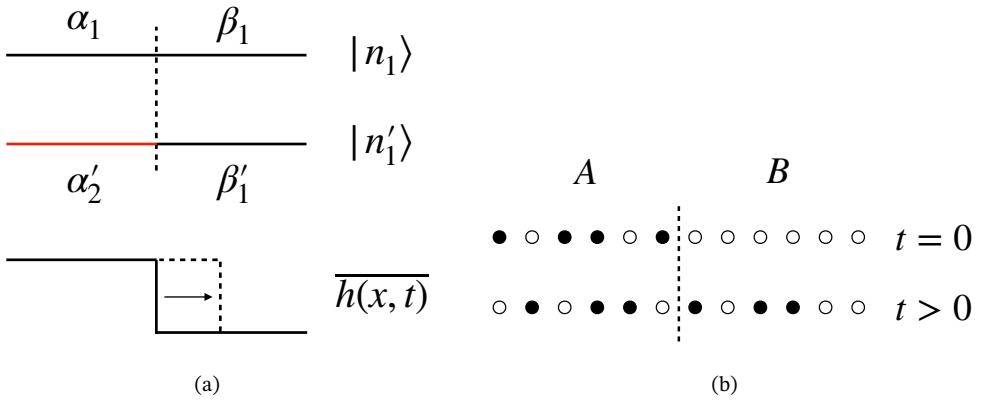

(a) (b)

Figure 2.4: (a) The spreading of the bit-string difference $\overline{h(x,t)}$ under the hybrid QA circuit with $\mathbb{Z}_2$ symmetry. Without the intervention of measurements, the front of $\overline{h(x,t)}$ moves to the right at constant velocity with possible broadening. (b) The particle representation of $h(x,t)$. Initially, all the particles are distributed randomly in region A. Under the CNN gates and measurements, the particles perform branching-annihilating random walks and can intrude into region B.

we have pair-annihilation $\bullet\bullet \to \circ\circ$ and diffusion $\bullet\circ \leftrightarrow \circ\bullet$. The particles diffuse on the lattice and annihilate in pairs with probability p when they encounter one another. Combining unitary dynamics and measurement together, the particles perform branching-annihilating random walks (BAW) with an even number of off-springs []

$$W \leftrightarrow 3W,\ W + W \xrightarrow{p} \emptyset. \tag{2.21}$$

The competition between the unitary evolution and the composite measurement leads to a continuous phase transition which can be characterized by the total particle number $D(t) \equiv \sum_x h(x,t)$ (The numerical details for this can found in Appendix.2.A). When $p < p_c$, $D(t \to \infty)/L$ in the steady state saturates to a finite constant. When $p \geq p_c$, if the initial state has an even number of particles, the steady state has $D(t \to \infty) = 0$. At p_c, $D(t)$ exhibits interesting and universal power law scaling behavior and this critical point belongs to the parity-conserving (PC) universality class with dynamical exponent $z = 1.744$[47, 48, 41]. When $p > p_c$, the dynamics is dominated by the annihilation process $W + W \to \emptyset$. Since annihilation only occurs when a pair of particles encounter one another, $D(t)$ decays diffusively in time and the $p > p_c$ phase has dynamical exponent $z = 2$. This is different from the DP universality class, where a single particle can

annihilate directly with probability p, which leads to an exponential decay of $D(t)$ with a finite rate at $p > p_c$. The $\mathbb{Z}_2$ symmetry protects the slow diffusive dynamics and is also responsible for the quantum critical phase when we take into account the phase gate.

Keeping the above classical bit-string dynamics in mind, we now introduce the phase gate and investigate the entanglement dynamics. We first consider entanglement entropy for a random phase state defined as

$$|\psi\rangle = \frac{1}{\sqrt{2^{L-1}}} \sum_n e^{i\theta_n} |n\rangle, \tag{2.22}$$

where θ_n is a random phase that takes the value in $\{0, \pi\}$ [1]. This wave function can be generated under random unitary QA evolution and has maximally entangled volume-law scaling. This can be understood as follows: from Eq. (2.14), we can see that when $|n_1\rangle = |\alpha_1\beta_1\rangle$ and $|n_2\rangle = |\alpha_2\beta_2\rangle$ share the same spin configuration in region A, they are invariant under the swap operator, which means that the random phases always cancel, i.e., $\theta_{n_1} - \theta_{n_1'} = 0$ and $\theta_{n_2} - \theta_{n_2'} = 0$. There are $2^{L_A} \times (2^{L-L_A-1})^2$ such pairs that each contributes $1/2^{2L-2}$ to the purity. For other bit-strings that are different in region A, the random phase terms will in general add up to zero and make no contribution to $\mathrm{Tr}(\rho_A^2)$.[2] Hence, the wave function has the volume-law scaling

$$S_A^{(2)} \approx -\ln \frac{2^{L_A} \times 4^{L-L_A-1}}{4^{L-1}} = L_A \ln 2. \tag{2.23}$$

In the above example, only the bit-string pairs without phase difference contribute to the purity. This is also true when we consider the entanglement dynamics starting from $|\psi_I\rangle$. Notice that in Eq. (2.14), there are four accumulated phases for each bit-string configuration $\{|n_1\rangle, |n_2\rangle, |n_1'\rangle, |n_2'\rangle\}$. We need to find out how these phases evolve in time and how they contribute to the purity. For simplicity, here we first consider the phase difference for $|n_1\rangle$ and $|n_1'\rangle$ only in regime B and define the quantity,

$$Q(t) \equiv \frac{1}{M} \sum_{n_1, n_1'} e^{-i\Theta^B_{n_1'} + i\Theta^B_{n_1}}, \tag{2.24}$$

where M is the total number of bit-string pairs. The complete analysis of the time evolution of all these phase terms in the purity will be deferred to Sec. 2.3.4.

Initially, $|n_1\rangle$ and $|n_1'\rangle$ are identical in B and are only different in A. The relative phase $-\Theta^B_{n_1'} + \Theta^B_{n_1}$ caused by CZ gates is zero and we have $Q(t = 0) = 1$. The nonzero relative phase can be generated when particles enter into B. Specifically, if we apply CZ gate on $\bullet\circ$ with the ensemble of possible bit-string configurations $\{\{|n_1\rangle, |n_1'\rangle\}\} = \{\{|10\rangle, |00\rangle\}, \{|11\rangle, |01\rangle\}, \{|01\rangle, |11\rangle\}, \{|00\rangle, |10\rangle\}\}$, the phase differences generated by the CZ gate are $\{0, \pi, \pi, 0\}$. We also get similar results for the particle configuration $\circ\bullet$ and $\bullet\bullet$. To summarize, for all these nonzero particle configurations, half of the corresponding bit-string pairs contribute a π phase to the accumulated phase, while half of them do not

[1] In the Clifford dynamics, θ_n can only take a discrete value $n\pi/2$ with n randomly chosen in 0,1 2 and 3.

[2] In fact, the pairs that are the same in region B also contribute to the purity. If we take them into account, the purity becomes $\mathrm{Tr}(\rho_A^2) = (2^{L_A} \times 4^{L-L_A-1} + 4^{L_A} \times 2^{L-L_A-1} - 2^{L_A} \times 2^{L-L_A-1})/4^{L-1} = 2^{-L_A} + 2^{-L+L_A} - 2^{-L+1}$, therefore the actual steady state entanglement $S_A^{(2)} < L_A \ln 2$. But now we care about the leading non-constant term so the last two terms are discarded temporarily.

contribute any phase terms. This result can be generalized to the many-qubit case. The accumulated phase terms of all the configurations that contain particles in B will add up to zero and make no contribution to Eq. (2.24). Meanwhile, the configurations that will contribute to $Q(t)$ are those with no particles in B and hence have zero relative phase. Therefore, $Q(t)$ can be alternatively viewed as the fraction of configurations in which the particles never reach the boundary between A and B,

$$Q(t) \approx \frac{K_0(t)}{K}, \tag{2.25}$$

where K is the total number of particle configurations in A and K_0 is the number of particle configurations in which particles never reach the boundary up to time t.

2.3.3 Single-species BAW model

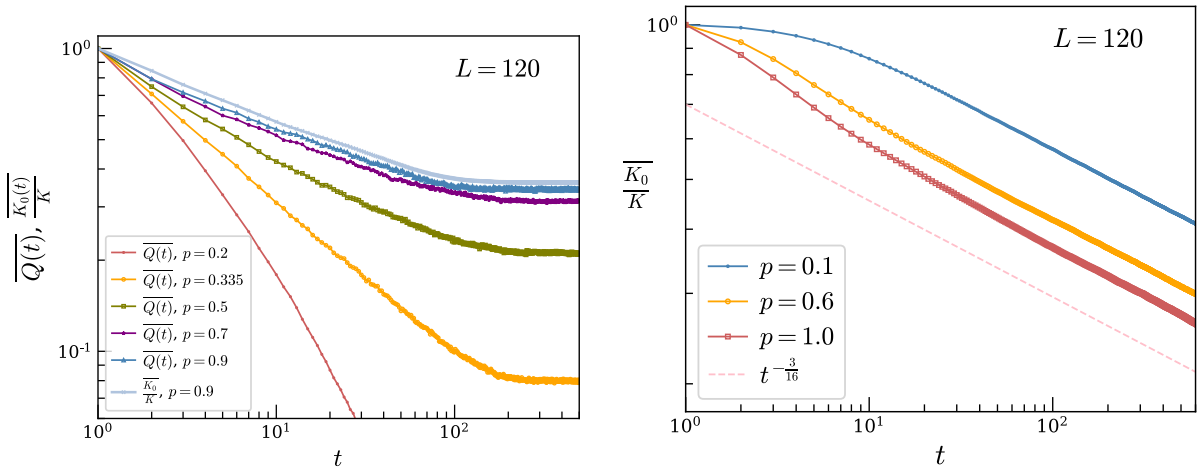

(a) (b)

Figure 2.5: (a) The evolution of $\overline{Q}$ on a log-log scale. The system size is $L = 120$. We also plot K_0/K at $p = 0.9$ for comparison. (b) We simulate the single-species BAW model with no CNN gates and plot $\overline{\frac{K_0}{K}}$ vs t for $L = 120$ on the log-log scale. $\overline{\frac{K_0}{K}}$ decays as a power law function with the exponent close to the analytical prediction $\frac{3}{16}$.

The above analysis motivates us to define a single-species BAW model. Initially, the particles are distributed randomly in A on a 1D lattice. We let them undergo the same dynamics as the QA circuit in which they perform BAW. Our aim is to find the probability $Q(t)$ that the particles have never reached the boundary between A and B up to time t. In the limit where $p = 0$, the particle front propagates with a constant velocity v. Then, only the initial configurations with no particles distributed within a distance vt to the boundary contribute to $K_0(t)$. This leads to $Q(t) \sim 2^{-vt}$, i.e., the probability that particles never cross the boundary decays exponentially in time. If we roughly take the entanglement entropy as $S_A \sim -\ln Q(t)$, it then grows linearly in time. As we increase p, the propagation slows down and eventually becomes diffusion-dominated when $p > p_c$. At this critical point p_c and in the critical phase $p > p_c$, we will see that $Q(t)$ decays algebraically as $Q(t) \sim t^{-\theta}$ where θ is the so-called persistence exponent in the first passage problem[67].

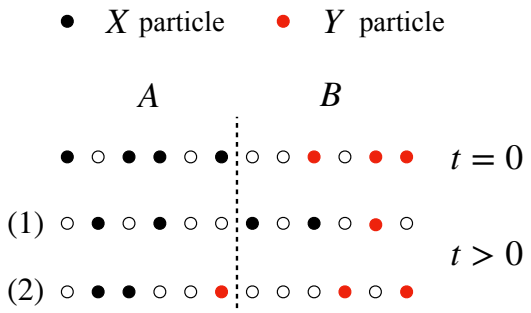

Figure 2.6: An example of the two-species BAW model. The black dots represent X particles, and the red dots represent Y particles. Initially, X and Y particles are distributed in region A and B respectively. Under the time evolution, the two species perform BAW before they encounter one another. There are two types of possible particle configurations in which the two species have not met up to time t: (1) X particles intrude into B and (2) Y particles intrude into A.

We first simulate the phase dynamics and numerically compute $Q(t)$ defined in Eq. (2.24) on an open-boundary 1D lattice in Fig. 2.5(a). We find that at $p = p_c$, $\overline{Q(t)} \sim t^{-\theta}$ with $\theta = 0.484$ before saturation; when $p > p_c$, θ decreases by increasing p and the system still stays in the critical phase. We also replace the CZ phase gate by a random phase gate and we observe the same scaling behavior (not presented in the plot). For comparison, we compute the fraction $K_0(t)/K$ and we find that it has the same scaling behavior as $Q(t)$, confirming their equivalence in Eq. (2.25) [See the curves for $p = 0.9$ in Fig. 2.5(a)]. In addition, we also consider the case when there are no CNN gates and the particles only diffuse and annihilate upon contact. As shown in Fig. 2.5(b), the probability that the particles never cross the boundary scales as $\overline{K_0(t)}/K \sim t^{-3/16}$ for all p. The exponent $\frac{3}{16}$ is the persistence rate for the 1D diffusion-annihilation process and has been analytically computed in Refs.[68, 69] (For more details, see Appendix. 2.B).

2.3.4 Two-species BAW model

Inspired by the single-species BAW model, in this section, we will take into account all of the phase terms and analyze the dynamics of the purity defined in Eq. (2.14).

Similar to $Q(t)$ in the previous section, only the bit-string pairs with zero relative phase up to time t, viz., those with $-\theta_{n_1'} - \theta_{n_2'} + \theta_{n_1} + \theta_{n_2} = 0$, can contribute to $\mathrm{Tr}[\rho_A^2(t)]$. Any other bit-string pairs will generate random accumulated phase terms, which sum up to zero.

To understand the zero relative phase constraint, we propose a two-species BAW model. Initially, the particles representing the difference of the bit-string pair $|n_1 - n_2|$ are distributed randomly along a 1D lattice. Let X (Y) particles denote the bit-string difference initially in region A (region B). We further define x as the location of the rightmost X particle and y as the location of the leftmost Y particle. As shown in Fig. 2.6, under the hybrid QA circuit with $\mathbb{Z}_2$ symmetry, the particles start to perform BAW. Before X and Y particles encounter one another, the generated phase in each layer θ_n is composed of three parts: $\theta_n^{[1,x]}$, $\theta_n^{(x,y)}$ and $\theta_n^{[y,L]}$, which denote the phases generated within the regimes $[1, x]$, (x, y) and $[y, L]$ respectively. Since the first regime occupied by X particles always satisfies $n_1([1, x]) = n_2'([1, x])$

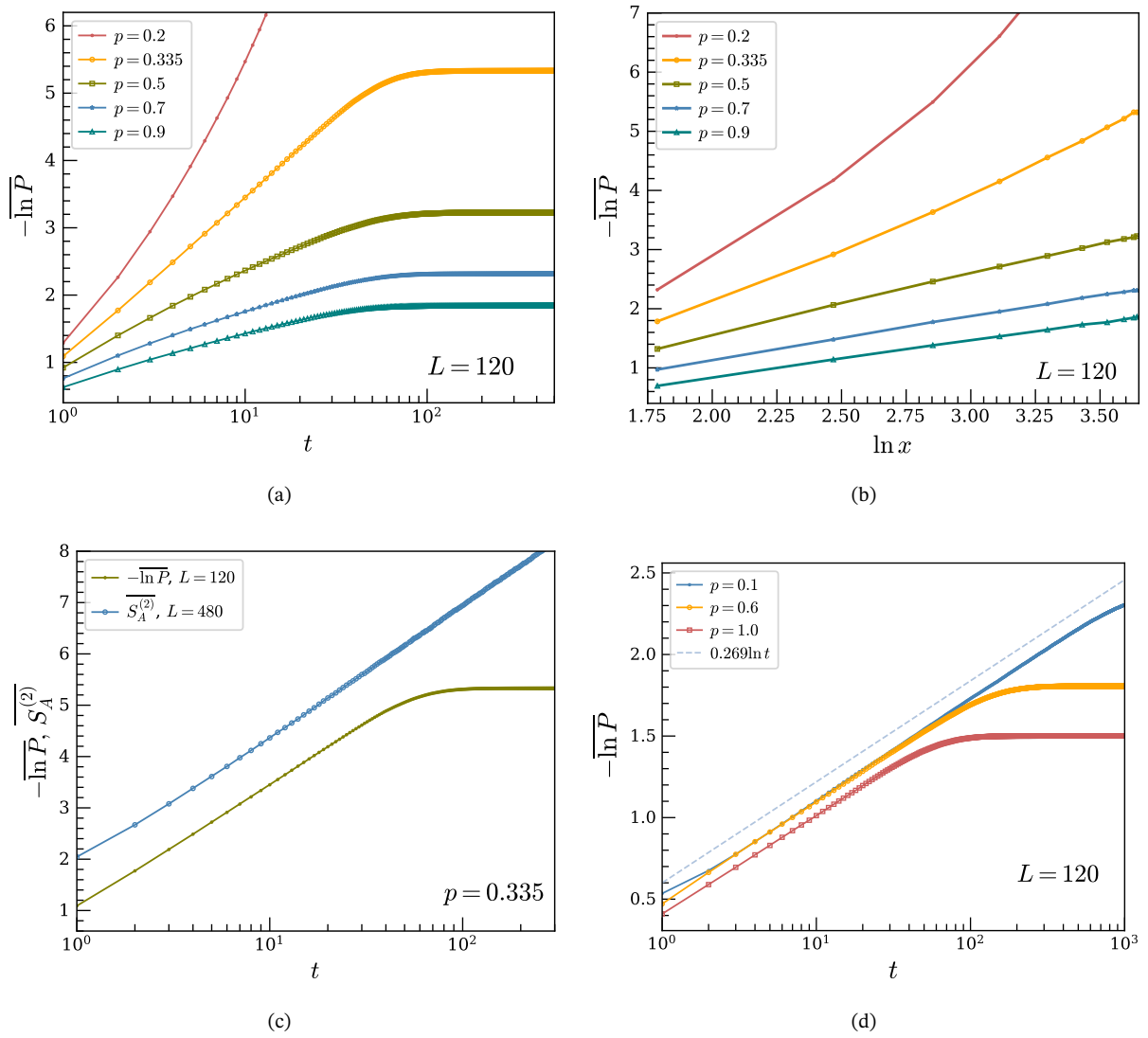

Figure 2.7: (a) $-\overline{\ln P}$ vs t on a semi-log scale, defined for a half-system-size cut with system size $L = 120$. (b) The steady state $-\overline{\ln P}$ vs $\ln(x)$, where $x \equiv \sin(\pi L_A/L)L/\pi$. (c) The comparison of $-\overline{\ln P(t)}$ and $\overline{S_A^{(2)}(t)}$ at $p = p_c$. (d) The scaling of $-\overline{\ln P(t)}$ when the CNN gates are absent. We find that $\lambda_1 = 0.269$ for all p. All of the numerical data of $-\ln P(t)$ are calculated under the periodic boundary condition.

and $n_2([1,x]) = n_1'([1,x])$, we have $\theta_{n_1}^{[1,x]} = \theta_{n_2'}^{[1,x]}$, $\theta_{n_2}^{[1,x]} = \theta_{n_1'}^{[1,x]}$. Similarly, in the third regime occupied by Y particles, $\theta_{n_1}^{[y,L]} = \theta_{n_1'}^{[y,L]}$, and $\theta_{n_2}^{[y,L]} = \theta_{n_2'}^{[y,L]}$. In addition, since there is no particle in the intermediate regime, we have $\theta_{n_1}^{(x,y)} = \theta_{n_2}^{(x,y)} = \theta_{n_1'}^{(x,y)} = \theta_{n_2'}^{(x,y)}$. Therefore the total phase difference vanishes: $-\theta_{n_1'} - \theta_{n_2'} + \theta_{n_1} + \theta_{n_2} = 0$.

Once the rightmost X particle comes across the leftmost Y particle, the two-qubit phase gate acting on sites x and y will generate a nonzero relative phase. For example, if we apply the CZ gate on •• with a possible corresponding bit string configuration $\{|n_1\rangle, |n_2\rangle, |n_1'\rangle, |n_2'\rangle\}_{x,y} = \{|10\rangle, |01\rangle, |00\rangle, |11\rangle\}$, a relative phase $0 + 0 - 0 - \pi = -\pi$ is generated. If we apply the CNOT gate on sites x and y, $\{|n_1\rangle, |n_2\rangle, |n_1'\rangle, |n_2'\rangle\}_{x,y} \to \{|11\rangle, |01\rangle, |00\rangle, |10\rangle\}$, i.e., another type of "particle" different from the two species with bit string configuration $|n_1\rangle_y = |n_2\rangle_y \neq |n_1'\rangle_y = |n_2'\rangle_y$ appears on site y and will

		$p = 0.335$	$p = 0.5$	$p = 0.7$	$p = 0.9$
$-\overline{\ln P}$	λ_1	1.053	0.507	0.355	0.293
	λ_2	1.858	0.999	0.716	0.615
	λ_2/λ_1	1.765	1.970	2.017	2.099
$\overline{S_A^{(2)}}$	λ_1	1.120	0.473	0.334	0.291
	λ_2	1.947	0.926	0.665	0.605
	λ_2/λ_1	1.738	1.958	1.991	2.079

Table 2.1: The comparison of scaling prefactors of the two-species BAW model and the $\mathbb{Z}_2$-symmetric Clifford QA model for various measurement rates $p \geq p_c$. Both of them are computed under periodic boundary condition.

spread along the lattice under further evolution. As time evolves, the configurations for which the two species have met will generate random accumulated phases, half of which are composed of odd numbers of π, while the other half are composed of even numbers of π. The accumulated phase terms $e^{i\Theta_r}$ of such configurations will add up to zero and make no contribution to Eq. 2.14. Therefore, we have

$$\begin{aligned} &\mathrm{Tr}\rho_A^2(t) \approx P(t) \equiv \frac{M_0(t)}{M}, \\ &S_A^{(2)}(t) \approx -\log_2 P(t), \end{aligned} \tag{2.26}$$

where M is the total number of particle configurations and M_0 is the number of configurations in which X and Y particles never encounter one another up to time t.

The validity of the two-species BAW model is numerically verified by simulating $-\ln P$ on a $1D$ lattice with periodic boundary condition. Compared with Fig. 2.6, there are two boundaries between A and B. As shown in Fig. 2.7, we find that this quantity exhibits a logarithmic growth before saturation, i.e., $-\ln P(t) = \lambda_1 \ln t$ for $p \geq p_c$. Specifically, we compare the value of $-\overline{\ln P(t)}$ and $\overline{S_A^{(2)}(t)}$ at $p = p_c$ in Fig. 2.7(c) and find that they have the same scaling. Numerically, $\lambda_1(p_c) = 1.053 \approx 1.12$ where 1.12 is the prefactor of the logarithmic scaling of $S_A^{(2)}(t)$ at $p = p_c$. In addition, we remove the CNN gates in Fig. 2.7(d) and let the particles perform diffusion-annihilation random walks. As a result, we find $-\overline{\ln P(t)} \sim 0.269 \ln(t)$ for all p, with the prefactor 0.269 being close to 0.283 which is the prefactor of the entanglement entropy without CNN gates.

We also investigate P in the steady state and use this to understand the steady state entanglement entropy. In the steady state, M_0 is the number of configurations in which X or Y particles have vanished by annihilating with themselves before they encounter one another. If the subsystem length $L_A \ll L$, it is highly possible that the X particle will vanish first. In this case, when $p \geq p_c$, the subsystem A reaches the steady state at $t \sim L_A^z$ and we have

$$P(t = L_A^z) \sim L_A^{-\lambda_1 z}, \tag{2.27}$$

this leads to a logarithmic scaling of entanglement entropy with respect to the subsystem length L_A. In particular, the prefactor is $\lambda_1 z$.

We simulate $-\ln P$ in the steady state in Fig. 3.5(b) to numerically verify the above analysis. Here we fix the total system length $L = 120$ and vary the subsystem length L_A. As expected, we observe a phase transition from the volume-

law phase to a critical phase in which

$$-\ln P = \lambda_2 \ln\left(\sin\left(\pi L_A/L\right)L/\pi\right) \tag{2.28}$$

for $p \geq p_c$. We calculate the ratio between λ_2 and λ_1 for different p and find that $\lambda_2/\lambda_1 = 1.765$ at $p = p_c$ and $\lambda_2/\lambda_1 = 2.029$ at $p > p_c$, which are consistent with the two dynamical exponents $z = 1.744$ at $p = p_c$ and $z = 2$ at $p > p_c$ in the PC universality class. These exponents are also very close to the numerical simulation of the Clifford QA model $\lambda_2/\lambda_1 = 1.738$ at p_c and $\lambda_2/\lambda_1 = 2.009$ for $p > p_c$. (For a more detailed comparison, see Table. 2.1). Consequently, we can confirm that the hybrid QA model with $\mathbb{Z}_2$ symmetry can be well-described by the classical two-species BAW model.

2.4 Purification Dynamics

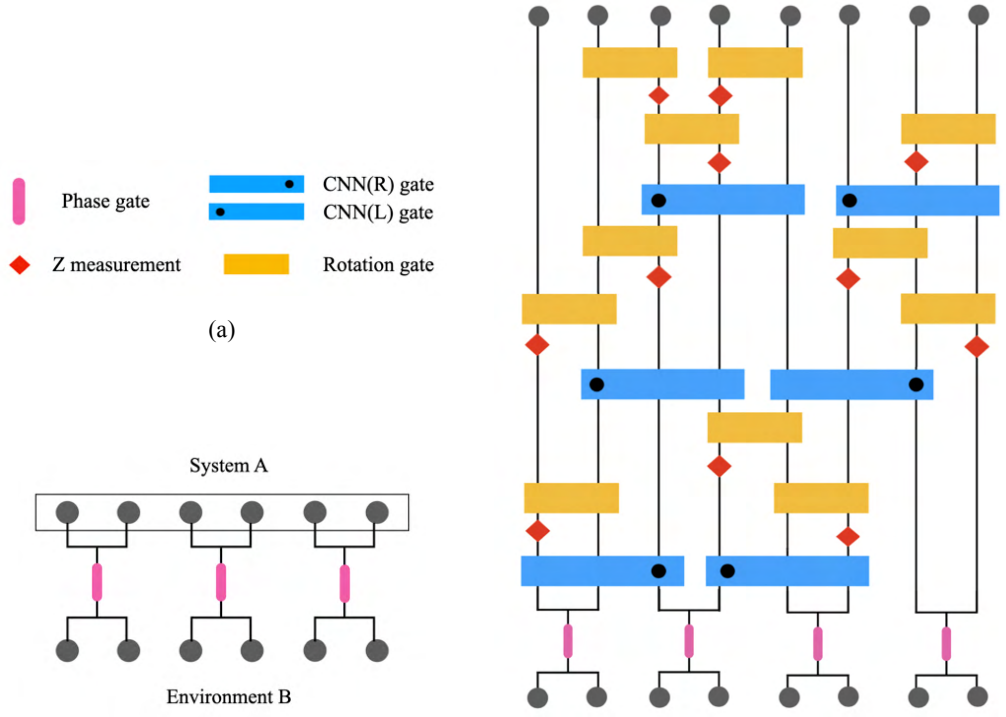

Figure 2.8: Illustration of the circuit used to explore purification dynamics. (a) Every phase gate acts on four qubits, two from system A and two from environment B, in order to form $\frac{L}{2}$ EPR pairs. (b) The symbols of the four-qubit phase gate, three-qubit CNN gate, the single-qubit Z measurement gate and two-qubit rotation gate . (c) The arrangement of gates in a time step for the purification process of $\mathbb{Z}_2$-symmetric hybrid QA circuit model. Except the initial setup in (a), the hybrid circuit is applied in system A only.

In this section we will study the purification dynamics of the hybrid QA model with $\mathbb{Z}_2$ symmetry [30]. We consider

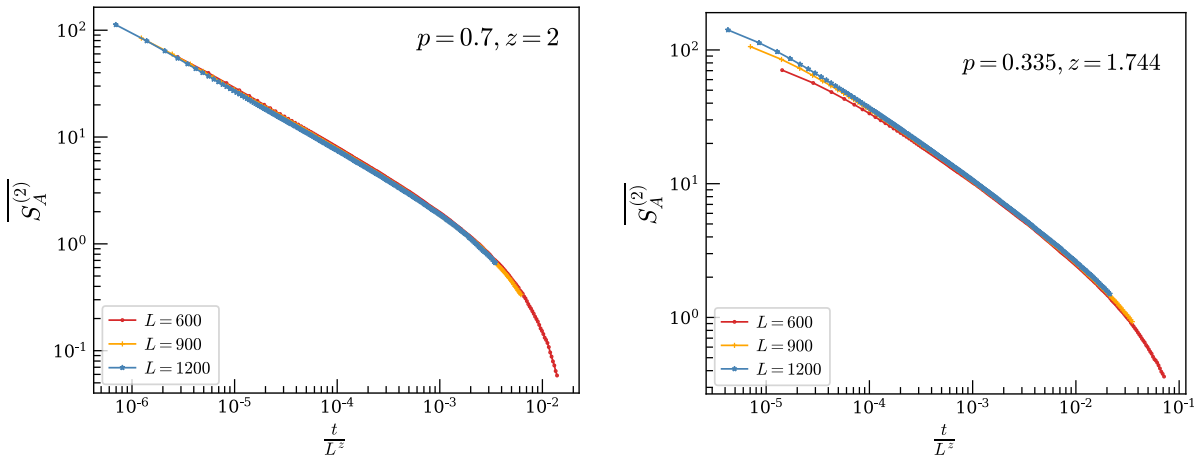

Figure 2.9: Data collapse of purification dynamics described in Fig. 3.6(c). (a) is the result at $p = 0.7 > p_c$ and (b) is the result at $p_c = 0.335$.

system A and environment B entangled together, and then apply the hybrid circuit solely on the system A. We aim to explore how the entropy of the system depends on the measurement rate.

Under a generic hybrid quantum dynamics, the system will eventually be purified. It is shown in Ref. [30] that the time of purification can be used to characterize the entanglement phase transition. In the volume-law phase with $p < p_c$, the purification time diverges exponentially in the system size L, while in the area-law phase with $p > p_c$, the entropy decays exponentially with a finite rate and the purification time is proportional to $\ln L$. At the critical point p_c, the entropy decays algebraically when $t \ll L^z$. This result also holds in the hybrid QA circuit without $\mathbb{Z}_2$ symmetry, where the purification dynamics can be further interpreted in terms of classical bit-string dynamics [40].

In the presence of the $\mathbb{Z}_2$ symmetry, we will show that the purification dynamics of the QA circuit will be modified when $p > p_c$, analogous to the entanglement dynamics we studied in the previous section. Numerically, we prepare a product state with $2L$ qubits polarized in the x direction, and then divide them into system A and environment B with equal size L. In order to impose the $\mathbb{Z}_2$ symmetry, we measure the Pauli string $Z_1 Z_2 \cdots Z_L$ in the system and $Z_{L+1} Z_{L+2} \cdots Z_{2L}$ in the environment. Then we apply a four-qubit diagonal phase gates onto the system A and environment B as in Fig. 3.6(a) to create entanglement between them. The phase gate assigns a π phase to the basis $|0110\rangle, |0111\rangle, |1110\rangle, |1111\rangle$ with the rest of the basis remaining invariant. Moreover, it is a Clifford gate and therefore the total initial state can be represented as a stabilizer state. Since each phase gate can create $\ln 2$ entanglement between the system and the environment, the system has an entropy $S_A^{(2)} = \frac{L}{2} \ln 2$.

In the purification dynamics, the unitary and measurement gates are applied solely on system A, as shown in Fig. 3.6(c). Notice that different from the entanglement process illustrated in Fig. 3.2(b), here we do not need to introduce phase gates, due to the fact that the phases between $\{|n_1\rangle, |n_2'\rangle\}$ and between $\{|n_2\rangle, |n_1'\rangle\}$ always cancel with each other. Therefore the unitary evolution consists solely of CNN gates, which simply map one basis state to another. These gates scramble the quantum information within system A, while the entropy of the full system remains the same. On the other hand,

the measurement gate disentangles the system from the environment, and the entropy decreases monotonically under the time evolution.

We simulate the purification dynamics of the above hybrid QA Clifford circuit. When $p > p_c$, we observe that the entropy has a slow diffusive power law decay for a long period of time due to the presence of the $\mathbb{Z}_2$ symmetry, while it takes a time exponentially long in system size to purify the system when $p < p_c$. The data collapse of different system sizes in Fig. 2.9(a) further indicates that $\overline{S_A^{(2)}} = F(t/L^z)$ with $z = 2$ when $p > p_c$. In addition, at critical point p_c, the above scaling form also works with different $z = 1.744$ [See Fig. 2.9(b)]. We believe that such scaling is universal in other non-Clifford hybrid QA circuits with $\mathbb{Z}_2$ symmetry and the dynamical exponents are consistent with what we found in the entanglement dynamics.

2.5 Conclusion

In this chapter, we explore the $\mathbb{Z}_2$-symmetric quantum automaton (QA) circuit subject to local composite measurements. By tuning the measurement rate p, we find an entanglement phase transition from a volume-law entangled phase to a critical phase with logarithmic entanglement scaling. By analyzing the underlying classical bit-string dynamics, we show that the critical point p_c belongs to the parity-conserving universality class. We further show that the critical phase is protected by the combination of $\mathbb{Z}_2$ symmetry and the special feature of QA circuit. We derive an effective two-species particle model in which particles perform branching-annihilating random walks. We use this model to understand the entanglement dynamics and illustrate that the purity of the wave function is equivalent to the fraction of particle configurations in which two different species of particles never encounter. Based on this result, we show that the prefactors of the logarithmic second Rényi entropy at the critical point and the critical phase are related to the local persistence exponents of the corresponding two-species particle models. In addition, the above critical behavior when $p \geq p_c$ is further demonstrated in the purification process.

The idea of presenting bit-string dynamics in the particle language can also be applied in Ref. [40] to explain the entanglement phase transition without $\mathbb{Z}_2$ symmetry that belongs to the directed percolation universality class. Based on this method, it is also possible to develop similar tools to understand the universality classes of entanglement phase transition in the hybrid Haar random circuit and hybrid Clifford random circuit[25, 26]. In addition, it can also be used to understand the subleading correction term in the non-thermal volume-law phase when $p < p_c$[33, 52]. This interesting question will be explored in the next chapter.

Acknowledgement.— We acknowledge Ethan Lake for his careful proofreading. We also acknowledge the helpful discussions with Jason Iaconis.

2.A parity-conserving universality class and the branching-annihilating random walks

Nonequilibrium phase transitions in classical dynamical lattice models can be classified purely by their scaling behavior. The most common nonequilibrium class is the directed percolation (DP) universality class. Another class called parity-conserving (PC) universality class emerges when we add extra symmetry, namely, parity conservation to the system. Like the DP universality class, the PC universality class is very robust in a sense that it contains many models that share the same critical exponents. In this appendix, we will show that the BAW model introduced in Sec. 2.3 belongs to the PC universality class.

In Sec. 2.3 we have established the connection between the hybrid QA model with $\mathbb{Z}_2$ symmetry and a classical particle model. Under the QA circuit composed of CNN gates and composite measurements, the particles perform the branching-annihilating random walks (BAW) where they diffuse on a one-dimensional lattice and annihilate when they come into contact with probability p. Furthermore, each particle can generate an even number of off-springs, $i.e.$

$$W \leftrightarrow 3W,\ W + W \xrightarrow{p} \emptyset. \tag{2.29}$$

There are three initial conditions which lead to different scaling behavior of various properties under the same dynamics: (a) the seeding process starting with a pair of adjacent particles, (b) the seeding process starting with a single particle, and (c) the purification process starting with a fully occupied state.

We first analyze the BAW model with initial condition (a) numerically. We vary p and measure the scaling behavior of the mean particle number $\overline{N(t)}$. As shown in Fig. 2.10(a), we observe a phase transition while adjusting p: when $p < p_c \approx 0.335$, an active steady state with finite number of particles emerges. At $p = p_c$, $\overline{N(t)} \sim t^{\theta}$ where $\theta = 0$. When $p > p_c$, the dynamics is dominated by annihilation of particles in pairs and the system enters an absorbing phase where the particle number is monotonically decreasing until $\overline{N(t \to \infty)} = 0$. In addition, we measure two other quantities: $P(t)$, the probability that the system has not entered the absorbing phase at time t; $\overline{R^2(t)}$, the mean-square distance from the center of the lattice chain, averaged over the surviving samples. From Fig. 2.10(b), when $p < p_c$, the system maintains a finite possibility to survive and stay away from the absorbing phase. When $p = p_c$, $P(t) \sim t^{-\delta}$ where $\delta = 0.286$. Notably, when $p > p_c$, $P(t)$ still decays as a power law with the exponent $1/z = 1/2$. P can also be viewed as an order parameter which marks the existence of a phase transition. Furthermore, the numerics in Fig. 2.10(c) shows that the mean-square distance $\overline{R^2(t)} \sim t^{2/z}$ at $p = p_c$ with the other dynamical exponent $z = 1.833$. These exponents are universal for the PC universality class and agree with the numerical findings that $\delta = 0.286$, $\theta = 0$, $z = 1.744$ when $p = p_c$ and $z = 2$ for $p > p_c$ in Ref.[47].

We also study the other initial conditions under the same dynamics. Fig. 2.11(a) exhibits the scaling of $\overline{N(t)}$ for the seeding process starting with a single particle. It is easy to see that the system will never reach an empty state for $N(0) = 1$ since the parity is conserved, therefore, the survival rate $P(t)$ is always zero, $\delta = 0$ for all p. On the other hand, $\overline{N(t)} \sim t^{0.286}$ when $p = p_c$. These exponents coincide with that of the seeding process starting with a pair of particles

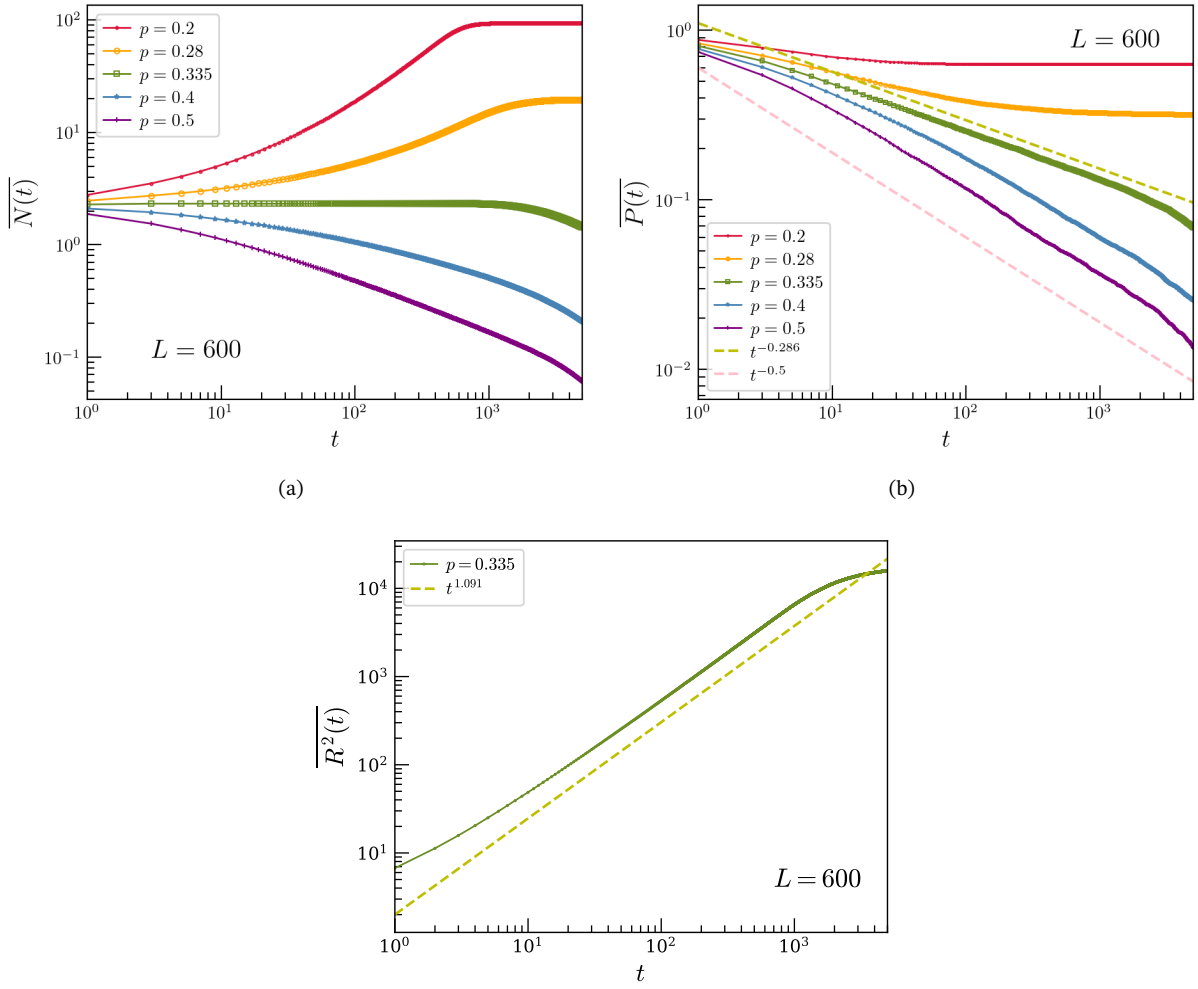

Figure 2.10: We simulate the BAW model of the seeding process starting with a pair of adjacent particles and find that the critical point is around $p_c = 0.335$. In the calculation done in the Appendix with $L = 600$, we find that if we choose $p_c = 0.335$, the critical exponents have the best match with the critical exponents of the PC universality class. (a) The mean particle number $\overline{N}$ vs t on the log-log scale for $L = 600$. (b) P vs t on a log-log scale for $L = 600$. When $p = p_c$, $P(t) \sim t^{-0.286}$ and when $p > p_c$, $P(t) \sim t^{-0.5}$. (c) The mean-square distance scales as $\overline{R^2(t)} \sim t^{1.091}$ at $p = p_c$ for $L = 600$.

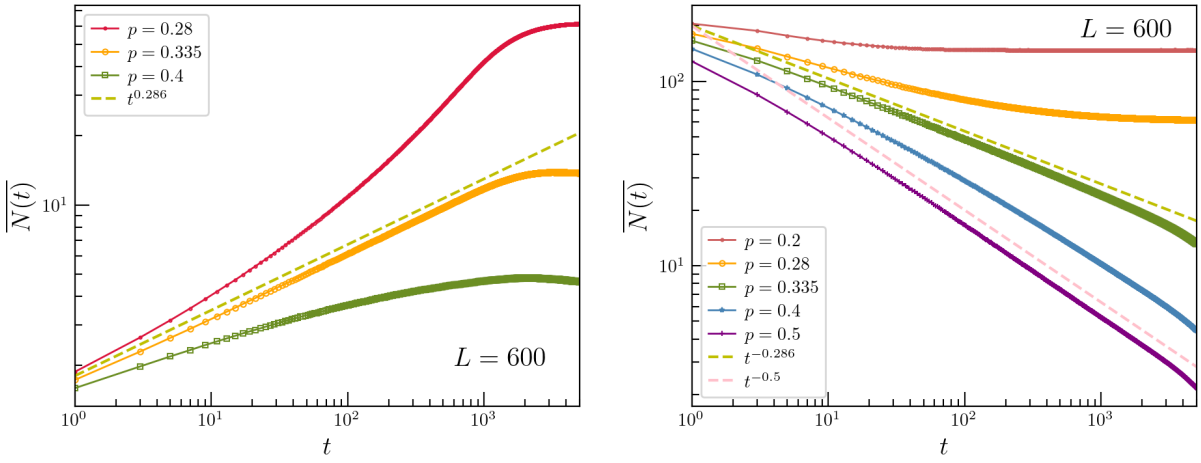

(a) (b)

Figure 2.11: The mean particle number $\overline{N(t)}$ vs t on a log-log scale for (a) the seeding process beginning with a single particle and (b) the purification process starting with a fully occupied state.

except that the values of δ and θ exchange, which is quite interesting.

As shown in Fig. 2.11(b), $\overline{N(t)}$ for the purification process has a similar scaling with $P(t)$ for the seeding process starting with a pair of adjacent particles. When the measurement rate $p < p_c$, the system approaches an active state with a finite number of particles. Once $p = p_c$, $\overline{N(t)} \sim t^{-0.286}$. When $p > p_c$, the particles are performing annihilation-dominated BAW, $\overline{N(t)}$ still decays algebraically, i.e., $\overline{N(t)} \sim t^{-1/2}$.

2.B Single-species BAW model and the first passage problem

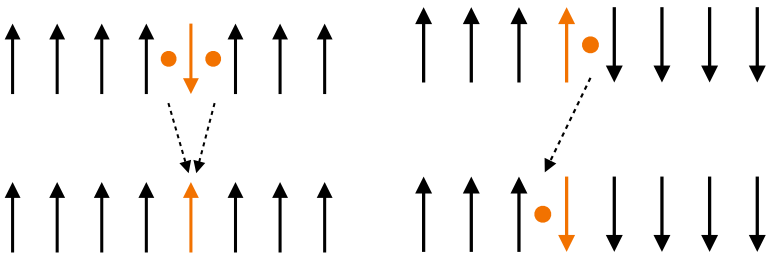

(a) (b)

Figure 2.12: Mapping between the zero-temperature Glauber dynamics in one dimension and the corresponding domain wall quasiparticles: (a) the spin marked in orange is updated and the domain wall quasiparticles annihilate; (b) the spin marked in orange is flipped to match the value of its right neighbor and the domain wall quasiparticle diffuses to the left.

In this appendix, we will investigate the correspondence between the single-species BAW model in Sec. 2.3.3 and the first passage problem of the 1D Ising model discussed in Ref.[68].

In Ref. [68], they studied the persistence probability $r(q, t)$ that a given spin stays in the same state up to time t

of an infinite 1D q-state Potts model whose update rule obeys the zero-temperature Glauber dynamics. If a random initial q-state spin configuration is quenched at zero temperature, the dynamics tends to align all the spins. At each time step, a chosen spin is updated according to the values of its two nearest neighbors, i.e., $S_i(t+1) = S_{i-1}(t)$ or $S_{i+1}(t)$ with equal probability. They proposed a coagulation model which treats $S_0(t)$ at different time steps as random walkers which coalesce upon contact in the time-reversed order and find that the persistence rate is just the probability that $S_0(1) = S_0(2) = \cdots = S_0(t)$ which scales as

$$r(q,t) \sim t^{-\theta(q)}, \tag{2.30}$$

where the exponent has the analytical expression

$$\theta(q) = -\frac{1}{8} + \frac{2}{\pi^2}\left[\cos^{-1}\left(\frac{2-q}{\sqrt{2}q}\right)\right]^2. \tag{2.31}$$

A single-species BAW model was introduced in Sec. 2.3.3. Initially, the particles are distributed randomly in the left half of the lattice chain. Under the unitary gates and composite measurements, the particles perform BAW. We have demonstrated that $Q(t)$ defined in Eq. 2.24 is equivalent to $-\ln(K_0/K)$, where $K_0(t)/K$ is the fraction of particle configurations in which the particles never diffuse into the right half of the lattice chain up to time t, or in other words, the probability that the boundary between A and B has never been visited by the particles. If we consider the case when the particles are performing diffusion-annihilation random walks, i.e., there are no CNN gates, and we treat them as domain walls between the spins, then their dynamics under the measurement-only circuit has a one-to-one correspondence to the zero-temperature Glauber dynamics of the 1D Ising model ($q = 2$). As illustrated in Fig. 2.12, when the spin different from both of its nearest neighbors is flipped, the domain walls annihilate; When its neighbors are in different states and the spin is aligned with one of them, the domain wall either diffuses or stays still. Besides, there is no creation of domain walls, i.e., no particle branching since the zero temperature prohibits any energy-raising move. Then $K_0(t)/K = \sqrt{r(q=2,t)}$, since it is equivalent to the probability that the spin on the boundary of a finite chain has never flipped. Thus, $K_0(t)/K$ decays as a power law with the exponent $\theta(q=2)/2 = 3/16$.

Chapter 3

Entanglement structure in the volume-law phase of hybrid quantum automaton circuits

3.1 Introduction

The past few years have witnessed a surge of interest in monitored quantum dynamics[25, 27, 26, 31, 30, 37, 36, 42, 46, 44, 45]. These non-unitary dynamics can exhibit many emergent phenomena which are inaccessible in pure unitary dynamics or in systems in equilibrium. It is by now well-known that in a generic interacting system, repeated measurements can induce a continuous phase transition from a highly-entangled volume-law phase to a disentangled area-law phase [25, 27, 26, 31, 30, 37, 36]. In addition, specific types of measurements can stabilize various quantum phases, including critical phases and ordered phases[42, 70, 46, 44, 45]. These rapid developments significantly broaden our understanding of non-equilibrium dynamics.

To understand these emergent phenomena in monitored quantum dynamics, various non-unitary random circuits have been constructed. This includes hybrid random Clifford circuits and hybrid random Haar circuits. For Clifford circuits, there exists a very efficient algorithm in terms of the stabilizer formalism which allows us to simulate non-unitary dynamics for very large system sizes [71, 26, 31, 30]. On the other hand, Haar circuits provide an important analytical approach which can map many quantum dynamics problems to statistical mechanics models [25, 37, 36].

Recently, a new type of circuit called hybrid quantum automaton (QA) circuit was constructed to investigate the entanglement dynamics in the monitored quantum systems [40]. This circuit is composed of QA unitaries and local composite measurements. Compared with random Haar/Clifford circuits, QA circuits not only provide an efficient method for large-scale numerical simulation, but also provide an analytical tool to understand the quantum dynamics. Due to the basis-preserving feature of QA circuits, the entanglement dynamics can be interpreted in terms of a classical bit-string

picture. Specifically, the second Rényi entropy can be mapped to the first-passage problem in the bit-string dynamics. Based on this mapping, it was further shown that the measurement-induced entanglement phase transition in a generic hybrid QA circuit belongs to the directed percolation (DP) universality class[40]. At the critical point, the prefactor of the logarithmic entanglement is related to the local persistent exponent in the DP universality class. By further imposing symmetries in the dynamics, new critical points or critical phases belonging to different universality classes can also be identified [70].

Inspired by the above bit-string picture, in this chapter we will study the weakly-monitored volume-law phase of one-dimensional (1d) hybrid QA circuits. In particular, we will study the fluctuation of the entanglement in this random dynamics and the quantum error correction property of the volume-law phase. Previous studies for 1d random Haar circuits suggested that the entanglement entropy can be mapped to the free energy of the directed polymer in a random environment (DPRE) which has fluctuation belonging to the Kardar-Parisi-Zhang (KPZ) universality class [28, 25, 49, 50]. Such fluctuations lead to a subleading correction term scaling as $L^{1/3}$ in the entanglement entropy in the volume-law phase, which has also been numerically verified for random Clifford circuits [51, 52]. We numerically show that the entanglement entropy of a subsystem in both the early-time dynamics and the steady state in the hybrid Clifford QA circuit also exhibit sample-to-sample fluctuations with the same scaling behavior. In order to understand this behavior, we construct a particle model based on the bit-string picture in which the particles undergo stochastic random dynamics. We compute the classical quantity in the particle model which corresponds to the second Rényi entropy in the QA circuit, and show that it exhibits similar fluctuation.

In addition, we study the purification dynamics in the hybrid QA circuit in the volume-law phase[30]. We modify the aforementioned particle model slightly and use this to give an interpretation of the entanglement entropy of a subsystem in the presence of the environment. Previously, it was shown that for purification dynamics, the hybrid quantum circuit can dynamically generate a quantum error correcting code (QECC) [30, 29, 33], whose property has been quantitatively investigated in the Clifford circuit [52]. We analyze this code in the hybrid QA circuit in terms of the particle model and show that it exhibits two types of contiguous code distance for different errors with both of them diverging in the thermodynamic limit.

Interestingly, the stochastic classical particle model itself has an error correction property, and can dynamically generate a classical linear code (CLC). We study this random CLC by analyzing the dynamics of the associated generator matrix and numerically compute its contiguous code distance.

3.2 Review of the hybrid QA circuit and two-species particle model

Ref. [40] establishes the relationship between the entanglement dynamics and the classical bit-string dynamics in the hybrid QA circuit. The subsequent work in Chapter 2 explicitly constructs a classical particle model to describe the entanglement dynamics of the $\mathbb{Z}_2$-symmetric hybrid QA circuit. In this section, we briefly review some of the important results in these two works and modify the two-species particle model so that it can be applied on hybrid QA circuits without any symmetry.

The hybrid QA circuit is composed of QA unitary operators and composite measurements. A QA unitary gate permutes product states in the computational basis up to a phase, i.e.,

$$U|n\rangle = e^{i\theta_n}|\pi(n)\rangle, \tag{3.1}$$

where $\pi \in S_{2^L}$ is an element of the permutation group on the computational basis of a lattice with L qubits. We choose the Pauli Z basis as the computational basis and take the initial state to be a product state polarized in x direction, $|\psi\rangle = |+x\rangle^{\otimes L}$. QA unitaries scramble the phase information stored in $|\psi\rangle$ and hence increase the entanglement of the state until it saturates to the volume-law scaling. Meanwhile, the wave function remains an equal-weight superposition of computational basis states, which is the characteristic of QA circuits.

On the other hand, local measurements can suppress the growth of entanglement. In the QA circuit, the composite measurement of the i-th qubit is defined as a projection operator followed by a Hadamard gate,

$$M_i^\sigma = H_i \circ P_i^\sigma, \tag{3.2}$$

where $P_i^\sigma = \frac{1\pm Z_i}{2}$ is the Pauli Z measurement on site i with the outcome $\sigma = \{0, 1\}$ and H_i rotates the state back to an equal-weight superposition over the computational basis. Therefore, after imposing M_i^σ, the phase information for half of the basis states is lost. The composite measurements disentangle the system while preserving the special feature of QA circuits.

It is shown in Ref. [40] that by increasing the measurement rate p, the one-dimensional hybrid QA circuit undergoes an entanglement phase transition from a volume-law entangled phase to an area-law disentangled phase, with the phase transition belonging to the $1+1$d directed percolation (DP) universality class. If we bipartition the system into subsystem A and its complement B, a common quantity to measure the entanglement between them is the n^{th} Rényi entropy:

$$\begin{aligned} S_A^{(n)} &= \frac{1}{1-n}\log_2\left[\mathrm{Tr}(\rho_A^n)\right] \\ \rho_A &= \mathrm{Tr}_B|\psi\rangle\langle\psi|. \end{aligned} \tag{3.3}$$

In this chapter, we focus on the second Rényi entropy with $n = 2$, whose purity equals the expectation value of the SWAP_A operator over two copies of the state [65, 66],

$$\mathrm{Tr}(\rho_A^2) = \langle\psi|_2 \otimes \langle\psi|_1 \mathsf{SWAP}_A |\psi\rangle_1 \otimes |\psi\rangle_2, \tag{3.4}$$

where the SWAP_A operator exchanges the spin configurations $|\alpha\rangle$ within subsystem A.

The entanglement dynamics of the hybrid QA circuit can be interpreted in terms of classical bit-string dynamics. By inserting two sets of complete basis on the right side of the SWAP_A operator in Eq. 4.9 and applying the circuit on the

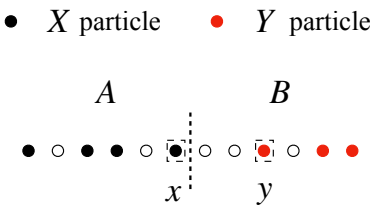

Figure 3.1: A cartoon of the two-species particle model. The black dots represent X particles, and the red dots represent Y particles. Initially, X and Y particles are distributed in region A and B respectively. We use x and y to denote the leftmost X particle and the rightmost Y particle.

bit-strings in a time-reversed order, we obtain

$$\mathrm{Tr}(\rho_A^2) = \frac{1}{4^L} \sum_{n_1,n_2} e^{-i\Theta_{n_1'}} e^{-i\Theta_{n_2'}} e^{i\Theta_{n_1}} e^{i\Theta_{n_2}}, \tag{3.5}$$

where

$$\begin{aligned} |n_1'\rangle|n_2'\rangle &\equiv \mathsf{SWAP}_A|n_1\rangle|n_2\rangle \\ &= \mathsf{SWAP}_A|\alpha_1\beta_1\rangle|\alpha_2\beta_2\rangle \\ &= |\alpha_2\beta_1\rangle|\alpha_1\beta_2\rangle, \end{aligned} \tag{3.6}$$

and $e^{i\Theta_{n_i}} = \sqrt{2^L}\langle n_i|\tilde{U}_t|\psi_0\rangle$, with $\tilde{U}_t$ denoting the circuit evolution. In order to compute $\mathrm{Tr}(\rho_A^2)$, we need to understand the dynamics of the relative phase $\Theta_r = -\Theta_{n_1'} - \Theta_{n_2'} + \Theta_{n_1} + \Theta_{n_2}$ for each bit-string pair $\{|n_1\rangle, |n_2\rangle\}$. Under QA evolution, nonzero randomly distributed Θ_r will lead to destructive interference, and as such only configurations with trivial relative phase contribute to the purity. This observation motivates us to construct a two-species particle model, as mentioned in the previous chapter.

The particles here characterize the difference between a bit-string pair $\{|n_1\rangle, |n_2\rangle\}$,

$$h(x,t) = |n_1(x,t) - n_2(x,t)|. \tag{3.7}$$

We use the empty site symbol $\circ$ to denote $h(x) = 0$ and the occupied site symbol $\bullet$ to denote $h(x) = 1$. Specifically, we represent the difference at $t = 0$ in A (B) by X (Y) particles, as illustrated in Fig. 3.1. Under the time evolution, these two species start to expand according to the update rule determined by the circuit. For the rest of the chapter, we focus on QA unitary gates U which are linear with respect to the bit-string addition defined in finite field $\mathbb{F}_2$, so that for any bit string pair n_1 and n_2, $U(|n_1\rangle + |n_2\rangle) = U|n_1 + n_2\rangle$. This means that we can directly work on the particle representation $h(x,t)$ without keeping track of the bit-string dynamics. One good example is the two-qubit CNOT gate. When the first qubit acts as the control, we have $\bullet\circ \leftrightarrow \bullet\bullet$. On the other hand, the composite measurement forces the spins on the same site to be identical, which results in particle annihilation, $\bullet \to \circ$. Only the configurations in which the X and Y particles do not meet up to time t yield $\Theta_r = 0$ and hence contribute to the purity (For more details, see Chapter 2). Therefore,

we have

$$\begin{aligned} \mathrm{Tr}\rho_A^2(t) &= \frac{N(t)}{2^L} \equiv P(t), \\ S_A^{(2)}(t) &= -\log_2 P(t), \end{aligned} \tag{3.8}$$

where $N(t)$ is the number of configurations in which the two species do not meet up to time t. At the critical point $p = p_c$, the fraction $P(t)$ decays algebraically as $P(t) \propto t^{-\alpha}$, where α is the persistence exponent. For the DP universality class, $\alpha = 0.938$ is a universal number [40]. This power-law decay is responsible for the logarithmic scaling of the entanglement entropy at criticality.

3.3 Entanglement dynamics in the volume-law phase

We now take a closer look at the entanglement entropy in the volume-law phase with $p < p_c$. Previous studies of these $1+1$d hybrid circuits indicate that randomness induces strong fluctuations in the entanglement entropy in both spatial and temporal directions. A nice way to understand this problem is through the minimal cut picture introduced in Ref. [28], which maps the entanglement dynamics to the first passage problem on a percolation lattice. Such a picture rigorously describes the zeroth Rényi entropy $S_A^{(0)}$ of the Haar random circuit subject to projective measurements. For the entropy with higher Rényi index, it is argued that it can be treated as the free energy of the domain wall in a disordered magnet[51, 72]. Notice that in both approaches, the entanglement entropy is mapped to the free energy of the $1+1$d directed polymer in a random environment (DPRE), whose fluctuation belongs to the KPZ universality class. As a result, there exists a sub-leading correction term in the ensemble averaged entanglement entropy in both the early-time dynamics and the steady states, i.e.,

$$\langle S_A(t) \rangle = \lambda_1 t + a t^\beta + \cdots, \tag{3.9}$$

$$\langle S_A(L_A) \rangle = \lambda_2 L_A + b L_A^\beta + \cdots, \tag{3.10}$$

where the brackets represent an ensemble average and $\beta = \frac{1}{3}$ is the "roughness exponent" of the DPRE[49]. The sub-leading correction term can be extracted by computing the standard deviation

$$\delta S_A(t) = \sqrt{\langle [S_A(t)]^2 \rangle - \langle S_A(t) \rangle^2} \propto t^\beta, \tag{3.11}$$

$$\delta S_A(L_A) = \sqrt{\langle [S_A(L_A)]^2 \rangle - \langle S_A(L_A) \rangle^2} \propto L_A^\beta, \tag{3.12}$$

which characterizes the sample-to-sample fluctuations with the same exponent β. This result has been confirmed numerically in Clifford circuits in Refs. [51, 52]. Below we will numerically examine the volume-law phase of the hybrid Clifford QA circuit and understand its physics in terms of the particle dynamics.

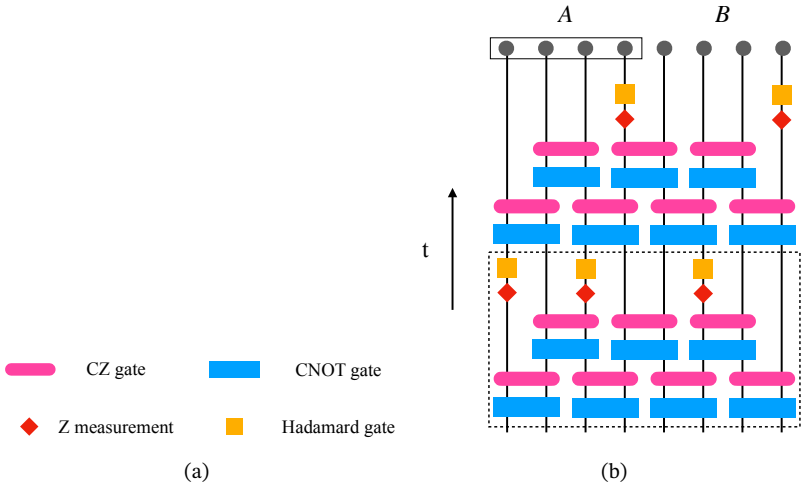

Figure 3.2: (a) A schematic for the gates appearing in the hybrid Clifford QA circuit. (b) The dashed box represents the arrangement of gates in a single time step. Each time step involves two layers of CNOT gates and two layers of CZ gates, interspersed with composite measurements with probability p.

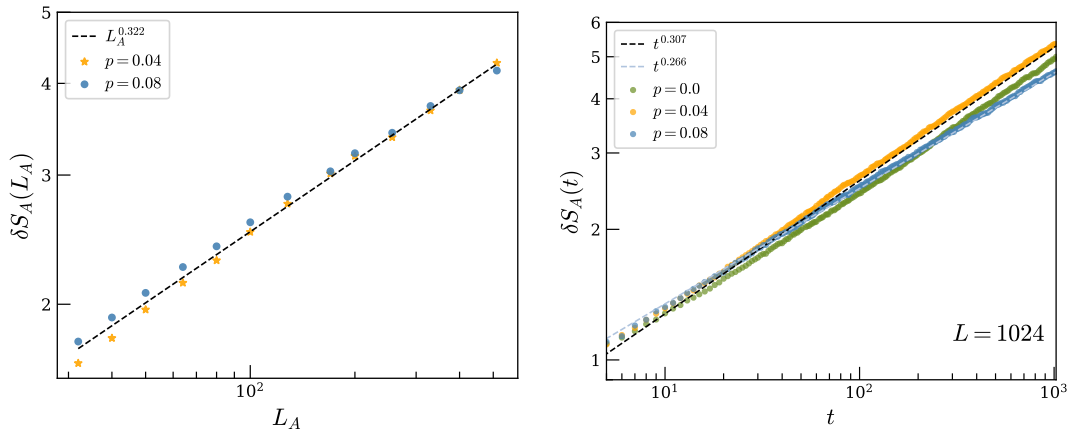

Figure 3.3: (a) The standard deviation of entanglement entropy δS_A vs L_A plotted on a log-log scale. The data are computed from the steady-state entanglement entropy S_A for half-system size $L_A = L/2$ over a variety of L. The measurement rates are taken to be $p = 0.04$ and $p = 0.08$. (b) The standard deviation of early-time entanglement entropy δS_A vs t for $p = 0, 0.04, 0.08$. All of the numerical data for entanglement entropy are calculated with periodic boundary conditions (PBC).

3.3.1 Numerical study in hybrid Clifford QA circuits

We consider a hybrid Clifford QA circuit in which the QA unitaries also belong to the Clifford group. According to the Gottesman-Knill theorem [71, 64], the Clifford circuit can be efficiently simulated on a classical computer using the stabilizer formalism. As illustrated in Fig. 3.2, the circuit is constructed from two types of unitary gates chosen from the two-qubit Clifford group, namely, CNOT and CZ gates, as well as sporadic composite measurements distributed with probability p. The critical point is at $p_c \approx 0.138$ [40]. The numerics in Fig. 3.3(a) indicates that for $0 < p < p_c$, the

standard deviation of the steady-state entanglement entropy scales as $\delta S_A \propto L_A^{\beta_1}$ with $\beta_1 \approx 0.322$.

Aside from the steady state, we also study the early-time entanglement dynamics in the volume-law phase. Similarly, we observe in Fig. 3.3(b) that for $p < p_c$ (not necessarily nonzero), $\delta S_A(t) \propto t^{\beta_2}$ with $\beta_2 \approx 0.307$ for $p = 0$ and $p = 0.04$, and $\beta_2 \approx 0.266$ for $p = 0.08$. For $p \leq 0.04$, The exponents of the sub-leading terms of the steady-state and early-time entanglement entropies are similar and are close to the roughness exponent, i.e., $\beta_1 \approx \beta_2 \approx \frac{1}{3}$. The exponent $\beta_2 \approx 0.266$ at $p = 0.08$ is smaller than $1/3$ and is probability due to the proximity to the critical point. We also consider the entanglement entropy in the purification dynamics of the same circuit and in the $\mathbb{Z}_2$-symmetric hybrid Clifford QA circuit. In both cases, we find that it exhibits similar fluctuation. The details can be found in App. 3.C and App. 3.A. Overall, these results provide numerical evidence that the entanglement entropy in the volume-law phase of the Clifford QA circuit has KPZ fluctuations.

3.3.2 Single-species particle dynamics

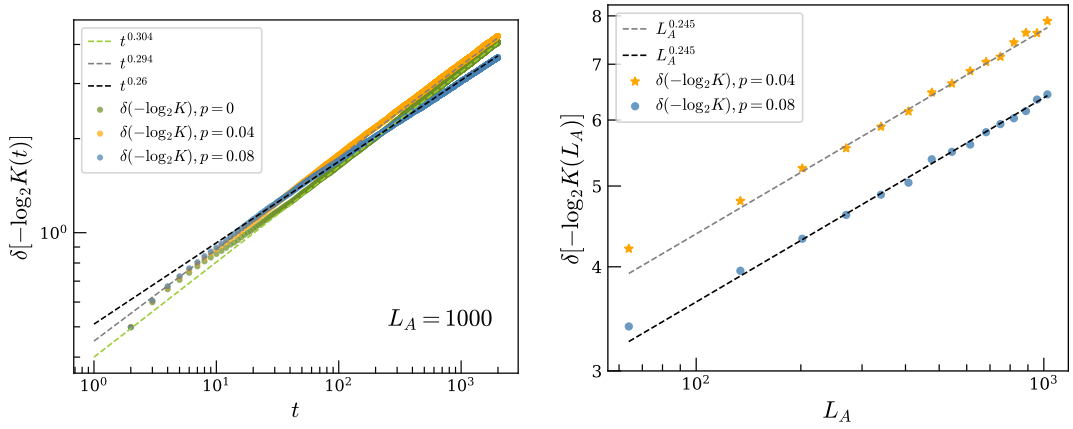

(a) (b)

Figure 3.4: (a) The early-time $\delta(-\log_2 K)$ vs t plotted on a log-log scale. (b) The steady state $\delta(-\log_2 K)$ of the single-species particle model vs L_A plotted on a log-log scale. The numerical data are calculated from the single-species particle model using the basis-decomposing method with particle annihilation rate $p = 0.04$ and $p = 0.08$.

Recall that in the two-species particle model, the entanglement entropy is related to the logarithm of $P(t)$, which is the fraction of configurations in which X particles do not encounter Y particles up to t. We denote x (y) as the rightmost X (leftmost Y) particle. In the volume-law phase, x and y move toward each other at roughly the same speed, so $P(t)$ decays exponentially in t, leading to the linear growth of $S_A^{(2)}(t)$. The subleading term in $S_A^{(2)}(t)$ is caused by the fluctuation of the velocities of x and y in different particle configurations. For simplicity, we fix the position of y to be next to the boundary between A and B, so that only the fluctuation of x is considered. This is equivalent as computing a subset of phase terms in Eq.(3.5) restricted in subsystem B,

$$\frac{1}{4^{L_A}} \sum_{\alpha_1,\alpha_2} e^{-i\Theta^B_{n'_1} + i\Theta^B_{n_1}}. \tag{3.13}$$

where $\{\alpha_1, \alpha_2\}$ are the spin configurations in subsystem A of the bit-string pairs $\{|n_1\rangle, |n_1'\rangle\}$. With this approximation, $P(t)$ is simplified to be $K(t)$, the fraction of configurations in which x never crosses the boundary between A and B up to time t.

One important advantage of taking the single-species approximation is that $K(t)$ can be efficiently computed using the following approach: (1) All of the particle configurations in subsystem A can be generated by a set of binary basis $H^0 = \{h_1, \ldots, h_{L_A}\}$. Hence, any particle configuration can be expressed as the linear combination

$$h = \sum_{i=1}^{L_A} h_i^{\alpha_i} \tag{3.14}$$

defined on the finite field $\mathbb{F}_2$ with $\alpha_i = \{0, 1\}$. Initially, we can set $h_i(t=0) = (0 \ldots 1_i \ldots 0)$. Under linear operators, we can evolve each basis separately and the above equation still holds with $\{\alpha_i\}$ remaining invariant. (2) $K(t)$ can be evaluated by simply evolving a set of basis $H(t)$ which span the ensemble of particle configurations which never enter B. Initially, $H(t=0) = H^0$ and therefore $K(t=0) = 1$. Under the time evolution, if the rightmost particle x of a single basis state, say, $h_j(t)$, crosses the boundary, then only the particle configurations with $\alpha_j = 0$ will contribute to $K(t)$. Hence, half of the configurations are ruled out, and the "entanglement entropy" $-\log_2 K(t)$ increases by one. This also means that h_j is excluded from $H(t)$ for further computation. On the other hand, if the x particles of multiple basis states, say, $G = \{h_1, \ldots, h_n\}$, cross the boundary at the same time, one can easily verify that $-\log_2 K(t)$ still increases by one, except that the updated basis set becomes $H(t) = \{h_1 + h_2, \ldots, h_1 + h_n\} \bigcup H(t-1) \setminus G$. As a result,

$$-\log_2 K(t) = L_A - |H(t)|, \tag{3.15}$$

where $|H(t)|$ is the number of existing basis at time t. This way of tracing the basis set which span the configurations whose boundary has not been visited by the particles resembles the stabilizer formalism in Clifford dynamics.

We use the above method to first study the $p = 0$ limit of the single-species particle model under the Clifford QA circuit defined in Fig. 3.2(b). With this limit, the particle basis states evolve under only unitary operators, i.e., random CNOT gates. The numerics in Fig. 3.4(a) shows that the early-time dynamics has the fluctuation $\delta[-\log_2 K(t)] \propto t^{0.304}$. In the steady state, the particles in all the basis states will pass the boundary and therefore $-\log_2 K(t \to \infty) = L_A$ without subleading correction.

When $0 < p < p_c$, we observe similar fluctuations in the early-time dynamics. Fig. 3.4(a) shows that $\delta[-\log_2 K(t)] \propto t^{0.294}$ at $p = 0.04$ and $\delta[-\log_2 K(t)] \propto t^{0.26}$ at $p = 0.08$. The power law exponent slightly decreases as we increase p. As opposed to the $p = 0$ case, the steady state entropy cannot reach the maximal value. Due to the local measurement which forces $\bullet \to \circ$ in all the basis states at the same location, the time-evolved basis states in $H(t)$ cease to remain mutually linearly independent. The steady state basis vectors $H(t \to \infty)$ are formed by zero vectors containing no particles. The fluctuation of the number of such zero vectors is the same as the fluctuation of $-\log_2 K(t \to \infty)$ and is shown in Fig. 3.4(b). By performing finite size scaling, we observe that $\delta[-\log_2 K(L_A)] \propto L_A^{0.245}$ for both $p = 0.04$ and $p = 0.08$, slightly off from $1/3$.

3.3.3 Two-species particle dynamics

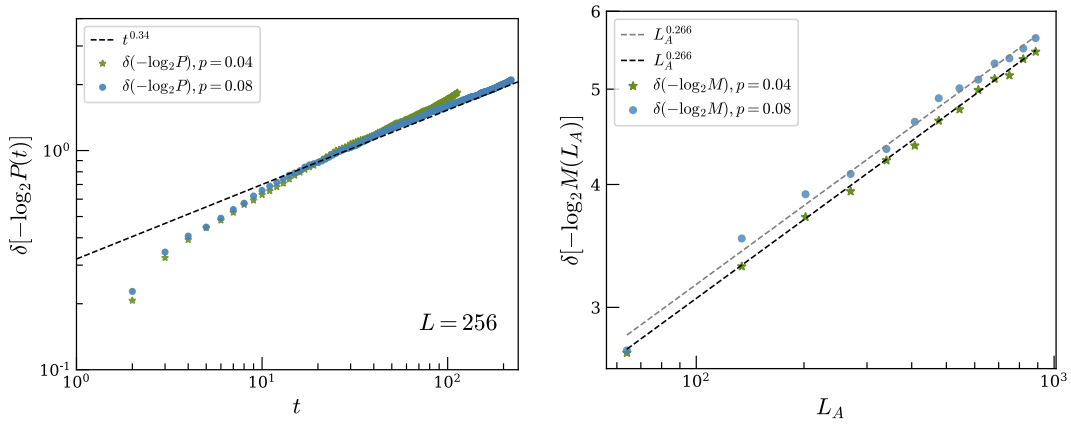

(a) (b)

Figure 3.5: (a) The early-time $\delta(-\log_2 P)$ vs t plotted on a log-log scale. The numerical data are calculated from the two-species particle model with the sampling method and with the system size $L = 256$. (b) The steady state $\delta(-\log_2 M)$ vs L_A plotted on a log-log scale, the ratio L_A/L is fixed to be $1/2$. M is one of the terms that contribute to P which can be computed using the basis-decomposing method.

In the two-species particle model, it is unclear if there exists an efficient algorithm to evaluate $P(t)$. The existence of two moving fronts makes the problem difficult to solve. Nevertheless, we can still simulate the early-time dynamics using Monte Carlo sampling method[40]. More specifically, we prepare a large sample of randomly generated particle configurations and estimate $P(t)$ by computing the fraction of configurations in which X and Y never meet up to time t. This method works well for subsystem with entanglement entropy smaller than ~ 20. Around p_c, the entanglement entropy is small and this sampling method has been successfully used to identify p_c and compute the critical exponents precisely over a few hundred qubits [70]. We apply the sampling method to the volume-law phase during the early time and as shown in Fig. 3.5(a), the standard deviation of the entropy $\delta[-\log_2 P(t)] \propto t^{0.34}$ at $p = 0.04$ and $p = 0.08$, which is consistent with the KPZ fluctuation.

Unfortunately, it is unrealistic for us to evaluate the sample fluctuation of $-\log_2 P$ of the steady state using the same method. This is because in the steady state, P is exponentially small and avoiding the contact between the two species becomes a rare event at late times. Below we analyze the physics of P and take some approximation to estimate the fluctuation of $\log_2 P$ in the steady state.

In the context of particle dynamics, the entanglement entropy saturates when all the particle configurations which contribute to $P(t)$ have at most one species left. The steady state P is therefore composed of three parts,

$$P = \frac{N_X}{2^L} + \frac{N_Y}{2^L} - \frac{N_{XY}}{2^L} = P_X + P_Y - P_{XY}, \tag{3.16}$$

where P_X (P_Y) denotes the fraction in which X (Y) particles annihilate first under the dynamics before they could encounter the other species, P_{XY} denotes the fraction in which both species extinguish at the same time before they

		$p=0$	$p=0.04$	$p=0.08$
δS_A	β_1	N/A	0.322	0.322
	β_2	0.307	0.307	0.266
$\delta(-\log_2 K)$	β_1	N/A	0.245	0.245
	β_2	0.304	0.294	0.26
$\delta(-\log_2 P)$	β_2	N/A	0.34	0.34
$\delta(-\log_2 M)$	β_1	N/A	0.266	0.266

Table 3.1: The comparison of the exponents of the fluctuation δS_A of Clifford QA entanglement entropy, $\delta(-\log_2 K)$ of the single-species particle model, the early-time $\delta[-\log_2 P(t)]$ of the two-species particle model using the sampling method, the steady-state $\delta[-\log_2 M(L_A)]$ where M is a term that contributes to P. The measurement rate or the particle annihilation rate is taken to be $p = 0, 0.04$ and 0.08. In the table, β_1 refers to the exponent of $L_A^{\beta_1}$ and β_2 refers to the exponent of t^{β_2}.

meet. In the volume-law phase, $P_X \propto \exp(-L_A)$, $P_Y \propto \exp(-L_B)$ and $P_{XY} \propto \exp(-L)$. In the thermodynamic limit, the last term can be ignored and the first two terms compete as we tune L_A. When $L_A < L_B$, P_X dominates and we have $P \approx P_X$. In contrast, when $L_A > L_B$, we have $P \approx P_Y$. This leads to

$$S_A^{(2)} \approx \begin{cases} -\log_2 P_X, & L_A < L/2 \\ -\log_2 P_Y, & L_A > L/2. \end{cases} \tag{3.17}$$

Computing P_X is still not an easy task. Instead we consider a subset of P_X that can be simulated efficiently using the basis-decomposing method in Sec. 3.3.2. We define the binary basis H_X^0 (H_Y^0) which span the X (Y) particle configurations in the absence of Y (X) particles. Both H_X^0 and H_Y^0 evolve under the same dynamics. At time t, we consider the configurations in which the X particles never encounter Y particles in any of the basis states of $H_Y^0(t)$ and denote this fraction as $M(t)$. In other words, $M(t)$ is equivalent to $K(t)$ in the single-species particle model, except that now the boundary determined by the leftmost Y particle in $H_Y^0(t)$ is spreading to the left. Therefore,

$$-\log_2 M(t) = -\log_2 \frac{2^{|H_X(t)|} \times 2^{L_B}}{2^L} = L_A - |H_X(t)|. \tag{3.18}$$

where $H_X(t)$ is the basis of X particle configurations which never meet the leftmost Y particle in $H_Y^0(t)$.

In the steady state, H_X is the set of basis in which the X particles have already vanished before encountering any Y particles in $H_Y^0(t)$. As shown in Fig. 3.5(b), there exists sample fluctuation in $-\log_2 M$ in the volume-law phase. In particular, we find that $\delta[-\log_2 M] \propto L_A^{0.266}$ for both $p = 0.04$ and $p = 0.08$. This exponent is smaller than the one computed in the Clifford QA circuit. The exponents for different models at various $p < p_c$ are listed in Table. 3.1 and we find that some of them are smaller than $1/3$.

Currently, it is unclear if this is a finite size effect, or if the fluctuations of these quantities in the one/two-species particle models belong to other universality classes. The main obstacle of this issue is the lack of rigorous analytical results. However, we want to mention that there are some known results about KPZ fluctuations in the particle dynamics. Under the hybrid QA circuit, each particle configuration experiences the same circuit dynamics, therefore the end points of the two species x and y can be treated as particles performing biased random walks in a fixed time-dependent random

environment. Mathematically, the dynamics of the endpoint is known as random walk in random environment (RWRE), in which the logarithm of the transition probability is proven to exhibit KPZ fluctuations in some limit [73, 74, 75]. Indeed, this quantity is similar to the second Rényi entropy and the detailed discussion about this connection can be found in App. 3.B.

3.4 Purification Process and quantum error correction

3.4.1 Purification process and hybrid QA QECC

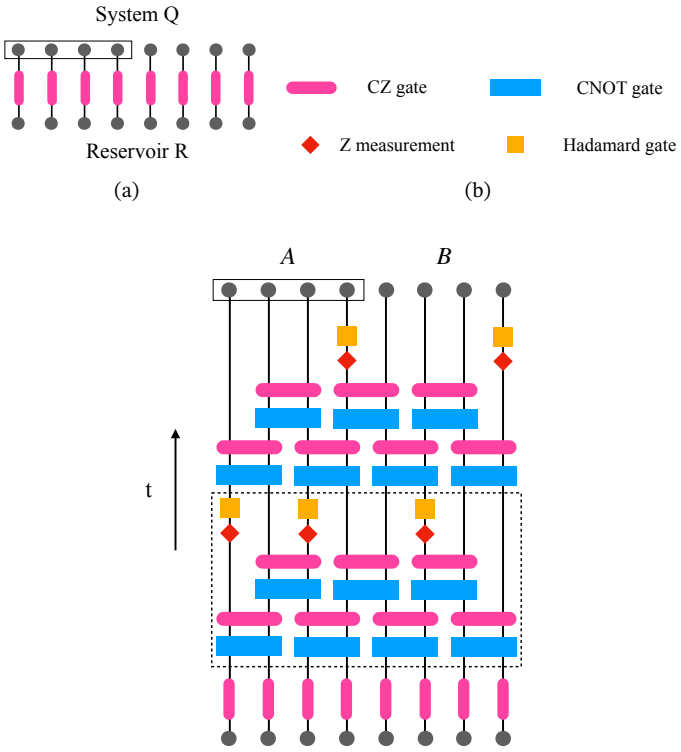

Figure 3.6: (a) We use CZ gates to generate entanglement between system Q and environment R. (b) The symbols of the CZ gate, CNOT gate, the single-qubit Z measurement gate and Hadamard gate. (c) The arrangement of gates for the purification process of the hybrid QA circuit. Except the initial setup in (a), the hybrid circuit is applied solely in system Q.

An alternative approach to understand the measurement-induced entanglement phase transition is through purification dynamics[30]. The basic idea is to prepare a system Q with an extensive entropy and evolve it under the hybrid quantum dynamics. Although the system will eventually be purified, in the weakly-monitored volume-law phase with $0 < p < p_c$, the purification time is exponentially long in system size L. On the other hand, when $p > p_c$, the entropy decays exponentially in time with a constant rate.

The existence of long purification time in the regime $0 < p < p_c$ suggests that the hybrid quantum circuits can dynamically generate a robust quantum error correcting code (QECC) at polynomial time[30]. The QECC can be compactly

denoted as $[L, k, d]$. Here L is the number of physical qubits in Q and k characterizes the amount of logical information encoded in the code space and is quantified by the entropy of ρ_Q. The third index d is the code distance, which is defined as the minimum weight of all uncorrectable errors. Here the errors can be interpreted as measurements which can potentially reduce the entropy when applied on ρ_Q. If an error changes the entropy of Q, then it is an uncorrectable error since it damages the encoded quantum information and hence can not be recovered. Due to the locality of the circuit model, a better measure is the contiguous code distance d_{cont}, which is the minimal length of a contiguous section of qubits that supports an uncorrectable error [30]. In the volume-law phase, d_{cont} diverges in the thermodynamic limit. The quantum information is stored non-locally under the unitary evolution and thus is protected against any local measurements. On the other hand, for $p > p_c$, the unitary dynamics fails to protect the encoded information under frequent measurements. Previous works have quantitatively analyzed the statistical property of QECC in hybrid random Clifford circuits [52, 51]. In this section, we will study the purification dynamics of the hybrid QA circuit and investigate the QECC in terms of the classical particle model.

Initially, we prepare a product state of $2L$ qubits polarized in $+x$ direction which can be evenly divided into system Q and environment R. Then, we create L EPR pairs between them by applying CZ gates as shown in Fig. 3.6(a). Thus, the system Q becomes maximally entangled with environment R, i.e., $S_Q^{(2)} = L$. To investigate the purification dynamics, a hybrid QA circuit is solely applied on system Q. Numerically, we consider the model described in Fig. 3.6(c), identical to the hybrid QA Clifford circuit in the entanglement dynamics in the last section. The composite measurements disentangle the qubits in Q from the environment R. Meanwhile, the unitary evolution scramble the quantum information within system Q, increasing the entanglement between any subsystem A in Q and its complement $B := Q \setminus A$, but not affecting $S_Q^{(2)}$. There is a phase transition in the purification time of $S_Q^{(2)}$ at $p = p_c \approx 0.138$ [40], consistent with the entanglement dynamics studied in the last section.

As we discussed before, an important measure of the error-correcting ability of our QECC is the contiguous code distance d_{cont}, which is the minimal length of a contiguous region supporting an uncorrectable error. It is thus natural to mark the existence of such errors supported on a contiguous subregion A using the mutual information between A and the environment R [76, 52, 77],

$$\begin{aligned} I_{A,R} &= S_A^{(2)} + S_R^{(2)} - S_{A,R}^{(2)} \\ &= S_A^{(2)} + S_Q^{(2)} - S_B^{(2)}. \end{aligned} \tag{3.19}$$

When $I_{A,R} = 0$, A and R are completely decoupled, we cannot acquire any information encoded in the state by observing any qubits within the subregion A. In other words, any measurements acting within A are correctable errors since they will not affect $S_Q^{(2)}$. Therefemphore, d_{cont} is the maximum length L_A^* such that $I_{A,R} = 0$ for $L_A < L_A^*$ [1].

We simulate the Clifford QA circuit to find the entanglement entropies $S_A^{(2)}$ and $S_B^{(2)}$ and the mutual information $I_{A,R}$ over various subsystem sizes L_A. The numerical results are given in Fig. 3.7. We take the code distance to be the maximum length L_A^* such that $\langle I_{A,R} \rangle \leq \epsilon$ for $L_A < L_A^*$. In the numerical simulation of the finite system size, we set $\epsilon = 1$. Remarkably, we find that $S_A^{(2)}$ starts to decrease at $L_A = L - L_A^*$ until it reaches $S_Q^{(2)}$ at $L_A = L$. This

[1] In the stabilizer QECC, d_{cont} can also be viewed as the minimal length of nontrivial logical operators acting within the code space. This is equivalent to the d_{cont} defined through the criterion $I_{A,R} = 0$.

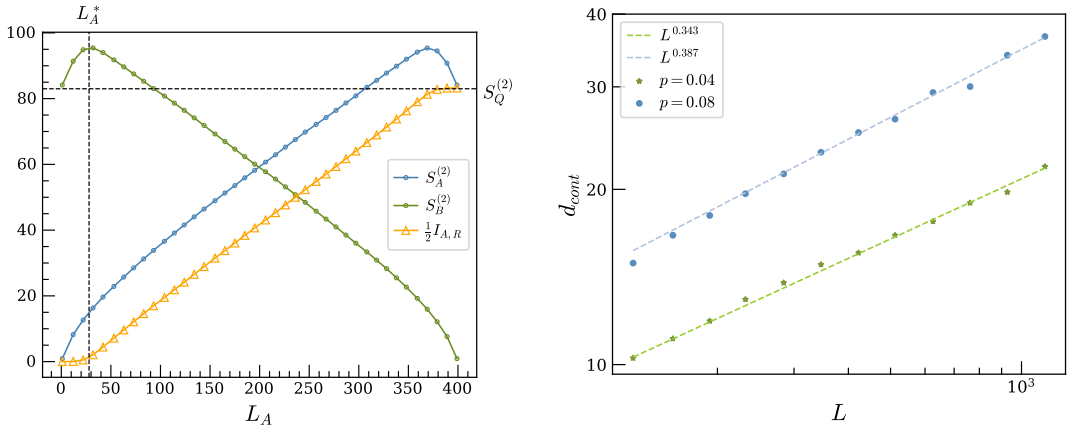

(a) (b)

Figure 3.7: (a) The entanglement entropies $S_A^{(2)}$ and $S_B^{(2)}$ and half of the mutual information $\frac{1}{2}I_{A,R}$ vs L_A computed from the Clifford QA circuit with system size $L = 400$ at $T = 2L$, and $p = 0.08$. (b) The contiguous code distance d_{cont} for different system size L at $p = 0.08$ and $p = 0.04$ at $T = 3L$ plotted on a log-log scale. Here we take d_{cont} to be the maximum length L_A^* such that $\langle I_{A,R}\rangle \leq 1$. All of the data are computed with PBC.

non-monotonic behavior coincides with that in the previous study of the hybrid Clifford circuits [52] and is crucial in understanding the code distance. We will modify the two-species particle model in the following section so as to give an interpretation for $S_A^{(2)}$. As shown in Fig. 3.7(b), d_{cont} has a sublinear power law scaling with L. Numerically, it scales as $L^{0.343}$ for $p = 0.04$ and $L^{0.387}$ for $p = 0.08$, and its value increases as the measurement rate increases.

3.4.2 QECC in classical particle language

To understand the dynamically generated QECC from the perspective of classical particle dynamics, we need to compute the mutual information defined in Eq. (3.19) in terms of the two-species particle model. An important task is to understand the entanglement entropy of a subsystem A in the presence of environment R. For the bit-string dynamics in the purification process, the hybrid QA circuit is applied only on system Q of the bit-strings in a time-reversed order, generating the relative phase Θ_r, followed by the CZ gates acting on both the system Q and environment R, generating another relative phase Δ_r. Therefore, only the configurations satisfying $\Theta_r = 0$ and $\Delta_r = 0$ contribute to the purity. As shown in App. 3.D, in the particle picture, this corresponds to the configurations in which all of the X particles have vanished before they can encounter any Y particles at time t. These configurations are a subset of $N(t)$ defined in Eq.(4.14) in the entanglement dynamics. Let the number of these configurations be $N_1(t)$, the entanglement entropy of A is then

$$S_A^{(2)}(t) = -\log_2 \frac{N_1(t)}{2^L} \equiv -\log_2 P_1(t). \tag{3.20}$$

Specifically, when $A = Q$, there are only one type of particles, we only need to count the configurations whose particles extinguish at time t. Letting the number of such configurations be denoted N_Q, we have

$$S_Q^{(2)}(t) = -\log_2 \frac{N_Q(t)}{2^L} \equiv -\log_2 P_Q(t). \tag{3.21}$$

Initially, $P_Q(t = 0) = 1/2^L$ and Q is maximally entangled with R. Under the hybrid QA circuit, more and more configurations become empty and S_Q decreases monotonically with time. The time scale for which the particles of all the configurations vanish depends on p and is consistent with that of the purification transition.

We are interested in the QECC generated at polynomial time $t = \lambda L$ with $\lambda \gg 1$. At this time, X or Y particles have already spread over the entire system and therefore the configurations that contribute to $P_1(t)$ can have at most one type of particle. Similar to the steady state P of the entanglement dynamics derived in Eq.(3.16), $P_1(t)$ can be expressed as

$$P_1(t) = \frac{\widetilde{N}_X(t)}{2^L} + \frac{\widetilde{N}_Y(t)}{2^L} \equiv P_X + \widetilde{P}_Y(t), \tag{3.22}$$

where $\widetilde{P}_Y(t)$ is a subset of P_Y, which further requires that X particles vanish at time t. There is also a small contribution from P_{XY} which we ignore here.

When $L_A < L_B$, since $P_X > P_Y > \widetilde{P}_Y(t)$, P_X dominates and we have $P_1(t) \approx P_X$. Therefore, $S_A^{(2)}(t)$ is the same as the steady state $S_A^{(2)}$ in the entanglement dynamics. The regime $L_A > L_B$ is different from that of the steady state in the entanglement dynamics. Since $\widetilde{P}_Y(t)$ is a small fraction of P_Y, when L_A is slightly larger than L_B, $P_X > \widetilde{P}_Y(t)$ and we still have $S_A^{(2)} \approx -\log_2 P_X$. We define L^c to be the threshold of the subsystem size L_A where $P_X = \widetilde{P}_Y(t)$. When $L_A > L^c$, $\widetilde{P}_Y(t)$ dominates and we have $S_A^{(2)}(t) \approx -\log_2 \widetilde{P}_Y(t)$. For $\widetilde{P}_Y(t)$, it can be understood as follows,

$$\widetilde{P}_Y(t) = \frac{\widetilde{N}_Y(t)}{2^L} = \frac{N_Y}{2^L}\frac{\widetilde{N}_Y(t)}{N_Y} \equiv P_Y P_2(t), \tag{3.23}$$

where $P_2(t) \equiv \widetilde{N}_Y(t)/N_Y$. Since the X particles of configurations in N_Y have already spread over the entire system when all of the Y particles extinguish, $P_2(t)$ actually counts the fraction of configurations which have no particles at time t. Directly evaluating $P_2(t)$ is difficult. However, due to the scrambling property of the unitaries, it is reasonable to assume that $P_2(t) \approx P_Q(t)$,

$$\widetilde{P}_Y(t) \approx P_Y P_Q(t). \tag{3.24}$$

Summarizing, we have

$$S_A^{(2)}(t) \approx \begin{cases} -\log_2 P_X, & L_A < L^c \\ -\log_2 P_Y - \log_2 P_Q(t), & L_A > L^c. \end{cases} \tag{3.25}$$

We numerically verify the above approximation in Fig. 3.8(a). Due to the difficulty for simulating highly-entangled state, we are only able to simulate the two-species particle model on a system with size $L = 32$ at $T = 3L$ in the volume-law phase. We find that there indeed exists a non-monotonic decay area for $S_A^{(2)} = -\log_2 P_1$ when L_A passes

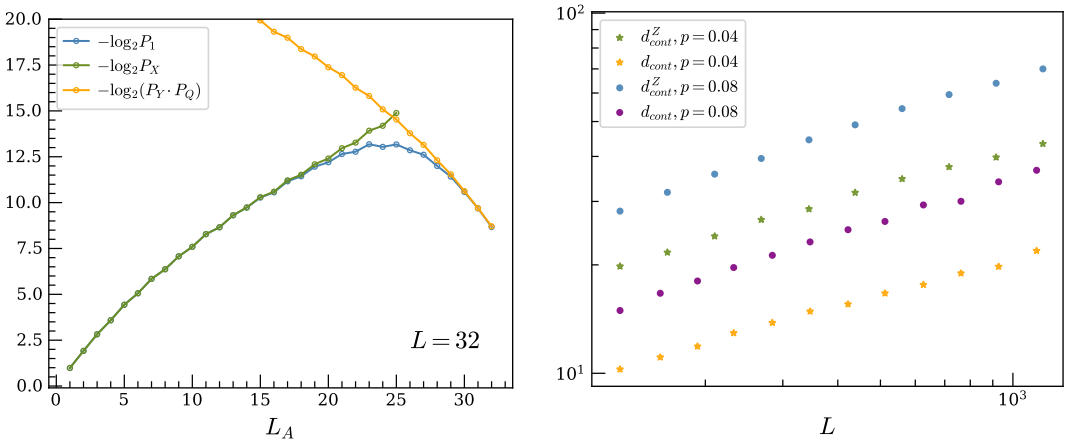

(a) (b)

Figure 3.8: (a) The entanglement entropy $S_A^{(2)} \approx -\log_2 P_1$ vs L_A computed from the two-species particle model, in comparison with the two approximate values $-\log_2 P_X$ and $-\log_2 (P_Y \cdot P_Q)$ for $L_A < L^c$ and $L_A > L^c$. The numerical data are calculated by the sampling method over a system of size $L = 32$, at $T = 3L$, $p = 0.08$ and under PBC. (b) The Z-error contiguous code distance d^Z_{cont} in comparison with d_{cont} for different system sizes at $p = 0.04$ and $p = 0.08$ at $T = 3L$ plotted on a log-log scale.

the threshold L^c, and that Eq.(3.25) holds within a small difference $\epsilon = O(1)$. The non-monotonicity comes from the competition of the two terms P_X and $\widetilde{P}_Y$. As subsystem A enlarges, P_Y increases and P_Q stays the same. As a result, when $L_A > L^c$ and $\widetilde{P}_Y$ dominates, $S_A^{(2)}$ starts to decline as L_A continues to increase. The location of the peak L^c depends on time and can eventually shift to $L/2$ when the system is completely purified.

Based on the above analysis of $S_A^{(2)}(t)$, we are now ready to understand the QECC in terms of particle dynamics. In the regime with $L_A \in [0, L - L^c)$ and hence $L_B \in (L^c, L]$, the mutual information becomes

$$\begin{aligned} I_{A,R} &= S_A^{(2)} + S_Q^{(2)} - S_B^{(2)} \\ &\approx -\log_2 P_X - \log_2 P_Q + \log_2 P_X + \log_2 P_Q \\ &= 0. \end{aligned} \tag{3.26}$$

It vanishes because the two terms in $S_B^{(2)}$ completely cancel with $S_A^{(2)}$ and $S_Q^{(2)}$, similar to the decoupling domain wall picture discussed in Ref. [52]. On the other hand, when $L^c > L_A > L - L^c$, it is easy to show that

$$I_{A,R} \approx -\log_2 P_X - \log_2 P_Q + \log_2 P_Y > 0. \tag{3.27}$$

We arrive at the conclusion that $I_{A,R} = 0$ *if and only if* $L_A < L - L^c$ and the contiguous code distance is $d_{\text{cont}} = L - L^c$. These results are consistent with the numerical results of hybrid Clifford QA circuit in Fig. 3.7(a).

The code distance specified by the mutual information works for *all* kinds of errors. In the QA circuit, we could consider a special type of error which is the Z error defined as the measurement operator $(1 \pm O)/2$ where O is a Pauli Z string. Suppose at time t, a QECC is prepared through the QA purification dynamics and some Z errors occur within a

contiguous subsystem A, which could possibly reduce the entropy of ρ_Q. We define the Z-error contiguous code distance d^Z_{cont} as the maximum length of subsystem A such that $S^{(2)}_Q$ does not change.

Since the particle dynamics is evolved in a time-reversed order, the Z error acts as annihilation on all of the particle configurations at $t = 0$. For subsystem A of size smaller than d^Z_{cont}, $S^{(2)}_Q$ is invariant under any Z error occurred within A, or in other words, with any initial particle distribution in A. Therefore, we start from an ensemble of particle configurations with *empty* subsystem A, so that the information about A is completely removed. The entanglement entropy of Q after the Z error becomes

$$S^{(2)}_Q(t) = -\log_2 P_B(t), \tag{3.28}$$

where $P_B(t)$ denotes that among all the configurations with only Y particles located in B initially, the fraction that becomes completely empty at time t. Consequently, d^Z_{cont} is the maximum length of subsystem A such that $-\log_2 P_B(t) = -\log_2 P_Q(t)$ for $L_A < d^Z_{\text{cont}}$.

Both $-\log_2 P_B(t)$ and $-\log_2 P_Q(t)$ can be efficiently calculated by evaluating the number of independent basis under the hybrid time evolution. We prepare two sets of binary basis, one is H whose rows are the basis spanning all the particle configurations in system Q, the other one is H' which is the truncation of H where a contiguous submatrix of size $L \times L_A$ is removed. Then, we evolve them under the same circuit dynamics. One can easily see that $-\log_2 P_Q(t) = \text{rank}_2(H(t))$ and $-\log_2 P_B(t) = \text{rank}_2(H'(t))$, which are the number of independent basis in $H(t)$ and $H'(t)$ respectively. The code distance $d^Z_{\text{cont}}(t)$ is therefore identified as the largest L_A such that the rank of $H(t)$ and $H'(t)$ agree within $\epsilon = 1$. As shown in Fig. 3.8(b), although d^Z_{cont} is much larger than d_{cont}, they have similar power-law scaling.

The sublinear power-law exponent in the contiguous code distance is a special feature of the hybrid random dynamics and is closely related to the subleading correction term in the entanglement entropy. In the Clifford circuit, this can be easily understood in the dynamics of the stabilizer generators, in which there exist a finite number of "short" stabilizers caused by local measurements[31]. These short stabilizers are responsible for both the fluctuation in the entanglement entropy and also the sublinear power-law exponent in the code distance[31]. Under pure unitary dynamics, these short stabilizers become long stabilizers and span over the whole system, the subleading correction term vanishes and the code distance becomes extensive and is proportional to L, the same as the conventional random QECC[78].

The above physics can also be understood in the hybrid QA circuit as shown in Fig. 3.9(a). Compared with Fig. 3.6(c), we add an extra pure unitary evolution for time T_2. Recall that the particle representation experiences the circuit dynamics in a time-reversed order, it first evolves under the pure unitary evolution for T_2 and then the hybrid dynamics for T_1. Here we take sufficiently long T_2 for unitary evolution so that the particles are fully scrambled and only the configurations with no X (Y) particles at the beginning can contribute to P_X (P_Y). Hence, $P_X = 2^{-L_A}$ and $P_Y = 2^{L_A - L}$ and we have

$$S^{(2)}_A(t) = \begin{cases} L_A, & L_A < L^c \\ L - L_A - \log_2 P_2(t), & L_A > L^c. \end{cases} \tag{3.29}$$

Here $-\log_2 P_2(t)$ is simply counting the number of independent basis initially defined in A.

To verify this result, we simulate the Clifford QA circuit and compare the results with that derived from the particle

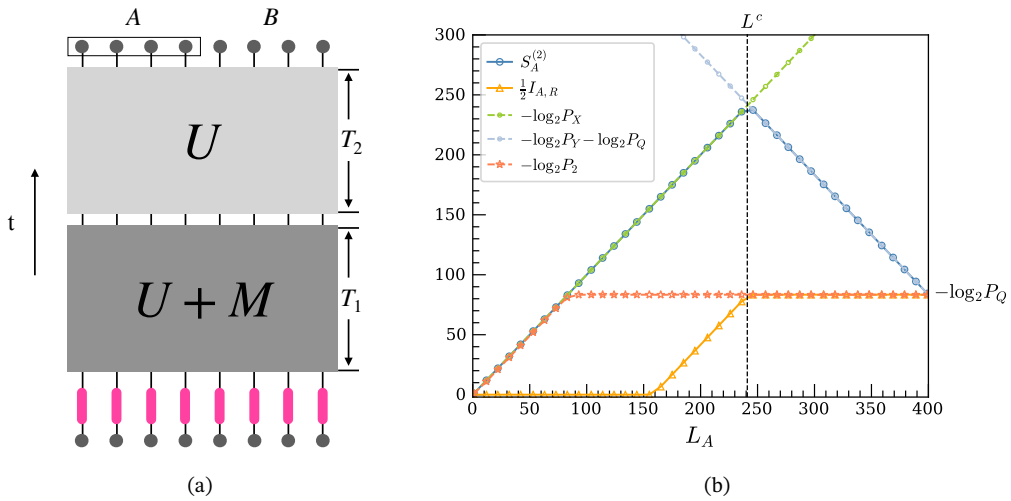

Figure 3.9: (a) The setup of the alternative hybrid QA circuit. "U+M" represents the original hybrid QA circuit composed of unitary gates and sporadic local composite measurements. "U" represents the circuit in the limit $p = 0$ with only QA unitaries. (b) The entanglement entropy $S_A^{(2)}$ and half of the mutual information $\frac{1}{2}I_{A,R}$ vs L_A computed from the Clifford model, in comparison with the two approximations $-\log_2 P_X$ and $-\log_2(P_Y \cdot P_Q)$. We also calculate $-\log_2 P_2$ and find that it grows linearly in L_A and saturates to $-\log_2 P_Q$ when $L_A = -\log_2 P_Q$. We take $L = 400$, $p = 0.08$ and $T_1 = T_2 = 2L$.

model. As shown in Fig. 3.9(b), we find that $S_A^{(2)}$ agrees with L_A for $L_A < L^c$ and $L - L_A - \log_2 P_2(t)$ for $L_A > L^c$ with negligible fluctuation. Different from the previous circuit defined in Fig. 3.6(c), it is easy to numerically evaluate $P_2(t)$ in this circuit. Due to the scrambling property of the unitary evolution in T_2, we find that over a large range of L_A, $-\log_2 P_2(t) = -\log_2 P_Q(t)$ and they become different only when $L_A < -\log_2 P_Q(t)$. There is no subleading correction term in $S_A^{(2)}$ anymore and the code distance is $L - L^c$ which is linearly proportional to L. These results indicate that the sublinear power-law scaling in both the contiguous code distance and the fluctuation of the entanglement entropy are emergent properties of the hybrid random circuit and disappear when the dynamics is fully scrambled under unitary evolution.

3.5 Classical linear code

The classical particle model discussed in this chapter has an interesting connection with the classical error correction. For a system with L sites, the total number of the particle configurations is 2^L and all of them can be generated from L independent particle string basis. Under the unitary dynamics, the number of basis is invariant, indicating that the total amount of the classical information is unchanged. On the other hand, the composite measurement forces $\bullet \to \circ$ at one site in all of the basis and can potentially reduce the number of independent basis, resulting in the loss of information.

The information retained in the classical particle model can be characterized by the number of independent basis k. Under the purification dynamics in Sec. 3.4.1, k is the same as the entropy S_Q. When $0 < p < p_c$, it takes $\exp(L)$ time for $k(t)$ decreasing to zero. On the other hand, when $p > p_c$, $k(t)$ decreases to zero exponentially fast with a finite decay rate. The phase transition at $p = p_c$ belongs to the directed percolation universality class.

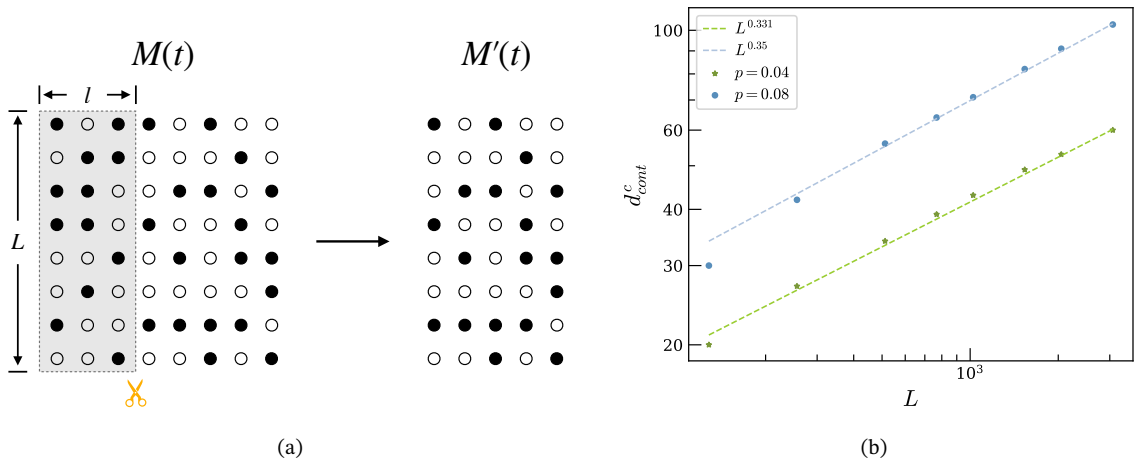

(a) (b)

Figure 3.10: (a) The CLC is determined by the binary square matrix $M(t)$ on the left. The occupied site symbol • denotes 1 and the empty site symbol ∘ denotes 0. To evaluate the contiguous CLC code distance d^c_{cont} at time t, an $L \times l$ submatrix is taken away from $M(t)$ and d^c_{cont} is the largest l such that the rank of the truncated matrix $M'(t)$ agrees with that of $M(t)$ within ϵ. In the numerical simulation, we set $\epsilon = 1$. (b) d^c_{cont} vs system size L for $p = 0.04$ and $p = 0.08$ at $T = 4L$ plotted on a log-log scale.

Similar to the dynamically generated QECC with $p < p_c$, the associated particle dynamics also generates a classical linear code (CLC) governed by a $k \times L$ generator matrix, whose rows are binary strings forming a basis for the k dimensional codespace. When the time t is linear in L, the encoded bit k is extensive and the information is protected by the scrambling property of the unitaries and is inaccessible by the local measurement. A CLC is typically denoted by $[L, k, d^c]$, in which L classical bits can store k bits of classical information. d^c is the classical code distance and is equal to the minimal number of flips mapping a codeword to another. Similar to the QECC discussed before, since we have local unitary dynamics, it is more reasonable to consider contiguous code distance d^c_{cont} for our CLC.

In a CLC $[L, k, d^c_{\text{cont}}]$, any bit flip occurring in a subsystem with length $l < d^c_{\text{cont}}$ does not change the encoded bit k. Numerically, this motivates us to evaluate d^c_{cont} in the following way as illustrated in Fig. 3.10(a): Consider an initial generator matrix M with $\text{rank}_2(M) = L$. We evolve all of the row vectors according to the hybrid QA circuit described in Fig. 3.6 (b). At any time t, the encoded bit is the number of the independent binary vectors in $M(t)$, i.e., $k = \text{rank}_2(M(t))$. We then remove a contiguous $L \times l$ submatrix from $M(t)$ and obtain a truncated $M'(t)$. The largest l which makes $k - \text{rank}_2(M'(t)) < \epsilon$ is d^c_{cont}. In the numerical simulation, we take $\epsilon = 1$ and we are interested in the regime $t = \alpha L$ with $\alpha \gg 1$. As shown in Fig. 3.10(b), we observe that $d^c_{\text{cont}} \propto L^{0.331}$ for $p = 0.04$ and $d^c_{\text{cont}} \propto L^{0.35}$ for $p = 0.08$. Similar to the QECC, the power law exponent is again smaller than 1. The diverging code distance is consistent with exponentially long purification time – the information is encoded non-locally and is resilient to any local errors.

3.6 Conclusion

In this chapter, we analyze entanglement entropy fluctuations in the volume-law phase of 1+1d hybrid QA circuits. We numerically show that the fluctuations belong to the KPZ universality class, just as for other random circuits studied

previously. Due to the special feature of the QA circuit, we are able to map the second Rényi entropy to a classical quantity in a particle model. We compute the fluctuations of this quantity in different approaches and show that they exhibit fluctuations with similar exponents. The existence of the strong fluctuations may have interesting connection with the multifractal behavior observed in the volume-law phase of hybrid Clifford circuits, where the entanglement entropy transition is mapped to an Anderson localization transition[79]. Besides this, we could also study fluctuations at the critical point in these hybrid random circuits. These critical points, dominated by randomness, are different from those clean systems. Since the hybrid QA circuit has an underlying particle picture, it could be a good starting point to explore this problem.

We also study the dynamically generated QECC in the purification dynamics of 1+1d hybrid QA circuits. Again, we give an interpretation of the error correction in terms of the particle model. In particular, we show that the particle model itself can be treated as a random classical linear code (CLC), and numerically compute the contiguous code distance for it. This observation motivates us to consider other random CLCs and use similar approaches to construct QECC. We leave this for the future study.

Acknowledgement.— We acknowledge Ethan Lake for his proofreading and the useful discussion with Yaodong Li.

3.A Entanglement dynamics in the volume-law phase of $\mathbb{Z}_2$ symmetric hybrid Clifford QA circuit

In this appendix, we study the subleading correction term of the volume-law phase entanglement entropy of the $\mathbb{Z}_2$-symmetric hybrid QA circuit. The $\mathbb{Z}_2$ symmetry requires that the parity of the computational basis remains fixed. This can be satisfied by measuring the Pauli string $Z_1 Z_2 \dots Z_L$ on an initial product state with L qubits polarized in the $+x$ direction. We choose a subset of Clifford gates to construct the QA circuit with $\mathbb{Z}_2$ symmetry and the setup is shown in Fig. 3.11. The unitary evolution composed of CNOTNOT(CNN) gates and CZ gates. The CNN gate flips two qubits according to the value of the third (control) qubit. If the control qubit is on the left we denote the corresponding gate as CNN_L; it acts as

$$\begin{aligned} \text{CNN}_L|1\sigma_1\sigma_2\rangle &= |1(1-\sigma_1)(1-\sigma_2)\rangle \\ \text{CNN}_L|0\sigma_1\sigma_2\rangle &= |0\sigma_1\sigma_2\rangle. \end{aligned} \tag{3.30}$$

Aside from the unitary evolution, we also introduce into the circuit the two-qubit composite measurements defined as

$$M^{\sigma}_{L/R} = R \circ P^{\sigma}_{L/R}. \tag{3.31}$$

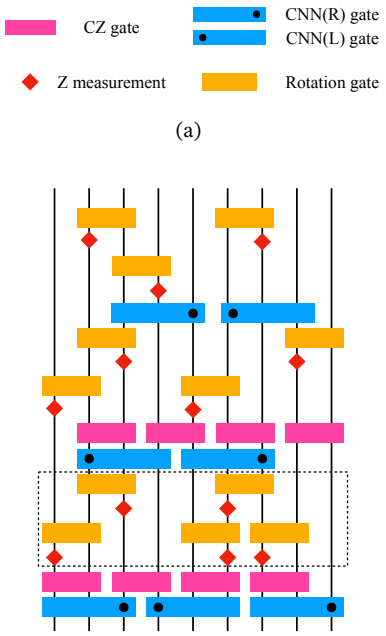

Figure 3.11: (a) A schematic for the gates appearing in the circuit. (b) The arrangement of gates in a single time step of the $\mathbb{Z}_2$-symmetric hybrid QA circuit. Each time step involves three layers of CNN gates and two layers of CZ gates, interspersed with three measured layers. The dashed box represents a measured layer enclosing two rows of composite measurements, with the first/second row containing randomly distributed $M^{\sigma}_{L/R}$ applied on sites $(2i-1, 2i)[(2i, 2i+1)]$ for $i \in [1, L/2]$. As with the CNN gates, the projection of $M^{\sigma}_{L/R}$ is chosen to be applied on the left/right qubit with equal probability. In general, the composite measurement appears in a measured layer with probability p.

This measurement is a combination of the projection operator $P^{\sigma}_{L/R}$ on the left/right qubit into the spin $\sigma = \{0, 1\}$, together with a two-site rotation operation

$$R = \frac{1}{\sqrt{2}} \begin{pmatrix} 1 & 0 & 0 & 1 \\ 0 & 1 & 1 & 0 \\ 0 & 1 & -1 & 0 \\ 1 & 0 & 0 & -1 \end{pmatrix}, \tag{3.32}$$

so that the wave function is always an equal weight superposition of $\mathbb{Z}_2$ symmetric computational basis.

As shown in Ref. [70], the competition of the unitary evolution and the composite measurements leads to an entanglement phase transition from a volume-law phase to a critical phase as the measurement rate p increases, and the critical point is $p_c = 0.335$. Here we focus on the subleading correction of the entanglement entropy in the volume-law phase $p < p_c$. We first compute the fluctuation of the steady state entanglement entropy. As shown in Fig. 3.12(a), $\delta S_A \propto L_A^{\beta_1}$ with $\beta_1 = 0.312$ for $p = 0.05$ and $p = 0.1$, $\beta_1 = 0.256$ for $p = 0.2$. In Fig. 3.12(b), we compute the fluctuation of the early-time entanglement entropy and find that $\delta S_A \propto t^{\beta_2}$ with $\beta_2 = 0.324$ for $p = 0$, $\beta_2 = 0.317$ for $p = 0.05$, $\beta_2 = 0.289$ for $p = 0.1$ and $\beta_2 = 0.214$ for $p = 0.2$. Similar to the case in the QA circuit without $\mathbb{Z}_2$ symmetry, the fluctuation exponents exhibit a drop from the roughness exponent $\beta = \frac{1}{3}$ as p approaches p_c.

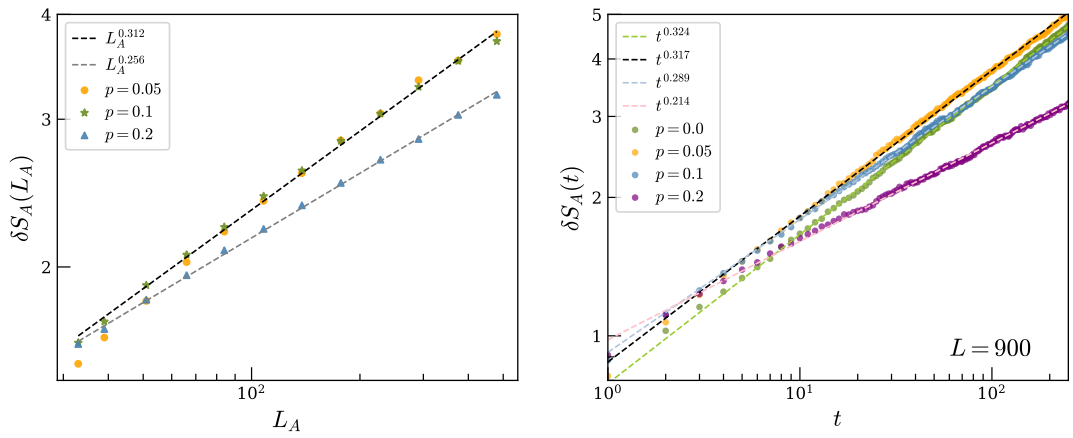

(a) (b)

Figure 3.12: The standard deviation of entanglement entropy of the $\mathbb{Z}_2$-symmetric hybrid Clifford QA circuit. (a) δS_A vs L_A plotted on a log-log scale. The data are computed from the steady-state entanglement entropy S_A for half-system size $L_A = L/2$ over a variety of L. The measurement rates are taken to be $p = 0.05, 0.1, 0.2$. (b) δS_A vs t for $p = 0, 0.05, 0.1, 0.2$. All of the numerical data for entanglement entropy are calculated with periodic boundary conditions (PBC).

3.B Single-species end-point RWRE model

TD-RWRE refers to random walks performed in a *fixed* random environment. Different from the diffusions in *time-independent* random media where the fluctuations are of order $\sqrt{t}$, it was found that in the large deviations regime of TD-RWRE, fluctuations of the logarithm of the transition probability are distributed with the roughness exponent $\beta = \frac{1}{3}$ of the DPRE, i.e.

$$\log_2 P(X_t > ut) \sim C_1(u)t + C_2(u)t^{\frac{1}{3}}\chi \tag{3.33}$$

at large time, where $u > u_c = 0$ and χ obeys the GUE Tracy-Widom distribution [73, 74, 75]. Hence, the large deviations regime of TD-RWRE belongs to the KPZ universality class.

In the two-species particle model, the rightmost X particle and the leftmost Y particle can be regarded as two end-point particles performing TD-RWRE since all the configurations experience the same circuit dynamics. To unravel the problem, we consider the single-species particle model introduced in Sec.3.3.2, in which we focus on the phase difference of $|n_1\rangle$ and $|n_1'\rangle$ in the B region measured by the quantity

$$\frac{1}{4^{L_A}} \sum_{\alpha_1,\alpha_2} e^{-i\Theta^B_{n_1'}} e^{i\Theta^B_{n_1}}. \tag{3.34}$$

Denoting the bit-string difference $|n_1 - n_1'|$ as particles, it is obvious that this quantity equals $K(t)$ which is the fraction of configurations in which the particles initially located in regime A never cross the boundary between A and B up to time t. Therefore, we only care about the dynamics of the end points of each particle configuration and can treat them as biased random walkers in a fixed random environment.

Based on the above analysis, we propose a single-species end-point RWRE model. Initially, we place the end points

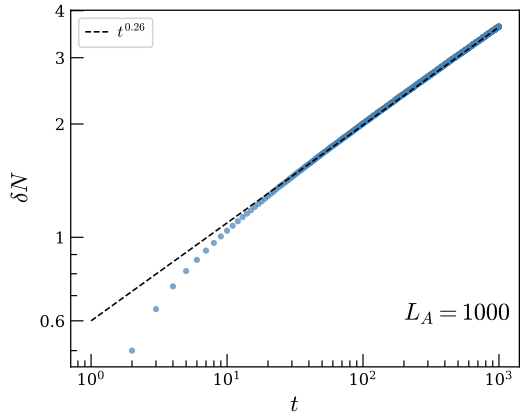

Figure 3.13: The standard deviation δN vs t for $L_A = 1000$.

of all the particle configurations on the lattice, which results in a lattice chain fully occupied in A and empty in B. We further simplify the problem by assuming that the configurations with the same end point *initially* share the same dynamics, so that each site can be viewed as being occupied by only one particle at $t = 0$. At each time step, a random value $\omega_i \in (0, 1)$ is assigned to each site i on which the particles have the probability ω_i to move to the right. Assume that when an end point originally located on site i arrives at the boundary, the end points originally sit on the right of i have already arrived. Define $N(t)$ as the number of particles that have already passed the boundary at time t, the "entanglement entropy" can be expressed as

$$\begin{aligned} -\log_2 K(t) &\approx -\log_2 \frac{2^{L_A} - 2^{L_A-1} - \dots 2^{L_A-N(t)}}{2^{L_A}} \\ &\approx -\log_2 \frac{2^{L_A-N(t)}}{2^{L_A}} = N(t). \end{aligned} \tag{3.35}$$

$N(t)$ grows linearly in time and eventually saturates to L_A. In Fig. 3.13, we compute the standard deviation $\delta N(t)$ and find that it scales as $t^{0.26}$.

3.C Purification dynamics in the volume-law phase

In this appendix, we numerically study the fluctuation exponent of the purification process of the hybrid Clifford QA model in the volume-law phase $p < p_c$. We first compute the fluctuation of the entanglement entropy of subsystem A in Fig. 3.14(a) and find that $\delta S_A \propto L_A^{0.318}$, with the exponent 0.318 close to the roughness exponent. We can also extract the subleading term out by computing the mutual information between the two subsystems $I_{A,B} = S_A + S_B - S_Q$. As shown in Fig. 3.14(b), $I_{A,B} \propto L_A^{0.324}$. This again indicates the correlation between the volume-law phase of hybrid QA circuits and the KPZ universality class.

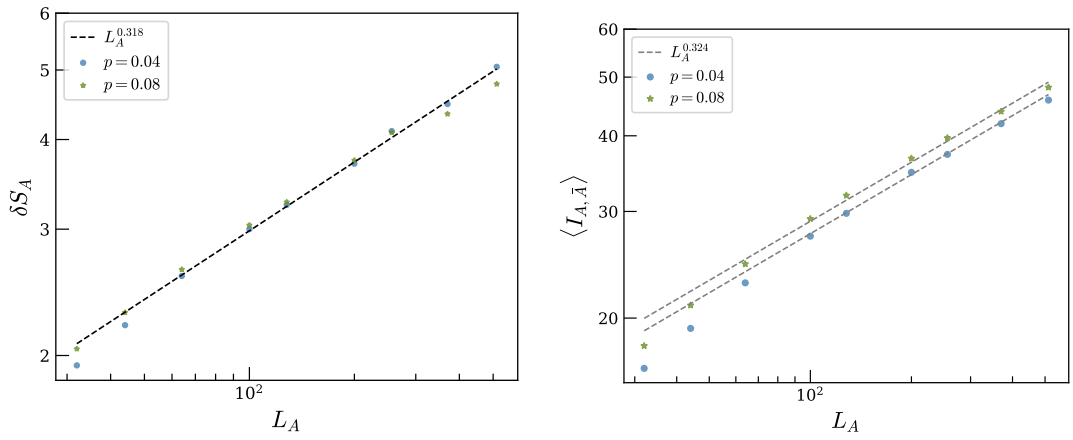

(a) (b)

Figure 3.14: (a) The standard deviation of the entanglement entropy δS_A vs L_A plotted on a log-log scale. (b) The mutual information between the two subsystems $I_{A,B}$ vs L_A plotted on a log-log scale. All of the data are collected from the hybrid Clifford QA circuit at half system size $L_A = L/2$ for a variety of L at $T = 3L$ and are computed under PBC.

3.D Two-species particle model of the purification process

In order to interpret the purification process in terms of the two-species particle model, we go back to the bit string picture and modify Eq. 2.14. The wave function can now be expanded in the basis in subsystems A and B and also the environment R,

$$\begin{aligned} |\psi(t)\rangle &= \tilde{U}_t \circ \mathsf{CZ}|\psi_0\rangle \\ &= \tilde{U}_t \circ \mathsf{CZ}|+x\rangle^{\otimes 2L} \\ &= \frac{1}{\sqrt{4^L}} \sum_{i,j,k} e^{i\theta_{i,j,k}} |\alpha_i\rangle_A |\beta_j\rangle_B |\gamma_k\rangle_R, \end{aligned} \tag{3.36}$$

where the CZ gate acts on both the system and the environment, creating L EPR pairs, and the following $\tilde{U}_t$ is the combination of the hybrid QA circuit applied solely on system Q. To compute the purity, we can still apply the SWAP_A operator which exchanges the spin configurations $|\alpha\rangle$ within subsystem A of the replicated states, and insert two complete sets of basis upon which the operators act in a time-reversed order,

$$\begin{aligned} \mathrm{Tr}(\rho_A^2) &= \sum_{n_1,n_2} \langle\psi|_2\langle\psi|_1 \mathsf{SWAP}_A |n_1\rangle|n_2\rangle\langle n_2|\langle n_1|\psi\rangle_1|\psi\rangle_2 \\ &= \sum_{n_1,n_2} \langle\psi_0|_1 \mathsf{CZ} \circ \tilde{U}_t^\dagger |n_1'\rangle\langle\psi_0|_2 \mathsf{CZ} \circ \tilde{U}_t^\dagger |n_2'\rangle \\ &\qquad \langle n_1|\tilde{U}_t \circ \mathsf{CZ}|\psi_0\rangle_1 \langle n_2|\tilde{U}_t \circ \mathsf{CZ}|\psi_0\rangle_2 \\ &= \frac{1}{4^{2L}} \sum_{n_1,n_2} e^{-i(\Delta_{n_1'} + \Theta_{n_1'})} e^{-i(\Delta_{n_2'} + \Theta_{n_2'})} \\ &\qquad \times e^{i(\Delta_{n_1} + \Theta_{n_1})} e^{i(\Delta_{n_2} + \Theta_{n_2})}, \end{aligned} \tag{3.37}$$

where

$$\begin{aligned} |n_1'\rangle|n_2'\rangle &= \mathsf{SWAP}_A|n_1\rangle|n_2\rangle \\ &= \mathsf{SWAP}_A|\alpha_1\beta_1\gamma_1\rangle|\alpha_2\beta_2\gamma_2\rangle \\ &= |\alpha_2\beta_1\gamma_1\rangle|\alpha_1\beta_2\gamma_2\rangle. \end{aligned} \tag{3.38}$$

Here Θ_n is the accumulated phase generated by the circuit within system Q of the bit string $|n\rangle$, and Δ_n is the phase generated by the CZ gate acting on both Q and R of the time-evolved bit string $\tilde{U}_t|n\rangle$.

Based on the analysis in Chapter 2, only the bit string configurations $\{|n_1\rangle, |n_2\rangle, |n_1'\rangle, |n_2'\rangle\}$ whose total accumulated phases are zero can contribute to $\mathrm{Tr}(\rho_A^2)$. We can take a further step by assuming that only the configurations satisfying $\Delta_r = -\Delta_{n_1'} - \Delta_{n_2'} + \Delta_{n_1} + \Delta_{n_2} = 0$ and $\Theta_r = -\Theta_{n_1'} - \Theta_{n_2'} + \Theta_{n_1} + \Theta_{n_2} = 0$ contribute to the purity. The former constraint is met when $|n_1(t)\rangle = |\alpha_1\beta_1\gamma_1\rangle = |n_1'(t)\rangle = |\alpha_2'\beta_1'\gamma_1\rangle$, and $|n_2(t)\rangle = |\alpha_2\beta_2\gamma_2\rangle = |n_2'(t)\rangle = |\alpha_1'\beta_2'\gamma_2\rangle$. In the particle language, it means that the particles representing the bit-string difference $|n_1 - n_1'|$ completely die out at time t. Meanwhile, the latter constraint is the same as in the entanglement dynamics, i.e., the X and Y particles representing the difference $|n_1(x,0) - n_2(x,0)|$ in A and B respectively never encounter each other up to time t. To summarize, we only need to count the configurations for which X and Y particles do not meet and X particles have become extinct at time t. Let the fraction of such configurations be P_1, the entanglement entropy of the subsystem A is then

$$S_A^{(2)}(t) \approx -\log_2 P_1(t). \tag{3.39}$$

Chapter 4

Entanglement dynamics in U(1) symmetric hybrid quantum automaton circuits

4.1 Introduction

Entanglement is an important measure of correlations between different degrees of freedom in many-body quantum systems. In a typical system with local interactions, quantum information propagates ballistically, resulting in linear growth of entanglement over time [24]. This physics can be understood through random circuit models, which offer a minimal model for investigating entanglement dynamics and information scrambling [80, 81, 82, 28, 83].

However, the above-described picture changes slightly when an additional continuous symmetry is present in the dynamics. If U(1) symmetry is imposed, it can lead to diffusive transport of the conserved charges. It has been demonstrated that although the von-Neumann entanglement entropy continues to grow linearly, the growth of higher Rényi entropies is limited by the diffusive transport and therefore exhibits sub-ballistic growth [53, 54, 55, 56]. Mathematically it is rigorously proven that the growth of $S^{(n>1)}$ is at most diffusive, with a logarithmic correction [53], i.e.,

$$S^{(n>1)} \leq \frac{n}{n-1}\mathcal{O}(\sqrt{t \ln t}). \tag{4.1}$$

Motivated by these findings, this paper investigates the entanglement dynamics in the U(1)-symmetric quantum automaton (QA) circuits with a focus on the second Rényi entropy $S^{(n=2)}$. In QA circuits, the quantum state is always an equal-weight superposition of all the allowed basis states with the phases carrying the quantum information. Due to this special property, $S^{(n=2)}$ can be mapped to a quantity of a classical bit string model [70, 84, 40]. Such a mapping enables us to study the entanglement dynamics analytically and also provides an efficient method for numerical simulation. We show that the growth of $S^{(n=2)}$ is governed by the presence of the rare bit strings that contain extensively long domains

comprising consecutive spin 0s or 1s, consistent with the physical picture introduced in Ref. [53, 54]. Additionally, we present numerical evidence demonstrating that the dynamics of $S^{(n=2)}$ actually saturates the upper bound defined in Eq. (4.1). This saturation is caused by the diffusive transport (up to a logarithmic correction) of the boundary of these long domains. Furthermore, for charge-fixed states, we study the coefficient in front of the diffusive scaling of $S^{(n=2)}(t)$ and find that it is linearly dependent on the charge filling factor ν when ν is small.

In addition, we are interested in the impact of U(1) symmetry on the entanglement dynamics of monitored QA circuits. Notably, recent research has revealed that monitored quantum dynamics give rise to a measurement-induced entanglement phase transition (MIPT) [25, 27, 26]. This occurs as a result of the interplay between random unitary evolution and local non-unitary measurements, driving the system from a highly-entangled volume-law phase to a disentangled area-law phase [25, 27, 26, 31, 30, 37, 36], or even to other quantum phases, such as the critical phase, depending on the symmetry and type of measurements imposed [42, 85, 46, 44, 45, 70]. When U(1)-symmetry is introduced in monitored Haar random circuits, it is found that any non-zero rate of single-qubit projective measurements will eliminate the rare slow modes containing extensively long domains, and the Rényi entropy grows linearly in time for $0 < p < p_c$ and exhibits $z = 1$ dynamical scaling at the critical point p_c [86].

With these insights in mind, our paper also investigates the entanglement dynamics of U(1)-symmetric QA circuits under specific measurements that preserve U(1) symmetry and keep the wave function as an equal weight superposition of basis states. Interestingly, different from Haar random circuits, the measurements leave these extensively long domains untouched and the second Rényi entropy still exhibits diffusive growth in the volume-law phase. As the measurement rate p increases, we observe a phase transition to a critical phase where the entanglement entropy grows logarithmically in time. The critical phase that we observe is a result of both the unique properties of QA circuits and the presence of U(1) symmetry. It is worth noting that similar behavior has also been observed in the monitored $\mathbb{Z}_2$ symmetric QA circuits [70].

4.2 U(1)-symmetric hybrid QA circuits and two-species particle model

In this chapter, we consider 1+1d U(1)-symmetric hybrid QA circuits. The dynamics consists of local QA unitary operators and composite measurements, which are chosen to preserve the total charge

$$Q = \sum_{i}^{L} \sigma_i, \text{ where } \sigma_i = (1 - Z_i)/2 \tag{4.2}$$

and Z_i is the Pauli Z matrix acting on the ith site of a chain with L qubits. A QA unitary operator permutes states in the computational basis up to a phase, i.e.,

$$U|n\rangle = e^{i\theta_n}|\pi(n)\rangle, \tag{4.3}$$

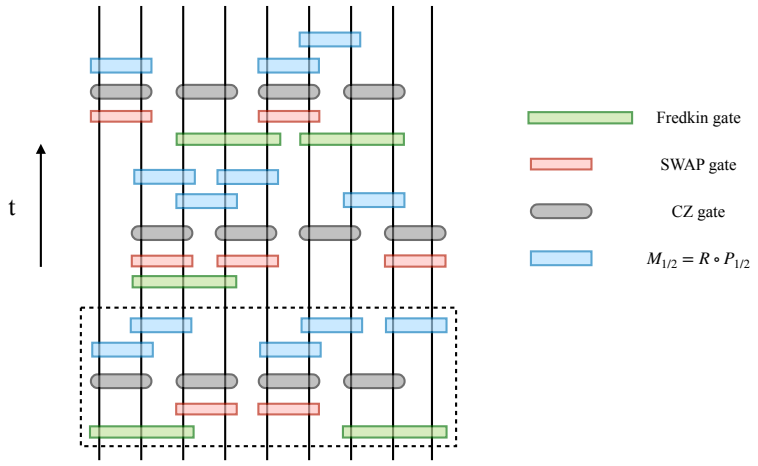

Figure 4.1: The setup of the U(1)-symmetric hybrid QA circuit of one time step. The dashed box encloses the gates within a single layer. Each time step involves three layers of Fredkin gates, SWAP gates, and CZ gates, interspersed with composite measurements. The Fredkin and SWAP gates are applied in each layer with probability $p_u < 1$, and the measurement appears in each measured sublayer with probability p. The Fredkin and SWAP gates determine the dynamics of bit string $|n\rangle$ and can be replaced by other QA gates preserving U(1) symmetry.

where $\pi \in S_N$ is an element of the permutation group on a computational basis with cardinality N. Here we take the initial state

$$|\psi_0\rangle = \sum_n \frac{|n\rangle}{\sqrt{N}} \tag{4.4}$$

to be an equal-weight superposition of two different sets of basis states: (i) $\{|n\rangle = |\sigma_1\sigma_2\ldots\sigma_L\rangle : \sigma_i = \{0,1\}\}$ is all the allowed Pauli Z basis with cardinality $N = 2^L$ so that

$$|\psi_0\rangle = |+x\rangle^{\otimes L} = \big[\frac{1}{\sqrt{2}}(|0\rangle + |1\rangle)\big]^{\otimes L}. \tag{4.5}$$

(ii) $\{|n\rangle = |\sigma_1\sigma_2\ldots\sigma_L\rangle : \sigma_i = \{0,1\}, \sum_i \sigma_i = Q\}$ is the subset of the Pauli Z basis with a fixed extensive charge filling $\nu \equiv Q/L$, so that $N = \binom{L}{Q} = L!/[(L-Q)!Q!]$.

Fig.4.1 depicts a brickwork-patterned U(1) symmetric hybrid QA circuit. Each time step consists of three layers of QA unitary operators interspersed with composite measurements with probability p. For the unitary part, we consider Fredkin gates and SWAP gates, along with CZ gates which assign a π phase to the spin configuration $|11\rangle$. The Fredkin gates are three-qubit gates that interchange qubits $i-1$ and $i+1$ according to the value of the middle (control) qubit, i.e., $|\sigma_i 1_{i+1}\sigma_{i+2}\rangle \mapsto |\sigma_{i+2}1_{i+1}\sigma_i\rangle$ and $|\sigma_i 0_{i+1}\sigma_{i+2}\rangle \mapsto |\sigma_i 0_{i+1}\sigma_{i+2}\rangle$. Meanwhile, the SWAP gates interchange two neighboring qubits. Together with CZ gates, they scramble the quantum information and increase the entanglement entropy of the state until it saturates to the volume-law scaling. As illustrated in Fig.4.1, in the first/ second/ third layer of each time step, the Fredkin gates are applied on sites $\{3j-2, 3j-1, 3j\}/\{3j-1, 3j, 3j+1\}/\{3j, 3j+1, 3j+2\}$ for $j \in [1, L/3]$, while the SWAP and CZ gates are applied on sites $\{2j-1, 2j\}/\{2j, 2j+1\}/\{2j-1, 2j\}$ for $j \in [1, L/2]$. Specifically, we set the occurring probability of the Fredkin and SWAP gates to be p_u and we take $p_u < 1$ throughout the

chapter.

Constructing the measurement gates can be quite tricky. To ensure that $|\psi_t\rangle$ remains an equal-weight superposition of basis states, we introduce a charge-preserving two-qubit composite measurement $M_{1/2} = R \circ P_{1/2}$. Here P_1 and P_2 are the Kraus operators,

$$P_1 = \begin{pmatrix} \frac{1}{\sqrt{2}} & 0 & 0 & 0 \\ 0 & 1 & 0 & 0 \\ 0 & 0 & 0 & 0 \\ 0 & 0 & 0 & \frac{1}{\sqrt{2}} \end{pmatrix}, \quad P_2 = \begin{pmatrix} \frac{1}{\sqrt{2}} & 0 & 0 & 0 \\ 0 & 0 & 0 & 0 \\ 0 & 0 & 1 & 0 \\ 0 & 0 & 0 & \frac{1}{\sqrt{2}} \end{pmatrix}, \tag{4.6}$$

followed by a two-site rotation operator,

$$R = \begin{pmatrix} 1 & 0 & 0 & 0 \\ 0 & \frac{1}{\sqrt{2}} & \frac{1}{\sqrt{2}} & 0 \\ 0 & \frac{1}{\sqrt{2}} & -\frac{1}{\sqrt{2}} & 0 \\ 0 & 0 & 0 & 1 \end{pmatrix}, \tag{4.7}$$

which maps $|01\rangle \mapsto (|01\rangle + |10\rangle)/\sqrt{2}$ and $|10\rangle \mapsto (|01\rangle - |10\rangle)/\sqrt{2}$ [1], and acts trivially on $|00\rangle$ and $|11\rangle$, so as to rotate the wave function back to equal weight (up to a phase) superposition of the computational basis. In general, the measurement disentangles the system by discarding the phase information of a quarter of the basis states. However, considering it is a two-qubit operator as required by the U(1) symmetry, as we will see later, the measurements together with phase gates can actually induce entanglement in certain circumstances. As shown in Fig.4.1, each measured layer contains two rows of composite measurements, with each row containing $M_{1/2}$ randomly distributed with probability p on sites $\{2j-1, 2j\}/\{2j, 2j+1\}$ for $i \in [1, L/2]$.

Throughout the chapter, we focus on the entanglement dynamics between subsystems A and B that the system is bi-partitioned into. Specifically, we consider the second Rényi entropy of A,

$$\begin{aligned} S_A^{(2)}(t) &= -\ln \mathrm{Tr}[\rho_A^2(t)], \\ \rho_A(t) &= \mathrm{Tr}_B |\psi_t\rangle\langle\psi_t| \end{aligned} \tag{4.8}$$

where $|\psi_t\rangle = \tilde{U}_t|\psi_0\rangle$ is the wave function of the quantum trajectory with $\tilde{U}_t$ representing the circuit evolution up to time t. We first consider the initial condition (i), where $|\psi_0\rangle = |+x\rangle^{\otimes L}$. In our earlier work, we discovered an efficient algorithm to compute $S_A^{(2)}(t)$ from this initial state [40]. Additionally, we presented a classical stochastic model to elucidate the entanglement dynamics [70]. In the following, we will provide a brief overview of them and apply these methods to our

[1] In numerical simulations, we omit the extra π phase in front of $|10\rangle$ obtained from the rotation of M_2. This is because it is equivalent to applying M_2 without the extra π phase followed by a controlled phase gate. As shown later, such a phase gate will not affect the entanglement phase transition from the volume-law phase to the critical phase. The location of the phase transition is only determined by the corresponding bit string dynamics.

QA circuit with U(1) symmetry.

The purity can be expressed as the expectation of the SWAP_A operator over double copies of the system [65],

$$\mathrm{Tr}[\rho_A^2(t)] = \langle\psi_t|_2 \otimes \langle\psi_t|_1 \mathsf{SWAP}_A |\psi_t\rangle_1 \otimes |\psi_t\rangle_2. \tag{4.9}$$

The SWAP_A operator swaps the configurations of the copies within region A. Since QA circuits preserve the computational basis that spans $|\psi_t\rangle$, we can insert into Eq.(4.9) two sets of complete basis which are acted upon by the circuit in a time-reversed order,

$$\begin{aligned}\mathrm{Tr}[\rho_A^2(t)] &= \sum_{n_1,n_2} \langle\psi_t|_2\langle\psi_t|_1 \mathsf{SWAP}_A |n_1\rangle|n_2\rangle \\ &\qquad \langle n_2|\langle n_1|\psi_t\rangle_1|\psi_t\rangle_2 \\ &= \frac{1}{4^L}\sum_{n_1,n_2} e^{-i\Theta_{n_1'}(t)} e^{-i\Theta_{n_2'}(t)} e^{i\Theta_{n_1}(t)} e^{i\Theta_{n_2}(t)},\end{aligned} \tag{4.10}$$

where

$$e^{i\Theta_{n_i}(t)} = \sqrt{2^L}\langle n_i|\tilde{U}_t|\psi_0\rangle, \tag{4.11}$$

and

$$\begin{aligned}|n_1'\rangle|n_2'\rangle &\equiv \mathsf{SWAP}_A|n_1\rangle|n_2\rangle \\ &= \mathsf{SWAP}_A|\alpha_1\beta_1\rangle|\alpha_2\beta_2\rangle \\ &= |\alpha_2\beta_1\rangle|\alpha_1\beta_2\rangle,\end{aligned} \tag{4.12}$$

where $|\alpha_i\rangle$ and $|\beta_i\rangle$ are the spin configurations in subsystems A and B of $|n_i\rangle$. Therefore, in the numerical simulation, instead of evolving the wave function $|\psi_t\rangle$, we can apply the circuit on the bit strings in a time-reversed order. When evaluating Eq. (4.11) from left to right, although the composite measurement M is non-unitary, we can still derive the effective action on the bit string $\langle n|$. For bit strings that have anti-parallel spins on the sites where M is applied, they are all forced to be either $\langle\ldots 01\ldots|$ or $\langle\ldots 10\ldots|$ after the measurement.

With a few modifications, the above equations used to compute the purity can also be applied to the initial condition (ii). When $|\psi_0\rangle$ is a charge-fixed state of filling factor ν, only the bit string pairs that share the same filling factor both before and after the SWAP, i.e., $\{|n_1\rangle, |n_2\rangle, |n_1'\rangle, |n_2'\rangle\}$ with the same ν, will have nonzero overlap with $|\psi_0\rangle$ and hence contribute to the purity.

Eq. (4.10) not only offers a numerical method but also helps us to understand the entanglement dynamics through the classical bit string dynamics. It is worth noting that this equation sums up the accumulated phase $\Theta_r = -\Theta_{n_1'} - \Theta_{n_2'} + \Theta_{n_1} + \Theta_{n_2}$ for each bit string pair $\{|n_1\rangle, |n_2\rangle\}$. Under random time evolution, Θ_r can become a nonzero random number, and we expect the sum over these phases to be zero. Therefore only the configurations with $\Theta_r = 0$ contribute to the purity. This observation leads to a stochastic particle model in which there are two particle species X and Y representing the bit string difference

$$h(x,t) = |n_1(x,t) - n_2(x,t)| \tag{4.13}$$

initially distributed in subregion A and B respectively [70, 84], as illustrated in Fig. 4.2. As time evolves, the two species

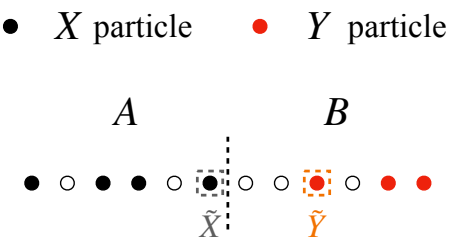

Figure 4.2: The cartoon of the two-species particle model. We use $\circ$ to denote $h(x) = 0$ and $\bullet$ to denote $h(x) = 1$, where the black dots represent X particles and the red dots represent Y particles, and $\tilde{X}(\tilde{Y})$ represents the rightmost X (leftmost Y) particle. At $t = 0$, the X and Y particles are distributed in region A and B respectively. As time evolves, both species begin to expand and intrude into each other's territory.

originally located in subregions A and B gradually expand. It is shown that only the configurations in which X and Y particles have never met up to time t satisfy $\Theta_r(t) = 0$ and hence contribute to the purity, i.e.,

$$S_A^{(2)}(t) = -\ln \mathrm{Tr}\rho_A^2(t) \approx -\ln \frac{N_0(t)}{4^L} \equiv -\ln P(t), \tag{4.14}$$

where $N_0(t)$ is the number of bit string pairs in which the two species never encounter each other up to time t (For more details, see chapter.2).

From the above analysis, the growth of the second Rényi entropy is determined by the dynamics of the endpoint $\tilde{X}$ and $\tilde{Y}$ particles of each bit string pair, i.e., the rightmost X particle and the leftmost Y particle. Let us first consider the system without any symmetry. Under unitary dynamics, the $\tilde{X}$ and $\tilde{Y}$ particles move ballistically toward each other at roughly the same speed, i.e., the distance that an endpoint particle travels over time t scales as $\Delta l(t) \propto t$. Therefore, only the configurations whose initial rightmost X and leftmost Y particles are situated a distance of at least $2\Delta l(t)$ apart can contribute to the purity. This leads to $P(t) = [2^{2\Delta l(t)} \times 4^{L-2\Delta l(t)}]/4^L = \mathcal{O}(e^{-t})$, which explains the linear growth of entanglement entropy in the absence of U(1) symmetry.

4.3 Unitary dynamics

We first study the U(1)-symmetric QA circuit without measurements, i.e., $p = 0$, and take the unitary rate $p_u = 0.5$. The classical bit string model allows for numerical simulations of the second Rényi entropy for relatively large system sizes. To be more specific, we prepare a large sample of randomly generated bit strings which can have either unfixed or fixed charge filling, and estimate $S_A^{(2)}$ using Eq.(4.10). In both cases, we find that the ensemble-averaged early-time $\overline{S_A^{(2)}(t)}$ exhibits a sub-ballistic power-law growth with the exponent close to $1/2$. We also evaluate $P(t)$ by calculating the fraction of the bit string configurations whose corresponding X and Y particles never meet up to time t. The numerics indicates that $\overline{-\ln P(t)}$ exhibits the same scaling as the one obtained using Eq.(4.10). Hence we conclude that $-\ln P(t)$ provides a reliable approximation for evaluating $S_A^{(2)}$ in U(1)-symmetric QA circuit. By studying the dynamics of the classical particle model, we can obtain valuable insights into the underlying physics.

More careful examination of $\overline{-\ln P(t)}$ and $\overline{S_A^{(2)}(t)}$ reveals that the power law growth exponent is slightly larger than

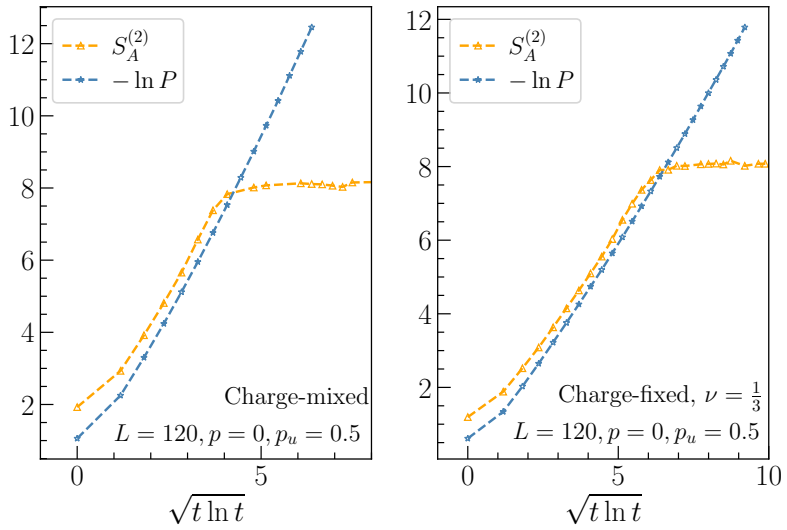

Figure 4.3: $\overline{S_A^{(2)}(t)}$ and $\overline{-\ln P(t)}$ in the QA circuit with $p = 0$. We consider two different initial conditions: the charge-mixed state and the charge-fixed state with the filling factor $\nu = 1/3$. We take the unitary rate $p_u = 0.5$ in each layer with the system size $L = 120$ and subsystem size $L_A = L/2 = 60$. Both the early-time $\overline{S_A^{(2)}(t)}$ and $\overline{-\ln P(t)}$ for the two initial conditions have $\sqrt{t \ln t}$ scaling.

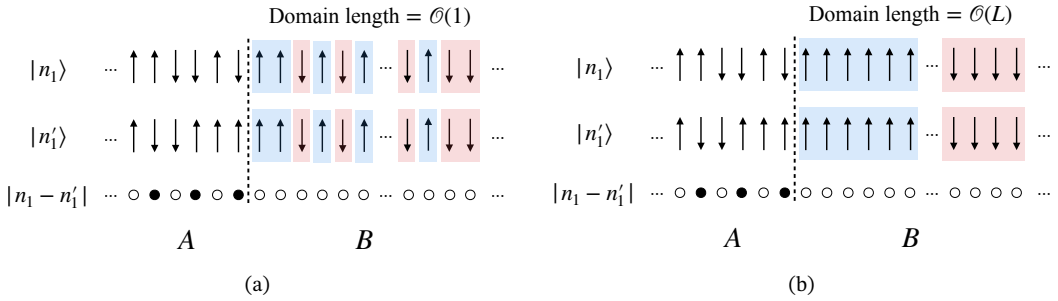

Figure 4.4: The illustration of the initial bit string configuration of (a) fast modes and (b) slow modes with the same particle representation. For convenience, we consider the bit strings $\{|n_1\rangle, |n_1'\rangle\}$ whose difference represents the particle configuration where there are only X particles located in the region A initially.

$1/2$, which has also been observed in the previous study [87]. Since the growth is constrained by Eq.(4.1), the power law exponent cannot exceed $1/2$. We propose that the deviation of the exponent from $1/2$ observed in the numerics is due to the logarithmic correction. As shown in Fig.4.3, both quantities are linearly proportional to $\sqrt{t \ln t}$. Therefore, in our QA circuit,

$$\overline{S_A^{(2)}(t)} = \lambda_{EE} \sqrt{t \ln t}. \tag{4.15}$$

To explain the above results, we study the dynamics of the two-species particle model. Since the dynamics of the $\tilde{X}$ and $\tilde{Y}$ particles are analogous, we will focus on the displacement $\Delta l(t)$ of the $\tilde{X}$ particle. Different from the case without U(1) symmetry where the particles move ballistically, in the presence of U(1) symmetry, there are two distinct modes

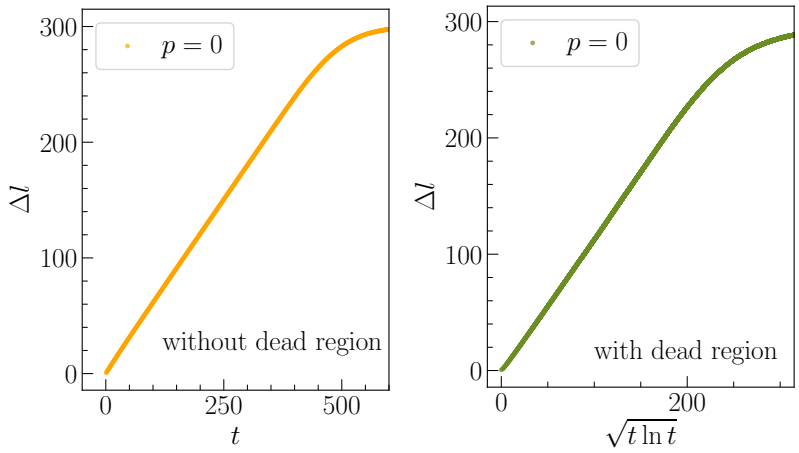

Figure 4.5: The distance that an endpoint particle travels $\Delta l(t)$ over time t under U(1)-symmetric QA unitaries for the initial configurations (a) without the dead region and (b) with the dead region. Without loss of generality, we take the probability of Fredkin and SWAP gates to be $p_u = 0.5$ in each layer, the system size $L = 600$, and the number of spin 1's to be $L/3$ in (a) and $L_A/3$ in (b), both of which have $\nu = 1/3$. We find that (a) $\overline{\Delta l} \propto t$ and (b) $\overline{\Delta l} \propto \sqrt{t \ln t}$ before saturation.

of $\tilde{X}$ particles depending on the corresponding bit string configuration to the right of $\tilde{X}$ particle. As illustrated in Fig. 4.4(a), in typical random bit strings whose domains are of $\mathcal{O}(1)$ length, the $\tilde{X}$ particle moves ballistically with a constant velocity. In contrast, in Fig. 4.4(b), for the bit string configurations with domains of $\mathcal{O}(L)$ length, the $\tilde{X}$ particle only moves diffusively (up to some logarithmic correction). Such configurations are rare and only comprise $\mathcal{O}(e^{-L})$ of the bit string ensemble. To verify the existence of the slow modes, in numerical simulations, we consider the extreme case where the initial bit string configurations in subsystem B are a single domain of spin 0's which is called "dead region", i.e.,

$$\begin{aligned} |n_1(t=0)\rangle &= |\alpha_1\rangle \otimes |0\rangle^{\otimes |B|}, \\ |n_1'(t=0)\rangle &= |\alpha_2\rangle \otimes |0\rangle^{\otimes |B|}. \end{aligned} \tag{4.16}$$

We also study $\Delta l(t)$ without the dead region for comparison.

As shown in Fig. 4.5, for the configurations without the dead region, $\overline{\Delta l}$ grows linearly in time. This is responsible for the ballistic information spreading observed in the out-of-time-ordered correlator (OTOC) in a similar U(1) symmetric QA circuit [42]. On the other hand, for configurations with the dead region, $\overline{\Delta l}$ exhibits diffusive growth over time, with a logarithmic correction, that is,

$$\overline{\Delta l} = \lambda_l \sqrt{t \ln t}. \tag{4.17}$$

The diffusive motion of the $\tilde{X}$ particle comes from the diffusive dynamics of the rightmost charge (spin 1) located at the boundary of the dead region. In the simple symmetric exclusion process, one of the most basic models with U(1) symmetry, it is analytically proven that the displacement of the rightmost charge expands as $\sqrt{t \ln t}$ [88]. Despite the greater complexity of our model involving the Fredkin gate, we believe that the underlying physics remains fundamentally the same. In Appendix.4.A, we examine a simple QA circuit with the kinetic constraint set by SWAP gates only,

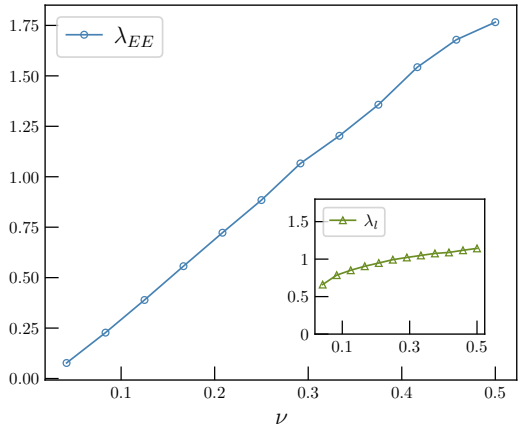

Figure 4.6: The coefficient λ_{EE} of $\overline{S_A^{(2)}} = \lambda_{EE}\sqrt{t \ln t}$ vs the filling factor ν. In the inset, we present λ_l of the endpoint displacement $\overline{\Delta l} = \lambda_l \sqrt{t \ln t}$ of the slow modes with dead region vs the filling factor ν_A in subsystem A.

enabling an exact mapping of the bit string dynamics to the simple symmetric exclusion processes. In addition, we also investigate another QA circuit involving a four-qubit gate. For both models, we provide numerical evidence confirming the existence of logarithmic corrections in both Eq.(4.17) and Eq.(4.15).

Based on this analysis, the bit string pairs that contribute to the purity (See Eq.(4.14)) can be divided into two parts, $P(t) = P^F(t) + P^S(t)$, where $P^F(t)$ and $P^S(t)$ are the fractions of fast modes and slow modes respectively whose X and Y particles have *not* encountered each other up to time t. Since the distance between the endpoint X and Y particles decreases by $2\Delta l(t)$ over time t, only the configurations whose initial two species are located a distance $2\Delta l(t)$ apart contribute to $P(t)$. Therefore, both $P^F(t)$ and $P^S(t)$ decay as $\exp(-\overline{\Delta l(t)})$, whereas $P^F(t) \propto \exp(-t)$ and $P^S(t) \propto \exp(-\sqrt{t \ln t})$. In the absence of U(1) symmetry, the bit string ensemble comprises only fast modes, which account for the linear growth of $S_A^{(2)}(t)$ as explained earlier. In the presence of U(1) symmetry, slow modes consisting of the bit string pairs with identical long domains with length $\mathcal{O}(L)$ between $\tilde{X}$ and $\tilde{Y}$ emerge. Therefore it takes $\mathcal{O}(L^2)$ time for $\tilde{X}$ particle to reach $\tilde{Y}$ particle. For $S_A^{(2)}(t) \approx -\ln[P^F(t) + P^S(t)]$, $P^F(t)$ vanishes at time $\mathcal{O}(L)$, leaving a diffusive growth of $S_A^{(2)}(t)$ caused by the slow modes up to time $\mathcal{O}(L^2)$.

Similar reasoning can also be applied to the charge-fixed state. In particular, we can also analyze the dependence of the coefficient λ_{EE} in Eq.(4.15) on the filling factor ν. As shown in Fig. 4.6, $\lambda_{EE} \propto \nu$ for $\nu \lessapprox 0.3$. To understand this behavior, we investigate the dependence of P^S on ν, given by

$$P^S = \left[\binom{L - 2\Delta l}{\nu L} \Big/ \binom{L}{\nu L} \right]^2 = \left[\frac{(L - 2\Delta l)!(L - \nu L)!}{(L - 2\Delta l - \nu L)! L!} \right]^2 . \tag{4.18}$$

If $\nu \ll 1 - 2\Delta l/L$, we can approximate as follows:

$$\begin{aligned} -\ln P^S &\approx -2[(L-2\Delta l)\ln(L-2\Delta l) + (L-\nu L)\ln(L-\nu L) - (L-2\Delta l-\nu L)\ln(L-2\Delta l-\nu L) - L\ln L] \\ &= -4\Delta l \ln\left(1-\frac{\nu L}{L-2\Delta l}\right) - 2\nu L \ln\left(1-\frac{2\Delta l}{L-\nu L}\right) + \mathcal{O}(\ln \Delta l) + \mathcal{O}(\ln \nu L) \\ &\approx 8\nu\Delta l + \mathcal{O}(\ln \Delta l) + \mathcal{O}(\ln \nu L). \end{aligned} \tag{4.19}$$

As time evolves, the entanglement entropy is dominated by the slow modes and has the scaling $S_A^{(2)}(t) \approx -\ln P^S(t) \propto \nu\Delta l$. We further investigate the dependence of Δl on ν. We examine the displacement of $\tilde{X}$ particle of the bit string configurations with the dead region as illustrated in Fig. 4.4(b). Specifically, we define ν_A to be the filling factor in subsystem A. As shown in Fig. 4.6, Δl remains largely unaffected by changes in ν_A.

Combining these findings, we can explain the numerical observation of the linear dependence of λ_{EE} on ν when ν is small. In addition, we also observe similar linear dependence on $1-\nu$ for $\nu \gtrapprox 0.7$ (not presented in the figure), which can be understood in a similar way.

4.4 Hybrid dynamics

Now we introduce the composite measurements into the circuit and examine its impact on the entanglement dynamics. As shown in Fig.4.7, our finding indicates that when p is small, the entanglement still grows diffusively with a logarithmic correction, as described in Eq.(4.15). This can be explained by the fact that our composite measurement only acts non-trivially on anti-parallel neighboring sites, while leaving the bit strings with extensively long domains unaffected. We expect that this scaling behavior persists throughout the entire volume-law phase. This is different from the single-qubit projective measurement which quickly destroys the slow modes with dead regions and leads to the linear growth of $S_A^{(2)}$ in the volume-law phase of the non-unitary U(1) symmetric Haar random circuit[86].

As p increases, we observe a decrease in the coefficient λ for $S_A^{(2)}(t)$. Eventually, this diffusive growth is replaced by logarithmic growth. To expand the tuning range for the ratio p/p_u, we fix p to be a finite constant and reduce p_u. Surprisingly, we find that even when p_u approaches zero, the logarithmic scaling persists. This observation suggests that there is an entanglement phase transition from a volume-law phase to a critical phase in our model.

Such a transition to a critical phase is a special feature of QA circuits and a similar transition has also been observed in the hybrid QA circuit with discrete $\mathbb{Z}_2$ symmetry [70]. To understand this phase transition, we can analyze the dynamics of the particles characterizing the bit string pairs difference, in particular, the particle density $n(t) \equiv \sum_x h(x,t)/L$ [70, 84, 40]. In the $\mathbb{Z}_2$ symmetric QA circuit, it is shown that the particles perform branching-annihilating random walks (BAW) with an even number of offspring:

$$W \leftrightarrow 3W, W + W \xrightarrow{p} \emptyset. \tag{4.20}$$

The first process arises from unitary dynamics, while the second annihilation process occurs due to the measurement. The competition between these processes gives rise to a phase transition at a critical value p_c, which falls into the parity-

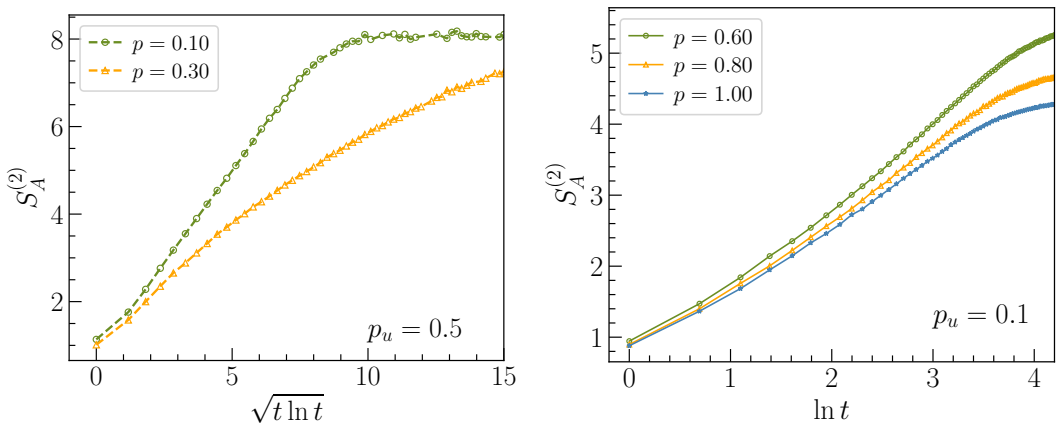

(a) (b)

Figure 4.7: (a) $S_A^{(2)}$ vs $\sqrt{t \ln t}$ for $p = 0.1$ and $p = 0.3$ with the unitary rate $p_u = 0.5$. (b) $S_A^{(2)}$ vs $\ln t$ for $p = 0.6$, 0.8 and 1 with $p_u = 0.1$. For both phases, we take the system size $L = 120$ and the filling factor $\nu = 1/3$, under the periodic boundary condition (PBC).

conserving (PC) universality class. In the absorbing phase with $p > p_c$, the dynamics are primarily governed by the random walking particles, which annihilate in pairs upon meeting. This particular dynamics leads to an algebraic decay with $n(t) \sim t^{-0.5}$, resulting in a power-law decay of $P(t)$. This, in turn, leads to a critical quantum phase characterized by logarithmic entanglement dynamics and a dynamical exponent of $z = 2$.

In our model, the particle dynamics is similar and still preserves parity, but is more complicated. For example, for the bit string pair $\{|011\rangle, |001\rangle\}$, under the Fredkin gate, it becomes $\{|110\rangle, |001\rangle\}$ and the particle representation $\circ \bullet \circ \mapsto \bullet \bullet \bullet$, i.e., the particles branch from 1 to 3. However, for the bit string pair $\{|111\rangle, |101\rangle\}$ which has the same particle representation as the previous one, it will remain invariant under the Fredkin gate. On the other hand, the SWAP gate enables particles to diffuse $\bullet\circ \leftrightarrow \circ\bullet$ regardless of the bit string configuration. Similarly, under the composite measurement, the particles will experience pair annihilation $\bullet\bullet \mapsto \circ\circ$ only when the bit string pair is $\{|10\rangle, |01\rangle\}$ instead of $\{|00\rangle, |11\rangle\}$. This leads to a phase transition belonging to a different universality class.

We first focus on the absorbing phase. In the limit $p_u = 0$, we observe that the particle density follows a power law behavior $n(t) \sim t^{-\alpha}$ with $\alpha = 0.28$ for all measurement rates $p > 0$, which is significantly smaller than the exponent of 0.5. This is because particle annihilation only occurs upon measurement based on specific bit string pairs, as illustrated earlier. More detailed data analysis suggests that $\overline{n(t)}$ for different system sizes can be collapsed onto the function

$$\overline{n(t)} = t^{-\alpha} f(t/L^z), \tag{4.21}$$

where $z = 1.95$, close to that of the critical phase observed in $\mathbb{Z}_2$ symmetric QA circuits. We also take a small but finite p_u and similar scaling behavior is observed. For instance, in Fig.4.8(b), we present the data collapse for $p_u = 0.1$ and $p = 1$, yielding exponents $\alpha = 0.27$ and $z = 2$. This absorbing phase with algebraic decay is responsible for a power law decay of $P(t)$, which further leads to a quantum critical phase with a logarithmic entanglement scaling. Notice that in

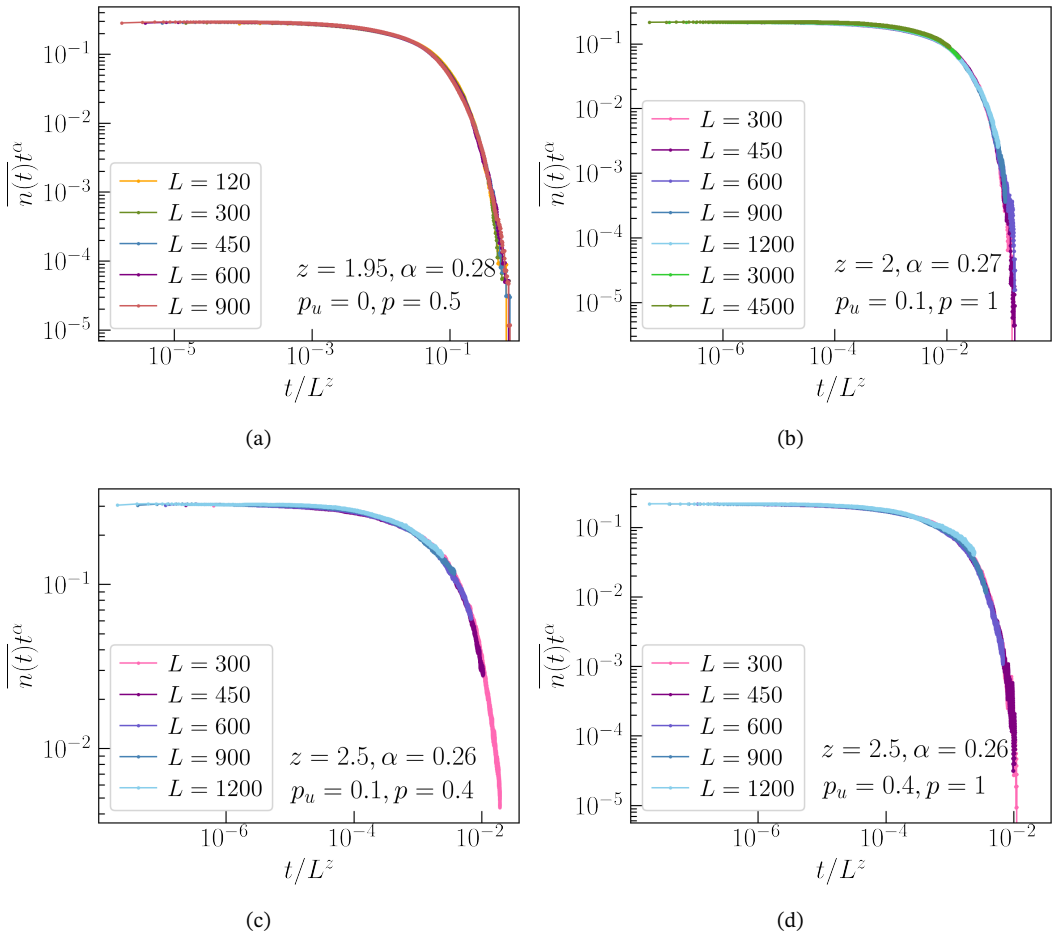

Figure 4.8: The finite-size data collapse $\overline{n(t)}t^\alpha$ vs t/L^z at: (a) $p_u = 0$, $p = 0.5$, with the dynamical exponent $z = 1.95$ and $\alpha = 0.28$. (b) $p_u = 0.1$, $p = 1$, with $z = 2$ and $\alpha = 0.27$. (c) $p_u = 0.1$, $p = 0.4$. (d) $p_u = 0.4$, $p = 1$. Both (c) and (d) have the same critical exponents $z = 2.5$ and $\alpha = 0.26$. The data are calculated over a variety of system sizes with the filling factor $\nu = 1/3$ under PBC.

this phase, $P(t)$ is mainly determined by the fraction $P^F(t)$ without extensively long domains.

We further analyze the transition point. By fixing the unitary rate at $p_u = 0.1$ and decreasing the measurement rate p, we can numerically identify the critical point. In Fig.4.8(c), it is observed that the critical point occurs at approximately $p = 0.4$, with $\alpha = 0.26$ and $z = 2.5$. The existence of the phase transition persists as the unitary rate p_u increases, until it reaches $p_u = 0.4$. At this point (as illustrated in Fig.4.8(d)), the critical point is found at the maximum allowed measurement rate $p = 1$. It is worth emphasizing that this phase transition does not fall into the PC universality class, where the critical exponents are $z^{PC} = 1.744$ and $\alpha^{PC} = 0.286$.

4.5 Discussions and outlook

In this chapter, we investigate the entanglement dynamics of U(1) symmetric QA circuits. We show that the second Rényi entropy saturates the upper bound introduced in Eq.(4.1), namely $S_A^{(2)}(t) \propto \sqrt{t \ln t}$. To understand this behavior,

we map the entanglement dynamics to a classical bit string model and demonstrate that the diffusive dynamics of $S_A^{(2)}(t)$ is caused by bit strings containing extensively long domains.

Additionally, we explore the monitored entanglement dynamics under U(1) symmetry and identify a phase transition from a volume-law phase to a critical phase as the measurement rate p increases. Within the volume-law phase, $S_A^{(2)}(t)$ continues to exhibit diffusive growth due to the presence of bit strings with long domains that remain unaffected by the introduced measurements. On the other hand, the critical phase is characterized by logarithmic scaling of the entanglement, and its stability is ensured by both the U(1) symmetry and the basis-preserving nature of QA circuits.

The analysis of the second Rényi entropy can be extended to higher integer Rényi indices n. By making slight modifications to Eq.(4.10), it can be shown straightforwardly that the evolution of $S_A^{(n)}$ is mapped to a classical dynamics that encompasses n copies of bit strings. In particular, the volume-law phase exhibits diffusive dynamics in the presence of a logarithmic correction. This behavior is governed by these bit string configurations with extensive long domains.

Notably, in both the volume-law phase and critical phase, the spin transport exhibits diffusive dynamics and fails to capture the entanglement phase transition. This is because this measurement-induced transition is visible solely in the non-linear observable of the density matrix. We confirm this diffusive transport by numerically computing the correlation functions and the detailed results are presented in Appendix.4.B.

It has been established that the volume-law phase can be alternatively understood as a quantum error correcting code [30, 29, 33, 52, 51]. In Chapter 2, we presented an interpretation of the quantum error correction property of the volume-law phase of a generic QA circuit, relating it to the dynamics of classical bit strings. Furthermore, we demonstrated a connection between quantum error-correcting codes and classical linear error-correcting codes. In the case of the QA circuit with U(1) symmetry, we expect that the volume-law phase continues to exhibit the characteristics of a quantum error-correcting code. In particular, the dynamics of the associated classical bit strings reveal that the difference between bit string pairs still preserves classical information in a non-local manner, thereby functioning as a classical error-correcting code. It is worth noting that, unfortunately, this classical error-correcting code is no longer linear. We leave this for future study.

Acknowledgement.— We thank Hisanori Oshima and Ethan Lake for the useful discussions. This research is supported in part by the Google Research Scholar Program and is supported in part by the National Science Foundation under Grant No. DMR-2219735. We gratefully acknowledge computing resources from Research Services at Boston College and the assistance provided by Wei Qiu.

4.A Entanglement dynamics of U(1) symmetric QA circuits with other kinetic constraints

4.A.1 The SWAP Model

We study the entanglement dynamics under the kinetic constraint determined by SWAP gates solely, so that our circuit is a U(1) symmetric Clifford QA circuit, which can be efficiently simulated at large system sizes using stabilizer formalism

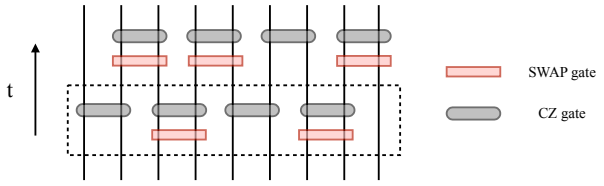

Figure 4.9: The arrangement of gates of the SWAP model in a time step. The dashed box encloses the gates within a single layer. Each time step involves two layers of SWAP gates with probability $p_u = 0.5$, and CZ gates.

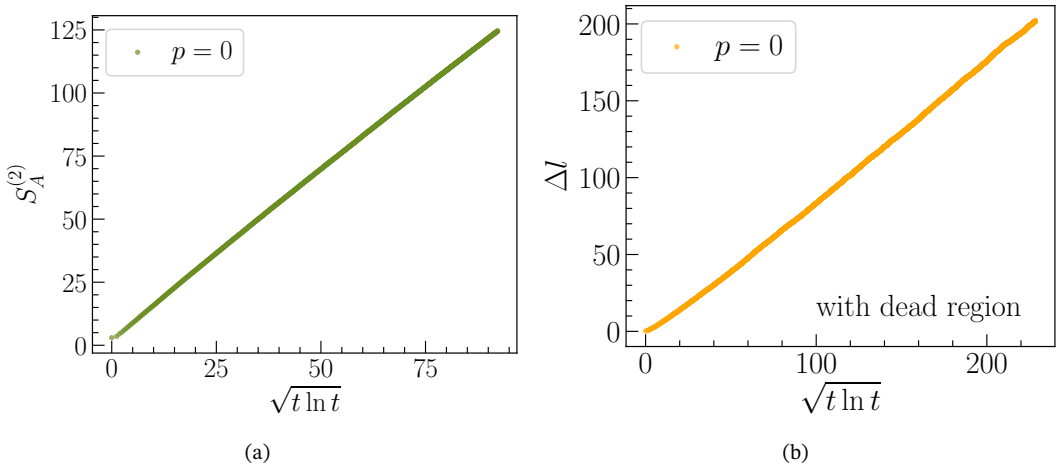

Figure 4.10: (a) $\overline{S_A^{(2)}(t)}$ of the SWAP model simulated using the stabilizer formalism. (b) The $\tilde{X}$ particle displacement $\overline{\Delta l(t)}$ of the slow modes. It is found that both $\overline{S_A^{(2)}(t)}$ and $\overline{\Delta l(t)}$ scale as $\sqrt{t \ln t}$. We take the system size $L = 600$ and $|\psi_0\rangle = |+x\rangle^{\otimes L}$ for (a) and the bit strings with dead regions with the charge filling $\nu_A = 1/3$ in subsystem A for (b).

[64]. We will only consider the unitary dynamics as the composite measurements can not be simulated by stabilizer formalism. As illustrated in Fig.4.9, we consider a circuit where each time step involves two layers of SWAP gates and CZ gates, with each applying on odd/even sites. To achieve enough randomness, we take the SWAP rate to be $p_u = 0.5 < 1$. In addition, we consider $|\psi_0\rangle = |+x\rangle^{\otimes L}$ as the initial state and take $L = 600$. As shown in Fig.4.10(a), the entanglement entropy grows diffusively with a logarithmic correction, i.e., $\overline{S_A^{(2)}} \propto \sqrt{t \ln t}$.

On the other hand, we examine the endpoint displacement $\overline{\Delta l(t)}$ of the bit strings with the dead region with a charge filling factor of $\nu_A = 1/3$. The numerics in Fig.4.10(b) indicates that $\overline{\Delta l(t)} \propto \sqrt{t \ln t}$ as well. This scaling can be explained by exactly mapping the spin dynamics of the SWAP model to the simple symmetric exclusion processes. In this process, each charge undertakes a symmetric random walk, while being prohibited from jumping to an already occupied site. It has been analytically shown in Ref. [88] that the position of the rightmost charge expands as $\sqrt{t \ln t}$.

It is worth noting that Clifford circuits with U(1) symmetry are highly restricted. For example, all Rényi entropies are equal for Clifford circuits, which fails to capture the ballistic growth of von Neumann entropy for generic U(1) symmetric random circuits. Nevertheless, the SWAP model enables us to verify at a large system size that the second Rényi entropy indeed saturates the upper bound in Eq. (4.1) and is dominated by rare slow modes with extensively long domains.

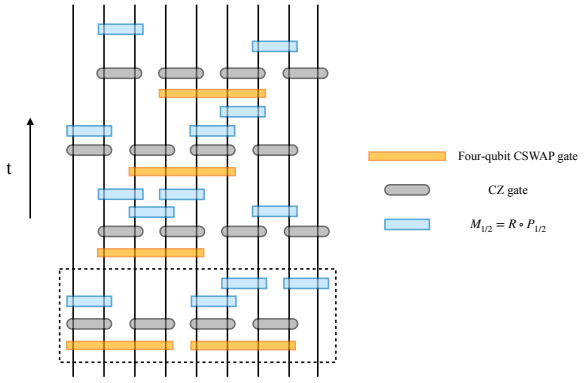

Figure 4.11: The arrangement of gates of the Four-qubit CSWAP model in a time step. The dashed box encloses the gates within a single layer. Each time step involves four layers of the four-qubit CSWAP gates with probability p_u, and CZ gates, interspersed with measurements with probability p.

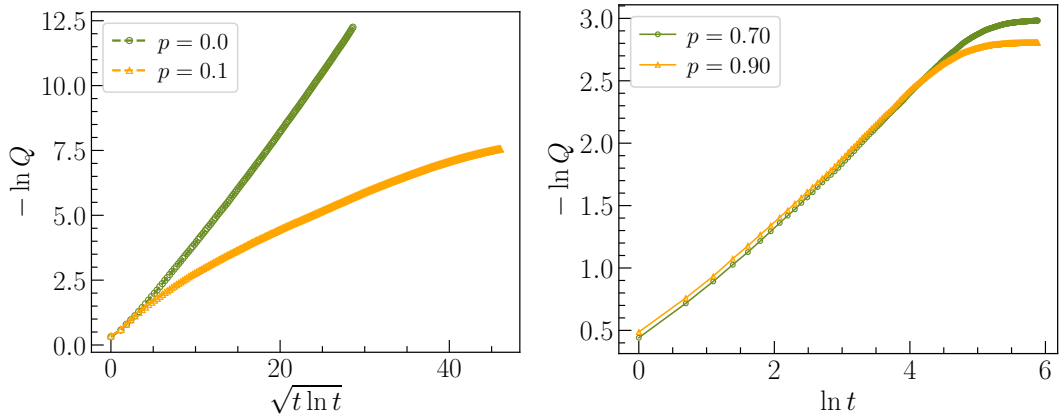

(a) (b)

Figure 4.12: $-\overline{\ln Q}$ of the Four-qubit CSWAP model at the measurement rate (a) $p = 0$ and $p = 0.1$, and (b) $p = 0.7$ and $p = 0.9$. We observe that $-\overline{\ln Q} \propto \sqrt{t \ln t}$ for (a) and $-\overline{\ln Q} \propto \ln t$ for (b). We take the system size $L = 120$, $p_u = 0.5$, and charge filling $\nu = 1/2$.

4.A.2 The Four-qubit CSWAP model

Now we consider the entanglement dynamics of the U(1) symmetric QA circuits with the kinetic constraint determined by a four-qubit gate, which swaps the spins σ_2 and σ_3 if the first spin $\sigma_1 = 0$ or the fourth spin $\sigma_4 = 1$. It is also called Fredkin gate in other works [87, 89], to distinguish it from the Fredkin gate in the main text, we call it the Four-qubit CSWAP gate. As shown in Fig.4.11, each time step of the circuit consists of four layers of gates under PBC and in each layer, the Four-qubit CSWAP gates are applied on sites $\{4j-3, 4j-2, 4j-1, 4j\}/\{4j-2, 4j-1, 4j, 4j+1\}/\{4j-1, 4j, 4j+1, 4j+2\}/\{4j, 4j+1, 4j+2, 4j+3\}$ for $j \in [1, L/4]$ with probability $p_u = 0.5$, and the CZ gates are applied on sites $\{2j-1, 2j\}/\{2j, 2j+1\}/\{2j-1, 2j\}/\{2j, 2j+1\}$, interspersed with composite measurements with probability p applied on both odd and even sites.

To simplify the numerical simulation, we can fix the position of $\tilde{Y}$ particle to be the boundary between subsystems

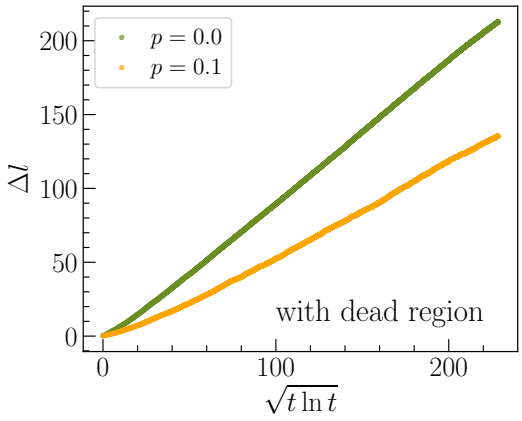

Figure 4.13: The endpoint displacement $\overline{\Delta l(t)}$ of the bit strings with the dead region of the Four-qubit CSWAP model vs $\sqrt{t \ln t}$ at $p = 0$ and $p = 0.1$. We take the system size $L = 600$, $p_u = 0.5$, and $\nu_A = 1/2$.

A and B. This is equivalent to focusing on the single species picture where there are only X particles and considering a subset of the phase difference in Eq. (**??**), i.e., the phase difference of $|n_1\rangle$ and $|n_1'\rangle$ restricted in regime B, denoted as

$$Q \equiv \frac{1}{M} \sum_{n_1, n_1'} e^{-i\Theta^B_{n_1'} + i\Theta^B_{n_1}}, \tag{4.22}$$

where M is the number of bit string pairs $\{|n_1\rangle, |n_1'\rangle\}$. With this approximation, the configurations which contribute to Q are those whose $\tilde{X}$ particles never reach the middle cut.

We numerically simulate $-\ln Q(t)$ for an ensemble of bit strings $\{|n_1\rangle, |n_1'\rangle\}$ with system size $L = 120$ and charge filling $\nu = 1/2$. As shown in Fig.4.12, there exists a similar phase transition from a volume-law phase to a critical phase: when $p < p_c$, $-\overline{\ln Q} \propto \sqrt{t \ln t}$, and when $p > p_c$, $-\overline{\ln Q} \propto \ln t$. We believe that this applies to $\overline{S_A^{(2)}(t)}$ as well.

Finally, we study the endpoint displacement $\Delta l(t)$ of the bit strings with the dead region evolved under the Four-qubit CSWAP gates. The numerics in Fig.4.13 confirms that $\overline{\Delta l} \propto \sqrt{t \ln t}$ for pure unitary dynamics and small measurement rate $p = 0.1$. We believe that this diffusive growth persists in the whole volume-law phase.

4.B Spin transport of hybrid QA circuits with U(1) symmetry

In this section, we consider the transport properties of the conserved charges which can be characterized by the spin correlation function

$$C(x, t) = \langle Z_x(t) Z_0(0) \rangle - \langle Z_x(t) \rangle \langle Z_0(0) \rangle, \tag{4.23}$$

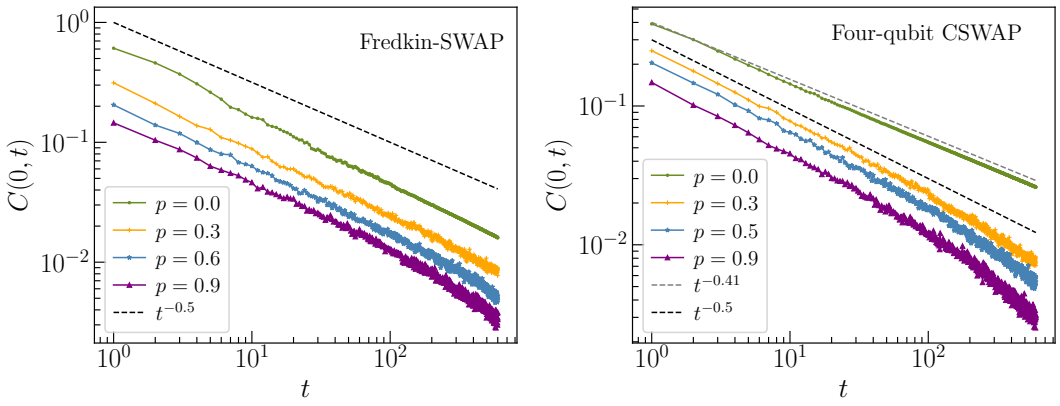

(a) (b)

Figure 4.14: The correlation function $C(0,t)$ of (a) the Fredkin-SWAP model and (b) the Four-qubit CSWAP model. We take the system size $L = 300$ and $p_u = 0.1$, $\nu = 1/3$ for (a), and $p_u = 0.5$, $\nu = 1/2$ for (b). It is found that for (a), $C(0,t) \propto t^{-0.5}$ for all p, and for (b), $C(0,t) \propto t^{-0.41}$ for $p = 0$ and $C(0,t) \propto t^{-0.5}$ for $p > 0$.

where site 0 is in the middle of the system. If we consider a charge-fixed state $|\psi_0\rangle = \frac{1}{\sqrt{N}} \sum_n |n\rangle$ with the filling factor ν, then the correlator of our QA circuit can be sampled using the classical bit strings via

$$\begin{aligned} C(x,t) &= \frac{1}{N}\sum_n \langle n|\tilde{U}_t^\dagger Z_x(0)\tilde{U}_t Z_0(0)|n\rangle - \frac{1}{N}\sum_n \langle n|\tilde{U}_t^\dagger Z_x(0)\tilde{U}_t|n\rangle \frac{1}{N}\sum_m \langle m|Z_0(0)|m\rangle \\ &= \frac{1}{N}\sum_n Z_{n(t),x} Z_{n,0} - \frac{1}{N^2}\sum_n Z_{n(t),x} \sum_m Z_{m,0}, \end{aligned} \tag{4.24}$$

where $Z_{n(t),x}$ is the spin value at site x of the bit string $|n(t)\rangle$ at time t. The correlation function for different system sizes can be collapsed onto the scaling form

$$C(x,t) = t^{-1/z} f(x/t^{1/z}). \tag{4.25}$$

Here we will only focus on the correlation in the time direction $C(0,t)$ for the Fredkin-SWAP model and the Four-qubit CSWAP model, and observe the dynamical exponents as we vary the measurement rate p.

As shown in Fig.4.14(a), for the Fredkin-SWAP model, $C(0,t) \propto t^{-1/z}$ with $z = 2$ for all p. The spin transport is diffusive with and without the measurements and hence fails to reflect the measurement-induced entanglement phase transition. This is because MIPTs are only visible in observables that are nonlinear in the density matrix. Similar diffusive dynamics is observed for all $p > 0$ in the Four-qubit CSWAP model, as shown in Fig.4.14(b). Interestingly, when $p = 0$, the dynamical exponent $z = 2.44 > 2$, consistent with $z = 8/3$ as discovered in previous literature [87, 89]. Nevertheless, the spin at the boundary of the extensively long domain still exhibits diffusive dynamics with a logarithmic correction.

Chapter 5

Entanglement Steering in Adaptive Circuits with Feedback

5.1 Introduction

Monitoring a quantum system can yield fascinating physics. The interplay between unitary dynamics and measurement creates an intriguing non-equilibrium phenomenon referred to as measurement-induced entanglement phase transitions (MIPTs) [26, 31, 25, 27, 30, 29]. In its most commonly explored setting, an initial unentangled state is evolved by a random quantum circuit subject to measurements at a rate p. Above (below) a critical rate p_c, the steady-state exhibits area-law (volume-law) entanglement scaling. To observe this transition, it is necessary to keep track of each individual quantum trajectory as the intrinsic randomness of measurement outcomes leads to the ensemble-averaged post-measurement state being a maximally mixed density matrix ($\rho \propto \mathbf{1}$) in the allowed Hilbert space. As a result, the MIPT remains invisible to the ensemble-averaged density matrix, presenting significant challenges for experimental observation, with only a few exceptions [90, 91, 92].

Despite these challenges, mid-circuit repeated measurements have become a valuable tool to create novel quantum phases dynamically. Recently, a new class of non-unitary dynamics has been proposed, where the outcome of a measurement can impact the dynamics themselves, leading to a non-trivial density matrix and stabilizing various quantum ordered phases through a feedback mechanism [57, 58, 59, 60, 61, 62].

In this chapter, we introduce a class of adaptive random circuits with feedback that exhibits phase transitions for both the quantum trajectory and the ensemble-averaged density matrix (i.e., quantum channel), as depicted schematically in Fig. 5.1. In addition to varying the measurement rate p, the post-measurement state is also locally corrected conditioned on the measurement outcome with a feedback rate $0 \leq r \leq 1$. The feedback is designed to "steer" the system towards particular final states. When $p \times r$ is large enough, the steady state is a mixture of two ferromagnetically ordered states instead of a maximally mixed state involving exponentially many configurations. Thus, there is an order-disorder phase transition in the quantum dynamics, which can be observed at the level of both quantum trajectory and quantum

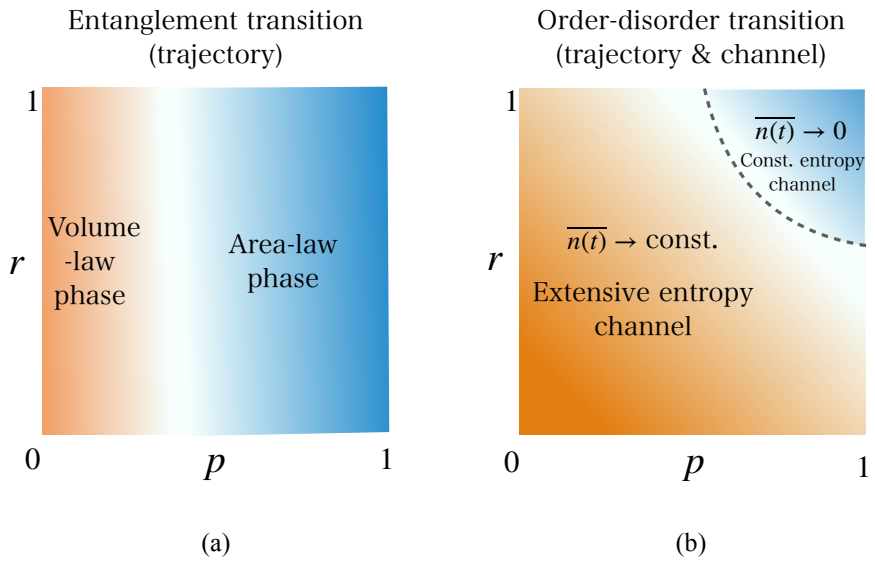

Figure 5.1: Schematic phase diagram illustrating (a) the entanglement phase transition for the individual quantum trajectories and (b) domain wall density transition as a function of the measurement rate p and feedback rate r. The transition in (b) also signals an entropy transition *at the level of quantum channel* (ensemble-averaged density matrix). The critical line in (b) belongs to the PC universality class and satisfies $p \times r = \text{const.}(\approx 0.55)$. The critical line in (a) is numerically upper bounded by $p_c^{EE} \leq 0.45$.

channel [59, 60]. A similar order-disorder transition has also been discussed recently in the context of dissipative phase transitions [93, 94]. However, we emphasize that the transitions discovered therein only exist in d-dimension with $d \geq 2$ or $1d$ systems with long-range interactions. Instead, by explicitly mapping the motion of domain walls to a classical branching-annihilating random walk (BAW) process, we show that the order-disorder phase transition in our adaptive circuit model belongs to the parity-conserving (PC) universality class which exists in $1d$ [41, 47, 48, 70]. Furthermore, the familiar MIPT is observed at the level of the quantum trajectory. Interestingly, we find that these two transitions typically occur at *different* critical measurement rates. Moreover, we show that the order-disorder phase transition can be probed experimentally from the measurement outcomes along the circuit evolution, and does not require post-selection.

5.2 Model

Our circuit model consists of three-qubit unitary gates and two-qubit measurements, as illustrated in Fig. 5.2. We take each three-qubit unitary gate to have a block structure: it leaves the basis states $|000\rangle$ and $|111\rangle$ unchanged up to a U(1) phase (forming blocks of size one), and acts as a Haar random unitary within the six-dimensional subspace spanned by $\{|001\rangle, |010\rangle, |100\rangle, |011\rangle, |101\rangle, |110\rangle\}$. We measure the product of Pauli-Z operators across a bond between two consecutive sites $Z_i Z_{i+1}$. Crucially, our construction includes *feedback*: if an "undesiredQQmeasurement outcome $Z_i Z_{i+1} = -1$ is obtained (meaning that the post-measurement state is $|01\rangle$ or $|10\rangle$), we apply a Pauli-X operator on either site with probability r to correct the state into $|00\rangle$ or $|11\rangle$; if the measurement outcome is +1, then no operator is applied. A set of measurements and corrections is implemented in two layers – first over odd and then even bonds.

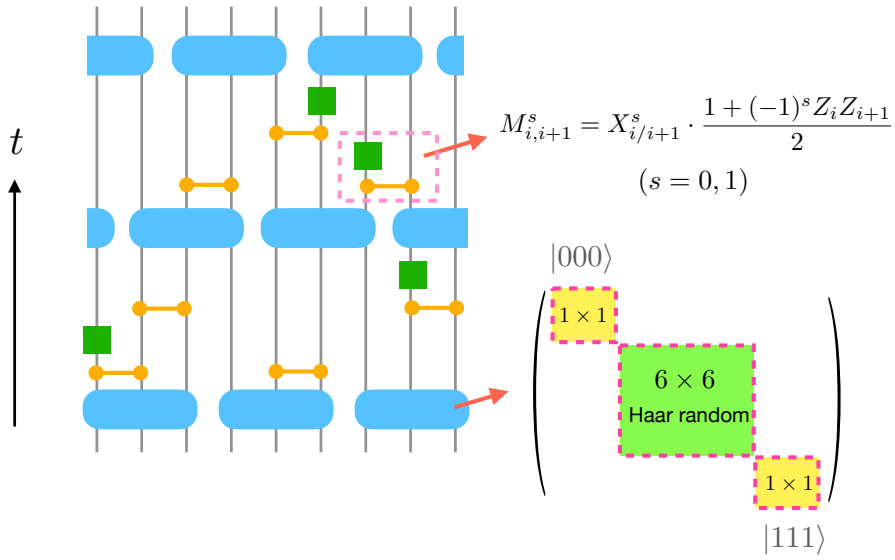

Figure 5.2: Setup of the adaptive circuit with feedback (one time unit). The circuit consists of three-qubit unitary gates (denoted by blue boxes) and two-qubit measurements (orange lines with dotted endpoints). The unitary gate leaves $|000\rangle$ and $|111\rangle$ unchanged, and acts as a Haar random unitary within the complementary subspace. If the measurement outcome $Z_i Z_{i+1} = -1$, a Pauli-X operator (green box) is applied on one site to correct the post-measurement state into $|11\rangle$ or $|00\rangle$. Each unit time step contains three layers of unitary gates related by translation by one site, and two sets of measurements. Each set consists of an even and an odd layer, forming a brickwork structure.

In each layer, measurements are made at a rate p per bond. Each unit time step contains three layers of unitary gates related by a translation by one site, interspersed with a set of measurements after each of the first and second, but not third, layers. Time evolution for each unnormalized quantum trajectory is thus given by:

$$\begin{aligned} |\psi(\{\boldsymbol{s}\}, T)\rangle &= \prod_{t=1}^{T} \left[U_3(t) M_2(t) U_2(t) M_1(t) U_1(t)\right] |\psi_0\rangle \\ &\equiv C(\{\boldsymbol{s}\})\, |\psi_0\rangle, \end{aligned} \tag{5.1}$$

where U_j denotes the j^{th} layer of unitary gates at each time step, $M_{1/2}$ denotes a set of measurements, and $\{\boldsymbol{s}\}$ records the full set of measurement outcomes along this particular trajectory.

Akin to previous studies on measurement-induced phase transitions in hybrid random circuits, we expect that there is an MIPT in our setup for individual quantum trajectories [Fig. 5.1(a)]. Upon increasing the measurement rate p, there is a transition in the time-evolved states (5.1) from a volume-law entangled phase to a weakly entangled area-law phase, where the spins almost point along the $\hat{z}$ direction. Without feedback ($r = 0$), each spin could randomly point along $\pm\hat{z}$ directions in each trajectory, depending on the measurement outcomes. Upon introducing feedback, the final states in all trajectories will approach a ferromagnetically ordered state $\alpha|00\ldots0\rangle + \beta|11\ldots1\rangle$, provided that the measurement and feedback rates are large enough. This indicates that besides the MIPT, the steady state also exhibits an order-disorder transition in a physical observable – the domain wall density – due to feedback [Fig. 5.1(b)][1]. Since the expectation value

[1] In our model, the steady state persists until a timescale $t \sim \text{poly}(L)$ with a power ≥ 2. For $t \sim \exp(L)$, the states will eventually approach a ferromagnetically ordered state, and both the entanglement and order-disorder phase transitions no longer exist.

of a physical observable is linear in the density matrix, the average domain wall density evaluated for the trajectories and the quantum channel (trajectory-averaged density matrix)

$$\rho = \sum_{\{\boldsymbol{s}\}} C(\{\boldsymbol{s}\})\, |\psi_0\rangle\langle\psi_0|\, C(\{\boldsymbol{s}\})^\dagger \tag{5.2}$$

are equivalent. Hence, this order-disorder transition can be observed both in the individual trajectories and the quantum channel.

5.3 Phase transition in the domain wall density

We demonstrate that there is indeed an order-disorder phase transition captured by the domain wall density by mapping the dynamics of domain walls under the hybrid circuit evolution to a classical stochastic process. We write the time-evolved wavefunction as a sum of world histories: $|\psi(t)\rangle = \sum_{\{m(\tau)\}} A(\{m(\tau)\})\, |m\rangle$, where $\{|m\rangle\}$ are bitstrings in the computational basis, and $A(\{m(\tau)\})$ is the amplitude of a particular world history $\{m(\tau)\}_{0\le\tau\le t}$. We consider each world history by constructing paths connecting bitstring configurations in the initial state to state at time t, as illustrated in Fig. 5.3(a)&(b).

Each individual path can be mapped to a classical stochastic process, which has a non-equilibrium phase transition. We denote the presence of each domain wall as a particle •, and the absence of which as an empty site ◦. The bitstring configuration is thus translated into one of particle occupations, as shown in Fig. 5.3(c). Under the action of unitary gates, the particles undergo two types of processes: $\bullet\circ\circ \leftrightarrow \bullet\bullet\bullet$ (branching), and diffusion. Under measurement, the particles can either diffuse: $\bullet\circ \leftrightarrow \circ\bullet$, or annihilate in pairs with probability $q \equiv pr$: $\bullet\bullet \to \circ\circ$. Combining these processes together, the particles perform BAW with an even number of offspring:

$$W \leftrightarrow 3W, \quad W + W \xrightarrow{q} \emptyset. \tag{5.3}$$

Since the parity of the total particle number is conserved, the classical dynamics described above belongs to the PC universality class, which has a continuous dynamical phase transition when the rate of particle annihilation exceeds a certain threshold [41, 47, 48, 70] [see the appendices for more details]. The two phases can be distinguished in terms of the average particle (domain wall) density in the steady state $n(t) = N(t)/L$.

For initial conditions with an extensive number of particles $N \propto L$, $n(t)$ saturates to a finite constant when $q < q_c$ after a finite amount of time. When $q > q_c$, $n(t) \sim t^{-1/2}$, and decays to zero at $t \sim L^2$ if the initial state has an even number of particles. At q_c, $n(t) \sim t^{-\theta}$ with a universal exponent $\theta = 0.286$ characteristic of PC universality class. For the initial condition with two adjacent particles, when $q < q_c$, the particle density grows linearly in time and saturates to a finite constant. At $q = q_c$, the particle density remains constant. When $q > q_c$, the particle density decays as $t^{-1/2}$. Therefore, our model exhibits an order-disorder phase transition at a critical effective measurement rate q_c. Below, we shall explicitly demonstrate both transitions depicted in Fig. 5.1 via numerical simulations of the hybrid circuit dynamics.

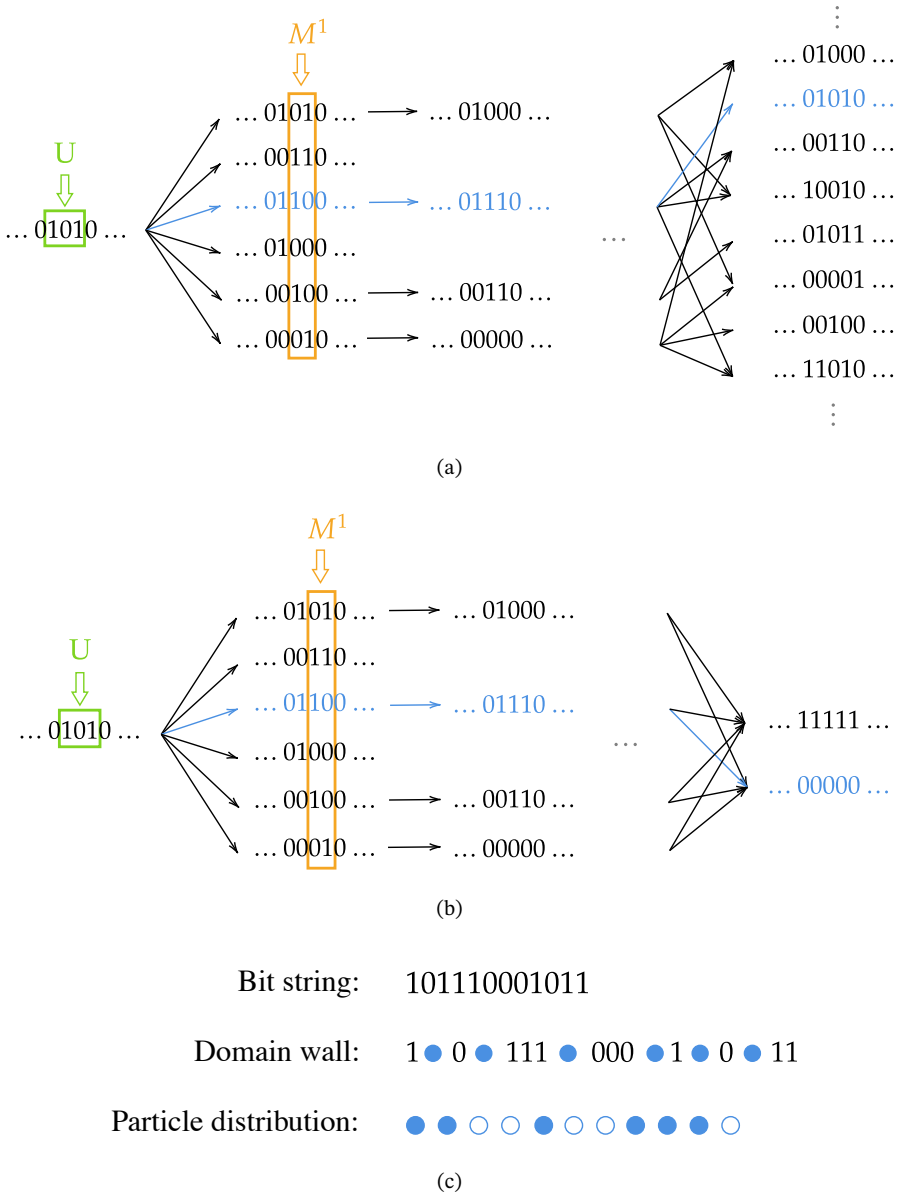

Figure 5.3: (a)&(b): Illustration of the bitstring dynamics in the quantum trajectory undergoing hybrid circuit evolution. The blue arrows indicate two representative paths ("world histories") of the bitstring dynamics. (a) When the measurement rate is small, the steady state involves exponentially many bistring configurations. (b) When the measurement rate is high, the steady state is spanned by two ordered bitstrings. (c) Mapping from a bitstring configuration to particle distribution, where a particle and an empty site represent the presence and absence of a domain wall, respectively.

5.4 Numerical results

In our simulations, initial states, which are product states in the computational basis, are evolved according to the setup in 5.2 with open boundary conditions. We record, at each time step, the second Rényi entropy $S_A^{(2)}(t) = -\log(\mathrm{tr}\rho_A^2)$, where ρ_A denotes the reduced density matrix of subsystem A composed of sites $1, 2 \ldots |A|$; $1 \leq |A| \leq \frac{L}{2}$, and the domain

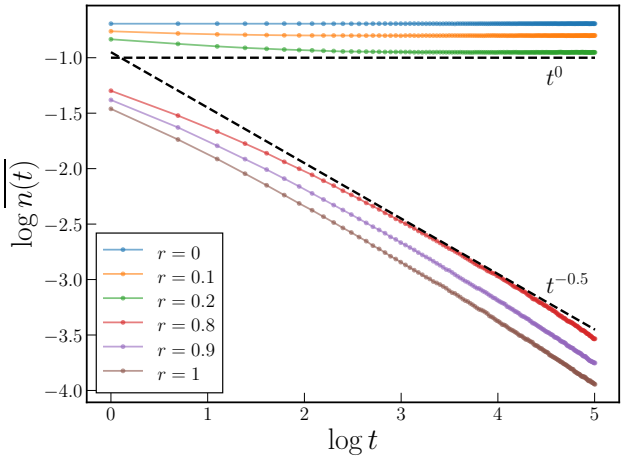

Figure 5.4: The trajectory-averaged domain wall density $\overline{n(t)}$ as a function of time, for different values of the feedback rate r while fixing $p = 1$, starting from random initial states. The result confirms the existence of two phases. Numerical simulations are performed for $L = 300$, and averaged over 10^4 realizations of circuits and initial states.

wall density

$$n(t) \equiv \frac{1}{L-1} \sum_{i=1}^{L-1} \frac{1 - Z_i Z_{i+1}}{2}_t . \tag{5.4}$$

We then compute the trajectory-averaged second Rényi entropy $\overline{S_A^{(2)}(t)}$ and domain wall density $\overline{n(t)}$. It is worth noting that in experimental platforms, the determination of $\overline{n}$ does not require an extra step; the measurement outcomes for any $p > 0$ provide an accurate sampling of $n(t)$. Our simulations are performed using the ITensor Julia package [95, 96] based on a matrix product state representation of the time-evolved wavefunctions.

We first set $p = 1$, and study $\overline{n(t)}$ as r is varied (along the right boundary of Fig. 5.1). Since the system is expected to be in the area-law phase, this serves as a benchmark to observe the order-disorder phase transition as revealed by the domain wall density $\overline{n(t)}$. Starting from a random state with $n(t = 0) \approx \frac{1}{2}$, we find clear evidence that the steady state is area law entangled and is independent of r (data not shown). Further study of $\overline{n(t)}$ indicates that when $r \lesssim 0.2$, $\overline{n(t)}$ saturates to a finite constant at long times; on the other hand, when $r \gtrsim 0.8$, $\overline{n(t)} \sim t^{-1/2}$ as shown in Fig. 5.4. This indicates the existence of two phases within the area-law entangled phase, distinguished by $\overline{n(t)}$. However, owing to finite-size effects, $\overline{n(t)}$ appears to decay with a continuously varying exponent (i.e. $n(t) \sim t^{-\theta_{n_0=0.5}(r)}$) for $0.2 \lesssim r \lesssim 0.8$, which makes identifying the critical r_c difficult. Instead, we consider an initial state with two neighboring domain walls centered in the lattice. Again, $n(t) \sim t^{\theta_{N_0=2}(r)}$ with a continuously varying exponent in the intermediate regime, but the critical point r_c is determined by the rate r at which $\overline{n(t)} \sim \text{const.}$ (or equivalently, when $\theta_{N_0=2}(r_c) \approx 0$ and changes sign). Using this criterion, we find that $r_c \approx 0.55$ in 5.5(a).

Next, we study the dynamics upon varying p, while fixing $r = 1$ (along the top boundary of Fig. 5.1). In this case, we expect to observe an entanglement phase transition *and* a transition in $\overline{n(t)}$. In Fig. 5.5(b), we find an order-disorder transition as revealed by $\overline{n(t)}$ at $p_c^n \approx 0.55$. In fact, we find, by considering various values of p and r, that the order-

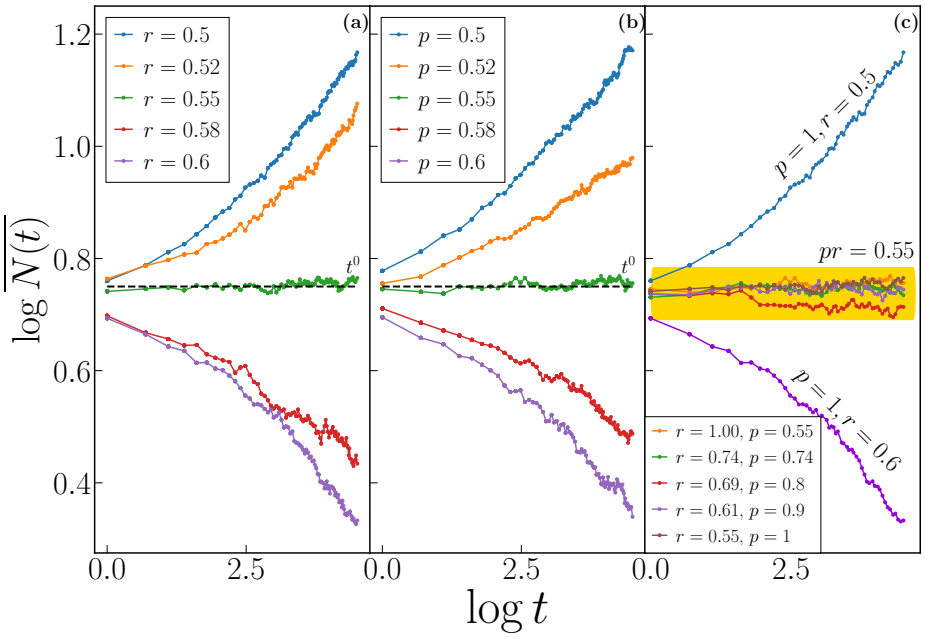

Figure 5.5: The averaged number of domain walls $\overline{N(t)}$ starting from an initial state with two domain walls. (a) For $p = 1$, the exponent θ as in $\overline{n(t)} \sim t^\theta$ changes sign at $r_c \approx 0.55$. (b) For $r = 1$, $p_c^n \approx 0.55$. (c) Demonstration that the order-disorder transition in $\overline{n(t)}$ is governed by a single parameter $q \equiv pr$.

disorder transition in our system is controlled by a single parameter $q \equiv pr$, and happens at $q_c \approx 0.55$ (see Fig. 5.5(c)), confirming our mapping to a classical BAW process in Fig. 5.3. An interesting question that naturally arises is whether the location of the order-disorder transition in $\overline{n(t)}$ coincides with that of the MIPT.

The computational resources required to simulate the system increase exponentially as one nears the critical point p_c^{EE} of the MIPT from above. Nonetheless, we provide strong evidence that these two transitions happen at *different* points in our system. As we further lower p such that $p < p_c^n \approx 0.55$, we find that the system remains in the area-law entangled phase despite a finite domain wall density, as is demonstrated by the scaling of $\overline{S_A^{(2)}}$ with subsystem size in Fig. 5.6(a). In appendices, we provide a heuristic argument based on the correlation length to explain why these two transitions in general should be different. We thus conclude that the critical point for the MIPT $p_c^{EE} < p_c^n$. This is also consistent with the general expectation that the entanglement transition for the individual trajectories must precede that for the quantum channel, if there is one.

5.5 Discussion

The physics discussed in this work remains unchanged if the 3-qubit unitary gates are replaced by k-qubit unitary gates ($k > 3$) which leave $\underbrace{|00\ldots0\rangle}_{k}$ and $\underbrace{|11\ldots1\rangle}_{k}$ invariant (up to a $U(1)$ phase) and act as Haar random unitaries within the remaining $(2^k - 2)$-dimensional subspace. When $k = 2$, however, the local unitary gates coincide with those for a $U(1)$-symmetric Haar random circuit. As a result, the particles can only spread out diffusively rather than ballistically and hence cannot compete with any non-zero rate of particle annihilations induced by feedback. $\overline{n(t)}$ always decays as

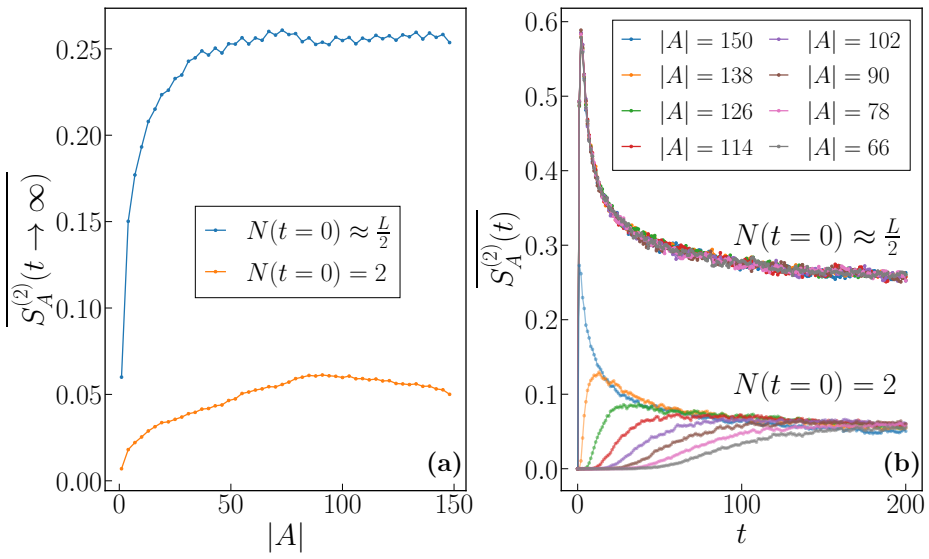

Figure 5.6: (a) The steady state entanglement entropy remains independent of subsystem size, regardless of the initial state. (b) The difference in the early time growth visualized across different initial conditions and subsystem sizes. In both figures, $p = 0.45 < p_c^n$ and $r = 1$.

$t^{-1/2}$ for any $q > 0$; there is *no* MIPT and individual trajectories are immediately driven to an area-law entangled phase. This is in sharp contrast to $U(1)$-symmetric hybrid circuits without feedback, where an MIPT is present [86].

In this work, we have argued that the two transitions – MIPTs and order-disorder transitions – are generally unrelated. As we increase r, the difference between p_c^{EE} and p_c^n becomes smaller but remains finite when $r = 1$. In appendices, we consider models in which the essential physics is unchanged, but the difference between these two transitions is more pronounced. This is in contrast to a free fermion system subject to non-unitary dynamics with feedback that was recently studied in Ref. [60]. It remains to be seen if models with interactions can exhibit these transitions at the same point, while a broader understanding of the conditions that can facilitate this coincidence of these transitions is desirable.

We conclude by commenting on the experimental realizability of the order-disorder transition, spurred by the recent implementation of adaptive quantum circuits with high fidelity [62, 61]. Overhead can be drastically reduced by estimating $\overline{n(t)}$ from measurement outcomes obtained over the course of the circuit evolution, instead of preparing the states at different times and then separately performing measurements. Furthermore, we numerically find that this transition is robust to imperfect rotations in the feedback and decoherence, but susceptible to other types of noise.

Note Added.— Shortly after our paper appeared on the arXiv, we became aware of an independent work where similar results were obtained in a different setup [97].

Acknowledgement.— We thank Sebastian Diehl for explaining the results of Ref. [60], and Ehud Altman for useful discussions. This research is supported in part by the Google Research Scholar Program and is supported in part by the National Science Foundation under Grant No. DMR-2219735. Z.-C.Y. is supported by a startup fund at Peking University. We gratefully acknowledge computing resources from Research Services at Boston College and the assistance provided by Wei Qiu.

5.A Particle density transition of the classical bit-string dynamics

Inspired by the quantum dynamics under the hybrid circuit with feedback, we proposed a classical stochastic process that traces the dynamics of the bit strings in the quantum state shown in Fig. 3. Under the 3-site unitary gates, the bit string either stays invariant if there are no domain walls or is mapped to another bit string within the ensemble $\{|001\rangle, |010\rangle, |100\rangle, |011\rangle, |101\rangle, |110\rangle\}$ with equal probability. On the other hand, when the measured sites have opposite spins, the Pauli-X operator rotates either spin and kills a pair of domain-walls (a pair of neighboring particles) with probability r. Since the measurement rate is p, this leads to an effective annihilation rate $q \equiv pr$. Therefore the domain-wall particles either diffuse, branch or annihilate in pairs. This is often referred to as branching-annihilating random walks (BAW) with even offspring,

$$W \leftrightarrow 3W, \quad W + W \xrightarrow{q} \emptyset. \tag{5.5}$$

BAW models with even offspring usually experience an absorbing phase transition that belongs to parity-conserving (PC) universality class, which is characterized by the additional symmetry that preserves the parity of the number of particles in the system.

In this appendix, through investigating the domain-wall particle density transition of three different circuit setups, *i.e.*, hybrid circuits with one/two/three sets of measurements with probability q per time step, we will show that our classical bit-string model belongs to PC universality class. We consider two initial conditions which lead to different scaling behaviors in the particle density under the same dynamics: (a) the seeding process beginning with a pair of adjacent domain-wall particles, and (b) the purification process beginning with a randomly occupied state (*i.e.*, a random bit-string).

The numerical results are shown in Fig. 5.7. We vary the annihilation rate q and calculate the scaling behavior of the mean domain-wall particle density $\overline{n(t)} \equiv \overline{N(t)}/L$, where $\overline{N(t)}$ is the mean domain-wall particle number and L is the system size. We find that except for the model with one layer of measurements per time step, the rest of the setups all experience a phase transition while adjusting q. For the purification process beginning with a random bit string state, when $q < q_c$, the system stays at an active steady state with a finite particle density. When $q = q_c$, $\overline{n(t)} \sim t^{-\theta}$ with $\theta = 0.286$. When $q > q_c$, the particles perform annihilation-dominated BAW and the particle density decays diffusively, i.e., $\overline{n(t)} \sim t^{-1/2}$. For the seeding process starting with a pair of adjacent domain-wall particles, despite the finite-size effect, when $q < q_c$, the system approaches an active state. At $q = q_c$, $\overline{n(t)} \sim t^{\delta}$ with $\delta = 0$. When $q > q_c$, $\overline{n(t)}$ still decreases diffusively (not shown in the plot). These exponents are universal and agree with the numerical findings of the PC universality class that $\theta = 0.286$, $\delta = 0$ for $q = q_c$, and $z = 2$ for $q > q_c$.

The two different initial conditions also help us to pin down the critical point. We do find that for $L = 300$, the bit-string model with one layer of measurements has a critical point $q_c = 0.99$. However, this is very close to $q = 1$ which is probably due to the finite size effect. Hence, we claim that the case with only one set of measurements per time step doesn't have a phase transition. For models with two and three sets of measurements per time step, the critical points are $q_c = 0.55$ and $q_c = 0.37$ respectively, which agree with the corresponding q_c's found via direct simulations of the

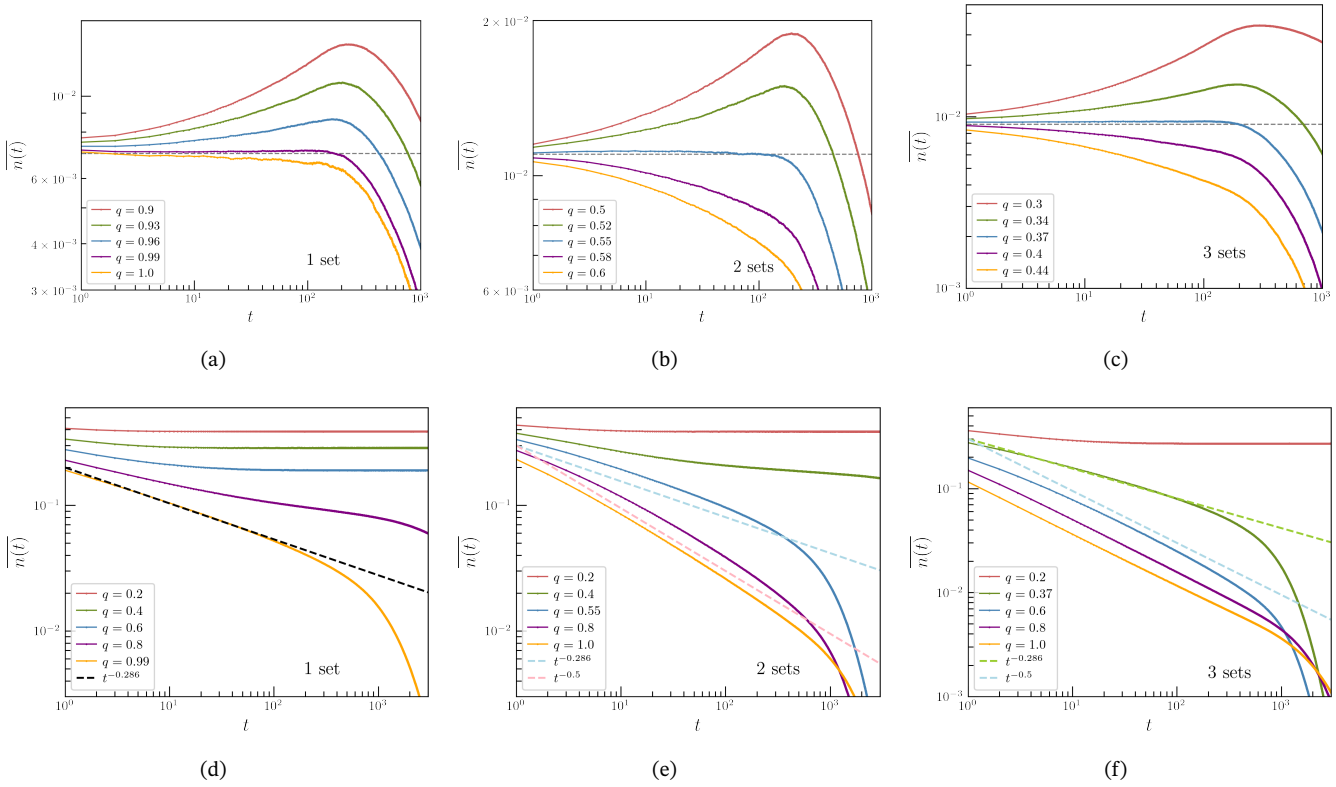

Figure 5.7: We simulate the domain-wall particle density $\overline{n(t)}$ of the bit-string model with one set of measurements in (a) and (c), two sets of measurements in (b) and (e), and three sets of measurements in (c) and (f). Among them, (a), (b), and (c) are the results of the seeding process starting with a pair of adjacent particles, (d), (e), and (f) are the results of the purification process starting with a random state. All of the data are computed for system size $L = 300$ under open boundary condition (OBC) over a variety of measurement rates q, and we plot $\overline{n(t)}$ vs t on a log-log scale.

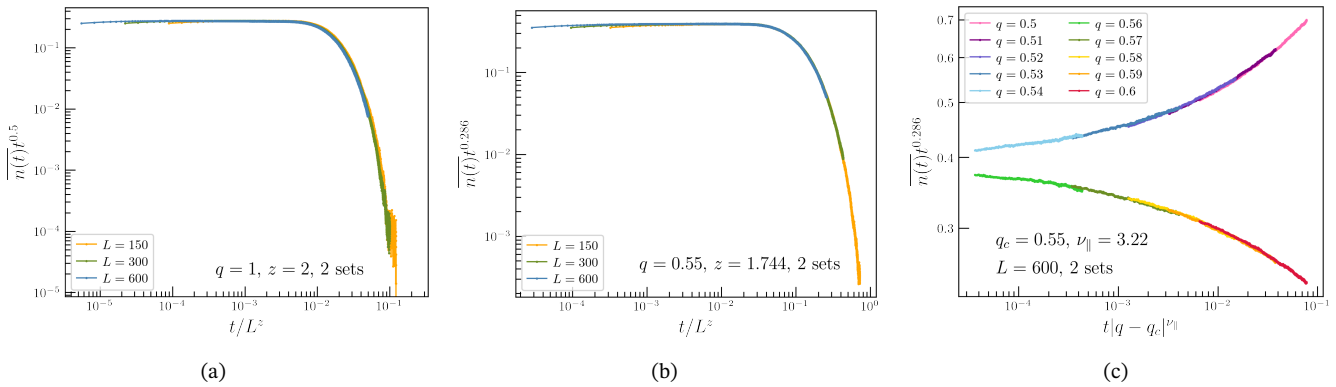

Figure 5.8: Finite-size data collapse of the domain-wall particle density $\overline{n(t)}$ of the classical bit-string model with two sets of measurements for different system sizes at (a) $q = 1$, and (b) $q = q_c = 0.55$, respectively. (c) Data collapse using the scaling form Eq. (5.6), for $|q - q_c| = 0.01, 0.02, \ldots, 0.05$ at $L = 600$ for $t \in [100, 1200]$. We use periodic boundary condition (PBC) for numerical simulations.

circuit evolution.

In addition, we have performed a detailed finite-size scaling analysis of the domain wall density of the purification

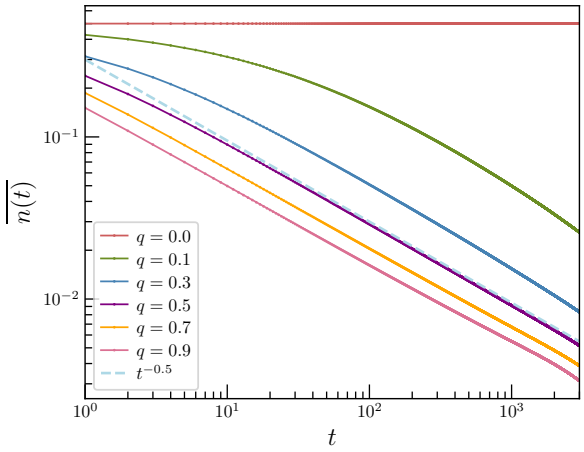

Figure 5.9: The particle density $\overline{n(t)}$ vs t plotted on a log-log scale for the purification process under the circuit with two sets of 2-site unitary gates and two sets of measurements with probability q per unit time step. When $q = 0$, $\overline{n(t)}$ does not decay with time. Once $q > 0$, the particle density decays as $\overline{n(t)} \sim t^{-1/2}$. All of the data are collected for system size $L = 300$ under OBC.

process in the vicinity of the critical point. We expect that the domain wall density satisfies the following scaling form:

$$n(t, q) = t^{-\theta} f(t/L^z, |q - q_c|t^{1/\nu_\parallel}), \tag{5.6}$$

where $z^{PC} = 1.744$ at the critical point $q_c = 0.55$ and $\nu_\parallel^{PC} = 3.22$ [47]. As shown in Fig.5.8(b) and 5.8(c), we find excellent agreement with the above scaling form using known exponents of the PC universality class. We have also examined the data collapse in the critical phase where $z^{PC} = 2$ for $q > q_c$ in Fig.5.8(a). This further confirms that our model belongs to the PC universality class.

Finally, we consider replacing the 3-site unitary gates with 2-site unitary gates, which keep the bit strings $\{|11\rangle, |00\rangle\}$ unchanged and map the bit strings with domain walls randomly within the ensemble $\{|10\rangle, |01\rangle\}$. The $U(1)$ symmetry imposed by the 2-site unitary gates preserves the total spin and the domain-wall particles propagate diffusively, which is too weak to compete with the particle annihilation due to measurements. Therefore, there is no particle density phase transition and we have $\overline{n(t)} \sim t^{-1/2}$ for any $q > 0$. This is verified by Fig.5.9 in which we simulate $\overline{n(t)}$ of the purification process with two sets of 2-site unitaries interspersed with two sets of measurements per unit time.

5.B Results with 1 set of measurements

In this section, we present results for the set-up where the feedback scheme is implemented with only 1 set of measurements per time step, *after* all 3 layers of unitary gates have been applied. As in the classical model, the transition in n appears to occur extremely close to $pr = 1$, rendering the observation of the ordered phase unfeasible, owing to finite-size effects. The transition points r_c and p_c^n are estimated as in the main text, by identifying the values of r and p at which $\overline{n(t)}$ does not change with time, beginning from an initial state with 2 adjacent domain walls in the center of the chain. It is found that when $p = 1$, $r_c \approx 0.99$, and $p_c^n \approx 0.99$ when $r = 1$.

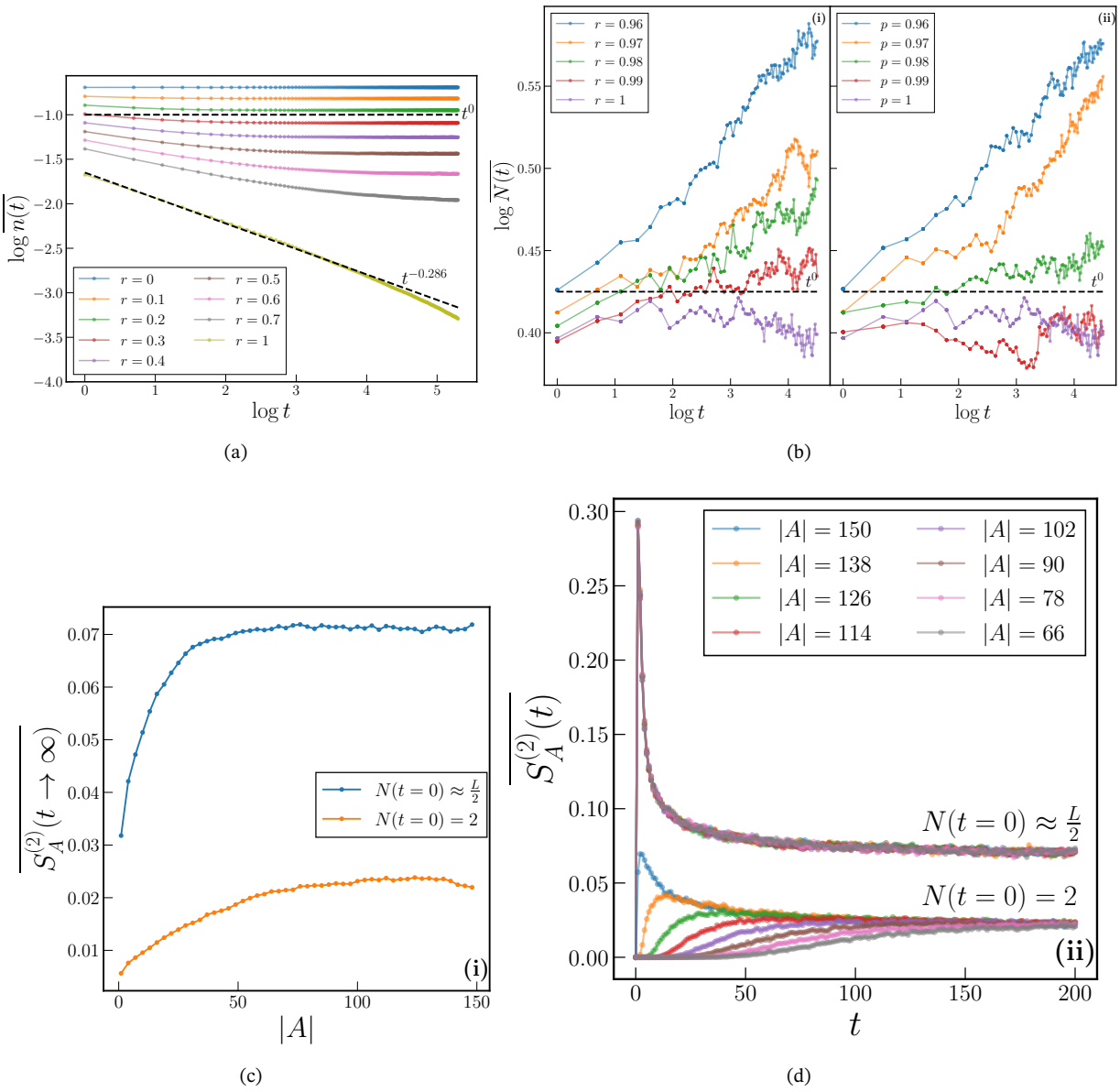

Figure 5.10: Numerically obtained results for the quantum model with 1 set of measurements after 3 layers of unitary gates, for $L = 300$, and results averaged over 2×10^4 realizations. (a) The domain wall density n at $p = 1$, showing a critical scaling of $\overline{n(t)} \approx t^{-0.286}$ near $r \approx 1$. The steady state domain wall density appears finite for $r \lesssim 0.5$, but finite size effects prevail for $r \gtrsim 0.7$. (b) The number of domain walls, beginning from an initial state with two adjacent domain walls in the center of the system. The data affords an estimation of $q_c^n \approx 0.99$. (i) $p = 1$ and (ii) $r = 1$. (c) The steady state entanglement scaling for $r = 1, p = 0.8 < p_c^n$. The entanglement satisfies area law scaling and shows a slight dependence on the initial condition. (d) The entanglement dynamics for two different initial states for $r = 1, p = 0.8 < p_c^n$. For $N(t = 0) = 2$, the two domain walls are located close to the center.

We find that $p_c^{EE} < p_c^n$ in this case as well. The characteristic dependence of the entanglement growth on the initial state is also present here, since the entangling unitary gates act trivially on large parts of the system when considering initial conditions with a vanishing *density* of domain walls. These results provide compelling evidence that (a) the two transitions are indeed different and (b) The qualitative features of this family of adaptive quantum circuits are largely in-

sensitive to the microscopic details of the circuit. These conclusions strengthen, and are strengthened by, the connection to the classical dynamics.

5.C Effects of Imperfect Circuits

We were initially motivated by strategies that could facilitate the realization of the measurement-induced phase transition in present-day NISQ-era quantum devices. In this spirit, we study the effects that noise might have on the different dynamical phenomena we observe. In particular, we consider (i) the effects of imperfect corrective rotations and (ii) the role of decoherence.

5.C.1 Imperfect Corrective Rotations

Our set-up involves measuring the operator $Z_i Z_{i+1}$ on neighboring sites, which can result in the outcomes ± 1. If the outcome -1 is observed, then, with probability r, either the qubit at location i or at $i+1$ is rotated by π about the X-axis. We account for imperfections in this process by considering noisy, imperfect rotations of the form

$$\begin{aligned} R_{\epsilon,i,t} &= e^{-i\theta_{\epsilon,i,t}X} \\ \theta_{\epsilon,i,t} &\equiv \frac{\pi}{2}\left(1+\epsilon\tilde{x}_{i,t}\right) \end{aligned} \tag{5.7}$$

where $\tilde{x}$ is a random number independently drawn from $[-1,1]$ at each time t and site i when a corrective rotation is to be applied. ϵ dictates the strength of the noise. The results are presented in 5.11.

The transition still persists even in the presence of noise. We see that the effect of the noise in the rotation angle is to merely renormalize the rate r at which errors are corrected. The renormalized value can be explicitly obtained by considering the bit-string picture. We fix $p = 1$ so that the feedback rate is solely controlled by r. In the absence of any noise ($\epsilon = 0$), upon finding an outcome of $Z_i Z_{i+1} = -1$, there are two possible scenarios -

$$Z_i Z_{i+1}{}_{a.m.} = \begin{cases} +1, & \text{with probability } r \\ -1, & \text{with probability } 1-r \end{cases} \tag{5.8}$$

($a.m.$ denotes "after measurement"). When $\epsilon \neq 0$, it will be helpful to write (with the i,t labels suppressed) $R_\epsilon = \cos\theta_\epsilon + iX\sin\theta_\epsilon$. Assuming the correction occurs at site i, 5.8 is modified to give

$$Z_i Z_{i+1}{}_{a.m.} = \begin{cases} R_\epsilon^\dagger Z_i R_\epsilon Z_{i+1}{}_{a.m.}, & \text{with probability } r \\ -1, & \text{with probability } 1-r \end{cases} \tag{5.9}$$

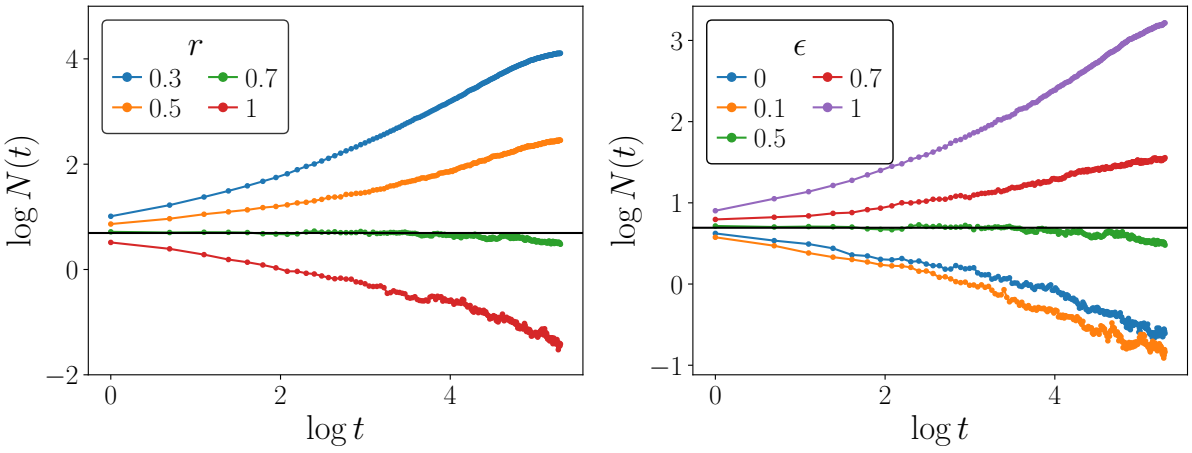

(a) (b)

Figure 5.11: The effects of imperfect rotations on the domain wall density, shown only to have the effect of renormalizing r as given in 5.12. Simulations are performed on $L = 300$ spins, starting with a pair of adjacent domain walls in the center of the chain, and averaged over 2×10^3 realizations. $r_c \approx 0.55$ in the absence of noise. (a) r is varied, holding $\epsilon = 0.5$ fixed. The critical r shifts downward to $r_c(\epsilon = 0.55) \approx 0.7$. (b) With r fixed at $r = 0.7$, a transition between the two dynamical phases is driven by tuning the strength of the noise ϵ.

We can further expand $R_\epsilon^\dagger Z_i R_\epsilon Z_{i+1}$ as

$$\begin{aligned} \cos^2(\theta_\epsilon) Z_i Z_{i+1} = -1_{a.m.} - \sin^2(\theta_\epsilon) Z_i Z_{i+1} = +1_{a.m.} \\ = \sin^2(\frac{\pi\epsilon\tilde{x}}{2})(-1) + \cos^2(\frac{\pi\epsilon\tilde{x}}{2})(+1). \end{aligned} \tag{5.10}$$

Since the measurements are frequent and we expect $Z_i Z_{i+1}$ to have a definite value, we can interpret the result of 5.10 as a stochastic process with the update rule

$$R_\epsilon^\dagger Z_i R_\epsilon Z_{i+1}{}_{a.m.} = \begin{cases} -1, & \text{with probability } \sin^2 \frac{\pi\epsilon\tilde{x}}{2} \\ +1, & \text{with probability } \cos^2 \frac{\pi\epsilon\tilde{x}}{2} \end{cases} \tag{5.11}$$

Combining **??**, we finally have

$$Z_i Z_{i+1}{}_{a.m.} = \begin{cases} +1, & \text{with probability } r\cos^2(\frac{\pi\epsilon\tilde{x}}{2}) \\ -1, & \text{with probability } 1 - r + r\sin^2(\frac{\pi\epsilon\tilde{x}}{2}). \end{cases} \tag{5.12}$$

By averaging over $\tilde{x}$, we arrive at an expression for the renormalized value of r

$$r_{\text{renorm}} = \frac{r}{2}(1 + \frac{\sin(\pi\epsilon)}{\pi\epsilon}). \tag{5.13}$$

We can use 5.13 to calculate the r_c as a function of ϵ for the case with 2 layers of measurements. We know from numerical simulations that $r_{c,renorm} \approx 0.55$ which implies $r_c(\epsilon) \approx \frac{1.1}{1+\frac{\sin(\pi\epsilon)}{\pi\epsilon}}$. Specifically, for $\epsilon = 0.5$, we find that

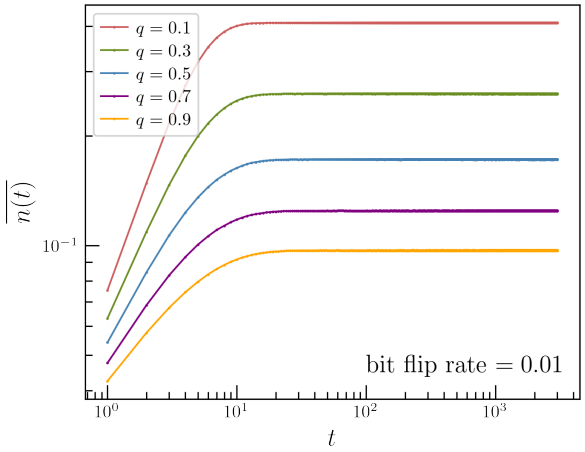

Figure 5.12: The particle density $\overline{n(t)}$ vs t for the seeding process starting with a pair of particles under bit flip errors with an error rate of 0.01. The circuit contains three sets of measurements with each set followed by a layer of random bit flip errors. There is a finite particle density in this case even at large q, which indicates that the absorbing state transition is unstable to bit-flip errors. Numerical simulations are performed for system size $L = 300$ under OBC.

$r_c \approx 0.68$, which is in agreement with what we find in 5.11(a).

5.C.2 Effects of Decoherence

Since present-day quantum computing platforms are not perfectly isolated from the environment, there is a natural decay of coherence. One way of modeling this decoherence is to consider the depolarizing channel [98], which is defined for a density matrix ρ as

$$\mathcal{E}(\rho) = (1-b)\rho + b\frac{\mathbb{1}}{D} \tag{5.14}$$

where $D = \mathrm{Tr}\mathbb{1}$ is the dimension of the Hilbert space under consideration, and $0 \leq b \leq 1$ represents an "error rate". ρ can refer to the density matrix of any part of the system (or the system in its entirety). In our case, we investigate the robustness of the absorbing phase transition to the effects of a depolarizing channel acting randomly on any qubit in the system. This can be implemented directly in the classical model by flipping each bit independently at a fixed rate. As shown in Fig. 5.12, for the seeding process starting with a pair of particles, even a tiny error rate of 0.01 leads to a finite particle density in the steady state for large q. Therefore, the absorbing state transition is unstable to the presence of depolarizing noise.

5.C.3 Effects of Off-Diagonal Dephasing

The final error we consider is that of the loss of coherence in the off-diagonal elements of the density matrix. Since both the ZZ measurements and the domain wall density n share a basis, and are both diagonal in the computational basis, we do not expect this dephasing to have an impact on the observation of the order-disorder transition.

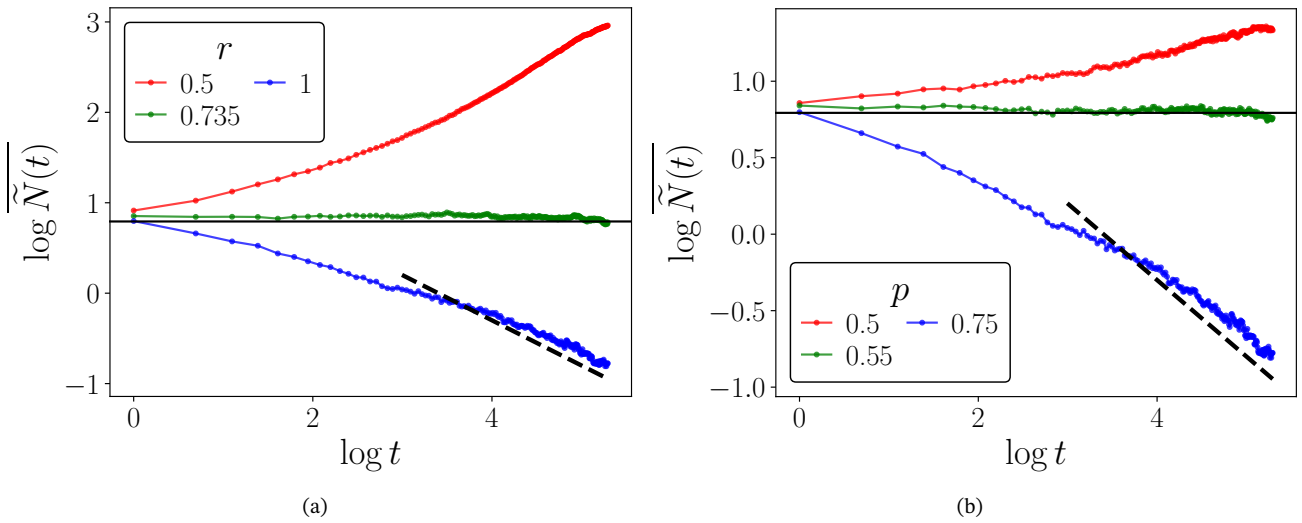

(a) (b)

Figure 5.13: The estimated number of domain walls $\widetilde{\overline{N}}$, as obtained from the sampling procedure detailed in Sec. IV, plotted for different values of (a) the feedback rate r, with $p = 0.75$ and (b) the measurement probability p, with $r = 1$. The dashed line denotes diffusive decay $\widetilde{N} \sim t^{-0.5}$. In both cases, this estimator reflects the order-disorder transition at the same value of $p \times r = q_c \approx 0.55$, where $\widetilde{N(t)} \sim t^0$ at the critical point, when starting from an initial condition with 2 adjacent domain walls at the center of the chain.

5.D Sampling Protocol

In this section, we elaborate on our proposal for obtaining the averaged domain wall density $\overline{n(t)}$. Recall that the definition of n is

$$n \equiv \sum_{j=1}^{L-1} \frac{1 - Z_j Z_{j+1}}{2}. \tag{5.15}$$

The protocol also involves measuring $Z_j Z_{j+1}$ (and applying feedback at some rate r), first for odd and then even j after a layer of random unitaries. In numerical simulations, we were able to directly calculate $\frac{1-Z_j Z_{j+1}}{2}$ without any additional steps. However, in practical experiments, one would have to first prepare a state and then perform several measurements in order to estimate the expectation value of $Z_j Z_{j+1}$, which a priori poses a large overhead. Since our protocol involves measurements of this operator, we can utilize these outcomes to estimate n.

For concreteness, we consider the set-up with 2 sets of measurements, one each after the first and second layers of random unitaries, but not the third. At each time step, the outcomes of the last set of measurements are recorded. Let the number of measurements at this time-step be N_m, and the measurement outcomes be $m_i{}_{i=1}^{N_m}$ with $m_i = \pm 1$. $N_m \leq (L-1)$ and on average, $N_m = p(L-1)$. The quantity $\widetilde{\overline{n}}$, defined as

$$\widetilde{n} \equiv \frac{1}{N_m} \sum_{i=1}^{N_m} \frac{1 - m_i}{2} \tag{5.16}$$

averaged over trajectories and circuit realizations, provides an accurate sampling of the true domain wall density $\overline{n}$. The

reason for this is that at any $p > 0$, an extensive number of measurements are still being made. We can straightforwardly obtain an estimate for the number of domain walls $\overline{\widetilde{N}}$ as $\overline{\widetilde{N}} \equiv (L-1) * \overline{\widetilde{n}}$. As shown in 5.13, the number of domain walls obtained from this sampling procedure $\overline{\widetilde{N}}$ captures the order-disorder transition, and agrees well with the true value of $\overline{n}$.

5.E Heuristic argument of the difference between entanglement transition and steering transition

When $r > r_c$, as we tune p, the quantum trajectory undergoes two transitions: the entanglement phase transition at p_c^{EE} and the steering (domain wall density) phase transition at p_c^n. First, it is easy to show that $p_c^{EE} \leq p_c^n$ in the steady state $|\psi\rangle$. This is because when $p > p_c^n$, $|\psi\rangle$ is spanned by $|00\ldots0\rangle$ and $|11\ldots1\rangle$ and the entanglement entropy S_A for a subsystem A is smaller than $\log 2$.

According to previous studies on the $1+1d$ measurement induced entanglement phase transition, we expect that when $p \geq p_c^{EE}$[25, 31],

$$S_A = \begin{cases} \log L_A, & L_A < \xi \\ \log \xi, & L_A > \xi \end{cases} \tag{5.17}$$

where ξ is the correlation length for the entanglement measure and diverges at $p = p_c^{EE}$. When p is slightly larger than p_c^{EE}, the correlation length is still quite large with $\log \xi > \log 2$. Increasing p will reduce ξ and eventually when p is large enough, we have $\log \xi < \log 2$. This implies that there is a finite separation between p_c^{EE} and p_c^n.

The difference between p_c^{EE} and p_c^n is more obvious in higher dimensional systems with spatial dimension $d > 1$. As we vary p, the entanglement entropy exhibits three different scaling behaviors. Here we consider a simple case where the subsystem A is d-dimensional sphere with radius L_A. The leading term of the entanglement entropy satisfies:

$$S_A : \begin{cases} \sim L_A^d, & p < p_c^{EE} \\ \sim L_A^{d-1}, & p_c^{EE} < p < p_c^n \\ < \log 2, & p > p_c^n. \end{cases} \tag{5.18}$$

5.F Simulation of the Volume-Law Phase

Lastly, we address the technical and conceptual difficulties with obtaining an accurate estimate of p_c^{EE}. The challenges are two-fold – (i) The rapidly burgeoning entanglement entropy as we approach the critical point or enter the volume law phase renders MPS methods (which are designed for states with low entanglement) computationally costly, and (ii) our specific family of models are particularly prone to finite-size effects owing to the absorbing nature of the steady state.

The volume-law phase of general (i.e. non Clifford [64]) non-unitary circuits requires exponential resources and is

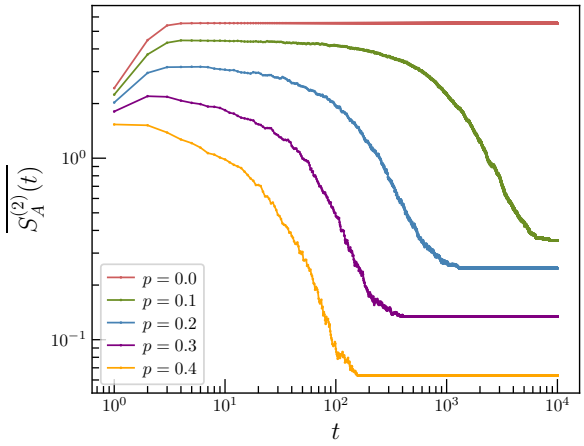

Figure 5.14: The entanglement entropy $\overline{S_A^{(2)}(t)}$ vs t plotted on a log-log scale using the exact diagonalization of the quantum trajectory under the circuit with two sets of measurements per unit time step over a variety of measurement rate p. All of the data are collected for system size $L = 18$ and feedback rate $r = 1$ under PBC.

difficult to simulate on classical computers. The exact diagonalization (ED) technique, commonly used to study the volume law phase, can only deal with small systems with $L \lesssim 30$. The detrimental effects of the resulting finite-size effects are especially germane to our system. In such a small system, if $q = p \times r > 0$, under BAW dynamics, any state with a finite density of domain walls quickly evolves to states with no domain walls $\{|0\cdots0\rangle, |1\cdots1\rangle\}$. The absorbing phase transition is no longer observable, since any initial configuration decays to the absorbing state. Consequently, since $p_c^{EE} < p_c^n$, the entanglement phase transition cannot be observed either in a small system with finite r. As shown in Fig. 5.14, the entanglement entropy calculated using ED for system size $L = 18$ with an initial product state polarized in the $+x$ direction shows a strong finite size effect and decays to a finite constant quickly for all $p > 0, r = 1$. This rapid decay obviates the usage of both the volume law scaling of the steady-state entanglement entropy $S_A^{(n)}(t \to \infty) \sim |A|$ and its linear growth at early times $S_A^{(n)}(t) \sim t$ as diagnostics for the volume law phase.

However, in a large system, we can observe an absorbing phase transition. In such a system, we can use the inefficacy of MPS methods in simulating states with large entanglement to obtain an upper bound on p_c^{EE} (i.e. when the infamous “exponential wall" has been encountered and the bond dimension grows too large to store the state on a classical computer). For the model with two sets of measurements, we find that the upper bound for p_c^{EE} is 0.45.

Chapter 6

Exponentially slow thermalization and the robustness of Hilbert space fragmentation

6.1 Introduction

A central theme in quantum dynamics is the understanding of mechanisms which impede or arrest thermalization [1, 2, 4, 5, 6]. Many such mechanisms, most prominently many body localization [7, 8], rely crucially on some form of spatial disorder. A recent body of work has demonstrated that even without recourse to strong disorder, the imposition of certain dynamical constraints can be rigorously shown to prevent thermalization [9, 10, 11, 12, 13, 14, 15, 16, 17, 18, 19, 20, 21, 22, 23]. In these systems, thermalization is evaded by virtue of the dynamics being non-ergodic, with the space of product states splitting into exponentially many dynamically-disconnected "fragments", in a phenomenon known as *Hilbert space fragmentation* (HSF).

Unfortunately, this form of ergodicity breaking relies on fine-tuning the dynamics to ensure that the dynamical constraints leading to HSF are exactly obeyed. What happens when the constraints are weakly broken is a relatively unexplored question, despite the fact that many experimental systems are close to fine-tuned points where the constraints are exact [99, 100, 101, 102, 103, 104, 105]. A natural question thus remains: how does the structure of HSF imprint itself on thermalization dynamics once its associated constraints are broken? In particular, can there exist models of constrained dynamics which display anomalous thermalization even in the presence of constraint-breaking, ergodicity-restoring perturbations?

In this work, we answer this question affirmatively by studying what happens when a 1d spin chain with "pair-flip" constraints is connected at its end to a chain undergoing generic unconstrained dynamics (Fig. 6.1 a). The coupling to the unconstrained system can be veiwed as a coupling to a thermal bath, and it renders the dynamics fully ergodic. Naively, one might expect the bath to initiate a thermalizing "avalanche" that spreads out and thermalizes the constrained region on the time scale needed for the influence of the bath to be felt across the system, viz. on a time of order L_{cons}, where L_{cons} is the size of the constrained region. We show that this intuition is in fact false, and that the thermalization time

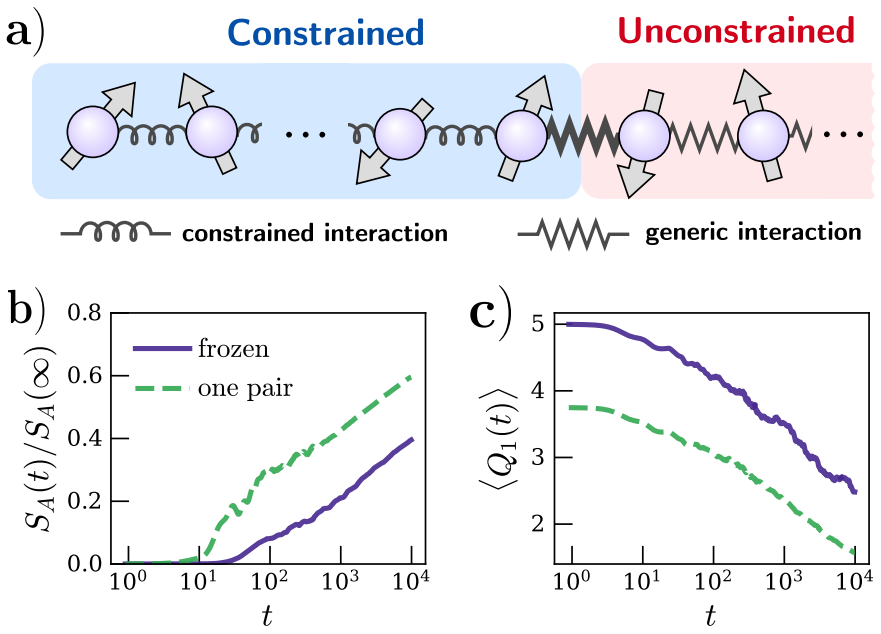

Figure 6.1: **a)** A schematic of the setup considered in this paper: a 1d chain is partitioned into a constrained region at sites $1 < i \leq L_{\rm cons}$ within which the dynamics is fragmented, and an unconstrained region at sites $L_{\rm cons} < i \leq L$ where the dynamics is generic. **b)** Growth of the normalized entanglement entropy for a quench from under Hamiltonian dynamics, calculated for the region $A = [1, L/2]$ with $L_{\rm cons} = 8, L = 10, N = 3$. The solid line shows a quench from the frozen state $|12\rangle^{\otimes L/2}$; for the dashed line the first site is changed to 2, creating a single flippable pair. In both cases, a slow logarithmic growth is observed. **c)** Relaxation of the charge Q_1 computed in region A for the same initial state, showing a similarly slow decay.

$t_{\rm th}$ instead scales *exponentially* in $L_{\rm cons}$. This slowness is due to strong bottlenecks that the system encounters as it tries to explore Hilbert space, a phenomenon which arises from the type of constraints and the local nature of the coupling to the bath. We rigorously prove an exponentially large lower bound on $t_{\rm th}$ in the setting where the system undergoes a constrained form of random unitary (RU) dynamics, and provide numerical evidence that $t_{\rm th}$ for Hamiltonian dynamics is similarly long. Remarkably, the long approach to equilibrium can be diagnosed simply by measuring expectation values of certain local operators, which take exponentially long to reach their steady-state values.

6.2 Slow thermalization in the pair-flip model:

We begin by studying Hamiltonian dynamics. We consider a spin-$(N-1)/2$ model of the form $H = H_0 + H_{\rm imp}$. Here the constrained Hamiltonian H_0 takes the form

$$H_0 = \sum_{i=1}^{L-1} \sum_{a,b=1}^{N} g_i^{a,b} |aa\rangle\langle bb|_{i,i+1}, \tag{6.1}$$

with g_i arbitrary $N \times N$ Hermitian matrices. The "impurity" Hamiltonian $H_{\rm imp}$ acts to break the constraints on sites $L_{\rm cons} < i \leq L$, with $L_{\rm cons}$ the size of the constrained region. H_0 only flips neighboring spins with identical values. As a

result, it preserves the $U(1)$ charges

$$Q_a \equiv \sum_i (-1)^i |a\rangle\langle a|_i. \tag{6.2}$$

When $N > 2$, which we will specify to unless explicitly noted otherwise, H_0 additionally possesses an exponentially large number of non-local conserved quantities [106]. Among these are the $N(N-1)^{L-1}$ "frozen" states of the form $|a_1, \ldots, a_L\rangle$, $a_i \neq a_{i+1}$, which are annihilated by H_0. We will denote the space spanned by these states as $\mathcal{H}_{\text{froz}}$.

To numerically study the robustness of the constrained dynamics with respect to H_{imp}, we investigate quantum quenches performed on initial states in $\mathcal{H}_{\text{froz}}$. For concreteness we will specify to the case where $g_i^{ab} = (-1)^i(1/N + \kappa\delta_{a,b})$; here the $(-1)^i$ ensures that the states in $\mathcal{H}_{\text{froz}}$ lie approximately in the middle of H_0's spectrum (since for this choice of g_i^{ab}, H_0 is an alternating-sign sum of frustration free projectors that annihilate $\mathcal{H}_{\text{froz}}$). The model obtained by setting $\kappa = 0$ is a form of Temperley-Lieb model [107, 108], which has $SU(N)$ symmetry, fragments in an entangled basis [109], and possesses a very large number of degenerate states. In Sec. 6.6 we prove that this model fails to thermalize even at infinite times when the constraint is broken only on a single site. In our numerics we will however fix $\kappa = 2/3$, breaking $SU(N)$ and yielding a more generic pair-flip model. For H_{imp}, we take for definiteness

$$H_{\text{imp}} = \mathcal{N}^{-1} \sum_{i=L_{\text{cons}}+1}^{L} (e^{i\pi/4} X_i + e^{-i\pi/4} X_i^T), \tag{6.3}$$

where $X_i \equiv \sum_{a=1}^{N} |a\rangle\langle[a+1]_N|_i$ with $[\cdot]_N$ denoting reduction modulo N, and with $\mathcal{N}$ ensuring that each term in H_{imp} has unit norm. This choice fully restores ergodicity, and can be numerically checked to render the spectrum of H completely non-degenerate.

Since states in $\mathcal{H}_{\text{froz}}$ are near the middle of H's spectrum, energy conservation does not present an obstacle for states in $\mathcal{H}_{\text{froz}}$ to thermalize to infinite temperature, even when the size of the impurity region is small. Furthermore, as we will see momentarily, only $O(L)$ applications of H_{imp} are required to connect any two computational basis product states. From these facts, a reasonable prior would be that states in $\mathcal{H}_{\text{froz}}$ rapidly thermalize to a volume-law infinite-temperature state, with this occurring on the time scale needed for the influence of H_{imp} to propagate throughout the full extent of the constrained region. Simulating the dynamics with TEBD for the simplest choice of $N = 3$ reveals that this is *not* what happens. In Fig. 6.1 we compute the bipartite entanglement entropy $S_A(t)$, with $A = [1, L_{\text{cons}}/2]$ half of the constrained region, together with the charge expectation values $\langle Q_a \rangle$, with Q_a computed on the sites $[1, L_{\text{cons}}]$ of the constrained region. Both of these quantities indicate an *exponentially* long thermalization time, with $S_A(t)$ exhibiting a slow logarithmic growth and $\langle Q_a \rangle$ a similarly slow decay. Slow thermalization is also observed for initial product states which are mostly frozen but contain a small number of flippable nearest-neighbor pairs; for these states $S_A(t)$ increases quickly at short times $t \lesssim L$ but then grows as $\sim \log(t)$ thereafter.

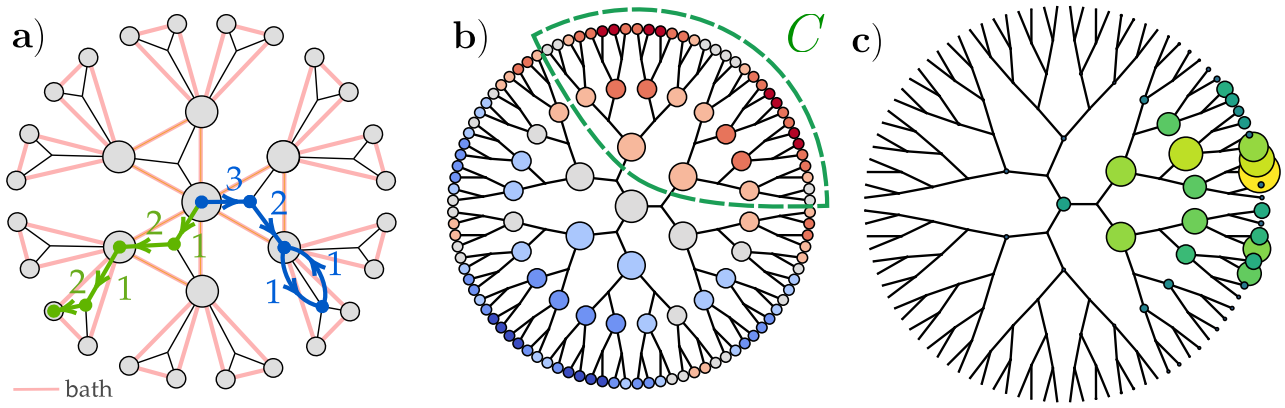

Figure 6.2: Krylov graph illustrations for $N = 3$. **a)** Each computational basis product state $|a_1, \ldots, a_L\rangle$ defines a length-L walk on the degree 3 tree, with the walk backtracking when two identical labels are encountered in a row. The constrained dynamics preserves walk endpoints (grey circles), each of which defines a Krylov sector; the sectors are thus enumerated by the even (odd) sublattice of the depth-L tree for even (odd) L. Paths which reach the edge of the tree are frozen under the constrained dynamics, while those with backtracks belong to sectors of dimension > 1. Breaking the constraints at the edge induces transitions between next-nearest-neighbor tree vertices in the manner indicated by the pink lines. **b)** Values of the charge Q_1 in each sector (shown for $L = 6$). Redder (bluer) colors indicate more positive (negative) values. Dynamics begun from a state in the region C will take exponentially long to escape C due to the bottleneck imposed by the tree structure. **c)** Krylov sector occupations for a quench under e^{-iHt}, starting from a frozen state on the edge of the tree. Circle sizes and colors are drawn according to $\langle\psi(t)|\Pi_{\mathcal{K}}|\psi(t)\rangle$ at time $t = 10^3$, where $\Pi_{\mathcal{K}}$ projects onto the sector $\mathcal{K}$.

6.3 Hilbert space connectivity and random walks

To understand these observations, it will be helpful to have a geometric understanding of how the dynamics acts in Hilbert space. To best illustrate this we will momentarily fix $L = L_{\text{cons}} + 1$, so that the pair-flip constraint is broken only on the last site of the chain. This understanding is obtained by associating each product state $|a_1, \ldots, a_L\rangle$ with a length-L walk on the N-valent tree T_N. The walk is determined by reading the product state from left to right: a_1 determines the direction of the first step of the walk, a_2 the second, and so on. The direction of the walk's travel is fixed by the convention that if two identical labels are encountered in a row ($a_i = a_{i+1}$), the walk backtracks (see Fig. 6.2 a for an illustration with $N = 3$). The merit of this is that the allowed processes implementable by H_0 are precisely those which *preserve walk endpoints*, since H_0 acts nontrivially only on locations with backtracks. Each vertex of T_N (more precisely, each vertex of T_N's even / odd sublattice, depending on the parity of L) thus defines a disconnected sector of the constrained dynamics. The sectors on the edge of T_N contain precisely those states whose walks have no backtracks; these states thus span $\mathcal{H}_{\text{froz}}$ and define $O((N-1)^L)$ one-dimensional sectors. As shown in [110], the sectors increase exponentially in size towards the center of the tree, with the largest sector at the tree center having dimension $|\mathcal{K}_{\max}| \sim L^{3/2}(2\sqrt{N-1})^L$.

The action of H_{imp} at the chain end breaks the constraint by allowing the *last step* of the walk to be changed. This restores ergodicity, connecting the sectors to their nearest neighbors on one sublattice of T_N, in the manner shown in Fig. 6.2 a. We will refer to the graph $G_{\mathcal{K}}$ of Krylov sectors so obtained as the *Krylov graph*. The dynamics thus induces a random walk on $G_{\mathcal{K}}$, and for a system to thermalize, its wavefunction must spread out across the entirety of $G_{\mathcal{K}}$ under

the action of this walk.

The tree structure of the Krylov graph suggests that this spreading is slow, since for a vertex of T_N at depth $1 < d < L$, there are $N-1$ ways of going "out" towards the boundary, but only one way of going "in" towards the center. This implies that a simple random walk on T_N will have an "outward" bias with velocity $v_N = (N-1)/N - 1/N = 1 - 2/N$, and suggests that the dynamics on $G_{\mathcal{K}}$ will take exponentially long to overcome this bias and thermalize. However, this argument ignores the fact that the sectors increase exponentially in size as one moves towards the center of $G_{\mathcal{K}}$, which introduces an opposing "inward" bias. Our main goal in the following will be to understand which one of these competing effects dominates.

As a first pass, one can quench a state in $\mathcal{H}_{\text{froz}}$ under e^{-iHt} and numerically compute the weight of $|\psi(t)\rangle$ in each sector. Doing so gives weights which are highly clustered around $G_{\mathcal{K}}$'s edge even when $t \gg L$, as shown in Fig. 6.2 c. This suggests that the "outward" bias—which acts to slow thermalization—wins out. To understand why, we shift our focus from Hamiltonian to RU dynamics, where rigorous bounds on thermalization times can be proven.

6.4 RU dynamics and Hilbert space bottlenecks

To simplify the dynamics, we replace the unconstrained region by a thermal bath which subjects the spin on the end of the chain to depolarizing noise. This models the situation where the unconstrained region is taken to be infinitely large (so that it can exchange an arbitrary amount of energy with the constrained region), and then traced out. Since there is no conserved energy in this setup, we will replace time evolution under H_0 by a constrained form RU dynamics, consisting of local gates which preserve the pair-flip constraint but are otherwise Haar random. The quantum channel implementing one step of the dynamics is

$$\mathcal{C}_{\mathsf{d}}(\rho) = \mathcal{U}_{\mathsf{d}}^{\dagger}(\text{Tr}_L[\rho] \otimes \mathbf{1}/N)\mathcal{U}_{\mathsf{d}}, \tag{6.4}$$

where $\text{Tr}_L[\cdot]$ denotes tracing out the spin at site L, and $\mathcal{U}_{\mathsf{d}}$ is a random depth-d constrained brickwork circuit. In our analytic arguments we will take $\mathsf{d} \gg L$, which simplifies things by making the *intra*-sector dynamics thermalize instantaneously. Regardless of d, $\mathcal{C}_{\mathsf{d}}$ should generically thermalize product states *faster* than the Hamiltonian dynamics studied above. We will nevertheless prove that the thermalization time under $\mathcal{C}_{\mathsf{d}}$ is *exponentially long* in L. Detailed proofs of the statements to follow are deferred to the supplementary information [110]; in what follows we will only discuss the most salient aspects.

Let us first examine the circuit-averaged state $\bar{\rho}_\psi(t) \equiv \mathbb{E}_{\{\mathcal{U}\}}\, \mathcal{C}_{\mathsf{d}}^t(|\psi\rangle\langle\psi|)$ obtained by evolving a computational basis product state $|\psi\rangle$ for time t. Using by-now standard techniques [111, 112], the circuit average can be performed exactly, mapping the RU evolution to a certain kind of Markov process. One finds $\bar{\rho}_\psi(t) = |\mathcal{M}^t\psi\rangle\langle\mathcal{M}^t\psi|$, where $|\mathcal{M}^t\psi\rangle$ is the state obtained from $|\psi\rangle$ by t applications of a Markov generator of the form $\mathcal{M} = \mathcal{M}_{PF}\mathcal{M}_L$. In this expression $\mathcal{M}_L = \mathbf{1}_{L-1} \otimes \frac{1}{N}\sum_{a,b} |a\rangle\langle b|_L$ randomizes the state of the spin on the end of the chain, and $\mathcal{M}_{PF}$ is a depth-d stochastic brickwork circuit implementing pair-flip dynamics, each brick being the 2-site gate $\frac{1}{N}\sum_{a,b} |aa\rangle\langle bb| + \sum_{a\neq b} |ab\rangle\langle ab|$ (see [110] for details).

Let $G_{\mathcal{H}}$ be the graph with a vertex for each computational basis product state, and an edge drawn between all pairs of vertices connected by a single step of the dynamics. The Krylov graph $G_{\mathcal{K}}$ is thus a "coarse-grained" version of $G_{\mathcal{H}}$, obtained by gathering all states in a given sector into a single "supernode", and merging all connections between states in bath-connected sectors into a single "superedge". $\mathcal{M}$ implements a random walk on $G_{\mathcal{H}}$, with $\rho = \mathbf{1}$ as its unique steady state. Thus all initial states thermalize under $\mathcal{C}_{\mathsf{d}}$, provided one waits long enough. How long one must wait is determined by the relaxation time t_{rel}, which is inversely proportional to the spectral gap $\Delta_{\mathcal{M}}$ of $\mathcal{M}$. As a first result, we prove

Theorem 1. *$\Delta_{\mathcal{M}}$ is exponentially small in system size:*

$$\Delta_{\mathcal{M}} \leq |\mathcal{K}_{\max}| N^{-L} \sim L^{-3/2} \rho_N^L, \tag{6.5}$$

where $\rho_N \equiv 2\sqrt{N-1}/N < 1$ is the spectral radius of T_N.

This result follows from the fact that states evolving under $\mathcal{M}$ encounter severe bottlenecks as they move throughout Hilbert space. To see this, define the *expansion* $\Phi(G)$ of a graph G as [113]

$$\Phi(G) \equiv \min_{C\,:\,|C|\leq |G|/2} |\partial C|/|C|, \tag{6.6}$$

where $|\partial C|$ denotes the number of edges connecting the subgraph C to $G \setminus C$. Graphs with strong bottlenecks have smaller values of $\Phi(G)$, and random walks on graphs with strong bottlenecks mix slowly. This is quantified using Cheeger's inequality [113], which reads

$$\frac{1}{2}\Phi(G_{\mathcal{H}})^2 \leq \Delta_{\mathcal{M}} \leq 2\Phi(G_{\mathcal{H}}). \tag{6.7}$$

Since $G_{\mathcal{K}}$ is formed by coarse-graining $G_{\mathcal{H}}$, we have $\Phi(G_{\mathcal{H}}) \leq \Phi(G_{\mathcal{K}})$, provided that $|\partial C|$ ($|C|$) in (6.6) are appropriately weighted by the sizes of the superedges (supernodes). The upper bound in (6.5) then follows by letting C be one full branch of the tree (shown in Fig. 6.2 b for $N = 3$), for which $|\partial C| \sim |\mathcal{K}_{\max}|$ and $|C| \sim N^L/N$. This gives an upper bound on $\Phi(G_{\mathcal{K}})$—and hence on $\Delta_{\mathcal{M}}$—scaling as $|\mathcal{K}_{\max}|/N^L$, which is exponentially small in L (exact diagonalization indicates that this bound is in fact saturated [110]). This demonstrates the existence of a large bottleneck and shows that the "outward" bias discussed above ultimately wins out at long times (the effect of the "inward" bias turns out to be to reduce the base of the exponential in (6.5) from $1/N$ to ρ_N).

An initial state $|\psi\rangle$ chosen randomly from C will thus typically take an exponentially long time to leave C, immediately yielding a bound on the circuit-averaged entropy $\overline{S}_\psi(t) = \mathbb{E}_{\{\mathcal{U}\}}\, S[\mathcal{C}_{\mathsf{d}}^t(|\psi\rangle\langle\psi|)]$. To this end, define $t_S(\gamma) \equiv \min\{t\,:\, \overline{S}_\psi(t) \geq \gamma L \ln(N)\}$ as the time at which $\overline{S}_\psi(t)$ first reaches a fraction γ of its maximal value. We find

Theorem 2. *Let γ satisfy $\gamma_* < \gamma < 1$, $\gamma_* \equiv 2(1 - v_N \ln(N-1)/\ln N)$. Then*

$$t_S(\gamma) \geq C_\gamma \sqrt{L} e^{L\lambda_\gamma}, \tag{6.8}$$

where C_γ is an unimportant $O(1)$ constant and $\lambda_\gamma \equiv \frac{1}{2}((1-\gamma/2)\ln(N)/\ln(N-1) - v_N)^2$.

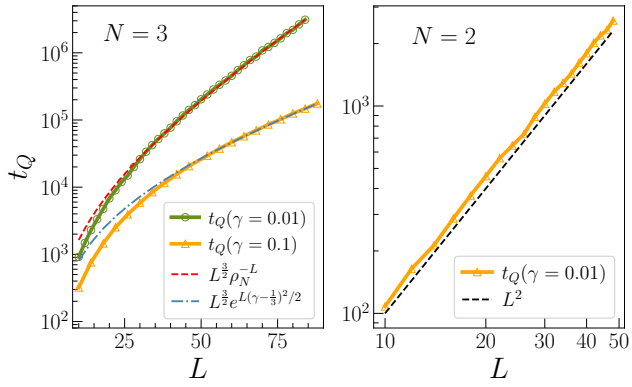

Figure 6.3: The charge relaxation time t_Q for the maximal-Q_1 initial state $|\psi(0)\rangle = |21\rangle^{\otimes L/2}$. *Left:* Slow charge relaxation for $N = 3$: t_Q for $\gamma = 0.1$ and $\gamma = 0.01$. The former fits well to L times the bound in (6.9) (blue dot-dashed line), while the latter saturates the $\gamma \to 0$ bound of $\sim 1/\Phi(G_{\mathcal{H}})$ (red dashed line). *Right:* Fast relaxation for $N = 2$: t_Q on a log-log scale, showing clear diffusive behavior.

This indicates that when initialized from a typical computational basis product state, the system rapidly reaches an entropy of $S_* = \gamma_* L \ln N$, but that after reaching S_* the entropy growth slows dramatically, taking exponentially long to fully saturate. This can be understood by appealing to the biased random walk introduced above, which implies that almost all product states are located at a depth near $d_* = v_N L$. A state initialized on the boundary of $G_{\mathcal{K}}$ may rapidly move inwards to a depth of d_* (during which the "inward" bias dominates), but then gets "stuck" at d_*, where the number of states is largest (and where the "outward" bias now dominates).

Remarkably, the small gap (6.5) imprints itself in the expectation values of the charges $Q_a \in [-L/2, L/2]$, despite the fact that expectation values of local operators do not allow one to distinguish different Krylov sectors. This occurs because the pattern of values that Q_a takes on different sectors is strongly anisotropic across $G_{\mathcal{K}}$, as illustrated in Fig. 6.2 b. The exponential smallness of $\Phi(G_{\mathcal{H}})$ means that the charge of a generic product state will also take exponentially long to relax. The upshot of this is that similarly to Thm. 2, we can bound $t_Q(\gamma)$, the time for $\langle Q_a(t)\rangle$ to drop below $\gamma L/2$ when initialized in a state $|\psi_{\max}\rangle$ of maximal Q_a charge, as follows:

Theorem 3. *Let γ satisfy $0 < \gamma < v_N/2$. Then when $\gamma = \Theta(L^0)$,*

$$t_Q(\gamma) \geq D_\gamma \sqrt{L} e^{L(2\gamma - v_N)^2/2} \tag{6.9}$$

where D_γ is another unimportant $O(1)$ constant. In the $\gamma \to 0$ limit, $t_Q(\gamma) \geq D_\gamma/\Phi(G_{\mathcal{H}})$.

The above theorems were all stated for the case of $N > 2$. When $N = 2$, the constrained dynamics is not strongly fragmented: it instead possesses only $O(L)$ sectors, the largest of which has a dimension smaller than 2^L by only a factor of $1/\sqrt{L}$. These sectors are connected by the bath to form a 2-valent tree (i.e. a line), yielding $\Phi(G_{\mathcal{H}}) \sim 1/\sqrt{L}$. The $N = 2$ dynamics thus possesses only a weak bottleneck, and thermalizes exponentially faster than the $N \geq 3$ models.

These results are corroborated in Fig. 6.3 by numerically simulating charge relaxation in the classical stochastic model defined by $\mathcal{M}$. In these simulations we fix the depth of each RU brickwork layer at $\mathsf{d} = 2$, constraining the intra-sector

dynamics by spatial locality. On general grounds we expect this to decrease $\Delta_{\mathcal{M}}$ by a factor of L^{-1}, so that Cheeger's inequality for $N = 2$ reads $L^{-2} \lesssim \Delta_{\mathcal{M}} \lesssim L^{-3/2}$. For $N = 2$ our numerics give a diffusive $t_Q \sim L^{-2}$, matching this lower bound. For $N = 3$ and $\gamma = \Theta(L^0)$, $t_Q(\gamma)$ is similarly observed to exceed the lower bound of Thm. 3 by a factor of L. Interestingly however, when $\gamma \to 0$ the lower bound of $1/\Phi(G_{\mathcal{H}}) \sim L^{3/2}\rho_3^{-L}$ appears to be quite nearly saturated, without an extra factor of L. Finally, we note that when $N = 3$, the base of the exponent in (6.9) is only $e^{1/18} \approx 1.06$ for small γ; this makes the $\mathrm{poly}(L)$ contribution to $t_Q(\gamma)$ dominate for moderate system sizes. In the future it would be interesting to explore models with stronger bottlenecks, where the exponential scaling may be more pronounced.

6.5 Discussion

In this work we have seen how HSF can be remarkably robust in the presence of local coupling to a thermal bath, with signatures of fragmentation remaining present even on times exponentially long in system size. Our results have focused on models with pair-flip constraints, where thermalization is arrested by the presence of strong bottlenecks encountered by the dynamics as it explores Hilbert space. This picture can be shown to generalize to a larger family of strongly-fragmented systems, including the dipole-conserving models of Refs. [9, 10] and the general family of semigroup-based dynamics introduced by one of the authors in Ref. [112]. Furthermore, by viewing one half of a fully-constrained system as a bath for the other half, our results imply that bottlenecks inevitably produce slow *intra*-sector dynamics in unperturbed models, a result which may be useful for understanding the slow charge transport of Refs. [112, 16].

Our analytic results have focused on the case of RU dynamics. Hamiltonian dynamics should generically thermalize at least as slowly, although there are other reasons why disorder-free Hamiltonian dynamics may be parametrically slower, and in the future it would be interesting to investigate this possibility in more detail. It would also be interesting to understand couplings to different types of baths and the resulting steady states, as in Ref. [23].

Acknowledgement.— E.L. is grateful to Shankar Balasubramanian, Sarang Gopalakrishnan, and Alexey Khudorozhkov for stimulating discussions and collaborations on a related project. He also thanks Ehud Altman, Soonwon Choi, Ilya Gruzberg, and the residents of the 5th floor of Birge Hall, Sam Garratt in particular, for helpful discussions. Y.H. thanks Hyeongjin Kim, Rahul Nandkishore, Anatoli Polkovnikov and Zhi-Cheng Yang for discussions. Some simulations were performed with the help of the ITensor library [114]. E.L. was supported by a Miller research fellowship. This research is supported in part by the National Science Foundation under Grant No. DMR-2219735 (Y. H. and X. C.).

6.A Notational preface

As discussed in the main text, each computational product state $|s\rangle$, $s_i \in \{1, \ldots, N\}$ can be associated to a random walk on the balanced N-tree T_N. Proceeding from left to right, each s_i determines where the walk proceeds, with the walk backtracking when $s_i = s_{i-1}$. Each walk which ends at a point of depth d on the tree can be associated with a length-d string which corresponds to the shortest path on the tree from the origin to that point. We will refer to the shortest path associated a string s as s's *irreducible string*, which we write as $\mathsf{irr}(s)$. We will let v_s denote the vertex of T_N at which s

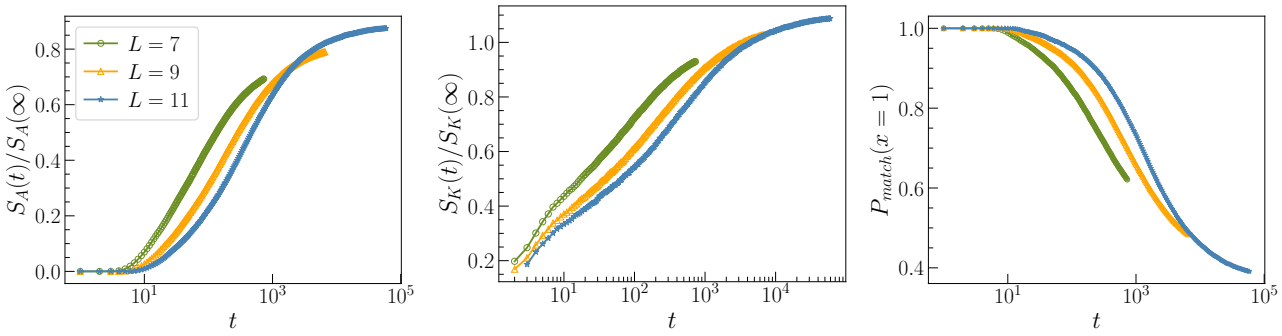

Figure 6.4: Numerical results of the $N = 3$ translation-invariant PF model with random $g^{ab} = (g^{ab})^*$ under a single-site random impurity of strength $\lambda = 1$ at L, starting from an initial state in $\mathcal{H}_{\text{froz}}$. *Left*: The normalized von-Neumann entropy $S_A(t)/S_A(\infty)$, where A is half of the constrained region and $S_A(\infty) = |A| \ln(N)/2 - 1/2$. *Center*: The Krylov entropy $S_K(t)$ normalized by $S_K(\infty)$, where $S_A(\infty)$ is calculated using $p_{v_s} = |\mathcal{K}_{v_s}|/|\mathcal{H}|$. *Right*: The probability of the spin on the first site to match with its original value.

ends. Since the walks on T_N are non-lazy, a string of length $|s| = L$ can only reach those nodes at a depth whose parity matches that of L. Writing $|v_s|$ for the depth of the node v_s (i.e. $|v_s| = |\mathsf{irr}(s)|$), this means that $[v_s]_2 = [L]_2$, where $[\cdot]_2$ denotes reduction mod 2.

We will let the $\mathcal{K}_{v_s}^{(L)}$ denote the set of all length-L strings with the same $\mathsf{irr}(s)$. The states in $\mathcal{K}_{v_s}^{(L)}$ form a basis of the Krylov sector associated with the node v_s. We will write $\mathcal{K}_d^{(L)}$ when we wish to refer to an arbitrary Krylov sector whose associated vertex is at a depth d on T_N. In addition, we will write $N_{\mathcal{K}}(L)$ for the total number of Krylov sectors on a system of size L. Finally, we will represent the projection operator onto the Krylov sector $\mathcal{K}_{v_s}^{(L)}$ as

$$\Pi_{\mathcal{K}_{v_s}^{(L)}} \equiv \sum_{|s\rangle \in \mathcal{K}_{v_s}^{(L)}} |s\rangle\langle s|. \tag{6.10}$$

6.B More numerical results

In this section we collect additional numerical results regarding the thermalization of Hamiltonian dynamics, with $N = 3$ unless explicitly stated otherwise. All of the Hamiltonians we will consider will act on open 1d chains, and will be of the form

$$H = H_0 + \lambda H_{\text{imp}}, \tag{6.11}$$

where H_0 acts on the entire system (of length L), and H_{imp} acts only on sites $L_{\text{cons}} < i \leq L$. H_{tot} will always be normalized such that $||H_{\text{imp}}||_\infty = L - L_{\text{cons}}$.

6.B.1 Entanglement and Krylov entropy

In this subsection we show the entanglement dynamics of a more general locally-perturbed PF model, including the half-chain entanglement entropy of the constrained system, and Krylov entropy, a quantity that measures the spreading

of the wave function over different Krylov subspaces, i.e.

$$S_K(t) \equiv -\sum_{v_s} p_{v_s} \ln p_{v_s}, \tag{6.12}$$

where

$$p_{v_s} \equiv \langle\psi(t)|\Pi_{\mathcal{K}_{v_s}}^{(L_{\text{cons}})} \otimes \mathbf{1}_{L-L_{\text{cons}}}|\psi(t)\rangle \tag{6.13}$$

is the probability that the first L_{cons} sites of the state are in sector $\mathcal{K}_{v_s}$.

We consider a *translation-invariant* PF model under a single-site perturbation, described by the Hamiltonian

$$H_0 = \sum_{a,b=1}^{3} g^{ab} \sum_{i=1}^{L-1} |aa\rangle\langle bb|_{i,i+1}, \qquad H_{\text{imp}} = \sum_{a,b=1}^{3} |a\rangle\langle b|_L, \tag{6.14}$$

where g is an arbitrary $N \times N$ Hermitian matrix that we take to be site-independent to avoid possible many-body localization caused by disorder. In Fig.6.4, we take $\lambda = 1$ and average over different realizations of g^{ab} and different initial frozen states. We first consider the half-chain von-Neumann entropy S_A where $A = [1, L_{\text{cons}}/2]$ is half of the constrained region. As shown in the left panel, $S_A(t) \sim \ln(t)$ as it approaches its thermal value $S_A(\infty) = L_{\text{cons}} \ln(3)/2$. Similarly, in the middle panel, the Krylov entropy increases logarithmically at early times. Here we plot $S_K(t)$ normalized by the value it takes when $p_{v_s} = |\mathcal{K}_{v_s}|/|\mathcal{H}|$, i.e. the value it takes when the wavefunction is spread out uniformly across Hilbert space. Since this is not the value of the p_{v_s} which maximizes the entropy, a non-monotonic time dependence is observed.

We additionally calculate $P_{\text{match}}(x)$, the probability of the spin on site x to be the same as its original value. As shown in the right panel, $P_{\text{match}}(x = 1)$ starts to deviate from 1 after the influence of the bath has propagated through the whole system, decreasing logarithmically in time to a value that approaches $1/3$ as $L \to \infty$. This further verifies that the time scale of thermalization of the general PF model under a constraint-breaking perturbation is exponentially long in system sizes.

6.B.2 Localization of eigenstates

To determine the extent that eigenstates of H are localized on T_N, we can measure the "expected depth" d_μ of each eigenstate $|\mu\rangle$, defined as

$$d_\mu \equiv \sum_{d=0}^{L/2} \sum_{v_s\,:\,\text{irr}(s)=d} d\langle\mu|\Pi_{\mathcal{K}_{v_s}}|\mu\rangle. \tag{6.15}$$

Histograms of d_μ and eigenstate energy E are shown in Figs. 6.5, 6.6, and 6.7 for $SU(3)$-symmetric pair-flip models, $SU(3)$-breaking pair-flip models, and the $N = 2$ variant of the symmetric model (unitarily equivalent to a perturbed XXX chain), respectively. For the $N = 3$ models we use a total system size of $L = 8$, while for $N = 2$ we set $L = 12$.

In Fig. 6.5 we study $SU(3)$-symmetric Temperley-Lieb chains of the form

$$H_{TL}(g_i) = \sum_i g_i P_{i,i+1} + \lambda H_{\text{imp}}, \qquad P_{i,i+1} \equiv \frac{1}{N} \sum_{a,b=1,\ldots,N} |a,a\rangle\langle b,b|_{i,i+1}, \tag{6.16}$$

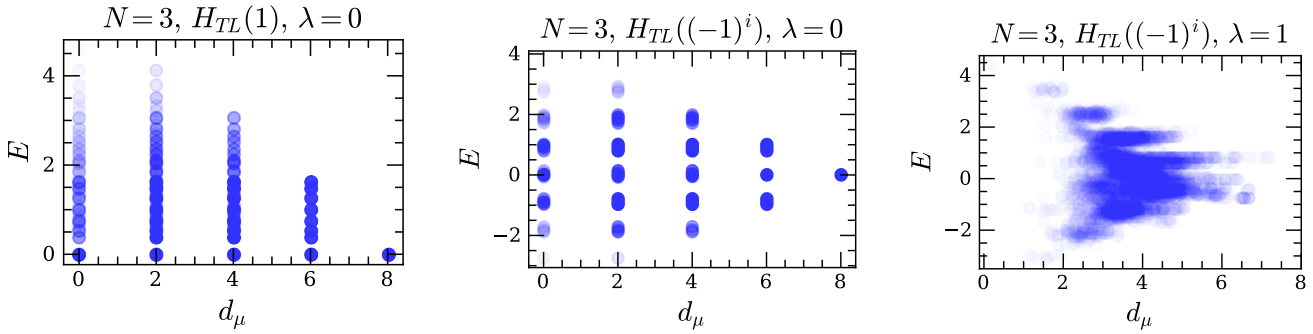

Figure 6.5: Eigenenergies in different variants of $SU(3)$-symmetric models for $L = 8$, arranged according to the Krylov distance d_μ (6.15) of each eigenstate. *Left:* Unperturbed TL model without sublattice staggering ($g_i = 1$). The frozen states at $d = 8$ all lie at the bottom of the spectrum. *Center:* The same model with with $g_i = (-1)^i$: the frozen states now lie in the middle of the spectrum. *Right:* The same model but now with a two-site impurity of strength $\lambda = 1$ at the end of the chain. States with large d_μ continue to be located roughly in the middle of the spectrum.

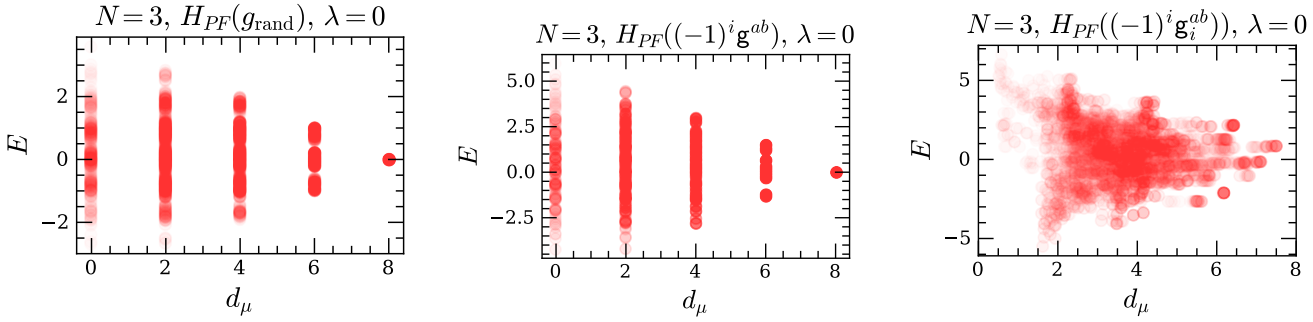

Figure 6.6: Eigenenergies in different $SU(3)$-breaking models for $L = 8$, arranged according to the Krylov distance d_μ (6.15) of each eigenstate. *Left:* A random translation-invariant choice of the pair-flip matrix g^{ab}. *Center:* The choice $g_i^{ab} = (-1)^i \mathrm{g}^{ab}$ adopted in the main text with $\lambda = 0$. The frozen states at $d_\mu = 0$ continue to lie roughly in the middle of the spectrum. *Right:* The same Hamiltonian but with $\lambda = 1$, showing a distribution of d_μ which continues to remain very broad.

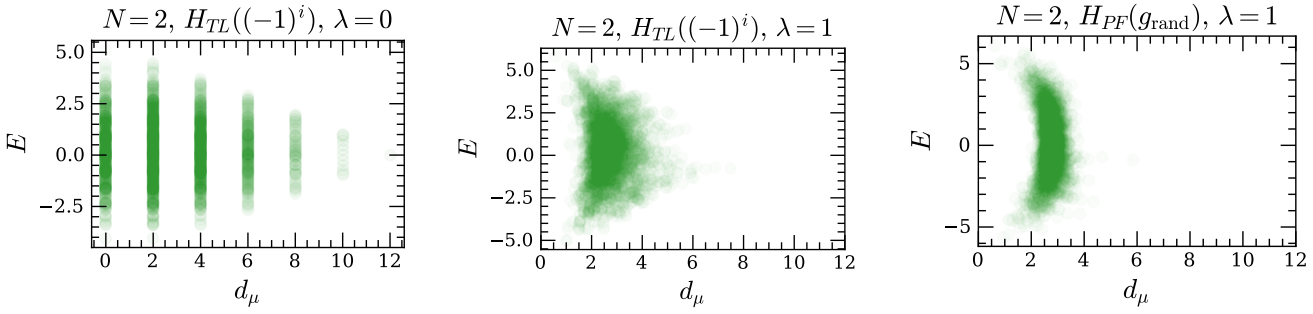

Figure 6.7: Eigenenergies for $N = 2$ models. *Left:* The $SU(2)$-symmetric model with $g_i = (-1)^i$ and $\lambda = 0$. *Center:* The same model but with $\lambda = 1$, with most eigenstates clustering around a small value of d_μ, as expected from a thermalizing Hamiltonian (on account of the absence of strong fragmentation). *Right:* An $SU(2)$-breaking model with random pair-flip matrix g^{ab}. The distribution of d_μs is even more tightly concentrated about the value one would obtain for a thermalizing Hamiltonian.

where $H_{\rm imp}$ is a random matrix supported only on the last two sites of the chain ($i = 7, 8$) and normalized so that $||H_{\rm imp}||_\infty = 1$. In the left panel we set $g_i = 1, \lambda = 0$ and observe a large dengeneracy of $E = 0$ states at the bottom of the spectrum. The model is strongly fragmented since $\lambda = 0$, and so d_μ is an integer for each $|\mu\rangle$. In the middle panel we take $g_i = (-1)^i$, which puts the frozen states at $E = 0$ into the middle of the spectrum. In the right panel we break the fragmentation by taking $\lambda = 1$, which is the value of λ for which $H_{\rm imp}$ has the strongest effect on the spectrum. Now the d_μ are no longer integers, but nevertheless a fairly broad distribution of d_μs is observed. A generic model with no localization on the Krylov space tree would have $d_\mu \approx v_N L = L/3$ for all eigenstates. The broad distribution of d_μ observed here suggests that some degree of localization persists, although future work will be needed to understand to what degree this is due to finite size effects.

We now consider pair-flip models which lack $SU(3)$ symmetry at $\lambda = 0$. The most general Hamiltonian we will consider is of the form

$$H_{PF}(g_i^{ab}) = \sum_i \sum_{a,b=1}^{N} g_i^{ab} |a, a\rangle\langle b, b|_{i,i+1} + \lambda H_{\rm imp}. \tag{6.17}$$

In the left panel of Fig. 6.6 we show the spectrum at $\lambda = 0$ for a random translation-invariant choice of g_i^{ab}. The frozen states at $d_\mu = 8$ are observed to lie roughly in the middle of the spectrum. In the center panel we show the choice of g_i^{ab} adopted in the main text, viz.

$$g_i^{ab} = (-1)^i \mathrm{g}^{ab} \equiv (-1)^i \left(\frac{1}{3} + \kappa \delta^{a,b}\right) \tag{6.18}$$

with κ fixed at $2/3$, as in the main text.

Fig. 6.7 shows the spectrum of analogous models with $N = 2$, which are not strongly fragmented. In the left panel we show (6.16) with $g_i = (-1)^i$ and $\lambda = 0$, which is unitarily equivalent to a staggered XXX chain. In the center panel we set $\lambda = 1$, which brings nearly all of the $|\mu\rangle$ down to $d_\mu/L \approx 1/4$, which is close to what we would expect for a generic Hamiltonian. Finally, in the right panel we let H be a random pair-flip Hamiltonian, observing an even more tightly clustered distribution of d_μ.

6.B.3 r statistics

The models with $N > 2$ that we study all exhibit strong HSF, with $|\mathcal{K}_{\rm max}|$ being exponentially smaller than $|\mathcal{H}|$. This implies that if one examines the spectrum of H, consecutive eigenstates will almost certainly belong to distinct Krylov sectors, and hence the spectrum of H will exhibit no nearest-neighbor level repulsion in the absence of constraint-breaking terms. How strongly the eigenstates in different sectors hybridize as a constraint-breaking term is applied provides a characterization of the severity by which thermalization is impeded, since such hybridization is a prerequisite for getting initial product states in $\mathcal{H}_{\rm froz}$ to thermalize. In this subsection we will take some first steps towards studying this question numerically by computing the *r-statistic* [115]

$$\langle r \rangle \equiv \langle r_n \rangle, \qquad r_n \equiv \frac{\min(\delta_n, \delta_{n+1})}{\max(\delta_n, \delta_{n+1})}, \tag{6.19}$$

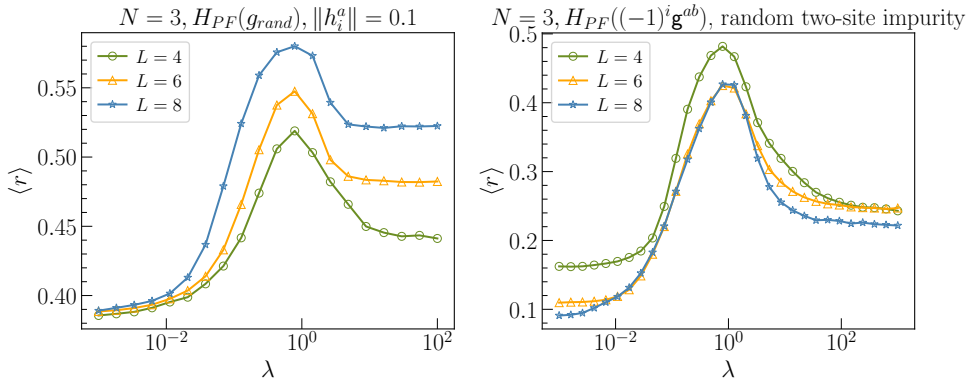

Figure 6.8: The $\langle r \rangle$ statistics of $N = 3$ models vs. perturbation strength λ for $L = 4, 6, 8$. *Left:* The translation-invariant PF model with random pair-flip matrix g^{ab}, a longitudinal field with strength $\|h_i^a\| = 0.1$, and a single-site perturbation. When $\lambda = \mathcal{O}(1)$, $\langle r \rangle \to 0.6$ as $L \to \infty$. *Right:* The model with $g_i^{ab} = (-1)^i \mathbf{g}^{ab}$ discussed in the main text, under a random two-site impurity.

where $\delta_n \equiv E_{n+1} - E_n$ is the gap between adjacent non-degenerate energy levels $E_{n+1} > E_n$. Computing $\langle r \rangle$ also allows us to make contact with research examining how the addition of local and/or weak generic perturbations to integrable Hamiltonians leads to the onset of chaos (see [116, 117] for two almost-randomly chosen references on this broad topic).

As mentioned above, when $\lambda = 0$ — viz. when the constraint-breaking term is turned off — we expect Poisson statistics, with $\langle r \rangle \approx 0.38$. On the other hand, if the constraint-breaking term strongly hybridizes the states in different sectors, we expect $\langle r \rangle$ to be given by the Gaussian unitary ensemble (GUE) value of $\langle r \rangle \approx 0.6$. In Fig.6.8, we study the $\langle r \rangle$ statistics of the $N = 3$ locally-perturbed PF models as a function of the perturbation strength λ. In the left panel, we consider the translation-invariant random PF model as in Eq.6.14, with an additional longitudinal field $H_f = \sum_i h_i^a |a\rangle\langle a|$. As $\lambda \to 0$, $\langle r \rangle \approx 0.38$ indicates that the unperturbed PF model possesses a spectrum with Poisson distribution, as expected. In the finite-size numerics, $\langle r \rangle$ continues to grow as λ increases and peaks at $\lambda \sim 1$, approaching 0.6 as L increases, followed by a slight decrease to a plateau as $\lambda \to \infty$. In the right panel, we consider the staggered PF model adopted in the main text, with the perturbation being replaced by a two-site random impurity. This model has similar but smaller finite-size $\langle r \rangle$ statistics which does not increase as L increases. This is consistent with the fact that the perturbed staggered PF model thermalizes slower than the perturbed random PF model. We conjecture that in the thermodynamic limit, $\langle r \rangle$ approaches the GUE value for all $\lambda = \Omega(1)$. If true, this indicates that the different Krylov sectors become well-hybridized in the thermodynamic limit. This of course does not preclude slow thermalization arising due to the Hilbert space bottleneck mechanism discussed in the main text, although it may mean that the thermalization times of typical Hamiltonian dynamics and the constrained RU dynamics studied in the main text are not parametrically different.

The plateau for large λ can be understood as follows. When $\lambda \to \infty$, λH_{imp} decouples the perturbed site from the system, splitting the spectrum of H into sectors labeled by the eigenstate $|\phi_m\rangle$ of H_{imp}, and the total eigenstate of H becomes $|\psi_L^m\rangle \approx |\psi_{L_{\text{cons}}}\rangle \otimes |\phi_m\rangle$. Taking the impurity to act on only a single site for simplicity, so that $L = L_{\text{cons}} + 1$,

the effective Hamiltonian in the sector labeled by m is

$$\begin{aligned} H^m_{\text{eff}} &= (\mathbf{1}_{L_{\text{cons}}} \otimes |\phi_m\rangle\langle\phi_m|) H (\mathbf{1}_{L_{\text{cons}}} \otimes |\phi_m\rangle\langle\phi_m|) \\ &= \sum_{a,b=1}^{N} \left(\sum_{i=1}^{L_{\text{cons}}-1} g_i^{ab} |aa\rangle\langle bb|_{i,i+1} + g^{ab}_{L_{\text{cons}}} \langle\phi_m|a\rangle\langle b|\phi_m\rangle |a\rangle\langle b|_{L_{\text{cons}}} \right) \otimes |\phi_m\rangle\langle\phi_m| \\ &\equiv \tilde{H}^m_{\text{eff}} \otimes |\phi_m\rangle\langle\phi_m|, \end{aligned} \tag{6.20}$$

with some constant terms ignored. $\tilde{H}^m_{\text{eff}}$ is essentially the same PF model as before, but now defined on a length $L-1$ chain with an impurity Hamiltonian acting on the boundary whose matrix elements are

$$[H^m_{\text{imp,eff}}]_{ab} = g^{ab}_{L_{\text{cons}}} \langle\phi_m|a\rangle\langle b|\phi_m\rangle \sim O(1). \tag{6.21}$$

Therefore, the $\langle r\rangle$ statistics on a system of size L at $\lambda \to \infty$ should be the same as that of a system of size $L-1$ at $\lambda = O(1)$.

From the numerics, there does not naively seem to be a well-defined transition in the $\langle r\rangle$ statistics from Poisson to GUE, as one finds in certain types of perturbed integrable models [117], although a more detailed numerical study will need to be carried out to properly address this question.

6.C Krylov sector dimensions

6.C.1 $N = 2$

We first dispatch with the easy case of $N = 2$, for which the dynamics is not fragmented. The tree T_2 is simply a line, and the different Krylov sectors can be fully distinguished by the charge Q_1 defined in (6.2), the value of which gives the distance of the Krylov sector along the line. The number of Kyrlov sectors is simply

$$N_{\mathcal{K}}(L) = L + 1. \tag{6.22}$$

The dimension of a sector whose irreducible string has length d is determined by counting the number of length-L non-lazy random walks on the line which end at a distance of $d > 0$ from the origin. This number is simply

$$\begin{aligned} \dim[\mathcal{K}_d(L)] &= \delta_{[d]_2,[L]_2} \binom{L}{\frac{L+d}{2}} \\ &\approx \sqrt{\frac{2L}{\pi(L^2-d^2)}} \exp(LH(p_d)), \end{aligned} \tag{6.23}$$

where $H(x) = -x\ln x - (1-x)\ln(1-x)$ is the binary Shannon entropy and $p_d \equiv (1+d/L)/2$.

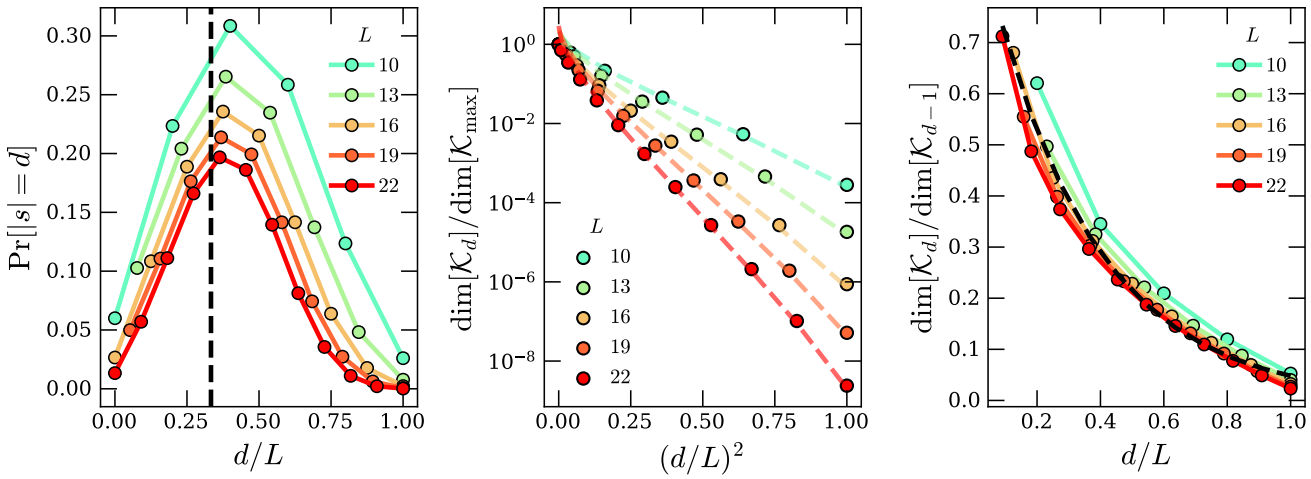

Figure 6.9: *Left:* The probability that a randomly chosen product state will lie in a Krylov sector with irreducible string of length d. The dashed black line lies at $d/L = (1 - 2/N)$ with $N = 3$, the most probable size in the $L \to \infty$ limit. *Center:* the sizes of Krylov sectors $\mathcal{K}_d$ with length-d irreducible string, compared with the size of the largest Krylov sector (dots). Dashed lines are plotted using the approximate expression in (6.46). *Right:* the relative size of succesive Krylov sectors arranged by distance d, exhibiting a decay scaling approximately exponentially with d/L. The dashed black line is drawn according to (6.46).

6.C.2 $N > 2$

When $N > 2$ the dynamics is strongly fragmented, and determining the sizes of the different Krylov sectors is less trivial. We start with the total number of Kyrlov sectors $N_{\mathcal{K}}(L)$. From thinking about the tree structure of T_N, it is clear that this number is

$$N_{\mathcal{K}}(L) = 1 + N\sum_{l=1}^{L/2}(N-1)^{2l-1}(L \text{ even}) \qquad = \frac{(N-1)^{L+1}-1}{N-2} = \Theta((N-1)^L).$$
$$N\sum_{l=1}^{(L+1)/2}(N-1)^{2l-2}(L \text{ odd})$$

(6.24)

Note that while this number is exponentially large in L, it is still exponentially smaller than the Hilbert space dimension $\dim \mathcal{H} = N^L$.

We now begin in our determination of the Krylov sector sizes. For simplicity of notation we will restrict our attention to the case when L is even. We start with the size of the largest Krylov sector $\mathcal{K}_0^{(L)}$, which is identified with the vertex at the center of the tree:

Proposition 1. *For even L, the size of the largest Krylov sector $\mathcal{K}_0^{(L)}$ is*

$$|\mathcal{K}_0^{(L)}| = N^L\left(1 + \frac{1}{2}\sum_{n=1}^{L/2} N^{-2n}\binom{1/2}{n}(-1)^n\gamma^{2n}\right). \tag{6.25}$$

For both even and odd L, in the large L limit $|\mathcal{K}_0^{(L)}|$ scales as

$$|\mathcal{K}_0^{(L)}| \sim L^{-3/2}(N\rho)^L, \tag{6.26}$$

where

$$\rho \equiv \frac{2\sqrt{N-1}}{N} \tag{6.27}$$

is the spectral radius of T_N [113].

Proof. As in Ref. [118], our proof will use generating functions to obtain an exact expression for $|\mathcal{K}_0^{(L)}|$. Since we are assuming L is even, the size of $\mathcal{K}_0^{(L)}$ can be determined by counting the number of non-lazy simple length-L random walks on T_N which begin and end at the origin.

Let $R(x)$ be the generating function for non-lazy simple random walks on T_N. $R(x)$ is easily seen to obey the recursion relation

$$R(x) = 1 + Nx^2R(x)B(x), \tag{6.28}$$

where $B(x)$ is the generating function for returning walks on the *rooted* N-regular tree $T_{N,r}$ which begin and end at the root vertex (which has degree $N-1$). We thus need a recursion relation for $B(x)$, which is readily obtained as

$$B(x) = 1 + x^2(N-1)B(x)^2, \tag{6.29}$$

which when solved yields [118]

$$B(x) = 2\frac{1-\sqrt{1-(x\gamma)^2}}{(x\gamma)^2} \qquad \gamma \equiv 2\sqrt{N-1}. \tag{6.30}$$

We can now use this expression to get $R(x)$, which we may write after some algebra as[1]

$$R(x) = \frac{2 + N(\sqrt{1-(\gamma x)^2}-1)}{2(1-(Nx)^2)}. \tag{6.33}$$

We now want to determine the long-walk asymptotics, which requires that we perform the series expansion

$$R(x) \equiv \sum_k x^{2k}|\mathcal{K}_0^{(2k)}|, \tag{6.34}$$

which takes the form of a convolution between a geometric series and the series coming from the expansion of the square

[1] An aside: one should not be alarmed that $R(1)$ is imaginary. If one wants the expected number of times an infinitely long walk returns to the origin, one needs to write down generating functions for probabilities, rather than for number of paths. Since each individual move has an equal probability of $1/N$, this amounts to sending $x \mapsto x/N$, which gives

$$R(x/N) = \frac{2(N-1)}{N-2+N\sqrt{1-(x\rho)^2}}, \tag{6.31}$$

and so sending $x \to 1$ then gives

$$\langle \text{number of returns} \rangle = \frac{N-1}{N-2}. \tag{6.32}$$

This appropriately diverges when $N = 2$ but is finite for all $N > 2$, and correctly approaches 1 as $N \to \infty$.

root in the denominator. From (6.33), a Taylor expansion gives

$$R(x) = \frac{1}{2}\sum_{m=0}^{\infty}(Nx)^{2m}\left(2 - N + N\sum_{n=0}^{\infty}\binom{1/2}{k}(-1)^k(\gamma x)^{2k}\right). \tag{6.35}$$

The Lth coefficient is then

$$|\mathcal{K}_0^{(L)}| = N^L\left(1 + \frac{1}{2}\sum_{n=1}^{L/2}N^{-2n+1}\binom{1/2}{n}(-1)^n\gamma^{2n}\right), \tag{6.36}$$

giving the exact result (6.25).

We now obtain the asymptotic result (6.26). For this we rewrite the fractional binomial coefficient above as

$$\binom{1/2}{n}(-1)^n = -\frac{(2n-3)!!}{2^n n!}. \tag{6.37}$$

Since the fraction of length-$2k$ walks which return to the origin vanishes as $l \to \infty$, we have $(|\mathcal{K}_0^{(L)}|/N^L)|_{L\to\infty} = 0$, which using the above implies

$$\sum_{n=1}^{\infty}\frac{N^{1-2n}\gamma^{2n}(2n-3)!!}{2^{n+1}n!} = 1. \tag{6.38}$$

Thus for large L we may write

$$\begin{aligned}\frac{|\mathcal{K}_0^{(L)}|}{N^L} &= \sum_{n=k+1}^{\infty}\frac{N^{1-2n}\gamma^{2n}(2n-3)!!}{2^{n+1}n!}\\ &\approx \sum_{n=L/2+1}^{\infty}\sqrt{\frac{e^3N^2(1-3/2n)}{16\pi}}(n-3/2)^{-3/2}\exp\left(n[-2\ln(N/\gamma)+\ln(1-3/2n)\right)\\ &\approx \int_{L/2}^{\infty}dn\sqrt{\frac{N^2e^3}{16\pi}}n^{-3/2}\exp(-2n\ln(N/\gamma)),\end{aligned} \tag{6.39}$$

where we used $k!! \approx \sqrt{2k}(k/e)^{k/2}$ at large k.

Doing the integral (whose exact expression is written in terms of $\Gamma(1/2, L\ln\gamma)$) then gives

$$|\mathcal{K}_0^{(L)}| \sim L^{-3/2}(N\rho)^L, \tag{6.40}$$

where $\rho = \gamma/N$ is the spectral radius introduced above. That the base of the exponential is $N\rho$ also follows more directly from the fact that ρ characterizes the return probability $p_{\text{ret}}(L)$ as $\rho \equiv \lim_{L\to\infty}(p_{\text{ret}}(L))^{1/L}$ [119]. □

Since $\rho < 1$ for all $N > 2$, the largest Krylov sector occupies an exponentially small subset of Hilbert space, and the PF model is strongly fragmented for all $N > 2$.

We will also have occasion to know the number of length-L random walks that end a distance d from the origin. To this end, we can generalize the above result about $|\mathcal{K}_0^{(L)}|$ to

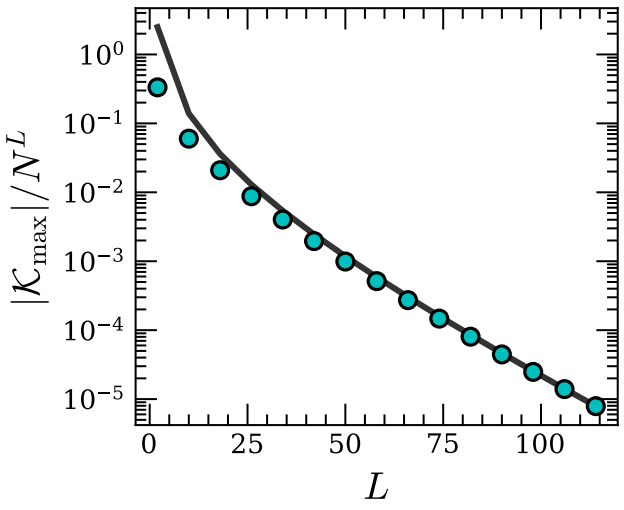

Figure 6.10: Scaling of the size of the largest Krylov sector $\mathcal{K}_0$ as a function of L, plotted for $N = 3$. Cyan circles are the exact result (6.25), and the gray line is the asymptotic expression (6.26).

Proposition 2. *The size of a Krylov sector $\mathcal{K}_d^{(L)}$ whose irreducible strings have length d is*

$$|\mathcal{K}_d^{(L)}| = 2^d \sum_{n=0}^{(L+d)/2} \sum_{k=0}^{d} |\mathcal{K}_0^{(L+d-2n)}| (-1)^{k+n} \binom{d}{k} \binom{k/2}{n} \gamma^{2(n-d)}. \tag{6.41}$$

Proof. Let $G(x;d)$ be the generating function for walks which travel to a specific vertex at distance d. In terms of the generating functions introduced above, this is seen to be

$$G(x;d) = x^d R(x) B^d(x). \tag{6.42}$$

Performing an expansion of $B^d(x)$, we have

$$G(x;d) = 2^d \sum_{l,n=0}^{\infty} \sum_{k=0}^{d} (-1)^{k+n} \binom{d}{k} \binom{k/2}{n} \gamma^{2(n-d)} |\mathcal{K}_0^{(2l)}| x^{2l+2n-d}, \tag{6.43}$$

and so writing $G(x;d) = \sum_{m=0}^{\infty} x^{d+2m} |\mathcal{K}_d^{(d+2m)}|$, we have

$$|\mathcal{K}_d^{(d+2m)}| = 2^d \sum_{n=0}^{d+m} \sum_{k=0}^{d} |\mathcal{K}_0^{(2(d+m-n))}| (-1)^{k+n} \binom{d}{k} \binom{k/2}{n} \gamma^{2(n-d)}. \tag{6.44}$$

For a length L random walk we will have $m = (L-d)/2$; inserting this above gives the exact expression (6.41). □

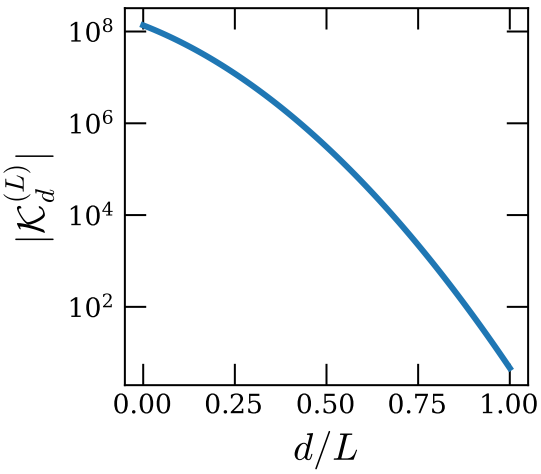

Figure 6.11: The asymptotic expression (6.46) for the size of $\mathcal{K}_d^{(L)}$, shown here with $L = 20$.

Intuition: biased random walks

We have already obtained an asymptotic expression for $|\mathcal{K}_0^{(L)}|$ valid at large L. When d/L is not very small, we can obtain a complementary asymptotic expression for $|\mathcal{K}_d^{(L)}|$. This can be done from a straightforward (if unilluminating) expansion of the binomial coefficients in (6.44). More physically, we can argue by realizing that $N(N-1)^{d-1}|\mathcal{K}_d^{(L)}|$ is equal to the probability for a length-L biased random walk on $\mathbb{N}$ to end a distance d from the origin; here the radial direction of T_N is identified with $\mathbb{N}$ and the factor of $N(N-1)^{d-1}$ is equal to the number of sectors at depth d. The bias of this walk is probability of moving outward $(1-1/N)$ minus the probability of moving inward $(1/N)$, and hence the walker has velocity

$$v_N \equiv 1 - 2/N. \tag{6.45}$$

Therefore

$$\begin{aligned} |\mathcal{K}_d^{(L)}| &\approx \frac{(1-1/N)^{\frac{L+d}{2}} N^{-\frac{L-d}{2}} \binom{L}{\frac{L+d}{2}}}{N(N-1)^{d-1}} N^L \\ &\approx \frac{2(N-1)}{N\sqrt{2\pi L}} N^L \exp\left(-\frac{(d-v_N L)^2}{2L} - d\ln(N-1)\right), \end{aligned} \tag{6.46}$$

where in the second line we have used that the probability distribution of a random walker on the real line with velocity v_N is $p(x,t) = \frac{1}{\sqrt{2\pi t}} e^{-(x-v_N t)^2/2t}$ (with $t = L$ and $x = d$ in the above), and the factor of 2 comes from the fact that d must have the same parity as L (with the $-d\ln(N-1)$ ensuring that $|\mathcal{K}_d^{(L)}|$ is always monotonically decreasing with d). This function is shown in Fig. 6.11.

6.4 From RU to stochastic dynamics

In this section we derive the generator of the stochastic dynamics that arises from studying circuit-averaged evolution in the model of open-system RU dynamics introduced in the main text. A single timestep of the dynamics corresponds to

evolution under the channel

$$\mathcal{C}(\rho) = \mathcal{U}^\dagger \left(\mathrm{Tr}_L[\rho] \otimes \frac{\mathbf{1}}{N} \right) \mathcal{U}, \tag{6.47}$$

where Tr_L denotes tracing out the last site of the system, the $\mathbf{1}$ acts on the Lth site, and $\mathcal{U}$ is a random constraint-preserving unitary defined via a depth-2 brickwork circuit:

$$\mathcal{U} = \left(\bigotimes_{i=1}^{L/2-1} U_{2i,2i+1} \right) \left(\bigotimes_{i=1}^{L/2} U_{2i-1,2i} \right), \tag{6.48}$$

where each $U_{i,i+1}$ are independent unitaries which preserve the constraint. We will view the $\mathrm{Tr}_L[\rho] \otimes \mathbf{1}$ part of (6.47) as arising from dynamics in which a "bath" system at sites $i > L$, which is coupled to the length-L system through a generic interaction at site L, is acted on by generic Haar-random unitary dynamics and then traced out, resulting in completely depolarizing noise being applied to the Lth site. In the following we will first consider the most general case in which the $U_{i,i+1}$ are constrained only by their preservation of walk endpoints in the computational basis; we refer to this as the case of "pair-flip" constraints. In a subsequent subsection we will consider a more restrictive case where the $U_{i,i+1}$ preserve walk endpoints in *all* single-site bases; this corresponds to a RU realization of the constraints present in the Temperley-Lieb model.

6.4.1 Pair-flip

For general pair-flip dynamics, the elementary gates $U_{i,i+1}$ take the form

$$U_{i,i+1} = \sum_{a,b} U^{PF}_{ab} |aa\rangle\langle bb| + \sum_{a \neq b} e^{i\phi_{ab}} |ab\rangle\langle ab| = U^{PF} \oplus \bigoplus_{a \neq b} e^{i\phi_{ab}}, \tag{6.49}$$

where the matrix U^{PF} is drawn from the Haar ensemble on $U(N)$, and the second term in the direct sum acts as a diagonal matrix of random phases on the subspace of states frozen under the PF dynamics, viz. those of the form $|a,b\rangle, a \neq b$.

We will be interested in understanding how an operator $\mathcal{O}$ evolves under the circuit-averaged dynamics, following [111] and the slightly modified treatment given in [112]. We let

$$\overline{\mathcal{O}}(t) \equiv \mathop{\mathbb{E}}_{\mathcal{C}_t} [\mathcal{C}_t(\mathcal{O})] \tag{6.50}$$

denote the circuit-averaged evolution of $\mathcal{O}$ over time t, where the $\mathbb{E}_{\mathcal{C}_t}$ denotes averaging over the unitaries constituting $\mathcal{U}$. To help with notation, we will divide each unit time interval into three steps of length $t = 1/3$: at $t \in \mathbb{N}$ the depolarizing noise is applied, at $t \in \mathbb{N} + 1/3$ the first layer of $\mathcal{U}$ is applied, and at $t \in \mathbb{N} + 2/3$ the second layer is applied. Thus

$$\overline{\mathcal{O}}(t + 1/3) = \mathrm{Tr}_L[\overline{\mathcal{O}}(t)] \otimes \mathbf{1}. \tag{6.51}$$

Decomposing $\overline{\mathcal{O}}$ as

$$\overline{\mathcal{O}}(t) = \bigotimes_{i=1}^{L/2-1} \overline{\mathcal{O}}_{2i,2i+1}(t) \tag{6.52}$$

without loss of generality, performing the Haar average gives

$$\overline{\mathcal{O}}_{2i,2i+1}(t+2/3) = \frac{\mathrm{Tr}[\overline{\mathcal{O}}_{2i,2i+1}(t+1/3)\Pi^{PF}]}{N}\Pi^{PF} + \sum_{a\neq b} \mathrm{Tr}[\overline{\mathcal{O}}_{2i,2i+1}(t+1/3)\Pi^{ab}]\Pi^{ab}, \tag{6.53}$$

where we have defined the projectors

$$\Pi^{PF} \equiv \sum_a |a,a\rangle\langle a,a|, \qquad \Pi^{ab} \equiv |a,b\rangle\langle a,b|. \tag{6.54}$$

The action of the second layer of the brickwork is obtained similarly.

Note that since Π^{PF}, Π^{ab} are diagonal in the computational basis, so too is $\overline{\mathcal{O}}$ after any nontrivial amount of time evolution. We may thus focus on diagonal operators, i.e. states, without loss of generality. From (6.51) and (6.53), the diagonal operator $|\psi\rangle\langle\psi|$ evolves according to

$$|\overline{\psi}(t+1)\rangle = \mathcal{M}_o\mathcal{M}_e\mathcal{M}_L|\overline{\psi}(t)\rangle, \tag{6.55}$$

where

$$\begin{aligned} \mathcal{M}_L &= \mathbf{1}_{L-1} \otimes \frac{1}{N}\sum_{a,b}|a\rangle\langle b| \\ \mathcal{M}_e &= \bigotimes_{i=1}^{L/2-1} M^{PF}_{2i,2i+1} \\ \mathcal{M}_o &= \bigotimes_{i=1}^{L/2} M^{PF}_{2i-1,2i}, \end{aligned} \tag{6.56}$$

where we have defined the 2-site stochastic matrix

$$M^{PF} \equiv \frac{1}{N}\sum_{a,b}|a,a\rangle\langle b,b| + \sum_{a\neq b}|a,b\rangle\langle a,b|. \tag{6.57}$$

Note that $\mathcal{M}_o\mathcal{M}_e\mathcal{M}_L$ is doubly stochastic and irreducible, and hence its unique steady state is the uniform distribution on $\mathcal{H}$ (irreducibility would of course fail if $\mathcal{M}_L$ were absent). This guarantees that RU dynamics will always thermalize to the uniform distribution at long enough times.

6.4.2 Temperley-Lieb

For Temperley-Lieb dynamics, the elementary unitary gates are constrained to preserve the pair-flip constraint in *any* on-site basis, which is done by enriching the previously studied pair-flip dynamics with $SU(N)$ symmetry. The elementary

unitary gates for this model take the form

$$U_{i,i+1} = e^{i\phi_{i,i+1}}\Pi^{TL} + (\mathbf{1} - \Pi^{TL}), \tag{6.58}$$

where

$$\Pi^{TL} \equiv \frac{1}{N}\sum_{a,b} |aa\rangle\langle bb|, \tag{6.59}$$

and where each $\phi_{i,i+1}$ is sampled randomly from $[0, 2\pi)$.

The first part of each timestep, whereby the spin at site L is depolarized, is of course unchanged from the more general pair-flip case. After averaging over the $\phi_{i,i+1}$, one sees that the first layer of the brickwork maps operators as

$$\overline{\mathcal{O}}_{2i,2i+1}(t + 2/3) = \Pi^{TL}\overline{\mathcal{O}}_{2i,2i+1}(t + 1/3)\Pi^{TL} + (\mathbf{1} - \Pi^{TL})\overline{\mathcal{O}}_{2i,2i+1}(t + 1/3)(\mathbf{1} - \Pi^{TL}), \tag{6.60}$$

with the second layer of the brickwork acting analogously.

Because of the $U(N)$ invariance of TL dynamics, an operator which is diagonal in any single site product state basis will remain diagonal in that basis. For concreteness we will continue to use the computational basis, although any other basis is equally fine. Diagonal operators, or equivalently states, evolve as $|\overline{\psi}(t+1)\rangle = \mathcal{M}|\overline{\psi}(t)\rangle$, where the Markov generator $\mathcal{M}$ has the same form as (6.56), except with M^{PF} replaced by the matrix M^{TL}, where

$$M^{TL} = \left(1 - \frac{2(N-1)}{N^2}\right)\sum_a |a,a\rangle\langle a,a| + \frac{2}{N^2}\sum_{a\neq b} |a,a\rangle\langle b,b| + \sum_{a\neq b} |a,b\rangle\langle a,b|, \tag{6.61}$$

which follows from (6.60) and reduces to M^{PF} when $N = 2$. Thus compared with M^{PF}, when $N > 2$ TL dynamics has a smaller probability for pairs to flip. In particular, pairs completely cease to flip in the $N \to \infty$ limit. As with pair-flip, $\mathcal{M}$ is doubly stochastic and irreducible, and hence the uniform distribution is $\mathcal{M}$'s unique steady state.

6.5 Rigorous bounds on relaxation and mixing times

In this section we will prove bounds on the relaxation and mixing times of the Markov process $\mathcal{M}$ associated with the pair-flip RU dynamics studied in the main text, as defined in Sec. 6.4.

Before we begin, some remarks and reminders on notation. The initial states we consider will always be computational basis product states, referred to simply as "product states" in what follows. ψ will be used to denote an arbitrary product state. We will write $\psi(t)$ for a sequence of product states obtained as a particular realization of the Markov process defined by $\mathcal{M}$. This is to be distinguished from the *probability distribution* one obtains from evolving a given state ψ for time t, which we write as $|\mathcal{M}^t\psi\rangle$. As mentioned above, the double stochasticity of $\mathcal{M}$ implies that $\mathcal{M}$'s equilibrium distribution is uniform on the space of product states, which we will denote as $\mathcal{H}$ by a slight abuse of notation.

The irreducible string associated with a product state ψ—which is obtained by iteratively removing pairs of adjacent identical characters in ψ—will be written as $\mathbf{s}_\psi$. In various places below we will write $\mathbf{s}_d$ when we wish only to emphasize

that the irreducible string in question has length d. As defined previously, $\mathcal{K}_{\mathbf{s}}$ will denote a specific Krylov sector with irreducible string $\mathbf{s}$; when we wish to denote an arbitrary $\mathcal{K}_{\mathbf{s}}$ with $|\mathbf{s}| = d$ we will instead similarly write $\mathcal{K}_d$, and when we wish to explicitly specify the system size we will write $\mathcal{K}_d^{(L)}$. In all of what follows we will assume for simplicity of notation that L is even, although all results can be readily generalized to odd L.

We will refer to the graph whose vertices are Krylov sectors and whose edges are drawn according to how the coupling to the bath connects the sectors as the *Krylov graph*. Since the constraint-breaking term moves the endpoint of the random walk by a distance of exactly 2, each sector in the Krylov graph is connected to $N(N-1)$ other sectors, and thus the Krylov graph is formed by the even / odd (depending on $L \mod 2$) sublattice of the symmetric depth L N-regular tree (see Fig. 6.2 a).

6.5.1 Markov chains and graph expansion

We begin by reviewing some central concepts in the theory of Markov chains,[2] letting $\mathcal{M}$ to denote the generator of a given Markov process. A key notion in what follows will be that of the expansion:

Definition 1. Let $R \subset \mathcal{H}$. The *expansion* of R is defined as the amount of probability flow that the uniform distribution experiences out of R during one step of the Markov process $\mathcal{M}$:

$$\Phi(R) \equiv \frac{1}{|R|} \sum_{\psi \in R} \sum_{\psi' \in R^c} \langle \psi' | \mathcal{M} | \psi \rangle, \tag{6.62}$$

where the sums run over sets of computational basis product states spanning R and R^c, respectively.

The utility of this definition is that when $\Phi(R)$ is small, states initially in R take a long time to diffuse to its complement R^c [113]:

Proposition 3. *The probability that a product state $\psi(0)$ randomly drawn from R will leave R in time t is upper bounded by*

$$P(\psi(t) \in R^c \,|\, \psi(0) \in R) \leq t\Phi(R). \tag{6.63}$$

Proof. We proceed following Ref. [113]. Using the Markovity of the dynamics,

$$\begin{aligned} P(\psi(t) \in R^c \,|\, \psi(0) \in R) &\leq \frac{|\mathcal{H}|}{|R|} \sum_{r=1}^{t} P(\psi(r) \in R^c,\, \psi(r-1) \in R) \\ &= \frac{t|\mathcal{H}|}{|R|} P(\psi(1) \in R^c,\, \psi(0) \in R) \\ &= t\Phi(R), \end{aligned} \tag{6.64}$$

where we have used that the probability of selecting any particular state ψ is $1/|\mathcal{H}|$. □

Regions with smaller R are more "cut off" from their complements R^c. The most isolated subregion of $\mathcal{H}$ defines the expansion of $\mathcal{M}$:

[2] See e.g. [113] for a good introduction.

Definition 2. The expansion of $\mathcal{M}$ is defined by the minimal expansion of a subregion of $\mathcal{H}$:

$$\Phi(\mathcal{M}) \equiv \min_{R\subset\mathcal{H}\,:\,|R|\leq\frac{1}{2}|\mathcal{H}|} \Phi(R). \tag{6.65}$$

$\Phi(\mathcal{M})$ thus provides a fundamental measure of the slowness of the dynamics. Its primary utility is that it can be used to bound two important timescales characterizing the slowness of $\mathcal{M}$, defined as follows:

Definition 3. The *relaxation time* is defined as the inverse gap of $\mathcal{M}$:

$$t_{\rm rel} \equiv \frac{1}{\Delta_{\mathcal{M}}}, \tag{6.66}$$

where $\Delta_{\mathcal{M}} \equiv 1-\lambda_2$, with λ_2 the second largest eigenvalue of $\mathcal{M}$. The *mixing time* is defined as the amount of time required for the distribution $\mathcal{M}^t\psi$ to become close to the uniform distribution π:

$$t_{\rm mix} \equiv \min\{t \,:\, \max_{\psi\in\mathcal{H}} ||\mathcal{M}^t\psi - \pi||_1 \leq \frac{1}{2}\}, \tag{6.67}$$

where the maximum is over all initial product states in $\mathcal{H}$.

$t_{\rm rel}$ and $t_{\rm mix}$ are essentially equivalent in their ability to capture the slowness of $\mathcal{M}$, as follows from the general bounds $(t_{\rm rel}-1)\ln 2 \leq t_{\rm mix} \leq t_{\rm rel}\ln(4|\mathcal{H}|)$ [120]. For concreteness we will focus on $t_{\rm rel}$ in what follows.

The expansion $\Phi(\mathcal{M})$ bounds $t_{\rm rel}$ via a fundamental result known as Cheeger's inequality (see e.g. [113]):

$$\frac{\Phi(\mathcal{M})^2}{2} \leq \Delta_{\mathcal{M}} \leq 2\Phi(\mathcal{M}). \tag{6.68}$$

In what follows, we will calculate $\Phi(\mathcal{M})$ for the Markov chains of interest and will use the above inequality to provide a rather tight constraint on the relaxation time. We will also see how the calculation of $\Phi(R)$ for appropriate choices of R can be used to bound entanglement growth and the relaxation times of local operators.

6.5.2 Local and non-local chains

The Markov generator derived in Sec. 6.4 was obtained by considering brickwork RU dynamics composed of three alternating layers: one layer of constrained 2-site gates on the even sublattice ($\mathcal{M}_e$ in the notation of Sec. 6.4), one layer on the odd sublattice ($\mathcal{M}_o$), and one layer consisting solely of depolarizing noise applied to the spin on site L ($\mathcal{M}_L$). In this section, we will write $\mathcal{M}_{\rm loc}$ for the Markov generator so obtained:

$$\mathcal{M}_{\rm loc} \equiv \mathcal{M}_o\mathcal{M}_e\mathcal{M}_L. \tag{6.69}$$

This dynamics is to be constrasted with a simpler "non-local" Markov process, obtained in the limit in which the depolarizing noise is weak, with the number of constrained RU brickwork layers being much larger than the number of applications of the depolarizing noise. In this limit, the constrained part of the dynamics thermalizes within each Krylov

sector much faster than the time scale over the constraint-breaking term acts. In this situation, the internal structure of the dynamics within each Krylov sector is trivial: as soon as a state reaches a new sector, it instantly spreads out uniformly across that sector, and the thermalization dynamics is consequently controlled solely by transitions between sectors. We will denote the Markov generator of this dynamics by $\mathcal{M}_{\mathrm{nonloc}}$:

$$\mathcal{M}_{\mathrm{nonloc}} \equiv (\mathcal{M}_o \mathcal{M}_e)^\infty \mathcal{M}_L = \Pi_{\mathrm{unif}} \mathcal{M}_L, \tag{6.70}$$

where

$$\Pi_{\mathrm{unif}} = \sum_{v_s} \frac{1}{|\mathcal{K}_{v_s}|} \sum_{s,s' \in \mathcal{K}_s} |s\rangle\langle s'| \tag{6.71}$$

projects product states onto the uniform distribution over the Krylov sector they belong to.

Analytic bounds on the gap of $\mathcal{M}_{\mathrm{nonloc}}$ are naturally easier to obtain than bounds on that of $\mathcal{M}_{\mathrm{loc}}$, since for the former, the locality of the dynamics does not come into play. In almost all of this section we will thus focus on $\mathcal{M}_{\mathrm{nonloc}}$, rather than $\mathcal{M}_{\mathrm{loc}}$. This is done without loss of generality since we are primarily interested in obtaining *upper* bounds on the gap, and naturally the lack of locality means that

$$\Delta_{\mathcal{M}_{\mathrm{nonloc}}} \geq \Delta_{\mathcal{M}_{\mathrm{loc}}}, \tag{6.72}$$

so that an upper bound on $\Delta_{\mathcal{M}_{\mathrm{nonloc}}}$ will also upper bound $\Delta_{\mathcal{M}_{\mathrm{loc}}}$. On physical grounds we in fact expect

$$\Delta_{\mathcal{M}_{\mathrm{loc}}} \sim \frac{\Delta_{\mathcal{M}_{\mathrm{nonloc}}}}{L}, \tag{6.73}$$

with the $1/L$ coming from the time needed for the dynamics to make transitions induced by the bath felt across the system. Indeed, we will see shortly that numerical determinations of the gap agree with this scaling.

6.5.3 $N > 2$

In this subsection we prove a variety of results establishing exponentially slow thermalization in the strongly fragmented models obtained when $N > 2$. The case of $N = 2$, where thermalization is expected to be much faster, is dealt with in a subsequent subsection.

The spectral gap

We begin by proving the following theorem:

Theorem 4. *For $N > 2$, the expansion of the Markov process $\mathcal{M}_{\mathrm{nonloc}}$ at large L satisfies*

$$\Phi(\mathcal{M}) \leq \frac{C}{L^{3/2}} \rho^L, \tag{6.74}$$

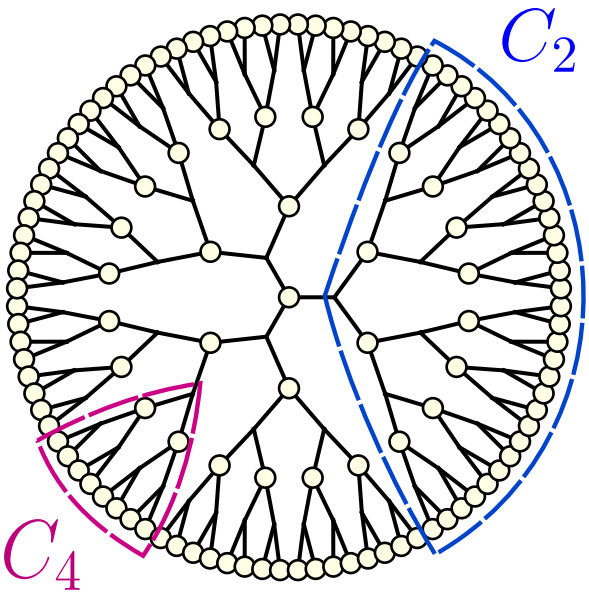

Figure 6.12: The krylov graph for $L = 6, N = 3$, with examples of regions C_2, C_4 indicated by the dashed lines.

where C is an unimportant $O(1)$ constant

$$\rho \equiv \frac{2\sqrt{N-1}}{N} < 1 \tag{6.75}$$

is the spectral radius of the symmetric N-ary tree.

To prove this, we need the following definition:

Definition 4. For a length $d-1$ irreducible string $\mathbf{s}_{d-1}$, define the *cone* $C_{\mathbf{s}_{d-1}} \subset \mathcal{H}$ as the subregion of Hilbert space spanned by the $N-1$ sectors which lie at depth d and whose parent vertex is associated with the string s_{d-1}, together with all sectors which are children of these sectors. More formally, we have

$$C_{s_{d-1}} \equiv \bigoplus_{s' \,:\, (s'_1 \ldots s'_{d-1}) = s_{d-1},\, |s'| \geq d} \mathcal{K}_{s'}, \tag{6.76}$$

where the sum is over all irreducible strings of length $\geq d$ whose first $d-1$ entries are equal to s_{d-1}. When the exact string s_{d-1} is not important, we will simply write C_d instead of $C_{s_{d-1}}$. A graphical illustration of this definition is shown in Fig. 6.12.

Our proof of Theorem 4 will rely on the following Lemma:

Lemma 1. *The expansion of C_d is*

$$\Phi(C_d) = \frac{N-1}{N} \frac{|\mathcal{K}_{d-1}^{(L-1)}|}{\sum_{c=0}^{(L-d)/2} |\mathcal{K}_{d+2c}^{(L)}| (N-1)^{2c+1}}. \tag{6.77}$$

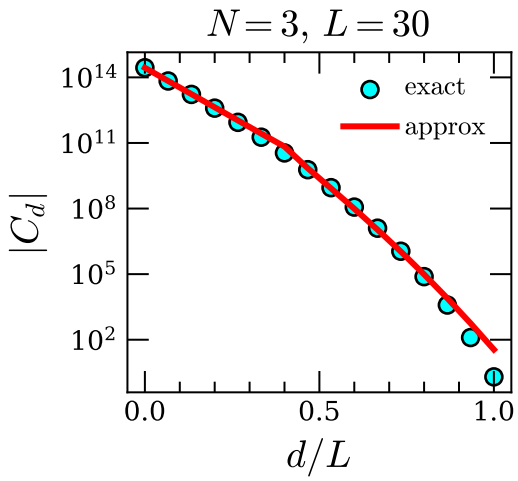

Figure 6.13: The number of states in the cone C_d for $N = 3, L = 30$. The exact result (circles) is compared with the asymptotic expression (6.81) (solid line).

In particular, when both L, d are large and $L - d = \Theta(L)$, $\Phi(C_d)$ behaves as

$$\Phi(C_d) \approx \frac{2(N-1)e^{(d/L-v_N)(1-v_N)}}{N^2}\left(\Theta(d-v_NL)(d/L-v_N)+\Theta(v_NL-d)\frac{e^{-\frac{(d-v_NL)^2}{2L}}}{\sqrt{2\pi L}}\right), \tag{6.78}$$

where $v_N = 1 - 2/N$ as before.

Proof. To determine $\Phi(C_d)$, we need to know the sizes of both C_d and its boundary. The exact size of C_d is

$$|C_d| = \sum_{c=0}^{(L-d)/2} |\mathcal{K}_{d+2c}|(N-1)^{2c+1}. \tag{6.79}$$

When both L and d are large, we may use (6.46) to write

$$|C_d| \approx \frac{(N-1)^{2-d}N^{L-1}}{\sqrt{2\pi L}}\int_0^{L-d} dx\ \exp\left(-\frac{(x+d-v_NL)^2}{2L}\right). \tag{6.80}$$

The value of this expression depends on the sign of $d/L - v_N$, which we will assume is $\Theta(L)$. If $d/L > v_N$, then the saddle point of the integrand does not lie within the integration domain, and we may approximate the integral by $e^{-(d-v_NL)^2/2L}/(d/L-v_N)$. If $d/L < v_N$ we may use the saddle point approximation, with the integral becoming $\sqrt{2\pi L}$. Thus

$$|C_d| \approx \frac{(N-1)^{2-d}N^{L-1}}{\sqrt{2\pi L}}\left(\Theta(d-v_NL)\frac{e^{-(d-v_NL)^2/(2L)}}{d/L-v_N}+\Theta(v_NL-d)\sqrt{2\pi L}\right), \tag{6.81}$$

which is shown plotted against the exact result (6.79) in Fig. 6.13. This result means that when $d > v_NL$, most of the states in C_d are concetrated at a depth of d, while when $d < v_NL$, most of the states are concentrated within a window of width $\sim \sqrt{L}$ around v_NL. This can be understood simply from the concentration of the biased random walk discussed

near (6.46).

To get $\Phi(C_d)$, we need to calculate the probability for states in C_d to move to the complement C_d^c under one step of $\mathcal{M}_{\text{nonloc}}$. Clearly the only states which can do so are those in the $N-1$ sectors at depth d. Under $\mathcal{M}_{\text{nonloc}}$, an arbitrary state is equally likely (with probability $1/N$) to move to each of the $N-1$ distinct sectors it is connected to. Therefore since there are $N-1$ sectors in C_d whose states can be connected to C_d^c,

$$\sum_{\psi\in C_d}\sum_{\psi'\in C_d^c}\langle\psi'|\mathcal{M}_{\text{nonloc}}|\psi\rangle = \frac{N-1}{N}|\{\psi\in\mathcal{K}_d\,:\,\partial\psi\cap\mathcal{K}_{d-2}\neq 0\}| \tag{6.82}$$

where $\mathcal{K}_d$ is one of the depth d sectors in C_d, $\mathcal{K}_{d-2}$ is the depth $d-2$ sector it is connected to, and $\partial\psi$ denotes those states that have nonzero overlap with $\mathcal{M}_{\text{nonloc}}|\psi\rangle$. If a state in $\mathcal{K}_d$ is to have $\partial\psi\cap\mathcal{K}_{d-2}\neq 0$, the length-$L$ walk on T_N associated to ψ must lie at depth $d-1$ at step $L-1$. Therefore

$$|\{\psi\in\mathcal{K}_d\,:\,\partial\psi\cap\mathcal{K}_{d-2}^{(L)}\}| = |\mathcal{K}_{d-1}^{(L-1)}|, \tag{6.83}$$

from which the exact expression (6.77) then follows. The approximate expression in (6.78) is then obtained using (6.46) and a bit of algebra. □

The most important aspect of (6.78) is that $\Phi(C_d)$ is exponentially small in L if $d<v_N L$, while it is $O(1)$ and roughly L-independent when $d>v_N L$. From (6.62), this means that a state initially localized in a random state in C_d will take exponentially long to diffuse out of C_d when $d<v_N L$, while it can take only $O(1)$ time when $d>v_N L$. This means that diffusion on the Krylov graph is fast for states corresponding to random walks that reach a distance further from the center of the graph than the expected distance of $v_N L$, and slow for states that reach a distance less than $v_N L$. The crossover between these two regimes occurs over a window of depths centered on $v_N L$ and of width $\sim\sqrt{L}$, which is where most of the states in $\mathcal{H}$ lie.

As a particular case of the previous lemma and (6.40), we have

Corollary 1. *The conductance of the region C_2 is*

$$\Phi(C_2) = (N-1)\frac{|\mathcal{K}_1^{(L-1)}|}{N^L-|\mathcal{K}_0^{(L)}|}\sim L^{-3/2}\rho^L, \tag{6.84}$$

where $\sim$ denotes equality in the asymptotic scaling sense.

This then gives the desired bound appearing in Theorem 4. □

By Cheeger's inequality, we thus have the following corollary:

Corollary 2. *The relaxation time $t_{\text{rel}}\equiv\Delta_{\mathcal{M}_{\text{nonloc}}}^{-1}$ satisfies*

$$t_{\text{rel}}\geq C' L^{3/2}\rho^{-L} \tag{6.85}$$

for an $O(1)$ constant C'.

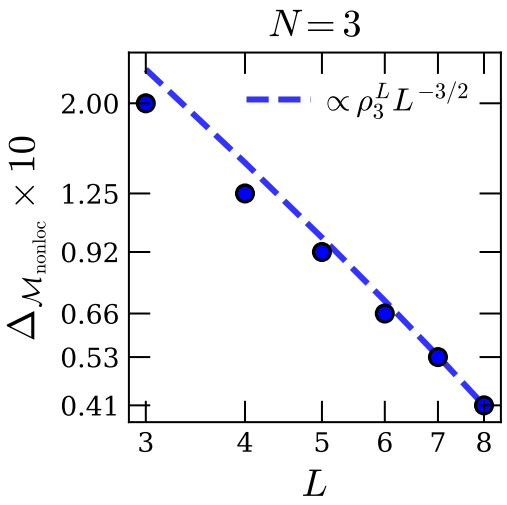

Figure 6.14: Markov gaps for $N = 3$, computed with exact diagonalization. *Left:* The gap $\Delta_{\mathcal{M}_{\rm nonloc}}$ of the non-local chain (blue circles) fit to the analytic bound $\propto \rho_3^L L^{-3/2}$ (dashed line). *Right:* As left, but for the local chain $\mathcal{M}_{\rm loc}$, and fit to $\propto \rho_3^L L^{-5/2}$.

The above arguments have only established an upper bound on the expansion, but in fact we expect this bound to be fairly tight, as we expect C_2 to be fairly close to the true region of minimal expansion. As steps in this direction, we note first that the region with minimal expansion will always be connected.[3] Suppose now that $\Phi(R)$ is minimized by a connected region whose boundary defines a cut between vertices on the Krylov graph, i.e. suppose that for all $\mathcal{K}_s$, either $\mathcal{K}_s \subset R$ or $\mathcal{K}_s \cap R = \emptyset$. If this is true then $\Phi(R)$ is obviously minimized for $R = C_d$ for some d, since for a given $\mathcal{K}_s \in R$, including every child sector of $\mathcal{K}_s$ in R increases $|R|$ but leaves $\sum_{\psi\in R}\sum_{\psi'\in R^c}\langle\psi'|\mathcal{M}_{\rm nonloc}|\psi\rangle$ unchanged. This C_2 defines a minimal expansion region if one can show that a minimal expansion cut must always be made *between* nodes on the Kyrlov graph, instead of being made *within* any particular node. This may not be true in complete generality, but we expect C_2 to be close enough to the region of minimal expansion that $\Phi(\mathcal{M}_{\rm nonloc})$ still follows the same asymptotic scaling as the upper bound (6.74). We thus conjecture that there exist constants C_1, C_2 such that

$$C_1 L^{-3}\rho^{2L} \leq \Delta_{\mathcal{M}_{\rm nonloc}} \leq C_2 L^{-3/2}\rho^L. \tag{6.87}$$

While $\rho < 1$—implying exponentially large relaxation times—the factors of $L^{-3/2}, L^{-3}$ appearing in the above inequality dominate over the exponentiall parts for modest values of L, meaning that for smaller system sizes we expect a mostly power-law scaling of $t_{\rm rel}$.

In Fig. 6.14 we determine the gaps of both $\mathcal{M}_{\rm nonloc}$ and its local variant $\mathcal{M}_{\rm loc}$ for very small system sizes using exact diagonalization. For the small values of L available, we observe a scaling of $\Delta_{\mathcal{M}_{\rm nonloc}} \sim \rho_3 L^{-3/2}$, consistent with a

[3] This follows simply from the fact that for positive numbers $A_{1,2}, V_{1,2}$,

$$\frac{A_1+A_2}{V_1+V_2} = \frac{A_1}{V_1}p + \frac{A_2}{V_2}(1-p) \geq \min(A_1/V_1, A_2/V_2), \tag{6.86}$$

where $p \equiv (1/V_2)/(1/V_1 + 1/V_2)$.

saturation of the upper bound on t_{rel} obtained from (6.87). We likewise observe a good fit of $\Delta_{\mathcal{M}_{\text{loc}}}$ to $\rho_3 L^{-5/2}$, with locality thus providing an extra factor of $1/L$, as advocated for around (6.73).

In the following subsections, we prove that the exponentially long thermalization time is also manifested in both the growth of entanglement entropy, and in the expectation values of certain local operators.

Entanglement entropy

We now use the formalism developed in the previous section to bound entropy growth. We will first focus on the case where the dynamics is that of a random unitary circuit perturbed by depolarizing noise on the boundary. In this setting, our diagnostic of thermalization will be the von Neumann entropy of the time-evolved state:

$$\overline{S}(t;\psi) \equiv \mathop{\mathbb{E}}_{\mathcal{C}_t} S(\mathcal{C}_t(|\psi\rangle\langle\psi|)), \tag{6.88}$$

where the average is over depth-t quantum circuits $\mathcal{C}_t$ defined as in the main text, and ψ is a product state of our choosing. More generally, for a subspace $R \subset \mathcal{H}$ spanned by product states, we will be interested in the average of the entanglement entropy when the initial states are sampled uniformly from R:

$$\overline{S}(t;R) \equiv \mathop{\mathbb{E}}_{\psi\in R} \overline{S}(t;\psi). \tag{6.89}$$

The ultimate fixed point of the dynamics we consider is always the maximally mixed state $\mathbf{1}$, so that regardless of R, $\overline{S}(t\to\infty;R) = L\ln N$.

We will prove the following:

Theorem 5. *Let C_d be as in (6.76), and suppose that d satisfies*

$$d < v_N L, \qquad v_N L - d = \Theta(L). \tag{6.90}$$

Then

$$\overline{S}(t;C_d) \lesssim L\ln(N)\left(1 - \frac{d}{L}\frac{\ln(N-1)}{\ln(N)} + t\frac{F_d}{\sqrt{L}}e^{-L\frac{(d/L-v_N)^2}{2}}\right) + c, \tag{6.91}$$

where $c = 1/e + 2\ln(N-1) - \ln(N)$ and F_d is an $O(1)$ constant:

$$F_d = \frac{4(N-1)}{\sqrt{2\pi}N^2} e^{(d/L-v_N)(1-v_N)}. \tag{6.92}$$

This means that the entropy of the system will take a time exponentially long in system size to saturate if initialized in a random state in C_d, although it may quickly approach the sub-maximal volume-law value of

$$\ln(|C_d|) \approx L\ln(N)\left(1 - \frac{d}{L}\frac{\ln(N-1)}{\ln(N)}\right). \tag{6.93}$$

In particular, it is easy to see that $\overline{S}(t;|\psi\rangle\langle\psi|) \le S(t;C_d)$ for all d if $|\psi\rangle$ is any state on the boundary of the Krylov graph,

and thus a bound on the thermalization times of such boundary states may be obtained by minimizing the RHS of (6.91) over d satisfying (6.90).

Proof. By the concavity of the entropy and linearity of the trace, we have

$$\overline{S}(t;C_d) \leq S(\mathop{\mathbb{E}}_{\mathcal{C}_t}\mathop{\mathbb{E}}_{\psi\in R_d}\mathcal{C}_t(|\psi\rangle\langle\psi|)) \equiv S(\bar{\rho}(t;d)), \tag{6.94}$$

where $\bar{\rho}(t;d)$ is the channel- and state-averaged density matrix:

$$\bar{\rho}(t;d) = \mathop{\mathbb{E}}_{\mathcal{C}_t}\mathop{\mathbb{E}}_{\psi\in C_d}\mathcal{C}_t(|\psi\rangle\langle\psi|). \tag{6.95}$$

Normally this inequality is of limited use when studying random unitary circuits, since the averaged reduced density matrix is usually rendered trivial by the average over the RU part of the dynamics. In our case, the slow mixing of $\mathcal{M}$ will mean this is not so; indeed our above result on t_{rel} will be seen to imply that for exponentially long times, $\bar{\rho}(t;d)$ has most of its support on only an exponentially small fraction of Hilbert space.

Anticipating this, we will first show that if σ is a density matrix mostly supported on some subspace R, and if σ does not connect R with its complement, then $S(\sigma)$ cannot be much more than $\ln|R|$. To this end, define

$$\sigma^R \equiv \frac{\Pi_R\sigma\Pi_R}{\text{Tr}[\Pi_R\sigma]}, \tag{6.96}$$

where Π_R projects onto R. If $\Pi_R\sigma\Pi_{\bar{R}}^{\perp} = 0$ (where $\Pi_{\bar{R}}^{\perp} \equiv \mathbf{1} - \Pi_R$), then the trace distance between σ and σ^R is

$$\begin{aligned} T(\sigma,\sigma^R) &= \text{Tr}|\sigma^R - \sigma| \\ &= \text{Tr}\left|\frac{\Pi_R\sigma\Pi_R}{\text{Tr}[\Pi_R\sigma]} - \Pi_R\sigma\Pi_R - \Pi_{\bar{R}}^{\perp}\sigma\Pi_{\bar{R}}^{\perp}\right| \\ &= 1 - \text{Tr}[\Pi_R\sigma] + \text{Tr}[\Pi_{\bar{R}}^{\perp}\sigma] \\ &= 2\text{Tr}[\Pi_{\bar{R}}^{\perp}\sigma]. \end{aligned} \tag{6.97}$$

Fannes' inequality then implies[4]

$$|S(\sigma) - S(\sigma^R)| \leq T(\sigma,\sigma^R)\ln(N^L) + \frac{1}{e} = 2L\ln(N)\text{Tr}[\Pi_{\bar{R}}^{\perp}\sigma] + \frac{1}{e}. \tag{6.98}$$

Since $\text{rank}(\sigma^R) \leq |R|$, we have $S(\sigma^R) \leq \ln|R|$. Therefore

$$S(\sigma) \leq \ln|R| + 2L\ln(N)\text{Tr}[\Pi_{\bar{R}}^{\perp}\sigma] + \frac{1}{e}. \tag{6.99}$$

[4]This is not the strongest version of Fannes' inequality, but strengthening it only modifies the unimportant L-independent part.

We now apply the above inequality to the model under study. From the definition of $\bar{\rho}_A(t;d)$,

$$\mathrm{Tr}[\Pi_{C_d}^{\perp}\bar{\rho}(t;d)] = P(\psi(t) \in C_d^c \,|\, \psi(0) \in C_d), \tag{6.100}$$

where the probability on the RHS is calculated using $\mathcal{M}$. From (6.63), we then know that

$$\mathrm{Tr}[\Pi_{C_d}^{\perp}\bar{\rho}(t;d)] \leq t\Phi(C_d). \tag{6.101}$$

Since $\bar{\rho}(t;d)$ is diagonal in the computational basis, we have $\Pi_{C_d}\bar{\rho}(t;d)\Pi_{C_d}^{\perp} = 0$, which allows us to apply (6.99) to give

$$\bar{S}(t;C_d) \leq \ln(|C_d|) + 2tL\ln(N)\Phi(C_d) + \frac{1}{e}. \tag{6.102}$$

By (6.78) and our assumption that $d < v_N L$, the expansion of C_d is

$$\Phi(C_d) \approx \frac{F_d}{2\sqrt{L}} e^{-L\frac{(d/L-v_N)^2}{2}}, \tag{6.103}$$

where the $O(1)$ constant F_d is defined as in (6.92). Relatedly, (6.81) gives $|C_d| \approx (N-1)^{2-d}N^{L-1}$ since $d < v_N L$, and so

$$\bar{S}(t;C_d) \lesssim L\ln(N)\left(1 - \frac{d}{L}\frac{\ln(N-1)}{\ln(N)} + t\frac{F_d}{\sqrt{L}}e^{-L\frac{(d/L-v_N)^2}{2}}\right), \tag{6.104}$$

where the $\lesssim$ indicates that we have dropped the constant c appearing in (6.91). □

This Theorem shows that the entropy for typical states in C_d will take a time exponential in system size to fully saturate provided $v_N - d/L$ is positive and order L^0. To make this more concrete, we define the entanglement saturation time $t_S(\gamma;\psi)$ as the time needed for $\bar{S}(t;\psi)$ to reach a fraction γ of its maximal value $\bar{S}(t\to\infty;\psi) = L\ln N$:

$$t_S(\gamma;\psi) \equiv \min\{t \,:\, \bar{S}(t;\psi) \geq \gamma L\ln N\}. \tag{6.105}$$

We then have:

Corollary 3. *Suppose that γ satisfies*

$$1 > \gamma > \gamma_*, \qquad \gamma_* \equiv 2\left(1 - v_N\frac{\ln(N-1)}{\ln(N)}\right), \tag{6.106}$$

with $|\gamma - \gamma_*| = \Theta(L^0)$. Then if $|\psi\rangle$ is a state on the boundary of the Krylov graph,

$$t_S(\gamma;\psi) \geq \frac{\gamma}{2F_{d_\gamma}}\sqrt{L}e^{L\frac{(d_\gamma/L-v_N)^2}{2}}, \tag{6.107}$$

where

$$d_\gamma = L(1-\gamma/2)\frac{\ln(N)}{\ln(N-1)}. \tag{6.108}$$

Proof. This follows directly from Theorem 5 after fixing $d = d_\gamma$, so that $1 - (d/L)\ln(N-1)/\ln(N) = \gamma/2$. □

Note that $|\gamma - \gamma_*| = \Theta(L^0)$ implies $|d_\gamma - v_N L| = \Theta(L)$, so that $t_S(\gamma;\psi)$ is exponentially large in L. The result (6.91) suggests that a product state at the boundary of the Krylov graph thermalizes in the following two-stage process. In the first stage, the system undergoes a period of rapid entanglement growth as it quickly occupies sectors at depths $d \geq v_N L$, with the entropy reaching a value of $\overline{S} \approx \ln|C_{v_N L}|$. In the second stage, it undergoes a gradual $\ln(t)$ growth which takes exponentially long in L to saturate to the steady state value. Note that the length of the first stage becomes smaller as N gets larger, on account of the fact that $v_{N\to\infty} = 1$.

While there are exponentially many states on the boundary of the Krylov graph, such states are still an exponentially small fraction of all computational basis product states. Nevertheless, a random product state is exponentially likely to have an entanglement saturation time scaling in the same way as states on the boundary of the Krylov graph:

Corollary 4. *For γ satisfying (6.106),*

$$P_\psi\left[t_S(\gamma;\psi) \geq \frac{\gamma}{2F_{d_\gamma}}\sqrt{L}e^{L\frac{(d_\gamma/L - v_N)^2}{2}}\right] \gtrsim 1 - \frac{\sqrt{L}}{\sqrt{2\pi}d_\gamma}e^{-L\frac{(d_\gamma/L-v_N)^2}{2}}, \tag{6.109}$$

where ψ is sampled uniformly from all computational basis product states.

Thus with unit probability in the $L \to \infty$ limit, the dynamics initialized from $|\psi\rangle$ takes exponentially long to thermalize.

Proof. As we have seen above, if ψ is sampled uniformly from $\mathcal{H}$, for large L, $|\mathsf{irr}(\psi)|$ will be distributed according to a biased random walk on $\mathbb{N}$ with velocity v_N, and hence $P_\psi[|\mathsf{irr}(\psi)| = d] \approx \frac{1}{\sqrt{2\pi L}}e^{-L(d/L-v_N)^2/2}$. Thus

$$P_\psi[|\mathsf{irr}(\psi)| \leq d_\gamma] \lesssim \frac{1}{\sqrt{2\pi L}}\int_0^{d_\gamma} dx\, e^{-L\frac{(x/L-v_N)^2}{2}} \approx \frac{\sqrt{L}}{\sqrt{2\pi}d_\gamma}e^{-L\frac{(d_\gamma/L-v_N)^2}{2}}, \tag{6.110}$$

which is exponentially small in L since $|d_\gamma - v_N L| = \Theta(L)$. Thus a randomly drawn ψ is exponentially likely to be contained in C_{d_γ}. Furthermore, the concentration of $|\mathsf{irr}(\psi)|$ about $v_N L$ means that the saturation time of this randomly chosen state will be bounded using $1/\Phi(C_{d_\gamma})$ in the same way as in Corollary 3. □

Thus far we have focused on the entropy of the full system's density matrix when undergoing evolution by the open dynamics $\mathcal{C}_t$. In the setting with closed system time evolution performed by an appropriate random unitary circuit $\mathcal{U}_t$,

Corollary 5. *For a spatial bipartition AB, $|A| = |B| = L/2$, define the circuit-averaged bipartite entanglement entropy as*

$$\overline{S}_A(t;\psi) \equiv \mathop{\mathbb{E}}_{\mathcal{U}_t} S(\mathrm{Tr}_B[\mathcal{U}_t^\dagger|\psi\rangle\langle\psi|\mathcal{U}_t]). \tag{6.111}$$

Then $\overline{S}_A(t;C_d) \equiv \mathbb{E}_{\psi\in C_d}\overline{S}_A(t;\psi)$ satisfies

$$\overline{S}_A(t;C_d) \lesssim L\ln(N)\left(1 - \frac{d}{L}\frac{\ln(N-1)}{\ln(N)} + t\frac{2F_d}{\sqrt{L}}e^{-L\frac{(d/L-v_N)^2}{2}}\right) + c, \tag{6.112}$$

whose only difference with respect to the bound (6.91) *is a factor of 2 in the term proportional to* t.

Proof. The reasoning is almost exactly the same as in the proof of Theorem 5. The only difference is in the anologue of (6.98) that one obtains, which instead reads

$$|S(\sigma_A) - S(\sigma_A^R)| \leq T(\sigma_A, \sigma_A^R) \ln(N^{L/2}) + \frac{1}{e} \leq L \text{Tr}[\Pi_{\overline{R}}^{\perp} \sigma] \ln N + \frac{1}{e}. \tag{6.113}$$

This follows from (6.98) after using the fact that the trace distance is monotonically decreasing under partial trace, so that the reduced density matrices σ_A, σ_A^R of the σ, σ^R appearing in (6.98) satisfy

$$T(\sigma_A, \sigma_A^R) \leq 2\text{Tr}[\Pi_{\overline{R}}^{\perp} \sigma]. \tag{6.114}$$

□

Note that the maximum possible value of $\overline{S}_A(t; C_d)$ is $\frac{L}{2} \ln N$, which is smaller than the $t = 0$ value of (6.112) only if

$$\ln(|C_{v_N L}|) = L \ln(N) \left(1 - \frac{d}{L} \frac{\ln(N-1)}{\ln(N)}\right) < \frac{L}{2} \ln N \implies N \geq 5, \tag{6.115}$$

from which we conclude that (6.112) provides a meaningful bound only if $N \geq 5$.

Operator relaxation times

We now examine how operator expectation values diagnose the long relaxation times computed above. For an operator $\mathcal{O}$ of unit norm and a computational basis product state $|\psi\rangle$, we define the relaxation time $t_{\mathcal{O}}(\gamma; \psi)$ by the time needed for the expectation value of $\mathcal{O}$ in the circuit-averaged state $\bar{\rho}(t; \psi) \equiv \mathbb{E}_{\mathcal{C}_t} \mathcal{C}_t(|\psi\rangle\langle\psi|)$ to relax to within an amount γ of its circuit-averaged equilibrium value, where we require that $0 < \gamma < 1$, $\gamma = \Theta(L^0)$. Since the circuit-averaged density matrix at long times is simply $\mathbf{1}/|\mathcal{H}|$, this definition reads

$$t_{\mathcal{O}}(\gamma; \psi) \equiv \min\{t \,:\, |\langle \mathcal{O} \rangle_{\bar{\rho}(t;\psi)} - \frac{1}{|\mathcal{H}|} \text{Tr}[\mathcal{O}]| \leq \gamma\}. \tag{6.116}$$

It is not obvious that operators with exponentially long relaxation times exist. If one was willing to give up locality, a naive guess would be to let $|\psi\rangle$ be a state at the edge of the Krylov graph, and to set $\mathcal{O} = |\widetilde{\psi}\rangle\langle\widetilde{\psi}|$, where $|\widetilde{\psi}\rangle$ is any product state on the edge of the tree whose Hamming distance with $|\psi\rangle$ is L. In this case $\langle \mathcal{O} \rangle_{\bar{\rho}_\psi(t)}$ vanishes at $t = 0$ and indeed takes a time of $\sim t_{\text{rel}}$ to increase to its equilibrium value, but that value is $\text{Tr}[|\widetilde{\psi}\rangle\langle\widetilde{\psi}|]/|\mathcal{H}| = N^{-L}$, whose smallness means that $t_{|\widetilde{\psi}\rangle\langle\widetilde{\psi}|}(\gamma; \psi) = 0$ by virtue of our requirement that $\gamma = \Theta(L^0)$.

Fortunately, there nevertheless exist local operators whose relaxation times are exponentially long. These are the normalized charge operators

$$Q_a = \frac{2}{L} \sum_i (-1)^i |a\rangle\langle a|_i. \tag{6.117}$$

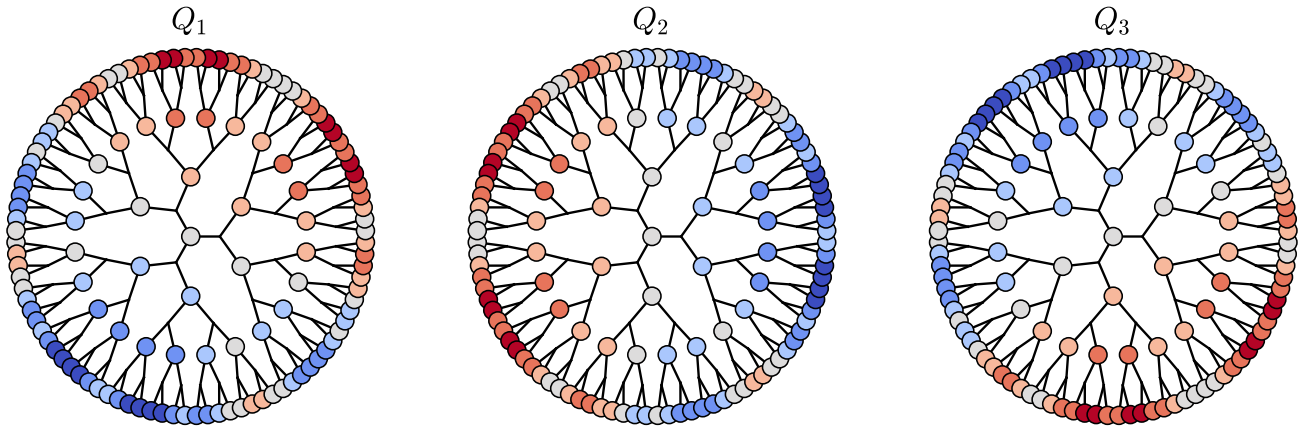

Figure 6.15: The quantum numbers of each Krylov sector under the symmetries Q_a for $N = 3$ and a system of size $L = 6$. The darkest red sectors have the maximum value of $Q_a = L/2$; the darkest blue have $Q_a = -L/2$.

Indeed, let $\psi_{\max,a}$ be a product state with maximal Q_a charge $\langle Q_a \rangle_{\psi_{\max,a}} = 1$. For concreteness, we will fix $\psi_{\max,a} = (ba)^{L/2}$ where $b = a + 1 \mod N$. In this section, we will prove the following theorem:

Theorem 6. *Let $0 < \gamma < v_N/2$, $\gamma = \Theta(L^0)$. Then the relaxation time of Q_a in the state $|\psi_{\max,a}\rangle$ is exponentially long:*

$$t_{Q_a}(\gamma; \psi_{\max,a}) \gtrsim D_\gamma \sqrt{L} e^{L \frac{(2\gamma - v_N)^2}{2}}, \tag{6.118}$$

where the $O(1)$ constant D_γ is defined as

$$D_\gamma \equiv \frac{2(1+2\gamma)(N-1)}{N^2\sqrt{2\pi}} e^{-(2\gamma - v_N)(1-v_N)}. \tag{6.119}$$

We will in fact prove a slightly more general version of this theorem which allows for more freedom in the choice of the initial state.

Proof. Our proof strategy is to define a subspace A of states in $\mathcal{H}$ which all have a large nonzero expectation value of Q_a, and then argue that a system initialized in A typically takes an exponentially long time to move to the complement A^c of A in $\mathcal{H}$. While knowing the values of Q_a in a given product state do not allow one to distinguish where in the Krylov graph that state lies, the distribution of Q_a charges in the Krylov graph is not homogeneous (see Fig. 6.15), and this can be used to select out an appropriate choice of A. Fixing $b \equiv (a+1) \mod N$ as above, and assuming that $L\eta \in 2\mathbb{N}$ in what follows for simplicity of notation, the space we choose is the cone

$$A = C_{(ba)^{L\eta/2}} = \{\psi : \mathsf{irr}(\psi) = (ba)^{\lfloor L\eta/2 \rfloor} \times \Sigma^*\}, \tag{6.120}$$

where Σ^* is the set of the irreducible strings of all the product states of length less than $L(1-\eta)$, namely A is the space of all product states whose irreducible strings have the first $2\lfloor L\eta/2 \rfloor$ elements equal to $(ba)^{L\eta/2}$ (c.f. (6.76)).

Let us compute the expected value of Q_a obtained after evolving a random state in A for time t,

$$\langle Q_a\rangle_A(t) \equiv \mathop{\mathbb{E}}_{\psi\in A}\langle Q_a\rangle_{\bar\rho(t;\psi)}. \tag{6.121}$$

This is

$$\begin{aligned}\langle Q_a\rangle_A(t) &= \mathop{\mathbb{E}}_{\psi\in A}\left(\sum_{\psi'\in A} P(\psi(t)=\psi'|\psi(0)=\psi)\langle Q_a\rangle_{\psi'} + \sum_{\psi'\in A^c} P(\psi(t)=\psi'|\psi(0)=\psi)\langle Q_a\rangle_{\psi'}\right)\\ &\geq \mathop{\mathbb{E}}_{\psi\in A}\left(\sum_{\psi'\in A} P(\psi(t)=\psi'|\psi(0)=\psi)\langle Q_a\rangle_{\psi'}\right) - P(\psi(t)\in A^c\,|\,\psi(0)\in A),\end{aligned} \tag{6.122}$$

where we used $\min_{\psi\in\mathcal{H}}\langle Q_a\rangle_\psi = -1$. To deal with the first term, we need

Lemma 2. *The average charge of states which begin in A and remain in A at time t satisfies*

$$\mathop{\mathbb{E}}_{\psi\in A}\sum_{\psi'\in A} P(\psi(t)=\psi'\,|\,\psi(0)=\psi)\langle Q_a\rangle_{\psi'} \geq \eta(1-P(\psi(t)\in A^c\,|\,\psi(0)\in A)). \tag{6.123}$$

Proof. This is true because the average value of Q_a for states in A is at least η. Showing this is complicated slightly by the fact that there exist states in A with $\langle Q_a\rangle_\psi$ as small as $\eta-(1-\eta)=2\eta-1$. Our strategy will be to show that these states always pair up with states of larger charge to give an average charge bounded below by η.

To this end, for each $\psi\in A$, write $\mathsf{irr}(\psi) = (ba)^{L\eta/2}\times s_\psi$ for some length $|\mathsf{irr}(\psi)|-L\eta$ irreducible string s_ψ. Suppose first that the second entry of s_ψ is not equal to a, $[s_\psi]_2\neq a$. Then define $\widetilde{\psi}$ as the state whose irreducible string differs from $\mathsf{irr}(\psi)$ by a cyclic permutation on the last $|s_\psi|$ entries:

$$s_{\widetilde{\psi}} = T(s_\psi), \tag{6.124}$$

where T is the cyclic permutation $T(a_1\cdots a_n)=a_2a_3\cdots a_{n-1}a_1$. Note that $\mathsf{irr}(\widetilde{\psi}) = \mathsf{irr}(\psi)\times s_{\widetilde{\psi}}$ is an allowed irreducible string since $[s_{\widetilde{\psi}}]_2\neq a$ by assumption. Thus

$$\mathop{\mathbb{E}}_{\psi'\in A} P(\psi(t)=\psi\,|\,\psi(0)=\psi') = \mathop{\mathbb{E}}_{\psi'\in A} P(\psi(t)=\widetilde{\psi}\,|\,\psi(0)=\psi'). \tag{6.125}$$

We may thus write

$$\begin{aligned}\mathop{\mathbb{E}}_{\psi\in A}\sum_{\psi'\in A} P(\psi(t)=\psi'|\psi(0)=\psi)\langle Q_a\rangle_{\psi'} = \mathop{\mathbb{E}}_{\psi\in A}\sum_{\psi'\in A\,:\,[s_{\psi'}]_2\neq a} P(\psi(t)=\psi'|\psi(0)=\psi)\frac{\langle Q_a\rangle_{\psi'}+\langle Q_a\rangle_{\widetilde{\psi}'}}{2}\\ + \mathop{\mathbb{E}}_{\psi\in A}\sum_{\psi'\in A\,:\,[s_{\psi'}]_2=a}\mathop{\mathbb{E}}_{\psi\in A} P(\psi(t)=\psi'\,|\,\psi(0)=\psi)\langle Q_a\rangle_\psi,\end{aligned} \tag{6.126}$$

The point of writing things like this is that $(\langle Q_a\rangle_{\psi'}+\langle Q_a\rangle_{\widetilde{\psi}'})/2=\eta$, simply because the Q_a charge of $s_{\widetilde{\psi}}$ is opposite to that of s_ψ (on account of the fact that T interchanges sublattices and thus $TQ_aT^{-1}=-Q_a$), meaning that $(\langle Q_a\rangle_{\psi'}+$

$\langle Q_a\rangle_{\widetilde{\psi'}})/2$ receives contributions only from the first $L\eta$ characters of $\mathsf{irr}(\psi')$, which carry a Q_a charge of η. Therefore

$$\begin{aligned}\mathop{\mathbb{E}}_{\psi\in A}\sum_{\psi'\in A}P(\psi(t)=\psi'|\psi(0)=\psi)\langle Q_a\rangle_{\psi'} = \eta \mathop{\mathbb{E}}_{\psi\in A}\sum_{\psi'\in A\,:\,[s_{\psi'}]_2\neq a}P(\psi(t)=\psi'|\psi(0)=\psi)\\ + \mathop{\mathbb{E}}_{\psi\in A}\sum_{\psi'\in A\,:\,[s_{\psi'}]_2= a}P(\psi(t)=\psi'\,|\,\psi(0)=\psi)\langle Q_a\rangle_{\psi}.\end{aligned} \tag{6.127}$$

The second summand in (6.127) can be dealt with similarly. Since this summand contains only states with $[s_{\psi'}]_2 = a$, $(ba)^{L\eta/2}\times T(s_{\psi'})$ is not an allowed irreducible string. We thus instead split up the states in the sum as $\psi' = (ba)^{L\eta/2}ca\times p_{\psi'}$ for some $c\neq a$, where $p_{\psi'}$ is a length $L-L\eta/2-2$ irreducible string with $[p_{\psi'}]_1\neq a$. We can then pair up the subset of these states with $[p_{\psi'}]_2\neq a$ in the same manner as was done above by defining an appropriate $\widetilde{\psi'}$ obtained from cyclically shifting $p_{\psi'}$; each pair appearing in the sum is then seen to have an average Q_a charge of $\eta+2/L$. Repeating this process, the successive paired states one generates are all seen to have average charge $\eta+2n/L$, with $0<n\leq(1-\eta)L/2$. Since these average charges are all strictly greater than η, we obtain the bound

$$\begin{aligned}\mathop{\mathbb{E}}_{\psi\in A}\sum_{\psi'\in A}P(\psi(t)=\psi'|\psi(0)=\psi)\langle Q_a\rangle_{\psi'} &\geq \eta \mathop{\mathbb{E}}_{\psi\in A}\sum_{\psi'\in A}P(\psi(t)=\psi'\,|\,\psi(0)=\psi)\\ &= \eta P(\psi(t)\in A\,|\,\psi(0)\in A)\\ &= \eta(1-P(\psi(t)\in A^c\,|\,\psi(0)\in A)),\end{aligned} \tag{6.128}$$

which is what we wanted to show. □

This result lets us write (6.122) as

$$\langle Q_a\rangle_A(t)\geq\eta-(1+\eta)P(\psi(t)\in A^c\,|\,\psi(0)\in A)), \tag{6.129}$$

with the second term being bounded from above by $t\Phi(A)$ as in (6.63). Since A is a union of cones, the expansion of A is simply

$$\Phi(A)=\Phi(C_{L\eta+2}), \tag{6.130}$$

and so

$$\langle Q_a\rangle_A(t)\geq\eta-t(1+\eta)\Phi(C_{L\eta+2}). \tag{6.131}$$

As we saw in (6.78), $\Phi(C_d)$ is exponentially small only when $d<v_NL, |d/L-v_N|=\Theta(L^0)$. To get a long relaxation time, we thus will need to assume that

$$\eta<v_N, \tag{6.132}$$

with $|\eta-v_N|=\Theta(L^0)$. If this is the case, we conclude from (6.78) that

$$\langle Q_a\rangle_A(t)\geq\eta-\frac{t}{D_{\eta/2}\sqrt{L}e^{L\frac{(\eta-v_N)^2}{2}}}, \tag{6.133}$$

with the constant

$$D_{\eta/2} \equiv \frac{N^2\sqrt{2\pi}}{2(1+\eta)(N-1)} e^{-(\eta - v_N)(1-v_N)}. \tag{6.134}$$

The advertised bound on $t_{Q_a}(\gamma; \psi_{\max,a})$ is then obtained by setting $\eta = 2\gamma$. Notably, when $\gamma \to 0$, $\langle Q_a \rangle_A(t) \gtrsim 2\gamma - t\Phi(C_2)$, so that the lower bound of t_Q is equal to that of the relaxation time, i.e.,

$$t_{Q_a}(\gamma \to 0; \psi_{\max,\mathrm{a}}) \gtrsim 1/\Phi(C_2) \sim L^{3/2}\rho_3^{-L}. \tag{6.135}$$

□

6.5.4 $N = 2$

We now compute the expansion for $N = 2$. In this case we expect a large expansion—and hence a fast mixing time—due to the absence of strong Hilbert space bottlenecks.

In this subsection we will find it most convenient to label the Krylov sectors by their charge Q, defined as

$$Q \equiv \sum_i (-1)^i Z_i, \tag{6.136}$$

with $\langle Q \rangle_\psi$ measuring the endpoint of the random walk defined by the product state ψ. For a length-L system, there are thus $L+1$ sectors $\mathcal{K}_Q$, with $Q \in \{-L, -L+2, \cdots, L-2, L\}$ (in the language of the charges Q_a discussed for $N > 2$, $Q = Q_1 - Q_2$). The dimensions of these sectors are accordingly determined as

$$|\mathcal{K}_Q| = \binom{L}{\frac{L+Q}{2}}. \tag{6.137}$$

We now argue that charge relaxation in this case is polynomially fast. In particular, we will argue that the spectral gap of $\mathcal{M}_{\mathrm{nonloc}}$ satisfies

$$\frac{1}{\pi L} \leq \Delta_{\mathcal{M}_{\mathrm{nonloc}}} \leq \sqrt{\frac{8}{\pi L}}. \tag{6.138}$$

We will give a rigorous proof of the upper bound, and a slightly less rigorous one for the lower bound. As in our analysis of the $N > 2$ case, the lack of rigour for the lower bound comes from making the assumption that the subset $S \subset \mathcal{H}$ with minimal expansion is determined by a cut which passes "between" two Krylov sectors, rather than cutting "within" a given sector. Even if this is not true, we expect the minimal expansion to be asymptotically the same as the minimum expansion of a region defined by making only inter-sector cuts.

With this assumption, it is straightforward to see that the S with minimal expansion can be taken without loss of generality to be of the form

$$S_Q = \bigcup_{Q' \geq Q} \mathcal{K}_{Q'}, \tag{6.139}$$

with the minimal S_Q having $Q \geq 0$ without loss of generality; in the language of our $N > 2$ discussion this is simply a

cone C_Q. To find the minimal S_Q, we use the recursion relation

$$|\mathcal{K}_Q| = |\partial S_Q| + |\partial S_{Q+2}|, \tag{6.140}$$

which holds for all $Q \geq 0$ and follows from the fact that each state in $\mathcal{K}_Q$ is connected to exactly one state in $\mathcal{K}_{Q+2} \cup \mathcal{K}_{Q-2}$. Solving this recursion relation for $|\partial S_Q|$ yields

$$|\partial S_Q| = \sum_{Q'=Q}^{L} (-1)^{\frac{Q'-Q}{2}} |\mathcal{K}_{Q'}|, \tag{6.141}$$

where the sum accordingly only includes those Q' with the same parity as L. Now the difference in expansions between adjacent sectors is

$$\Phi(S_{Q+2}) - \Phi(S_Q) = \frac{|S_Q||\partial S_{Q+2}| - |S_{Q+2}||\partial S_Q|}{|S_Q||S_{Q+2}|}, \tag{6.142}$$

which can be evalulated using (6.141) and the dimensions $|\mathcal{K}_Q|$, with some unilluminating algebra showing that the RHS is always positive, meaning that $\Phi(S_Q)$ is minimized on the smallest value of Q (viz. $Q_{min} = L \mod 2$). Taking $L \in 2\mathbb{N}+1$ for notational simplicity, this gives

$$\Phi_* = \Phi(S_1) = 2^{1-L} \sum_{k=0}^{(L-1)/2} (-1)^k \binom{L}{\frac{L+1}{2}+k} = \frac{L+1}{L2^L} \binom{L}{\frac{L+1}{2}} \approx \sqrt{\frac{2}{\pi}} L, \tag{6.143}$$

where we used $|S_1| = |\mathcal{H}|/2$ in the second equality, $\sum_{k=0}^{l} (-1)^k \binom{2l+1}{l+k+1} = \frac{l+1}{2l+1} \binom{2l+1}{l+1}$ in the third, and Stirling's approximation in the fourth. Cheeger's inequality thus tells us that

$$\frac{1}{\pi L} \leq \Delta_{\mathcal{M}_{\text{nonloc}}} \leq \sqrt{\frac{8}{\pi L}}, \tag{6.144}$$

which is what we wanted to show.

Calculating the gaps of $\Delta_{\mathcal{M}_{\text{loc}}}, \Delta_{\mathcal{M}_{\text{nonloc}}}$ exactly for small values of L with exact diagonalization yields the scaling shown in Fig. 6.16. Even for very small values of L, the scaling of $\Delta_{\mathcal{M}_{\text{nonloc}}}$ fits very well to the linear lower bound of $\sim L^{-1}$. The gap of the local chain $\mathcal{M}_{\text{loc}}$ is (as expected) observed to scale slower by one power of L as $\Delta_{\mathcal{M}_{\text{loc}}} \sim L^{-2}$, consistent with the simulations of Fig. 6.3. These finding are consistent with those reported in Ref. [121].

6.6 Lack of thermalization in Temperley-Lieb models perturbed by a single-site impurity

In this section we show that a certain class of $SU(N)$ symmetric models—referred to as Temperely-Lieb Hamiltonians in what follows—are such that they remain fragmented even when perturbed by an arbitrary term that has support only

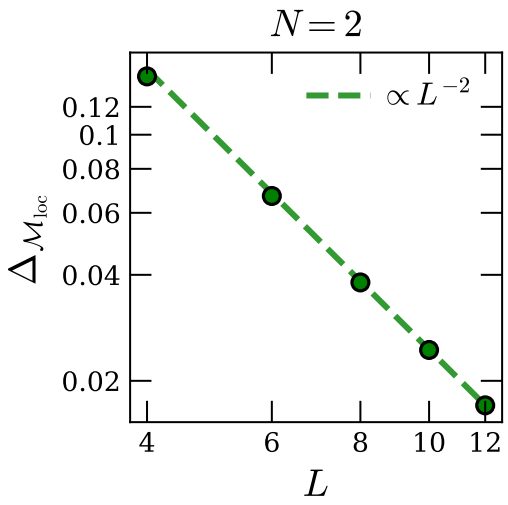

Figure 6.16: Markov gaps for $N = 2$, computed with exact diagonalization. *Left:* The gap $\Delta_{\mathcal{M}_{\rm nonloc}}$ of the non-local chain (green circles) fit to the analytic bound $\propto L^{-1}$ (dashed line). *Right:* As left, but for the local chain $\mathcal{M}_{\rm loc}$, and fit to $\propto L^{-2}$.

on a *single site*. The Hamiltonians we consider are of the form [107, 108, 109]

$$H_{TL} = \sum_{i=1}^{L} g_i P_{i,i+1}, \qquad P_{i,i+1} \equiv \frac{1}{N} \sum_{a,b=1}^{N} |a,a\rangle\langle b,b|_{i,i+1} \equiv |\Psi\rangle\langle\Psi|_{i,i+1} \tag{6.145}$$

with $N > 2$ in all of what follows. The projectors $P_{i,i+1}$ satisfy $P_{i,i+1}^2 = P_{i,i+1}$ and obey the Temperly-Lieb algebra

$$\begin{aligned} P_{i,i+1}P_{j,j+1}P_{i,i+1} &= \frac{1}{N^2} P_{i,i+1}, \quad i = j \pm 1 \\ P_{i,i+1}P_{j,j+1} &= P_{j,j+1}P_{i,i+1}, \quad |i-j| > 1. \end{aligned} \tag{6.146}$$

The product states $|s\rangle = \bigotimes_{i=1}^{L} |s_i\rangle$ with $s_i \neq s_{i+1}$ for all $i = 1, \ldots, L-1$ are clearly annihilated by H_{TL}. However, these are far from the only types of states in the kernel of H_{TL}. Frozen states can be constructed using "singlets" like $|\Phi_{ab}\rangle \propto |aa\rangle - |bb\rangle$, which are orthogonal to $|\Psi\rangle$, as well as more complicated states. For example, when $L = 3$ we may write down the state

$$|\Lambda\rangle \propto \sum_{a=1,\ldots,N} \zeta_N^{a-1}(|1aa\rangle + |aa1\rangle) - |111\rangle, \tag{6.147}$$

where $\zeta_N = e^{2\pi i/N}$. $|\Lambda\rangle$ is annihilated by both $P_{1,2}$ and $P_{2,3}$ but is not constructible from the $|\Phi_{ab}\rangle$ or the $|s\rangle$. This makes enumerating H_{TL}'s frozen states rather complicated.

Nevertheless, owing to the TL algebra obeyed by the projectors $P_{i,i+1}$, quite a large amount of information about the spectrum of H_{TL} can be determined analytically, even without explicitly constructing any eigenstates. We will only need to know a few facts about the counting of H_{TL}'s degenerate levels, the first of which is [108]

Proposition 4. *On an open chain of length L, the number of zero-energy eigenstates of H_{TL} is*

$$|\Omega_L| = \frac{(N+\sqrt{N^2-4})^{L+1} + (N-\sqrt{N^2-4})^{L+1}}{2^{L+1}\sqrt{N^2-4}}. \tag{6.148}$$

If $g_i \geq 0$ for all i, H_{TL} is frustration free, and the states in Ω_L are in one-to-one correspondence with the ground states of H_{TL}. Our results however will hold for arbitrary g_i.

Proof. To keep our presentation self-contained, we will reproduce the proof from Ref. [108]. Let Ω_L denote the space of states annihilated by all of the $P_{i,i+1}$:

$$\Omega_L \equiv \bigcap_i \ker P_{i,i+1}. \tag{6.149}$$

We are interested in obtaining the dimension $|\Omega_L|$ of this space.

We proceed by induction. Given Ω_{L-1}, we determine Ω_L as

$$\Omega_L = \ker(P_{1,2} : \mathcal{H} \otimes \Omega_{L-1} \to |\Psi\rangle \otimes \Omega_{L-2}), \tag{6.150}$$

where $\mathcal{H}$ is the onsite Hilbert space. It is easy to check that the map $P_{1,2}$ is surjective, and thus $|\Omega_L|$ is determined as

$$|\Omega_L| = \dim[\mathcal{H} \otimes \Omega_{L-1}] - \dim[|\Psi\rangle \otimes \Omega_{L-2}] = N|\Omega_{L-1}| - |\Omega_{L-2}|. \tag{6.151}$$

The initial values needed to set up a recurrence relation are $|\Omega_0| = 1$, $|\Omega_1| = N$. The soltuion to this recurrence relation is precisely (6.148). □

We now ask about the spectrum of the model

$$H = H_{TL} + H_{\text{imp}}, \tag{6.152}$$

where H_{imp} is an arbitrary $N \times N$ single-site Hamiltonian acting on the first site only. Cases with impurities acting in the middle of the chain, or with multiple non-adjacent impurities, can be treated similarly at the expense of more complicated notation.

We can use a similar approach as the one used in the computation of $|\Omega_L|$ to determine a large number of degenerate states of H:

Proposition 5. *Let $|\alpha\rangle$ be the eigenstates of H_{imp} and ε_α be the corresponding eigenvalues. Let Ω_L^α denote the eigenstates of H with eigenvalue ε_α. Then Ω_L^α is always non-empty, and in particular has degeneracy*

$$|\Omega_L^{\varepsilon_\alpha}| = |\Omega_{L-1}| - |\Omega_{L-2}|. \tag{6.153}$$

This proposition is rather surprising at face value: since $[H_{\text{imp}}, H_{TL}] \neq 0$ we would not generically expect H to have eigenvalues equal to those of H_{imp}, and (6.153) says that the number of such eigenvalues is in fact exponentially large in

L. Indeed though, such states can be readily constructed, as we now prove.

Proof. Consder the space $|\alpha\rangle \otimes \Omega_{L-1}$. States in this space are almost the desired eigenstates of H, but they are not annihilated by $P_{1,2}$. The desired eigenstates are thus identified with the kernel

$$\Omega_L^\alpha = \ker(P_{1,2} : |\alpha\rangle \otimes \Omega_{L-1} \to |\Psi\rangle \otimes \Omega_{L-2}). \tag{6.154}$$

The map $P_{1,2}$ here is surjective for almost all choices of H_{imp}. Therefore using similar reasoning as above,

$$\begin{aligned} |\Omega_L^\alpha| &= \dim[|\alpha\rangle \otimes \Omega_{L-1}] - \dim[|\Psi\rangle \otimes \Omega_{L-2}] \\ &= |\Omega_{L-1}| - |\Omega_{L-2}| \\ &= \frac{1}{N}|\Omega_L| - \left(1 - \frac{1}{N}\right)|\Omega_{L-2}|. \end{aligned} \tag{6.155}$$

□

A similar result holds in a situation where one places impurities on both ends of the chain:

Corollary 6. *Let*

$$H_{two-imp} = H_{TL} + H_{\text{imp},1} + H_{\text{imp},L}, \tag{6.156}$$

where $H_{\text{imp},1/L}$ are independently random single-site Hamiltonians on the left and right ends of the chain, respectively. Let $\varepsilon_{\alpha_{1/L}}$ be their corresponding eigenvalues. Let also $\Omega_L^{\alpha_1+\beta_L}$ be the set of eigenstates of $H_{two-imp}$ with energy $\varepsilon_{\alpha_1} + \varepsilon_{\beta_L}$. Then

$$|\Omega_L^{\alpha_1+\beta_L}| = |\Omega_{L-2}| - |\Omega_{L-3}|. \tag{6.157}$$

This result is true even if the left and right impurities do not possess a common eigenbasis; all that matters is that they act only on single sites.

Proof. The proof proceeds as in the previous proposition, except with the starting state drawn from the vector space $\Omega_{L-1}^{\alpha_1} \otimes |\beta_L\rangle$. □

The above results tell us that even in the presence of local impurities, the spectrum of H contains exponentially large degeneracies. This leads to initially frozen states possessing memory of their initial conditions for infinitely long times, since the large number of degeneracies mean that a large number of energy levels of H do not dephase relative to one another. The following theorem makes this intuition precise:

Theorem 7 (non-thermalization of the TL + impurity model)**.** *Let $\mathcal{M}$ be the memory that typical fozen states in Ω_L have of their initial conditions:*

$$\mathcal{M} \equiv \mathop{\mathbb{E}}_{f\in\Omega_L} \lim_{T\to\infty} \frac{1}{T}\int_0^T dt\, |\langle f|e^{-iHt}|f\rangle|^2, \tag{6.158}$$

where $\mathbb{E}_{f\in\Omega_L}$ denotes an average over states in Ω_L. Then in the $L\to\infty$ limit,

$$\mathcal{M} = \frac{1}{N}\left(1 - \frac{4(N-1)}{(N+\sqrt{N^2-4})^2}\right)^2 + \cdots \tag{6.159}$$

is an order one constant (with the $\cdots$ denoting terms vanishing as $L\to\infty$).

Proof. Our proof will proceed by making use of the degenerate eigenstates in Ω_L^α. We start by writing

$$\begin{aligned}
\mathcal{M} &= \mathop{\mathbb{E}}_{f\in\Omega_L} \sum_{\mu,\nu\in\text{Spec}(H)} \delta_{E_\mu,E_\nu} |\langle\mu|f\rangle|^2 |\langle\nu|f\rangle|^2 \\
&\geq \mathop{\mathbb{E}}_{f\in\Omega_L} \sum_{\alpha\in\text{Spec}(H_{\text{imp}})} \sum_{\mu,\nu\in\Omega_L^\alpha} |\langle\mu|f\rangle|^2 |\langle\nu|f\rangle|^2 \\
&= \mathop{\mathbb{E}}_{f\in\Omega_L} \sum_{\alpha\in\text{Spec}(H_{\text{imp}})} \langle f|\Pi_{\Omega_L^\alpha}|f\rangle^2,
\end{aligned} \tag{6.160}$$

where

$$\Pi_{\Omega_L^\alpha} = \sum_{\mu\in\Omega_L^\alpha} |\mu\rangle\langle\mu| \tag{6.161}$$

and the $|\mu\rangle, |\nu\rangle$ are orthonormal eigenstates of H.

We then use $||v||_2^2 \geq \frac{1}{N}||v||_1^2$ for any $v\in\mathbb{R}^N$ together with an application of Jensen's inequality $\mathbb{E}_x[f(x)^2] \geq (\mathbb{E}_x[f(x)])^2$ to write

$$\begin{aligned}
\mathcal{M} &\geq \frac{1}{N} \mathop{\mathbb{E}}_{f\in\Omega_L} \left(\sum_{\alpha\in\text{Spec}(H_{\text{imp}})} \langle f|\Pi_{\Omega_L^\alpha}|f\rangle\right)^2 \\
&\geq \frac{1}{N} \left(\sum_{\alpha\in\text{Spec}(H_{\text{imp}})} \mathop{\mathbb{E}}_{f\in\Omega_L} \langle f|\Pi_{\Omega_L^\alpha}|f\rangle\right)^2.
\end{aligned} \tag{6.162}$$

The average over frozen states gives $\mathbb{E}_{f\in\Omega_L} |f\rangle\langle f| = \Pi_{\Omega_L}/|\Omega_L|$, so

$$\mathcal{M} \geq \frac{1}{N|\Omega_L|^2} \left(\sum_{\alpha\in\text{Spec}(H_{\text{imp}})} \text{Tr}[\Pi_{\Omega_L^\alpha}\Pi_{\Omega_L}]\right)^2. \tag{6.163}$$

Since $\Omega_L^\alpha \subset \Omega_L$, the trace is simply $|\Omega_L^\alpha|$ for all α. Thus

$$\begin{aligned}
\mathcal{M} &\geq N\left(\frac{|\Omega_L^\alpha|}{|\Omega_L|}\right)^2 \\
&= \frac{1}{N}\left(1 - (N-1)\frac{|\Omega_{L-2}|}{|\Omega_L|}\right)^2 \\
&\sim \frac{1}{N}\left(1 - \frac{4(N-1)}{(N+\sqrt{N^2-4})^2}\right)^2,
\end{aligned} \tag{6.164}$$

where the $\sim$ in the tast line denotes the leading scaling in the $L\to\infty$ limit. □

Since $\mathcal{M} \sim O(1)$ but $|\Omega_L|$ is exponentially large, almost all frozen states are guaranteed to retain memory of their intitial conditions for infinitely long times. From our numerical results we believe this result should remain true even when a term

$$H_Z = \sum_i \sum_{a=1} h_i^a |a\rangle\langle a|_i \tag{6.165}$$

is added to H, although the proof techniques for this case must necessarily be different on account of the fact that the degeneracy of H's spectrum is completely lifted for a generic choice of h_i^a.

Bibliography

[1] J. M. Deutsch. Quantum statistical mechanics in a closed system. *Phys. Rev. A*, 43:2046–2049, Feb 1991.

[2] Mark Srednicki. Chaos and quantum thermalization. *Phys. Rev. E*, 50:888–901, Aug 1994.

[3] Joshua M Deutsch. Eigenstate thermalization hypothesis. *Reports on Progress in Physics*, 81(8):082001, jul 2018.

[4] Marcos Rigol, Vanja Dunjko, and Maxim Olshanii. Thermalization and its mechanism for generic isolated quantum systems. *Nature*, 452(7189):854–858, 2008.

[5] Rahul Nandkishore and David A. Huse. Many-body localization and thermalization in quantum statistical mechanics. *Annual Review of Condensed Matter Physics*, 6(1):15–38, 2015.

[6] Luca D'Alessio, Yariv Kafri, Anatoli Polkovnikov, and Marcos Rigol. From quantum chaos and eigenstate thermalization to statistical mechanics and thermodynamics. *Advances in Physics*, 65(3):239–362, 2016.

[7] Fabien Alet and Nicolas Laflorencie. Many-body localization: An introduction and selected topics. *Comptes Rendus Physique*, 19(6):498–525, 2018. Quantum simulation / Simulation quantique.

[8] Dmitry A. Abanin, Ehud Altman, Immanuel Bloch, and Maksym Serbyn. Colloquium: Many-body localization, thermalization, and entanglement. *Rev. Mod. Phys.*, 91:021001, May 2019.

[9] Pablo Sala, Tibor Rakovszky, Ruben Verresen, Michael Knap, and Frank Pollmann. Ergodicity breaking arising from hilbert space fragmentation in dipole-conserving hamiltonians. *Phys. Rev. X*, 10:011047, Feb 2020.

[10] Vedika Khemani, Michael Hermele, and Rahul Nandkishore. Localization from hilbert space shattering: From theory to physical realizations. *Phys. Rev. B*, 101:174204, May 2020.

[11] Sanjay Moudgalya and Olexei I. Motrunich. Hilbert space fragmentation and commutant algebras. *Phys. Rev. X*, 12:011050, Mar 2022.

[12] Nicola Pancotti, Giacomo Giudice, J Ignacio Cirac, Juan P Garrahan, and Mari Carmen Bañuls. Quantum east model: Localization, nonthermal eigenstates, and slow dynamics. *Physical Review X*, 10(2):021051, 2020.

[13] Merlijn van Horssen, Emanuele Levi, and Juan P Garrahan. Dynamics of many-body localization in a translation-invariant quantum glass model. *Physical Review B*, 92(10):100305, 2015.

[14] Bhaskar Mukherjee, Debasish Banerjee, K Sengupta, and Arnab Sen. Minimal model for hilbert space fragmentation with local constraints. *Physical Review B*, 104(15):155117, 2021.

[15] Zhi-Cheng Yang, Fangli Liu, Alexey V Gorshkov, and Thomas Iadecola. Hilbert-space fragmentation from strict confinement. *Physical review letters*, 124(20):207602, 2020.

[16] Pietro Brighi, Marko Ljubotina, and Maksym Serbyn. Hilbert space fragmentation and slow dynamics in particle-conserving quantum east models. *SciPost Physics*, 15(3):093, 2023.

[17] Zhihao Lan, Merlijn van Horssen, Stephen Powell, and Juan P Garrahan. Quantum slow relaxation and metastability due to dynamical constraints. *Physical review letters*, 121(4):040603, 2018.

[18] Juan P Garrahan. Aspects of non-equilibrium in classical and quantum systems: Slow relaxation and glasses, dynamical large deviations, quantum non-ergodicity, and open quantum dynamics. *Physica A: Statistical Mechanics and its Applications*, 504:130–154, 2018.

[19] Giuseppe De Tomasi, Daniel Hetterich, Pablo Sala, and Frank Pollmann. Dynamics of strongly interacting systems: From fock-space fragmentation to many-body localization. *Phys. Rev. B*, 100:214313, Dec 2019.

[20] Sanjay Moudgalya, Abhinav Prem, Rahul Nandkishore, Nicolas Regnault, and B Andrei Bernevig. Thermalization and its absence within krylov subspaces of a constrained hamiltonian. In *Memorial Volume for Shoucheng Zhang*, pages 147–209. World Scientific, 2022.

[21] Melissa Will, Roderich Moessner, and Frank Pollmann. Realization of hilbert space fragmentation and fracton dynamics in 2d. *arXiv preprint arXiv:2311.05695*, 2023.

[22] Yves H Kwan, Patrick H Wilhelm, Sounak Biswas, and SA Parameswaran. Minimal hubbard models of maximal hilbert space fragmentation. *arXiv preprint arXiv:2304.02669*, 2023.

[23] Yahui Li, Pablo Sala, and Frank Pollmann. Hilbert space fragmentation in open quantum systems. *Physical Review Research*, 5, 2023.

[24] Hyungwon Kim and David A. Huse. Ballistic spreading of entanglement in a diffusive nonintegrable system. *Phys. Rev. Lett.*, 111:127205, Sep 2013.

[25] Brian Skinner, Jonathan Ruhman, and Adam Nahum. Measurement-induced phase transitions in the dynamics of entanglement. *Physical Review X*, 9(3):031009, 2019.

[26] Yaodong Li, Xiao Chen, and Matthew P. A. Fisher. Quantum zeno effect and the many-body entanglement transition. *Phys. Rev. B*, 98:205136, Nov 2018.

[27] Amos Chan, Rahul M. Nandkishore, Michael Pretko, and Graeme Smith. Unitary-projective entanglement dynamics. *Phys. Rev. B*, 99:224307, Jun 2019.

[28] Adam Nahum, Jonathan Ruhman, Sagar Vijay, and Jeongwan Haah. Quantum entanglement growth under random unitary dynamics. *Physical Review X*, 7(3), Jul 2017.

[29] Soonwon Choi, Yimu Bao, Xiao-Liang Qi, and Ehud Altman. Quantum error correction in scrambling dynamics and measurement-induced phase transition. *Phys. Rev. Lett.*, 125:030505, Jul 2020.

[30] Michael J. Gullans and David A. Huse. Dynamical purification phase transition induced by quantum measurements. *Physical Review X*, 10(4), Oct 2020.

[31] Yaodong Li, Xiao Chen, and Matthew P. A. Fisher. Measurement-driven entanglement transition in hybrid quantum circuits. *Phys. Rev. B*, 100:134306, Oct 2019.

[32] Yaodong Li, Xiao Chen, Andreas W. W. Ludwig, and Matthew P. A. Fisher. Conformal invariance and quantum non-locality in hybrid quantum circuits, 2020.

[33] Ruihua Fan, Sagar Vijay, Ashvin Vishwanath, and Yi-Zhuang You. Self-organized error correction in random unitary circuits with measurement. *Phys. Rev. B*, 103:174309, May 2021.

[34] Qicheng Tang and W. Zhu. Measurement-induced phase transition: A case study in the nonintegrable model by density-matrix renormalization group calculations. *Physical Review Research*, 2(1), Jan 2020.

[35] M. Szyniszewski, A. Romito, and H. Schomerus. Entanglement transition from variable-strength weak measurements. *Physical Review B*, 100(6), Aug 2019.

[36] Chao-Ming Jian, Yi-Zhuang You, Romain Vasseur, and Andreas W. W. Ludwig. Measurement-induced criticality in random quantum circuits. *Phys. Rev. B*, 101:104302, Mar 2020.

[37] Yimu Bao, Soonwon Choi, and Ehud Altman. Theory of the phase transition in random unitary circuits with measurements. *Physical Review B*, 101(10):104301, 2020.

[38] Shao-Kai Jian, Chunxiao Liu, Xiao Chen, Brian Swingle, and Pengfei Zhang. Measurement-induced phase transition in the monitored sachdev-ye-kitaev model. *Physical Review Letters*, 127(14), Sep 2021.

[39] Yimu Bao, Soonwon Choi, and Ehud Altman. Symmetry enriched phases of quantum circuits. *Annals of Physics*, 435:168618, 2021. Special issue on Philip W. Anderson.

[40] Jason Iaconis, Andrew Lucas, and Xiao Chen. Measurement-induced phase transitions in quantum automaton circuits. *Phys. Rev. B*, 102:224311, Dec 2020.

[41] Malte Henkel, Haye Hinrichsen, Sven Lübeck, and Michel Pleimling. *Non-equilibrium phase transitions*, volume 1. Springer, 2008.

[42] Xiao Chen, Yaodong Li, Matthew P. A. Fisher, and Andrew Lucas. Emergent conformal symmetry in nonunitary random dynamics of free fermions. *Physical Review Research*, 2(3):033017, Jul 2020.

[43] Ori Alberton, Michael Buchhold, and Sebastian Diehl. Trajectory dependent entanglement transition in a free fermion chain–from extended criticality to area law. *arXiv preprint arXiv:2005.09722*, 2020.

[44] Shengqi Sang and Timothy H. Hsieh. Measurement-protected quantum phases. *Physical Review Research*, 3(2), Jun 2021.

[45] Ali Lavasani, Yahya Alavirad, and Maissam Barkeshli. Measurement-induced topological entanglement transitions in symmetric random quantum circuits. *Nature Physics*, 17(3):342–347, Jan 2021.

[46] Matteo Ippoliti, Michael J. Gullans, Sarang Gopalakrishnan, David A. Huse, and Vedika Khemani. Entanglement phase transitions in measurement-only dynamics. *Physical Review X*, 11(1), Feb 2021.

[47] Dexin Zhong and Daniel ben Avraham. Universality class of two-offspring branching annihilating random walks. *Physics Letters A*, 209(5):333–337, 1995.

[48] Kwangho Park, Haye Hinrichsen, and In-mook Kim. Binary spreading process with parity conservation. *Phys. Rev. E*, 63:065103, May 2001.

[49] Mehran Kardar, Giorgio Parisi, and Yi-Cheng Zhang. Dynamic scaling of growing interfaces. *Phys. Rev. Lett.*, 56:889–892, Mar 1986.

[50] Mehran Kardar and Yi-Cheng Zhang. Scaling of directed polymers in random media. *Phys. Rev. Lett.*, 58:2087–2090, May 1987.

[51] Yaodong Li, Sagar Vijay, and Matthew P.A. Fisher. Entanglement domain walls in monitored quantum circuits and the directed polymer in a random environment. *PRX Quantum*, 4:010331, Mar 2023.

[52] Yaodong Li and Matthew P. A. Fisher. Statistical mechanics of quantum error correcting codes. *Phys. Rev. B*, 103:104306, Mar 2021.

[53] Yichen Huang. Dynamics of rényi entanglement entropy in diffusive qudit systems. *IOP SciNotes*, 1(3):035205, dec 2020.

[54] Tibor Rakovszky, Frank Pollmann, and C. W. von Keyserlingk. Sub-ballistic growth of rényi entropies due to diffusion. *Phys. Rev. Lett.*, 122:250602, Jun 2019.

[55] Marko Žnidarič. Entanglement growth in diffusive systems. *Communications Physics*, 3(1):100, 2020.

[56] Tianci Zhou and Andreas W. W. Ludwig. Diffusive scaling of rényi entanglement entropy. *Phys. Rev. Res.*, 2:033020, Jul 2020.

[57] Max McGinley, Sthitadhi Roy, and S. A. Parameswaran. Absolutely stable spatiotemporal order in noisy quantum systems. *Phys. Rev. Lett.*, 129:090404, Aug 2022.

[58] Aaron J Friedman, Oliver Hart, and Rahul Nandkishore. Measurement-induced phases of matter require adaptive dynamics. *arXiv:2210.07256*, 2022.

[59] Thomas Iadecola, Sriram Ganeshan, JH Pixley, and Justin H Wilson. Dynamical entanglement transition in the probabilistic control of chaos. *arXiv:2207.12415*, 2022.

[60] Michael Buchhold, Thomas Mueller, and Sebastian Diehl. Revealing measurement-induced phase transitions by pre-selection. *arXiv:2208.10506*, 2022.

[61] Mohsin Iqbal, Nathanan Tantivasadakarn, Thomas M Gatterman, Justin A Gerber, Kevin Gilmore, Dan Gresh, Aaron Hankin, Nathan Hewitt, Chandler V Horst, Mitchell Matheny, et al. Topological order from measurements and feed-forward on a trapped ion quantum computer. *arXiv preprint arXiv:2302.01917*, 2023.

[62] Michael Foss-Feig, Arkin Tikku, Tsung-Cheng Lu, Karl Mayer, Mohsin Iqbal, Thomas M Gatterman, Justin A Gerber, Kevin Gilmore, Dan Gresh, Aaron Hankin, et al. Experimental demonstration of the advantage of adaptive quantum circuits. *arXiv preprint arXiv:2302.03029*, 2023.

[63] Libor Caha and Daniel Nagaj. The pair-flip model: a very entangled translationally invariant spin chain. *arXiv preprint arXiv:1805.07168*, 2018.

[64] Scott Aaronson and Daniel Gottesman. Improved simulation of stabilizer circuits. *Phys. Rev. A*, 70:052328, Nov 2004.

[65] Matthew B. Hastings, Iván González, Ann B. Kallin, and Roger G. Melko. Measuring renyi entanglement entropy in quantum monte carlo simulations. *Phys. Rev. Lett.*, 104:157201, Apr 2010.

[66] Rajibul Islam, Ruichao Ma, Philipp M. Preiss, M. Eric Tai, Alexander Lukin, Matthew Rispoli, and Markus Greiner. Measuring entanglement entropy in a quantum many-body system. *Nature*, 528(7580):77–83, 2015.

[67] Alan J. Bray, Satya N. Majumdar, and Grégory Schehr. Persistence and first-passage properties in nonequilibrium systems. *Advances in Physics*, 62(3):225–361, Jun 2013.

[68] Bernard Derrida, Vincent Hakim, and Vincent Pasquier. Exact exponent for the number of persistent spins in the zero-temperature dynamics of the one-dimensional potts model. *Journal of Statistical Physics*, 85(5):763–797, 1996.

[69] Bernard Derrida, Vincent Hakim, and Vincent Pasquier. Exact first-passage exponents of 1d domain growth: Relation to a reaction-diffusion model. *Physical Review Letters*, 75(4):751–754, Jul 1995.

[70] Yiqiu Han and Xiao Chen. Measurement-induced criticality in $\mathbb{Z}_2$-symmetric quantum automaton circuits. *Phys. Rev. B*, 105:064306, Feb 2022.

[71] Daniel Gottesman. *Stabilizer Codes and Quantum Error Correction*. PhD thesis, California Institute of Technology, 1997.

[72] Tianci Zhou and Adam Nahum. Emergent statistical mechanics of entanglement in random unitary circuits. *Physical Review B*, 99(17), May 2019.

[73] Ivan Corwin and Yu Gu. Kardar–parisi–zhang equation and large deviations for random walks in weak random environments. *Journal of Statistical Physics*, 166(1):150–168, 2017.

[74] Guillaume Barraquand and Ivan Corwin. Random-walk in beta-distributed random environment. *Probability Theory and Related Fields*, 167(3):1057–1116, 2017.

[75] Pierre Le Doussal and Thimothée Thiery. Diffusion in time-dependent random media and the kardar-parisi-zhang equation. *Phys. Rev. E*, 96:010102, Jul 2017.

[76] Patrick Hayden, Micha Horodecki, Andreas Winter, and Jon Yard. A decoupling approach to the quantum capacity. *Open Systems & Information Dynamics*, 15(01):7–19, mar 2008.

[77] Winton Brown and Omar Fawzi. Decoupling with random quantum circuits. *Communications in Mathematical Physics*, 340(3):867–900, sep 2015.

[78] Winton Brown and Omar Fawzi. Short random circuits define good quantum error correcting codes. In *2013 IEEE International Symposium on Information Theory*. IEEE, jul 2013.

[79] Jason Iaconis and Xiao Chen. Multifractality in nonunitary random dynamics. *Physical Review B*, 104(21), dec 2021.

[80] Elliott H. Lieb and Derek W. Robinson. The finite group velocity of quantum spin systems. *Communications in Mathematical Physics*, 28(3):251–257, 1972.

[81] Pasquale Calabrese and John Cardy. Evolution of entanglement entropy in one-dimensional systems. *Journal of Statistical Mechanics: Theory and Experiment*, 2005(04):P04010, Apr 2005.

[82] Christian K. Burrell and Tobias J. Osborne. Bounds on the speed of information propagation in disordered quantum spin chains. *Phys. Rev. Lett.*, 99:167201, Oct 2007.

[83] Winton Brown and Omar Fawzi. Scrambling speed of random quantum circuits, 2013.

[84] Yiqiu Han and Xiao Chen. Entanglement structure in the volume-law phase of hybrid quantum automaton circuits. *Phys. Rev. B*, 107:014306, Jan 2023.

[85] O. Alberton, M. Buchhold, and S. Diehl. Entanglement transition in a monitored free-fermion chain: From extended criticality to area law. *Physical Review Letters*, 126(17), apr 2021.

[86] Utkarsh Agrawal, Aidan Zabalo, Kun Chen, Justin H. Wilson, Andrew C. Potter, J. H. Pixley, Sarang Gopalakrishnan, and Romain Vasseur. Entanglement and charge-sharpening transitions in u(1) symmetric monitored quantum circuits. *Phys. Rev. X*, 12:041002, Oct 2022.

[87] Zhi-Cheng Yang. Distinction between transport and rényi entropy growth in kinetically constrained models. *Phys. Rev. B*, 106:L220303, Dec 2022.

[88] Richard Arratia. The motion of a tagged particle in the simple symmetric exclusion system on z. *The Annals of Probability*, 11(2):362 – 373, 1983.

[89] Hansveer Singh, Brayden A. Ware, Romain Vasseur, and Aaron J. Friedman. Subdiffusion and many-body quantum chaos with kinetic constraints. *Phys. Rev. Lett.*, 127:230602, Dec 2021.

[90] Matteo Ippoliti and Vedika Khemani. Postselection-free entanglement dynamics via spacetime duality. *Phys. Rev. Lett.*, 126:060501, Feb 2021.

[91] Crystal Noel, Pradeep Niroula, Daiwei Zhu, Andrew Risinger, Laird Egan, Debopriyo Biswas, Marko Cetina, Alexey V Gorshkov, Michael J Gullans, David A Huse, et al. Measurement-induced quantum phases realized in a trapped-ion quantum computer. *Nature Physics*, pages 1–5, 2022.

[92] Jin Ming Koh, Shi-Ning Sun, Mario Motta, and Austin J Minnich. Experimental realization of a measurement-induced entanglement phase transition on a superconducting quantum processor. *arXiv:2203.04338*, 2022.

[93] Piotr Sierant, Giuliano Chiriacò, Federica M Surace, Shraddha Sharma, Xhek Turkeshi, Marcello Dalmonte, Rosario Fazio, and Guido Pagano. Dissipative floquet dynamics: from steady state to measurement induced criticality in trapped-ion chains. *Quantum*, 6:638, 2022.

[94] Nicolai Lang and Hans Peter Büchler. Exploring quantum phases by driven dissipation. *Phys. Rev. A*, 92:012128, Jul 2015.

[95] Matthew Fishman, Steven R. White, and E. Miles Stoudenmire. The ITensor Software Library for Tensor Network Calculations. *SciPost Phys. Codebases*, page 4, 2022.

[96] Matthew Fishman, Steven R. White, and E. Miles Stoudenmire. Codebase release 0.3 for ITensor. *SciPost Phys. Codebases*, pages 4–r0.3, 2022.

[97] Nicholas O'Dea, Alan Morningstar, Sarang Gopalakrishnan, and Vedika Khemani. Entanglement and absorbing-state transitions in interactive quantum dynamics. *arXiv:2211.12526*, 2022.

[98] Mark M. Wilde. *Quantum Information Theory*. Cambridge University Press, 2 edition, 2017.

[99] Thomas Kohlert, Sebastian Scherg, Pablo Sala, Frank Pollmann, Bharath Hebbe Madhusudhana, Immanuel Bloch, and Monika Aidelsburger. Exploring the regime of fragmentation in strongly tilted fermi-hubbard chains. *Phys. Rev. Lett.*, 130:010201, Jan 2023.

[100] Toshiya Kinoshita, Trevor Wenger, and David S Weiss. A quantum newton's cradle. *Nature*, 440(7086):900–903, 2006.

[101] Allen Scheie, NE Sherman, M Dupont, SE Nagler, MB Stone, GE Granroth, JE Moore, and DA Tennant. Detection of kardar–parisi–zhang hydrodynamics in a quantum heisenberg spin-1/2 chain. *Nature Physics*, 17(6):726–730, 2021.

[102] Neel Malvania, Yicheng Zhang, Yuan Le, Jerome Dubail, Marcos Rigol, and David S Weiss. Generalized hydrodynamics in strongly interacting 1d bose gases. *Science*, 373(6559):1129–1133, 2021.

[103] David Wei, Antonio Rubio-Abadal, Bingtian Ye, Francisco Machado, Jack Kemp, Kritsana Srakaew, Simon Hollerith, Jun Rui, Sarang Gopalakrishnan, Norman Y Yao, et al. Quantum gas microscopy of kardar-parisi-zhang superdiffusion. *Science*, 376(6594):716–720, 2022.

[104] Elmer Guardado-Sanchez, Alan Morningstar, Benjamin M Spar, Peter T Brown, David A Huse, and Waseem S Bakr. Subdiffusion and heat transport in a tilted two-dimensional fermi-hubbard system. *Physical Review X*, 10(1):011042, 2020.

[105] Sebastian Scherg, Thomas Kohlert, Pablo Sala, Frank Pollmann, Bharath Hebbe Madhusudhana, Immanuel Bloch, and Monika Aidelsburger. Observing non-ergodicity due to kinetic constraints in tilted fermi-hubbard chains. *Nature Communications*, 12(1):4490, 2021.

[106] Sanjay Moudgalya, Stephan Rachel, B. Andrei Bernevig, and Nicolas Regnault. Exact excited states of nonintegrable models. *Phys. Rev. B*, 98:235155, Dec 2018.

[107] Murray T Batchelor and Atsuo Kuniba. Temperley-lieb lattice models arising from quantum groups. *Journal of Physics A: Mathematical and General*, 24(11):2599, 1991.

[108] Britta Aufgebauer and Andreas Klümper. Quantum spin chains of temperley–lieb type: periodic boundary conditions, spectral multiplicities and finite temperature. *Journal of Statistical Mechanics: Theory and Experiment*, 2010(05):P05018, 2010.

[109] Sanjay Moudgalya and Olexei I Motrunich. Hilbert space fragmentation and commutant algebras. *Physical Review X*, 12(1):011050, 2022.

[110] See the supplemental materials for details.

[111] Hansveer Singh, Brayden A. Ware, Romain Vasseur, and Aaron J. Friedman. Subdiffusion and many-body quantum chaos with kinetic constraints. *Phys. Rev. Lett.*, 127:230602, Dec 2021.

[112] Shankar Balasubramanian, Sarang Gopalakrishnan, Alexey Khudorozhkov, and Ethan Lake. Glassy word problems: Ultraslow relaxation, hilbert space jamming, and computational complexity. *Phys. Rev. X*, 14:021034, May 2024.

[113] Russell Lyons and Yuval Peres. *Probability on trees and networks*, volume 42. Cambridge University Press, 2017.

[114] Matthew Fishman, Steven White, and Edwin Stoudenmire. The itensor software library for tensor network calculations. *SciPost Physics Codebases*, page 004, 2022.

[115] Vadim Oganesyan and David A. Huse. Localization of interacting fermions at high temperature. *Phys. Rev. B*, 75:155111, Apr 2007.

[116] LF Santos. Integrability of a disordered heisenberg spin-1/2 chain. *Journal of Physics A: Mathematical and General*, 37(17):4723, 2004.

[117] Vir B Bulchandani, David A Huse, and Sarang Gopalakrishnan. Onset of many-body quantum chaos due to breaking integrability. *Physical Review B*, 105(21):214308, 2022.

[118] Oliver Hart. Exact mazur bounds in the pair-flip model and beyond. *arXiv preprint arXiv:2308.00738*, 2023.

[119] Wolfgang Woess. *Random walks on infinite graphs and groups*. Number 138. Cambridge university press, 2000.

[120] David A Levin and Yuval Peres. *Markov chains and mixing times*, volume 107. American Mathematical Soc., 2017.

[121] Qucheng Gao, Pengfei Zhang, and Xiao Chen. Information scrambling in free fermion systems with a sole interaction, 2023.